Technische Universität München
TUM School of Natural Sciences

Optoelectronic Properties and Interactions of Molecular Monolayers on Semiconductor Substrates for Photoelectrocatalytic Applications

Felix Rauh

Vollständiger Abdruck der von der TUM School of Natural Sciences der

Technischen Universität München zur Erlangung eines

Doktors der Naturwissenschaften (Dr. rer. nat.)

genehmigten Dissertation.

Vorsitz: Prof. Dr. Martin Zacharias

Prüfer*innen der Dissertation:

1. Prof. Dr. Martin Stutzmann
2. Prof. Dr. Emiliano Cortés

Die Dissertation wurde am 12.10.2023 bei der Technischen Universität München eingereicht

und durch die TUM School of Natural Sciences am 21.02.2024 angenommen.

Zusammenfassung

Diese Arbeit befasst sich mit grundlegenden Eigenschaften von Hybridsystemen zur Verwendung in der Katalyse und der Entwicklung von Messmethoden zur *in-situ* Charakterisierung selbiger. Unter einem Hybridsystem wird in diesem Kontext eine Struktur aus einem anorganischen Halbleitersubstrat verstanden, dass mit einer Monolage eines organischen, katalytisch aktiven Moleküls bedeckt ist. Durch die Kombination dieser beiden Materialsysteme werden synergetische Effekte möglich, wie zum Beispiel der Ladungs- oder Energietransfer von Halbleiter zu Katalysator. Diese können zu einer Steigerung der Leistungsfähigkeit des Gesamtystems führen. Die erhofften synergetischen Effekte basieren auf bisher nur wenig untersuchten elektronischen Interaktionen von Halbleitersubstraten und darauf aufgebrachten Molekülen.

Zur Charakterisierung der Grenzfläche zwischen diesen Materialien werden daher im Rahmen dieser Arbeit Untersuchungen an einem Modellsystem, bestehend aus verschiedenen Halbleitermaterialen und den Molekülen Protoporphyrin IX oder Mabiq, herangezogen. Die Proben werden durch Langmuir-Blodgett-Deposition hergestellt, was eine reproduzierbare und vergleichbare Monolagenstruktur auf allen Halbleitermaterialien ermöglicht. Die Morphologie der Monolagen wird mit Hilfe von Rasterkraftmikroskopie untersucht und so optimiert, dass dichte Monolagen aufgebracht werden können. Die Dicke der jeweiligen Schichten deuten auf eine aufrechte Orientierung von Protoporphyrin IX hin, während Mabiq flach auf der Oberfläche liegt. Während die chemische Analyse mittels Röntgenphotoelektronenspektroskopie im Allgemeinen auf keine Veränderungen des Moleküls durch die durchgeführten Prozesse hindeutet, zeigt Ultraviolettphotoelektronenspektroskopie eine Veränderung der Austrittsarbeit des Halbleiters nach Bedeckung mit der Monolage. Dies ist ein Hinweis auf ein verschobenes Vakuumpotential, hervorgerufen entweder durch die inheränten Dipolmomente in den Molekülen oder durch partiellen Ladungstransfer zwischen den beiden Materialsystemen. Durch eine Kombination der Bestimmung der Bindungsenergie des höchsten besetzten Molekularorbitals mit der Analyse des Absorptionsspektrums wurde die Ausrichtung der Energieniveaus des Halbleiters mit dem Molekül für unterschiedliche Halbleitersubstrate bestimmt. Hierbei zeigt sich, dass die Position der Molekularorbitale unabhängig von den darunterliegenden Substraten ist. Die Energieniveaus des Moleküls sind durch die Position des Vakuumpotentials definiert. Für Protoporphyrin IX ließ sich des Weiteren zeigen, dass die Position der unbesetzten Orbitale relativ zum Leitungsband des Substrats einen Einfluss auf die Lumineszenzintensität hat, welche sich weitgehend durch Ladungstransfer entsprechend der Marcus-Theorie erklären lässt. Diskrepanzen zu dieser Theorie für Silizium, welches eine im Vergleich der untersuchten Materialien verhältnismässig kleine Bandlücke hat, zeigen allerdings, dass auch Interaktion mittels Energietransfer möglich sein könnte. Weiterführende Analyse von Metallo-Protoporphyrin IX mit verschiedenen Metallzentren offenbart

nur geringfügige Änderungen der relativen Energieniveau-Positionen, was die Relevanz der erbrachten Erkenntnisse für katalytische Systeme hervorhebt. Eine erfolgreiche Integration der untersuchten Langmuir-Blodgett-Filme in der Katalyse erfordert eine starke Adhäsion der Moleküle auf der Oberfläche. Dahingehend wird ein möglicher Prozess zur Erzeugung von kovalenten Bindungen zwischen einem mittels Langmuir-Blodgett-Deposition aufgebrachten Molekül und einem Halbleiter aufgezeigt. Zunächst wird eine selbstassemblierte Monolage von Aminopropyltriethoxysilan auf die Halbleiteroberfläche aufgebracht, welche mittels Silanbindungen eine kovalente Bindung and den Hydroxylgruppen der Oberfläche des Halbleiter eingeht. Die Amingruppe des Aminopropyltriethoxysilans ermöglicht die Erzeugung einer Amidbindung mit den Carboxylgruppen der danach aufgebrachten Langmuir-Blodgett-Schicht aus Protoporphyrin IX. Mittels *in-situ* Analyse durch Röntgenphotoelektronenspektroskopie nach Ausheizen bei moderaten Temperaturen lässt sich die intendierte Reaktion nachweisen. Rasterkraftmikroskopie deutet darauf hin, dass der Ausheizprozess zu keinen signifikanten Änderungen in der Morphologie führt. Die kovalente Bindung verbessert die Adhäsion, sodass die daraufhin bestimmten Kontaktwinkel von Wasser deutlich erhöht sind.

Die Möglichkeiten zur Erzeugung einer kovalenten Bindung und das gewonnene Wissen zur Interaktion der Materialsysteme können damit unter realen Katalysebedingungen getestet werden. Die analytischen Methoden zur Untersuchung solcher Hybridsysteme während der Katalyse sind limitiert, was die Gewinnung von aufschlussreichen Daten erschwert. Dieses Problem verschärft sich mit der gewählten flachen Oberflächenmorphologie, welche für die Analyse der grundlegen Interaktionen notwendig ist, bei der Katalyse allerdings auf Grund des schlechten Oberflächen-Volumen Verhältnisses zu niedrigen Produktkonzentrationen führt. Daher wird im Rahmen dieser Arbeit eine elektrochemische *in-situ* Methode basierend auf Infrarotspektroskopie in abgeschwächter Totalreflexion optimiert. Hierbei werden metallische Nanostrukturen auf Halbleiteroberflächen aufgebracht, welche mittels plasmonischer Verstärkung und lokaler Feldverstärkung die Oberflächensensitivität der Messung so stark verbessern, dass geringe Konzentrationen organischer Moleküle mit Bedeckungen deutlich unter einer Monolage auf der Oberfläche spektroskopisch untersucht werden können. Ähnliche Systeme finden bereits Verwendung in der Untersuchung von katalytischen Prozessen, sind aber insbesondere wegen ihrer eingeschränkten mechanischen Stabilität ungeeignet für Langzeit- oder zeitaufgelöste Messungen. Daher wurde im Rahmen dieser Arbeit eine Oberflächenstruktur basierend auf der Nanostrukturierung von Siliziumoberflächen entwickelt, welche neben einer leichten Verbesserung der Signalverstärkung eine deutliche Stabilitätsverbesserung erreicht. Zur Verifizierung der Eignung solcher Oberflächen für die Analyse von Katalyseprozessen mittels zeitaufgelöster Spektroskopie wurde die potentialabhängige Ad- und Desorption von 4-Methoxypyridin auf Goldoberflächen untersucht. Hierbei wurde eine Konzentrationsabhängigkeit der Zeitkonstanten festgestellt, welche durch eine Diffusionslimitierung des Moleküls im Elektrolyt erklärt werden konnte. Die erreichbare Zeitauflösung solcher potentialabhängiger Messungen ist durch die RC-Zeitkonstante des elektrochemischen Aufbaus limitiert. Hierbei kommt der im Rahmen dieser Arbeit entwickelten Oberflächenstruktur eine deutlich verbesserte laterale elektronische Leitfähigkeit zu Gute, welche die Messung von elektrochemischen Prozessen bis in den niedrigen Millisekundenbereich ermöglicht.

List of Abbreviations

AFM	Atomic Force Microscopy
APTES	(3-Aminopropyl)triethoxysilane
ATR	Attenuated Total Reflection
BSG	Black Silicon Gold (see Fig. 8.2)
BSGE	Black Silicon Gold Evaporated (see Fig. 8.2)
CB	Conduction Band
CCD	Charge-Coupled Device
CE	Counter Electrode
CM	Contact Mode
CPD	Contact Potential Difference
CV	Cyclic Voltammetry
DI	Deionized
DMSO	Dimethyl Sulfoxide
DOS	Density of States
EPDM	Ethylene Propylene Diene Monomer Rubber
FRET	Förster Resonant Energy Transfer
FSG	Flat Silicon Gold (see Fig. 8.2)
FTIR	Fourier Transform Infrared
FTO	Fluorine-Doped Tin Oxide
FWHM	Full Width at Half Maximum
HF	Hydrofluoric Acid
HOMO	Highest Occupied Molecular Orbital
HOPG	Highly Ordered Pyrolytic Graphite
ILG	Indium Tin Oxide Layer Gold (see Fig. 8.2)
IMFP	Inelastic Mean Free Path
IR	Infrared
IRE	Internal Reflective Element
ITO	Indium Tin Oxide
IZO	Indium Zinc Oxide
LB	Langmuir–Blodgett
LED	Light-Emitting Diode
LUMO	Lowest Unoccupied Molecular Orbital
MMA	Mean Molecular Area
MOP	4-Methoxypyridine
NEXAFS	Near-Edge X-Ray Absorption Fine Structure
NHS	*N*-Hydroxysuccinimide
NIR	Near-Infrared

NIST	National Institute of Standards and Technology
PEEK	Polyether Ether Ketone
PF	Peak Force
POM	Polyoxymethylene
PPIX	Protoporphyrin IX
PTFE	Polytetrafluorethylene
PVD	Physical Vapor Deposition
QNM	Quantitative Nanomechanical Mapping
RC	Resistance–Capacitance
RE	Reference Electrode
RMS	Root Mean Square
SAM	Self-Assembled Monolayer
SCA	Static Contact Angle
SECO	Secondary Electron Cut-Off
SEIRAS	Surface-Enhanced Infrared Reflection–Absorption Spectroscopy
SEM	Scanning Electron Microscopy
SMU	Source-Measure Unit
SNR	Signal-to-Noise Ratio
SPV	Surface Photovoltage
TCO	Transparent Conductive Oxide
TM	Tapping Mode
TOF	Turnover Frequency
TON	Turnover Number
UHV	Ultra-High Vacuum
UI	Voltage–Current
ULSI	Ultra-Large Semiconductor Integration
UPS	Ultraviolet Photoelectron Spectroscopy
UV	Ultraviolet
VB	Valence Band
WE	Working Electrode
XPS	X-Ray Photoelectron Spectroscopy
XRD	X-Ray Diffraction

Table of Contents

1. Introduction

1.1. Hybrid Catalysts: Invoking Synergies for Enhanced Conversion Performance

The ongoing emission of carbon dioxide (CO_2), largely driven by the preference for using fossil fuels for mobility, chemical and construction industry, and electricity generation, is a significant promoter of the greenhouse effect. The effort to reduce the greenhouse effect and thus minimize global warming, therefore, must include a solution that substantially reduces or eliminates carbon emission in the responsible sectors. Switching to renewable energy sources is the most viable way of solving this problem sustainably. Nevertheless, this switch comes with significant challenges associated with unreliable generation rates, leading to the need for efficient energy storage solutions [1]–[3].

Unfortunately, all industrially viable renewable energy storage methods have significant shortcomings compared to fossil fuels, particularly regarding their energy densities. While the energy in fossil fuels is stored in the chemical bonds of the material and can be released by simply burning the fuel, renewable energy storage either requires significant overheads, such as the electrodes, electrolytes, and structural material needed for batteries, or relies on approaches that are limited to much lower energy densities, such as those based on gravitational energy [4], [5]. This is especially problematic for mobility applications, in which both energy density and specific energy are important factors in the viability of achieving a meaningful range while maintaining reasonable vehicle mass and dimensions [6].

This challenge has sparked an interest in alternative solutions based on using electrocatalytic (or photoelectrocatalytic) processes to generate fuels, such as producing hydrogen and carbohydrates from water and CO_2, respectively. Such fuels exhibit energy densities much more comparable to fossil fuels and could, thus, be used interchangeably with them [7]–[9]. While the electrolysis of water has already reached a high level of maturity, there are still major challenges to overcome in photochemical water splitting and CO_2 reduction, associated with either the energy efficiency, reaction rate, or stability of the required catalysts [10]–[13].

Catalytic processes are generally divided into homogeneous processes occurring in solution and heterogeneous processes occurring on the surface of a solid material. In the context of water splitting and CO_2 reduction, both approaches have been pursued extensively. While substantial progress has been achieved, the currently available catalyst materials are still far from industrially viable due to the unique challenges associated with each approach [11], [14]. Combining homogeneous catalyst molecules with semiconducting or metallic substrates into a hybrid material by immobilizing them on the surface could provide a solution due to possible beneficial interactions between the molecules and the substrate. This could lead to a synergetic performance increase [15].

Compared to classical catalysts, hybrid approaches are relatively new. Many questions concerning the interaction between the molecules and the substrates remain unanswered, especially for semiconducting substrates. These involve possible performance penalties due to the catalytic properties being altered by intermolecular interactions in a dense monolayer arrangement, steric hindrance associated with the immobilization, and significant changes in electrolyte properties close to the surface of an electrode. Additional complexities of these systems include the semiconductor bulk properties, such as band gap and electron affinity, but also surface states and band bending in the near-surface regions. Finally, achieving a stable immobilization of a molecular monolayer on the surface strongly depends on the associated interface chemistry. Therefore, monolayer formation strategies need to be tailored to each semiconductor, leading to possible variations in the interactions due to changes in the interface states, the distance between the semiconductor and the molecules, and the packing density of molecules on the surface [15]–[17].

Despite these complexities, initial attempts have indicated a strong potential for hybrid approaches to outperform established catalyst systems [15], [18]–[20]. While the early results on hybrid catalysts appear promising, they are generally focused on the catalytic performance and not necessarily on understanding the fundamental processes at play. For many of the catalytic systems employed in these studies, a comprehensive analysis of these processes is challenging since it is difficult to control and analyze the interface, monolayer morphology, and other basic properties, with morphologies often based on nanoparticle structures.

1.2. Scope of this Work

This work attempts to disentangle the complex interconnected properties of hybrid catalytic systems through a systematic approach.

The first part of this thesis focuses on analyzing interface properties—such as energy level alignment, and charge and energy transfer processes—at model interfaces that closely resemble viable hybrid systems. These include various semiconductor substrates, such as silicon (Si), zinc oxide (ZnO), gallium nitride (GaN), aluminum gallium nitride (AlGaN), and aluminum nitride (AlN), in combination with model molecules based on protoporphyrin IX (PPIX) and Mabiq. The semiconductors were chosen so that the band gap and electron affinity could be varied continuously to investigate the influence of these material parameters accurately and independently. PPIX was chosen for the model system as a representative of a broad group of porphyrin and phthalocyanine catalysts [21]–[24]. Mabiq was chosen to represent a class of molecules that are capable of bimetallic functionality since they can coordinate with two metal centers, which could yield significant performance enhancement over standard organometallic catalysts [25]–[27].

The influence of varying monolayer formation processes due to different surface properties of the investigated semiconductors was circumvented through Langmuir–Blodgett (LB) deposition. In-depth investigations of the morphological properties of different molecules deposited under controlled, varying conditions resulted in a good understanding of the molecular orientation in the monolayer. Densely packed monolayers were achieved by optimizing the deposition parameters for all semiconductor–molecule combinations investigated in this work. These model systems were studied in controlled environments using surface-sensitive measurement methods to probe their chemical states and electronic interactions. The observed patterns and dependencies are explained using observations and theories that mainly originate from investigations of dye-sensitized solar cells, which are very similar in both structure and the processes that occur in the interaction between dye molecules and semiconducting substrates [28]–[31]. The insight gained through such fundamental studies can be applied to achieve more stable and efficient catalytic systems by matching a semiconducting substrate with a molecular catalyst, ensuring beneficial interaction.

Further investigations on the molecule–semiconductor interface were carried out by studying the effect of PPIX monolayers on the band bending at Si surfaces with different doping types and concentrations. In addition, the alignment of PPIX and its influence on Schottky junctions between Si and mercury (Hg) were investigated through electronic characterization techniques such as investigations of the voltage–current (UI) characteristics. These yield insight into the influence of doping on the energy level alignment at the interface and highlight possible applications of such hybrid structures for molecular electronics [32].

LB deposition generally leads to weakly attached, physisorbed monolayers. While this may suffice to study electronic interactions, such structures are not suitable for applications in catalytic devices. Therefore, a possible pathway to form chemical bonds between molecules and semiconductors was explored through the pretreatment of the substrate with (3-aminopropyl)triethoxysilane (APTES). A process to achieve chemisorbed PPIX on surfaces functionalized with APTES was demonstrated via amide bond formation through annealing. The initial physisorption and monolayer formation with a controlled subsequent chemical bonding reaction allows for further modification of monolayer structures, which is significantly harder to achieve with other functionalization techniques.

In addition to investigating such model systems, a method to study the synthesized devices under *in situ* conditions has been developed and optimized over the course of this work. This method is based on the combination of attenuated total reflection Fourier transform infrared (ATR-FTIR) spectroscopy and surface-enhanced infrared reflection–absorption spectroscopy (SEIRAS) to measure the surface properties of a working electrode (WE) in an electrochemical cell. While this measurement approach has been used in the past [33], [34], the implementation of time-resolved measurements imposes significantly higher demands on the sample structure, which are difficult to meet for the samples used so far. Therefore, an adapted approach based on nanostructuring the surface of the internal reflective element (IRE) itself via black Si etching is presented in this work [35]. These structures are compared to established surface structures, showing slightly better signal enhancement, improved surface conductivity, and improved adhesion using a model system based on the potential-dependent adsorption of 4-methoxypyridine (MOP) [36]. Time-resolved measurements of this system indicated diffusion-limited adsorption for low concentrations of MOP in the supporting electrolyte. The implemented device morphology could be a powerful measurement platform for *in situ* studies of hybrid systems since its surface enhancement allows for time-resolved measurements at sub-monolayer sensitivity. This could enable the determination of rate-limiting steps in the catalytic cycle of a molecular catalyst attached to the surface and could, thus, yield valuable insights into pathways for future device optimization.

2. Semiconductor Bulk and Surface Properties

2.1. Bulk Properties of the Semiconductors used in this Work

This chapter gives a broad overview of the basic properties of the semiconductors studied in this thesis. The semiconductor substrate materials were selected based on criteria such as their suitability for catalysis, the amount of information already available on their bulk properties, the possibility of obtaining or synthesizing samples with a reasonably flat surface, and, most importantly, their bulk electronic properties. Specifically, the band gaps and electron affinities of the chosen materials needed to span a broad range to enable the accurate determination of their influence on the electronic interaction with molecular monolayers.

2.1.1. Silicon

Si is the by far most widely adapted and studied semiconductor with a broad range of applications in industry, ranging from electronic components to photovoltaic devices. Due to its dominance across nearly all semiconductor-based devices, the properties of Si are well explored and understood. It is thus easily obtainable with very high purity and with polished surfaces that exhibit a low root-mean-square (RMS) roughness of 0.15 nm, making it an ideal substrate for the analysis of molecular monolayers [37], [38].

Si crystallizes in the diamond structure, in which every atom is sp^3 hybridized. The most prevalent crystal orientation in commercial use is the (100) surface, which was also used in this work. Si exhibits an indirect band gap of 1.12 eV at 300 K and an electron affinity of 4.05 eV, thus yielding an ionization potential of 5.17 eV [39], [40]. Si surfaces are typically covered with a self-passivating native surface oxide with a thickness of a few nanometers that forms upon exposure to environmental conditions. Si can be doped using elements such as phosphorus, arsenic, and antimony (n-type doping), or boron and aluminum (p-type), allowing for the convenient synthesis of p–n junctions or transistors. The native oxide can be removed through chemical processes involving, for example, hydrofluoric acid (HF). This treatment introduces a metastable H-termination to the surface, which passivates the Si surface and prevents reoxidation for up to a few hours [41], [42].

Compared to the semiconductors typically used in catalytic applications, the band gap of Si is smaller and its electron affinity is larger. This can yield unfavorable energy alignment with the redox potentials of the reaction intended to be catalyzed. The band gap needs to straddle the redox potentials to ensure the charge carriers have sufficient potential to drive the reaction. On the other hand, the narrow band gap results in very high solar conversion efficiencies close to the theoretical Shockley–Queisser limit.

2.1.2. Gallium Nitride, Aluminum Gallium Nitride, and Aluminum Nitride

GaN, AlGaN, and AlN are III–V nitride semiconductors that are commonly used in power electronics and for light-emitting diodes (LEDs) in the blue to ultraviolet (UV) wavelength range [43]–[46]. These materials can crystallize in either the wurtzite or zinc blende structure. All samples of this material group used in this work exhibit the wurtzite structure, which is made up of a stacked ABAB bilayer arrangement of hexagonally close-packed N^{3-} anions and Ga^{3+} or Al^{3+} cations. The ionic bonds between the metal and nitrogen ions cause an asymmetry, resulting in a slight variation of the tetrahedral angles of the structure. Therefore, the dipoles within the tetrahedra do not fully cancel out, leading to a spontaneous polarization along the ABAB stacking direction. Crystal surfaces normal to the stacking direction—the (0001) direction, also called c-plane—have different properties depending on the stacking direction of the crystal [47], [48]. The investigations described in this work were all carried out on c-plane surfaces, but care was taken to ensure that all experiments were carried out on the metal-polar crystal facet.

The abovementioned materials exhibit direct band gaps, with GaN having the lowest at 3.4 eV and AlN the highest at 6.2 eV (at 300 K). The ability to alloy these materials into $Al_xGa_{1-x}N$ provides the useful option to tune between these extreme cases by varying the Al to Ga ratio. This allows the electronic material parameters of the substrate to be varied continuously, which is not only useful for LED development but also for investigating interactions with molecular monolayers. This band gap variation also causes a change in the electron affinity of the material, ranging from 3.8 eV (GaN) [49] to 1.3 eV (AlN) [50]. The large shift in electron affinity is comparable to the change in the band gap energy, meaning that the ionization potentials of these semiconductors are similar at 7.2 eV and 7.5 eV. These values vary in the literature by more than 1 eV depending on the report [51]–[54]. This could be a result of the added complexity due to the crystal polarity, which could yield a significant electron affinity variation depending on the measured side of the crystal, but could also be a consequence of the measurement conditions [49], [55], [56]. Similarly to Si, all these materials are prone to surface oxide formation. While similar wet etching methods can be used to remove the oxide, the surface termination formed is generally considered unstable [56], [57]. This leads to a significantly faster reoxidation of the surface and typically requires *in situ* sample preparation techniques in ultra-high vacuum (UHV) systems to allow for an accurate determination of pristine surface properties.

Doping of these materials is significantly more challenging than with Si, since naturally occurring defects act like n-type dopants, leading to unintentional doping. Adding n-type dopants such as Si leads to a further increase in doping concentration. P-type doping is significantly more challenging to achieve because the intrinsic doping has to be overcome. This requires significantly higher doping concentrations and leads to decreased performance [44], [58],

[59]. To keep the analysis as reproducible as possible, the comparative studies carried out in this work only used not intentionally doped substrates.

2.1.3. Zinc Oxide

The last semiconductor material system to be studied in this work is ZnO, which is a II–VI oxide semiconductor. While its properties are similar to GaN, it is significantly less prevalent in commercial applications [60], [61]. It exhibits a similar unintentional n-type doping and is challenging to synthesize with p-type characteristics. Like III–V nitrides, ZnO crystallizes in the wurtzite structure and exhibits spontaneous polarization [61]. To maximize the compatibility, the ZnO surface investigated in this work is also c-plane and metal-polar. The studied samples are not intentionally doped. Since it is already fully oxidized, ZnO does not form any surface oxides.

While the band gap of ZnO is 3.4 eV [61], [62] and therefore similar to that of GaN, its electron affinity is significantly higher at 4.5 eV [63]. This provides decoupled information between band gap and electron affinity and is, thus, crucial to the analysis, since an increasing band gap is accompanied by an increasing electron affinity for all previously mentioned samples. Therefore, any differences in the electronic response between GaN and ZnO have a high probability of being a result of the variation in electron affinity.

2.2. Semiconductor Surfaces

While the bulk of a crystalline semiconductor is a predominantly well-defined periodic structure in which all atoms have a fixed coordination environment, the periodicity is inevitably interrupted as the material terminates. Atoms close to the surface are missing some of their coordination environment, leading to changes in the near-surface crystalline structure to minimize the free energy. In addition, dangling bonds can remain or interact with adsorbates. Non-oxide semiconductors generally form a thin surface oxide layer due to oxidation by atmospheric water or oxygen. All these influences lead to the formation of surface states, which are localized states that typically arise within the band gap of the semiconductor. These are partially filled by the electrons left over from the dangling bonds but also provide additional states to be filled by charge carriers from either the conduction band (CB) or valence band (VB) [64], [65].

A schematic depiction of the described surface processes can be found in Fig. 2.1. In the case of an n-type semiconductor, the additional unoccupied states within the band gap allow free charge carriers in the CB to occupy lower energy states. This leads to Fermi level alignment between the surface states and the bulk. A region of fixed positive charges from the dopant atoms remains. The electric field caused by the charge separation of these positive charges and the negatively charged occupied surface states leads to upward band bending of the CBs and VBs. For a p-type semiconductor, the acceptor states in the near-surface

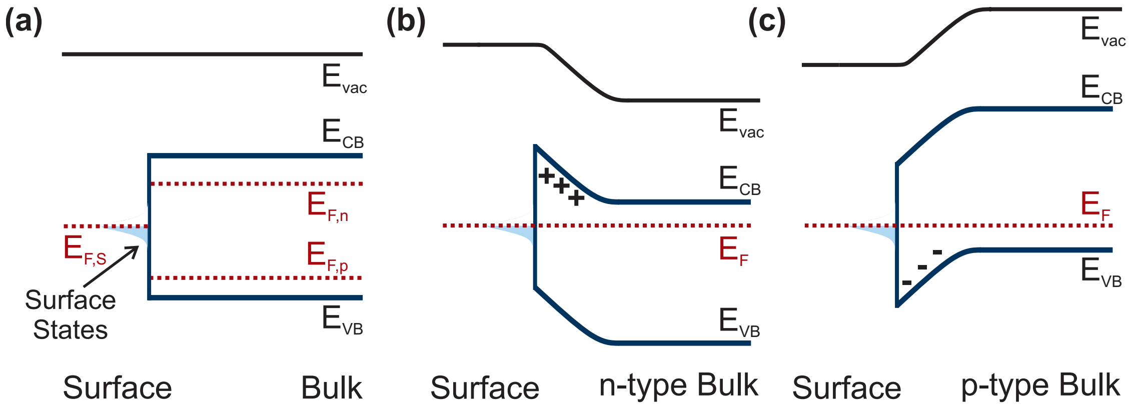

Figure 2.1 Simplified schematic depiction of the Fermi level alignment process between the semiconductor surface states and the bulk Fermi level. (a) The energy levels at their theoretical positions in the absence of interaction before any alignment has occurred, depicting the Fermi level of the surface $E_{F,S}$, the partially filled surface states, the Fermi level of a semiconductor with either n- or p-type doping $E_{F,n}$ or $E_{F,p}$, and the semiconductor CB and VB edge positions. (b)–(c) The equilibrium after Fermi level alignment for n- and p-type semiconductors: Remaining fixed charges from ionized donors or acceptors result in upward or downward band bending in the depletion region, respectively.

region can be filled by the electrons partially occupying the surface states, thus leading to Fermi level alignment and the depletion of holes in the near-surface region. The remaining fixed negative charges result in a downward band bending toward the surface [64], [65]. Due to the absence of free charge carriers in this surface-near region, it is called the depletion region.

Since the density of states (DOS) of the surface states usually is large compared to viable doping concentrations, the resulting change of the Fermi level at the surface due to this alignment process is relatively small. Therefore, the Fermi level is generally assumed to be pinned at a position defined mainly by the energy level of the surface states and largely independent of the bulk doping concentration [64], [65].

Above-band gap illumination of a surface causes a response in the surface band bending. An electron–hole pair generated upon the absorption of a photon is separated due to the electric field in the depletion region. In the case of an n-type semiconductor, holes drift toward the surface while electrons move into the bulk of the semiconductor. Holes accumulating at the surface counteract the band bending and result in a flattening of the band structure, as shown in Fig. 2.2(a). These holes can recombine with the electrons in the acceptor states or the surface states, but increasing excitation rates eventually lead to an asymptotic approach of flat band potential conditions, for which no band bending is present, as depicted in Fig. 2.2(b). Similarly, electrons diffuse to the surface for p-type semiconductors and cause an analogous process [67]–[69].

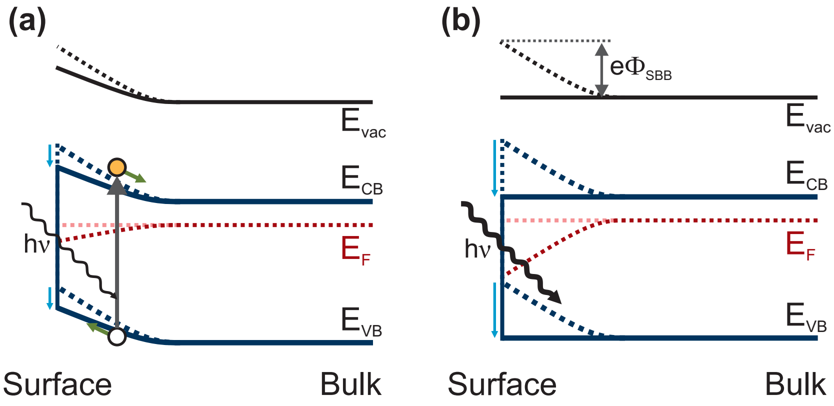

Figure 2.2 Simplified schematic depiction of the band flattening with increasing illumination intensity impinging on a semiconductor surface. (a) Response of free charge carriers generated in the depletion region near the surface, leading to a flattening of the surface band bending. (b) Completely saturated flat band structure as a result of high illumination intensity [66].

The surface band bending has major implications for the performance of a semiconductor-based catalyst because it determines the prevalent free charge carrier type at the surface. Supposing the semiconductor is intended for a reduction process, such as CO_2 reduction, it is necessary to provide electrons to the surface [64]. Thus, the near-surface region of the sample intended to perform catalysis should be a p-type semiconductor to ensure adequate amounts of photo-exited charge carriers. The implications for hybrid catalysts are described in more detail in Sec. 3.5.

2.3. Metal–Semiconductor Junctions

Establishing contact between a metal and a semiconductor typically results in the formation of a Schottky junction with an accompanying potential barrier and the formation of a space charge region. In a highly simplified picture, these properties arise solely from the Fermi level alignment process between the two materials, thus only depending on the difference in work functions of the materials (the Schottky–Mott limit).

For example, the alignment of an n-type semiconductor with a metal that has a lower Fermi level requires electrons to transfer from the semiconductor CB to the metal until the levels align. The transferred electrons leave localized charges from the ionized dopant atoms within the space charge region. This charge separation leads to an electric field resulting in band bending of the semiconductor VB and CB. Its magnitude is equal to the difference between the Fermi potentials of the separated materials and is called the built-in potential $U_{BI} = |\Phi_M - \Phi_{SC}|$. This band bending can either be mitigated or increased by applying an external bias, depending on its polarity. A decrease in band bending due to forward bias reduces the width of the space charge region and enables electrons to cross the junction. A reverse bias increases band bending and the width of the space charge region. The fixed potential barrier

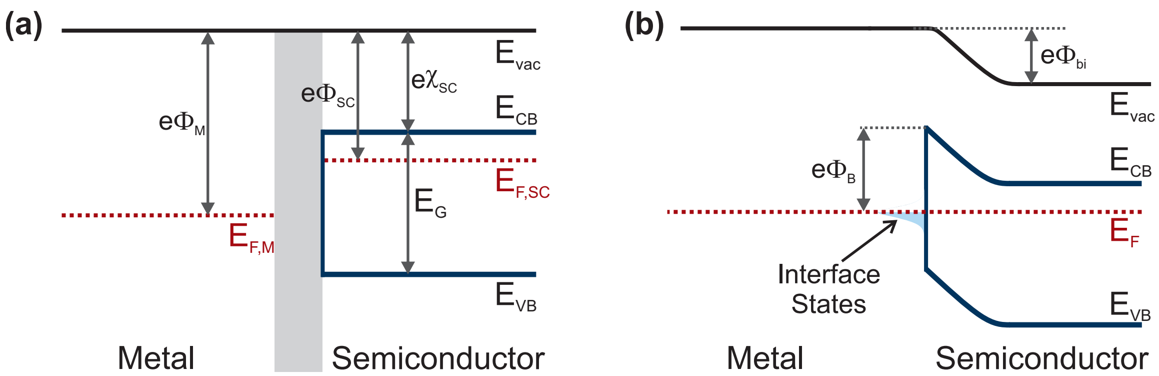

Figure 2.3 Simplified schematic depiction of the Fermi level alignment process between a metal and an n-type semiconductor. (a) Both materials in the absence of any interaction, showing the metal's work function $e\Phi_m$ and the semiconductor's electron affinity $e\chi_{SC}$, work function $e\Phi_{SC}$, band gap E_G, conduction band level E_{CB}, Fermi Level $E_{F,SC}$, and valence band level E_{VB}. (b) Energy level alignment between the metal and semiconductor, highlighting the influence of interface states, which pin the Fermi level. The resulting Schottky junction is characterized by a built-in potential Φ_{bi} and a potential barrier Φ_B.

defined by the semiconductor electron affinity and metal work function ($\Phi_B = |\Phi_M - \chi_{SC}|$) prevents significant charge transfer rates. Thus, the exemplary semiconductor–metal contact becomes rectifying [40].

In this simple picture, the junction properties depend solely on the bulk properties of the materials involved, as visualized in Fig. 2.3(a). This is inaccurate since the influence of interface states changes the energy level alignment significantly. Similarly to the previously described surface states, interface states generally arise at the metal–semiconductor interface due to the broken periodicity and associated dangling bonds. While these are generally also assumed to reside in the middle of the band gap of the semiconductor, their properties can differ slightly depending on the particular interface chemistry. This can lead to, for example, covalent bonds at the interface, thus changing their energy level position and/or recombination dynamics at the interface [70], [71].

Analogously to semiconductor surfaces, interface states lead to Fermi level pinning in the band gap. The alignment process, including these interface states, is depicted in Fig. 2.3(b). This pinning decreases the relevance of the bulk properties of the materials, particularly the difference in Fermi level [70], [71].

2.3.1. Thermionic Emission Theory

As described in the previous section, the energy level alignment at a metal–semiconductor junction leads to a rectifying behavior as current is passed through the junction. This behavior is generally investigated via UI measurements using the charge transport theory. The current across a Schottky junction is mainly caused by the majority charge carriers, which can cross the interface via various mechanisms, including carrier diffusion, thermionic emission, and tunneling.

At room temperature, the dominant transport mechanism for these contacts is thermionic emission over the potential barrier. The majority charge carriers in the sample have a finite probability of acquiring enough thermal energy to pass over the potential barrier. The occupation probability of higher states is reduced exponentially as the energy difference to the Fermi level increases:

$$n = N_C \exp\left(-\left(\frac{e\Phi_B}{k_B T}\right)\right). \tag{2.1}$$

where N_C is the effective density of states in the CB. This probability is proportional to the thermionic emission current. In equilibrium conditions without any external potential applied, the thermionic emission current matches in both directions, thus leading to no net current, as depicted in Fig. 2.4(a) for an exemplary n-type semiconductor.

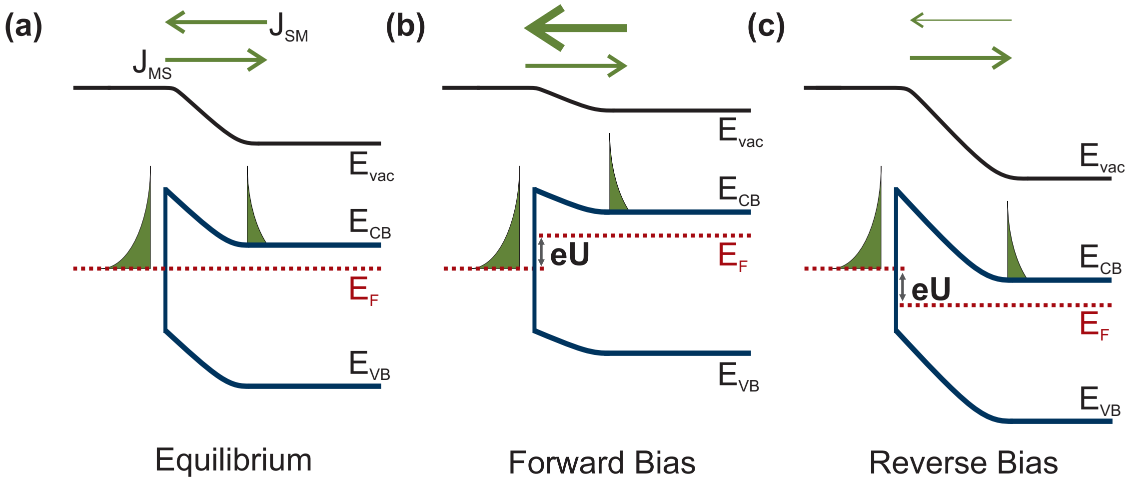

Figure 2.4 Schematic depiction of a Schottky junction between a large work function metal and an n-type semiconductor (a) without an external bias applied, (b) under a forward bias, and (c) under a reverse bias. The occupation probability of higher states due to thermal excitation and the resulting currents from and to the semiconductor are depicted in green.

Upon applying an external potential U, the Fermi level shifts at both sides of the interfaces. For a forward bias, this shift leads to a reduction of the effective potential barrier, thus shifting the electron distribution in the semiconductor accordingly:

$$n = N_C \exp\left(-\frac{e\Phi_B - eU}{k_B T}\right), \tag{2.2}$$

The current in the reverse direction remains unchanged, yielding the UI relationship

$$I = C N_C \exp\left(\frac{-e\Phi_B}{k_B T}\right)\left(\exp\left(-\frac{eU}{k_B T}\right) - 1\right). \tag{2.3}$$

This equation remains valid for the reverse bias direction. While the current from the metal to the semiconductor remains the same, the current in the opposite direction decreases exponentially. The prefactor CN_C is equal to A^*T^2, where A^* is the Richardson constant. Thus, the UI characteristics of a metal–semiconductor junction can be described by

$$I = I_S \left(\exp\left(\frac{-eU}{k_B T} \right) - 1 \right), \tag{2.4}$$

where I_S is the saturation current, given by

$$I_S = A^* T^2 \exp\left(\frac{-e\Phi_B}{k_B T} \right). \tag{2.5}$$

The barrier height for the thermionic emission can be determined by calculating I_S over a range of temperatures. Transforming the formula for the saturation current yields

$$\ln\left(\frac{I_S}{T^2} \right) = -\frac{e}{k_B T} \Phi_B + \ln(A^*). \tag{2.6}$$

Therefore, plotting $\ln\left(I_S/T^2\right)$ against $e/k_B T$ should result in a linear relationship for which the negative slope corresponds to the potential barrier Φ_B. This plot is called the Richardson plot and is commonly used to determine barrier heights.

3. Molecular Monolayers on Semiconductor Substrates

3.1. Langmuir–Blodgett Deposition

Langmuir–Blodgett deposition is a well-established method commonly applied in thin film deposition processes. It was introduced by Irving Langmuir and Katharine Blodgett in the early 20th century [72], [73], but still plays an important role in current research due to its ability to deposit high-quality thin films at large scales [74], [75]. This process is capable of monolayer deposition of organic molecules [76] or nanoparticles [77] by forced transfer from an air–liquid interface to a solid substrate surface. An exemplary schematic for LB deposition is shown in Fig. 3.1. The setup consists of a trough holding a subphase liquid (typically deionized [DI] water), motorized barriers that divide the subphase surface into regions of variable size, a sensitive force meter attached to a Wilhelmy plate used to determine changes in surface tension, and a motorized sample movement mechanism used to extract the sample intended to be coated with the monolayer.

An LB deposition process starts with the spreading of a low-concentration solution containing the material to be deposited on the surface of the liquid subphase. The surface coverage is determined by the amount deposited per subphase area and should be relatively low at this initial stage. The layer covering the surface of the subphase is called the Langmuir layer. Gradually reducing the accessible surface area through barrier movement leads to a compression of the layer constituents, which in turn results in changes of the relative surface coverage, packing, and orientation. The monolayer can be deposited onto the sample surface by controlled extraction of the sample as soon as the desired compression is reached.

The properties of the initial Langmuir layer before it is transferred to the sample have a great influence on the final monolayer. It is, therefore, important to initialize deposition after the optimal Langmuir layer is achieved. Insight into the properties of the Langmuir layer can be gained from its response to compression, which can be recorded as a surface pressure–area isotherm (often simply described as an isotherm). Surface pressure in the context of Langmuir films and LB deposition refers to the reduction of the surface tension of the subphase caused by the monolayer, and is described by

$$\Pi = \gamma_0 - \gamma_L, \tag{3.1}$$

where Π is the surface pressure, γ_0 is the surface tension of the pure subphase, and γ_L is the surface tension of the film-covered surface. This implies that the maximum achievable surface pressure is limited by the surface tension of the subphase, which is 72.8 mN m^{-1} in the case of water at room temperature [78].

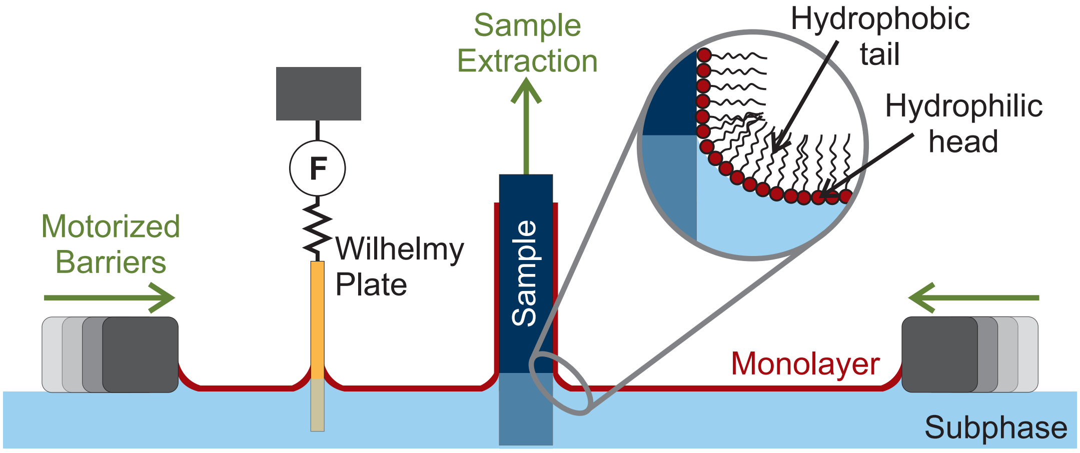

Figure 3.1 Schematic depiction of an LB deposition of a monolayer of amphiphilic molecules. The setup consists of a subphase with the amphiphilic molecules floating on its surface, motorized barriers to compress these molecules into a dense monolayer, a Wilhelmy plate to measure the resulting increase in surface pressure, and a sample that the monolayer is to be deposited on. This particular schematic depicts a deposition in which a hydrophilic sample is covered with the amphiphilic head of the molecule facing the sample. The opposite orientation can be achieved by using a hydrophobic surface that is immersed for deposition.

The surface pressure is measured using a Wilhelmy plate placed at the surface of the subphase. A force meter tracks the force exerted on the plate, which is the sum of the weight of the plate, the buoyancy associated with the displaced subphase, and the force associated with the surface tension. Correcting for the former two leaves the force associated with the surface tension, which can be related to the surface pressure through the adapted Wilhelmy equation

$$\Delta F = \Pi \cdot l \cos(\theta), \tag{3.2}$$

where ΔF is the measured change in force, l is the perimeter of the Wilhelmy plate, and θ is the static contact angle (SCA) at the surface of the Wilhelmy plate. In practice, the Wilhelmy plate is assumed to be fully wetted, resulting in an SCA of $\theta = 0$ and thus $\cos(\theta) = 1$ [79], [80].

A typical isotherm of a Langmuir film is depicted in Fig. 3.2(a). The isotherm exhibits various features associated with different monolayer phases. These can be understood as two-dimensional analogues of the three-dimensional gaseous, liquid, and solid phases, as shown in Fig. 3.2(b). At a low surface concentration of molecules, the film behaves analogously to the gaseous phase in three dimensions and is characterized by a small increase in surface pressure with decreased surface area, which can be described by the ideal gas equation modified for a 2-dimensional system:

$$\Pi a = k_B T, \tag{3.3}$$

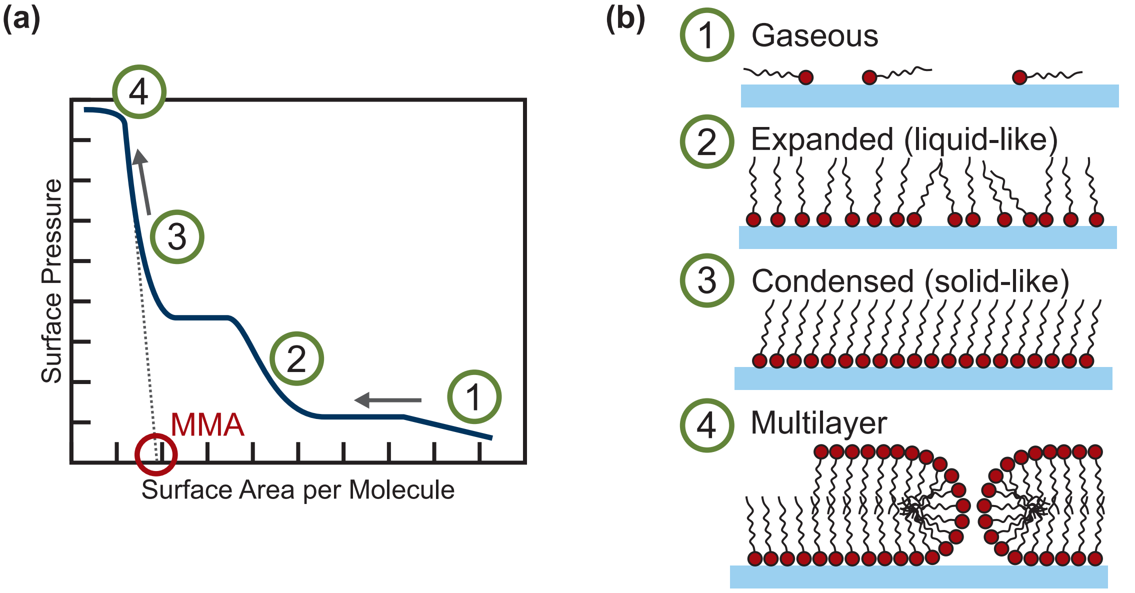

Figure 3.2 (a) Schematic diagram of a typical isotherm of a Langmuir layer depicting the increase in surface pressure with reduced subphase surface area. The isotherm generally consists of four distinct regions. (b) Microscopic view of the molecular orientation and interaction in these four regions, which are described by analogy to states of matter of three-dimensional materials for the three regions of lower pressure. With exceedingly large pressures beyond the stability limit, the monolayer breaks down and forms multilayer structures.

where a is the amount of area per molecule on the surface, called the mean molecular area (MMA), k_B is the Boltzmann constant, and T is the temperature of the system. As the surface area is reduced, the Langmuir film transitions to a liquid-like expanded phase. The phase change can be accompanied by a region of constant surface pressure associated with the coexistence of both phases. As soon as the film reaches phase purity, the surface pressure increases at a significantly higher rate. The expanded phase consists of molecules that experience substantial intermolecular interaction but maintain a rather random orientation. Further reduction of area initiates a phase transition to the solid-like condensed phase. Again, the transition region can be accompanied by a region of constant surface pressure. The pure condensed phase experiences an even higher surface pressure increase and is made up of a well-ordered and densely packed monolayer of molecules. The cut-off of this linear region of surface pressure increase yields the surface area occupied by a molecule in the condensed phase and, thus, allows for insight into the molecular orientation of the monolayer. The Langmuir layer collapses when the surface area decreases beyond the condensed phase. This is indicated by a saturation of the surface pressure. Further compression leads to the formation of increasingly large multilayers and agglomerates [78], [81], [82].

Similar to isotherms of three-dimensional materials, the occurrence or absence of these phases strongly depends on the molecular interaction, the molecular weight, and the temperature. Larger molecules transition directly from the gaseous to the condensed phase without exhibiting an intermediate phase. Depending on the intermolecular interaction, condensation of the Langmuir film might occur even without additional compression. In this case, the Langmuir film consists of self-assembled grains of molecules. The distance between grains decreases upon compression, resulting in the immediate observation of the condensed phase when the grains reach full surface coverage. In contrast, some molecules exhibit various expanded and condensed phases with more than two phase transitions [78], [80], [81].

A molecule must meet certain requirements to enable Langmuir film formation. A strict requirement is insolubility in the subphase because any solubility would imply that material deposited on the subphase surface would be dissolved and diffuse into the solution. Due to the small amount of material deposited on the subphase, even a very low solubility would cause substantial material loss from the surface. Other criteria, which do not rule out Langmuir film formation entirely but can render it significantly more challenging, are for the molecule to be soluble in a volatile solvent and for it to have an amphiphilic structure. The volatility of the solvent is important to allow for complete evaporation after deposition on the subphase surface. Any remaining solvent can disturb the formation of the Langmuir film and diminish the monolayer quality. An amphiphilic molecular structure aids in the formation of well-ordered monolayers since it provides a preferential orientation of the molecule depending on the subphase [78]. For DI water, the hydrophilic head group of an amphiphilic molecule would be preferentially oriented towards the subphase. The associated hydrogen bond formation between this head group and the water stabilizes the film and allows for significantly higher compression before the layer collapses [83].

An additional property of interest that can be derived from isotherm analysis is the compression modulus of the Langmuir film. This is defined analogously to the three-dimensional compression modulus as

$$K = -A\frac{d\Pi}{dA}, \tag{3.4}$$

where K is the compression modulus, A is the area per molecule, and Π is the surface pressure. This quantity gives an indication of how resistant the Langmuir film is to compression. It can yield information on how well the monolayer is packed. A plateau of the compression modulus is expected for elastic deformation and is commonly observed in the condensed phase. The magnitude of the compression modulus on this plateau is a measure of the intermolecular forces within the layer. Stronger interaction yields a higher compression modulus [78], [84], [85].

LB deposition of the formed Langmuir film is usually performed in its condensed phase since deposition from this phase provides the best homogeneity, the highest degree of order within the monolayer, and the largest relative coverage. The deposition is performed by extracting or immersing a substrate orthogonally oriented to the subphase surface. Depending on the direction of travel and the SCA between the sample and subphase, the orientation of an amphiphilic monolayer on the sample can be changed. In the case of a water subphase, extraction of a hydrophilic surface (with a SCA significantly less than 90°) leads to the hydrophilic head group facing the sample surface. Immersion of a hydrophobic surface leads to the hydrophilic group facing away from the sample. Other permutations of SCA and deposition direction generally do not result in a successful transfer. Therefore, the success of LB deposition depends primarily on the properties of the molecule to be deposited if the appropriate SCA of the subphase on the substrate is attained [78].

Repetition of multiple LB deposition cycles on the same substrate can yield multilayer structures with precisely controlled thicknesses. Due to the amphiphilic nature of the deposited molecules, the surface usually changes its SCA after a successful LB deposition. Therefore, the dipping direction is reversed for the subsequent monolayer, resulting in an ABAB structure of molecules facing in opposite directions [73], [78], [80].

3.2. Self-Assembled Monolayers

There are many alternative approaches to achieve a molecular monolayer of macroscopic horizontal dimensions on semiconductor surfaces. Most developed concepts revolve around self-assembled monolayers (SAMs) and include a functional anchoring group for chemical bond formation between the molecule and the substrate surface.

Self-assembly in the context of molecular monolayers describes an adsorption process onto a solid surface that forms highly ordered structures. The diffusion and adsorption of single molecules on the surface initiate the self-assembly process. Subsequent molecules form an initially amorphous layer that becomes increasingly more crystalline as the packing density increases and intermolecular interactions become relevant. After this nucleation process, well-ordered domains grow as more and more molecules are adsorbed at border sites. Therefore, SAM formation requires an anchoring group compatible with the substrate surface to be covered, as well as molecules that exhibit favorable molecular interactions. The complex interplay between the adsorption rate, surface anchoring, and intermolecular interaction must be balanced to achieve a well-ordered monolayer structure. Unsuitable conditions can lead to multilayer formation or incomplete attachment of the anchoring groups to the surface [86]–[88]. Some molecules are, thus, only suitable for SAM formation on a narrow subset of surfaces, rendering comparative studies of a molecule–semiconductor interaction, as intended in this work, challenging.

The self-assembly process can be supported through special immersion techniques. Most processes require tightly controlled reaction conditions in which the sample is submerged in an appropriate concentration of molecules in a solvent, but others rely on solvent evaporation to increase the concentration gradually. For example, the so-called "tethering by aggregation and growth" method uses solvent evaporation to deposit a monolayer comparably to LB deposition. Here, the sample is submerged in the solvent with the molecules, and the solvent evaporates slowly. The amphiphilic molecules to be deposited form well-ordered layers on the surface if the right conditions are met. As the solvent evaporates, the liquid level decreases and the sample surface slowly passes through this interface, leading to SAM formation [89], [90].

Popular SAM systems include, for example, thiol-based systems intended for deposition on gold (Au) [91] and organosilanes intended for metal and semiconductor oxides [92]. Other, less common options for anchoring groups include carboxylic acids, alkenes, and phosphonic acids [88], [89], [93]. These are typically combined with alkane backbones, polyethylene glycol oligomers, or extended π-systems to provide the intermolecular interaction necessary to establish a highly ordered structure. They can also be combined with end groups that provide various functions, such as the provision of additional binding sites [88].

The great advantage of SAMs over LB layers is the significantly increased stability associated with the covalent attachment to the surface. The physisorption of LB layers is likely unsuitable for a viable hybrid catalytic device since the device could easily be damaged via desorption of the catalyst layer [94]. Therefore, the possibility of a combination of SAMs and LB layers is explored within this work.

To this end, an organosilane approach was chosen to deposit an APTES SAM, mediating chemisorption through silane attachment to a Si substrate and provision of an amine functional end group. The intended purpose of this end group is amide bond formation to an LB-deposited PPIX monolayer. SAM formation of APTES on Si has been thoroughly explored in the literature; researchers have developed a variety of deposition procedures and a thorough understanding of the reaction mechanisms at play [95], [96]. Trisilanes pose significant challenges concerning their reaction mechanism due to the ability to polymerize along this functional group, which often causes multilayer formation if specific reaction conditions are not met. Therefore, the protective ethoxy group is necessary to prevent any unwanted reactions. If the molecule is exposed to humidity, however, the silane group is reduced and polymerization becomes likely [97], [98]. The resulting reproducibility issues regarding silane SAM formation and their comparatively low stability limit their viability for applications in catalytic devices. Nevertheless, they suffice for the demonstration of the chemisorption of LB layers.

3.3. Energy Level Alignment of Molecular Monolayers and Semiconductors

The relative positions of the highest occupied molecular orbital (HOMO) and the lowest unoccupied molecular orbital (LUMO) of the molecular monolayer compared to the semiconductor

CB and VB have a significant impact on how charges move between these two entities. It is, therefore, important to understand the processes and the outcome of energy level alignment between the monolayer and the substrate. This includes not only interactions between the molecules and the substrate but also between molecules within the thin film.

3.3.1. Intermolecular Interactions

Intermolecular interactions, including van der Waals, Coulomb, and π-orbital interactions, can have a significant impact on the formation of the Langmuir film and the electronic properties of the molecules within. These interactions are short-range and, thus, generally occur between adjacent molecules. They govern the molecular order within a Langmuir film. Sufficiently strong attractive interactions can lead to self-assembly processes of molecules on the subphase without the need for additional compression. This can, for example, be observed for molecules that exhibit extended π-orbitals, for which the molecules often tend to stack along the π-orbital axis to form a well-ordered structure [78].

Intermolecular interactions can also have a significant impact on the electronic structure of the molecule. Their impact can be observed in solvated and solid systems and can lead to changes in, for example, absorption or luminescence properties.

Due to the close packing of molecules in a condensed Langmuir film, these intermolecular interactions can become highly relevant for the electronic structure of an individual molecule. Depending on the type of molecule, the governing interactions can be very different. Due to the extended π-orbital systems and dipole moments of the molecules studied in this work, intermolecular interactions are assumed to be the governing contributions in the LB monolayers studied.

Extended π-orbital systems have been studied extensively in the context of organic semiconductors. Small-molecule organic semiconductors have a very similar molecular structure and exhibit a comparable ordering when synthesized as molecular crystals. The overlapping π-orbitals within this ordered structure lead to hybridization, as depicted in Fig. 3.3 for an exemplary system of ethylene molecules. As more molecules interact, this hybridization leads to the formation of narrowly separated states and can, depending on the interaction strength, lead to the establishment of band-like structures [99], [100]. This is accompanied by a broadening of the absorption features and a narrowing of the HOMO–LUMO splitting, as shown in Fig. 3.3 [99], [101]. The interaction strength is strongly coupled to the molecular orientation and the resulting overlap of neighboring π-orbitals. Most organic semiconductors contain aromatic heterocycles, such as benzene, pyrrole, pyridine, or thiophene, which leads to the establishment of π-orbitals that extend perpendicular to the heterocycles. The relative distances and orientations of these heterocycles determine the interaction. Many organic semiconductors crystallize in a herringbone-like layer-by-layer structure. This yields high orbital overlap between molecules within the same layer and reduced overlap between molecules of adjacent layers. Consequently, these materials can exhibit strongly anisotropic physical properties [99], [100].

A limitation of the analogy between the studied LB films and organic semiconductors is their extent along the direction perpendicular to the substrate surface, since the films studied in this work consist of only a single layer. This is a significant departure from the interaction, and thus it is unclear whether the synthesized LB layers hybridize to the extent observed for organic semiconductor systems. Nevertheless, they still exhibit a strong resemblance to a single layer of the previously described layer-by-layer structure that some organic semiconductors crystallize in.

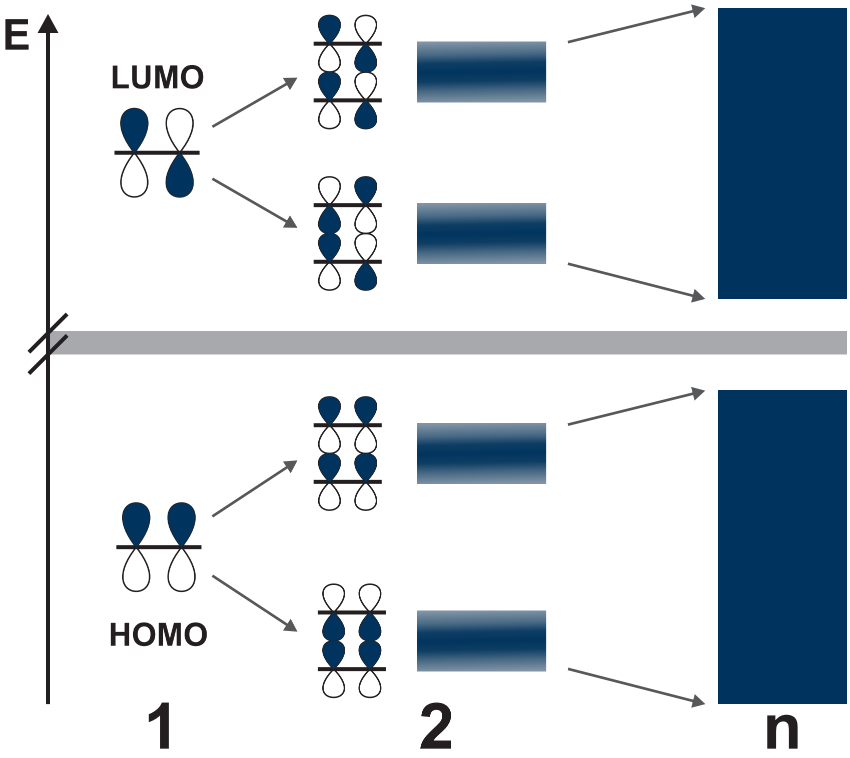

Figure 3.3 Schematic representation of the molecular orbital hybridization of ethylene π-orbitals, highlighting the broadening and energy gap reduction upon dimer (2) and oligomer (n) formation.

The resulting changes in molecular orbital energies can alter the catalytic performance of a potential catalyst. The possibility of charge transfer between molecules in the catalyst monolayer has so far only been explored in a limited manner, but could have a significant impact. In addition, the close packing could lead to steric hindrance and, therefore, reduce the catalytic performance. It is, therefore, not guaranteed that a well-performing homogeneous catalyst will perform well within a close-packed system such as an LB layer or a SAM. It might, therefore, be desirable to reduce the density of catalyst molecules and control their orientation on the surface to prevent any adverse effects associated with the interactions enabled by close packing. Such a structure can be challenging to synthesize because many catalytically active molecules also contain aromatic heterocyclic structures that tend to self-assemble. Deposition of a sub-monolayer to homogeneously cover the substrate surface with a lower density of molecules is likely to result in undesirable islands of close-packed molecules. This can, for example, be mitigated in the SAM formation process by forcing the π-orbital structure to be normal to the semiconductor surface through axial ligation [102]. A covalent bond in the axial direction limits the ability of the molecule to tilt upright, thereby leading to a horizontal orientation on the surface. This axial ligation leads to a partial overlap of the π-orbital structure with the semiconductor, possibly leading to stronger interactions with the substrate [103].

In addition to these hybridization and self-assembly phenomena, π-orbital systems can form J- or H-aggregates, which exhibit unique properties due to the dipole–dipole interactions of the transition dipole moments of the aggregated molecules. The physical properties of an aggregated set of molecules change depending on the orientation and stacking of the molecules [104]. In the case of a J-aggregate, this results in reduced Stokes shift and a sharpening of the spectral absorption and luminescence features. An H-aggregate exhibits an increased Stokes shift, generally broader features, and significantly reduced luminescence [105], [106]. These special aggregates were initially found by Kasha *et al.* and were interpreted as a consequence of dipole interactions between the adjacent monomers [107], [108].

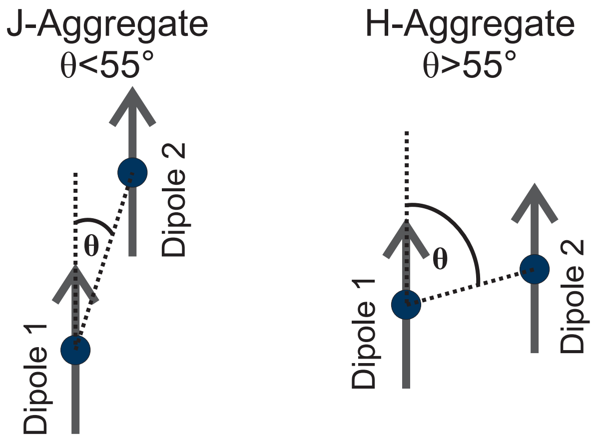

Figure 3.4 Depiction of dipole arrangement and slip angle θ leading to the formation of J- and H-aggregates.

As the slip angle θ between the origins of the dipole moments changes, the resulting interaction either causes a decrease (J-aggregate) or an increase (H-aggregate) in the exciton energy, leading to the observed spectral shift [107], [108]. The transition between H- and J-aggregates is expected to occur at a slip angle of 55° [104], as shown in Fig. 3.4.

3.3.2. Substrate–Molecule Energy Level Alignment

The molecules can interact not only with each other but also with the substrate. This interaction is especially relevant in the case of monolayers since all molecules are in intimate contact with the substrate. The system under investigation shares many similarities with the metal–semiconductor junctions described in Sec. 2.3, presumably because similar semiconductor interface properties are involved. In addition, the molecular system adds some complexity since it cannot be approximated by only considering its work function, as was the case for a metallic interaction partner. The parameters needed to accurately describe the energy level alignment are the electron affinity χ, the band gap E_G, the Fermi level E_F relative to the vacuum level (work function Φ), the ionization potential $\Phi_{IE,SC}$, and the HOMO and LUMO positions of the molecule relative to the vacuum level, which are depicted in Fig. 3.5(a) [109]. The ability for charges to cross over the interface is influenced by the positions of the HOMO and LUMO relative to the CB and VB edges of the semiconductor. Therefore, this alignment should be favorable to provide the charges necessary for the molecule to perform the intended catalytic reaction. For example, a catalytic reduction reaction, such as that of CO_2, can benefit from electron transfer to the molecule. The specific transfer mechanisms and different schemes involving photoexcitation are described in more detail in the following Sec. 3.4.

The simplest approach to predicting the alignment of the electronic structure at hybrid interfaces is simply lining up the separately determined energy levels of the two constituent materials at the Fermi level. This method was commonly used in early research into hybrid systems. Analogously to the analysis of metal–semiconductor junctions, another approach employs the Schottky–Mott rule, only relying on the difference in Fermi levels of the two materials. However, in the case of semiconductor–monolayer interactions, this oversimplifies the interaction due to neglecting influences from other effects. Because of the complexity of the system, a variety of approaches have been developed to describe the energy level alignment process at hybrid interfaces, mainly focusing on the interaction with metallic substrates and involving multilayer organic films. Due to the lack of studies explicitly discussing semiconducting substrates, these offer the best available starting point to understand the observed alignment processes.

More in-depth investigations of hybrid interfaces have revealed the presence of an abrupt vacuum level shift at the interface [109], [110]. The magnitude of the shift varies depending on the substrate and molecule studied. In addition, the molecule orientation in the monolayer can have a significant impact on the alignment since the involved molecules are generally asymmetric. To this end, a polar molecule can yield potential shifts at the interface due to the induced net polarization that might arise for a well-ordered film of uniform molecular orientation. Similarly, chemical bond formation in SAMs can also affect the potential shift [111]–

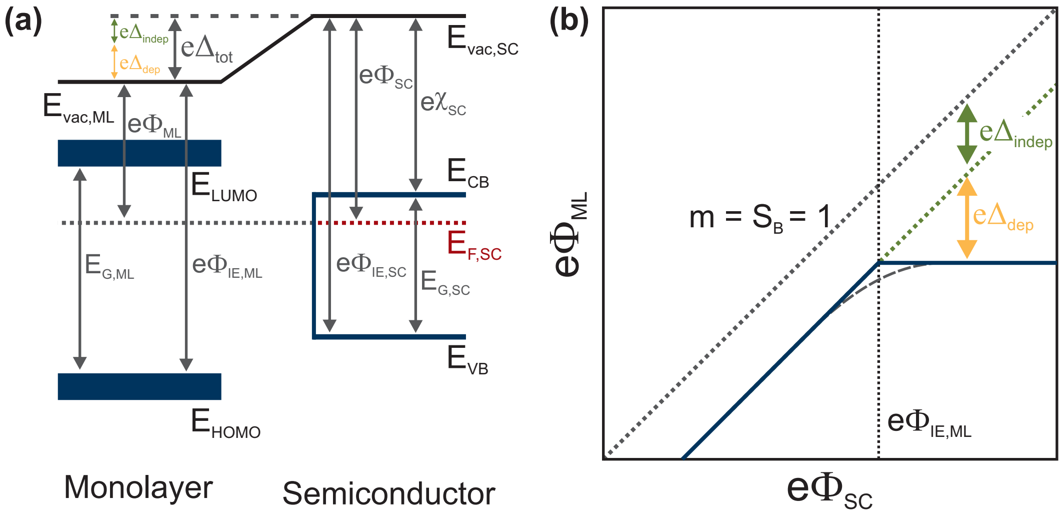

Figure 3.5 (a) Energy level diagram of a monolayer semiconductor interface including a depiction of all parameters needed to determine the alignment. Surface band bending in the semiconductor is omitted for readability. An interface dipole (Δ) emerges at the interface, which is in part due to the molecular properties and other influences independent of the substrate work function (Δ_{indep}), and in part due to charge carrier transfer depending on the work function if the work function of the substrate is in the vicinity of the molecule HOMO (Δ_{dep}). (b) Depiction of the dependence of the work function of the substrate with monolayer on the bare substrate work function in blue, which is offset by the independent dipole (green). The alignment initially follows the expected linear behavior, with a slope, or proportionality factor, of $m = S_B = 1$. As the work function of the semiconductor approaches the ionization energy of the molecular structure, charge transfer leads to the pinning of the Fermi level at the HOMO edge due to the formation of an additional dipole (yellow).

[113]. Lastly, the compression of the substrate work function due to the adsorbed molecules (the pillow effect) also induces a potential shift [114].

Some studies have observed a shift that is nearly independent of the substrate work function, indicating that only the molecular structure contributes. Others have determined that this shift can be influenced by the substrate. This influence is characterized by the interface parameter S_B, which describes the proportionality between the work function of a substrate covered with molecules and the reference work function of the material, as shown in Fig. 3.5(b). The parameter S_B varies between 0 and 1, with 0 indicating that the work function of a metal substrate covered with a molecule is independent of the substrate work function, and 1 meaning that the work function of the surface of the layer of molecules directly follows the substrate work function [115]. Therefore, an interface parameter of 0 would indicate a pinned interface, while 1 would point to full agreement with the Schottky–Mott rule. Initially, it was not clear what characteristics of an interface would result in a specific interface parameter, but UHV studies of a wider range of substrate work functions and molecules revealed that departure from the Schottky–Mott rule is associated with the substrate Fermi level approaching the HOMO of the molecule. This initiates charge transfer from the HOMO to the substrate, thus forming an additional surface dipole dependent on the difference between the HOMO and the substrate work function [116]–[118]. This additional dipole pins the Fermi level of the semiconductor at the HOMO level, leading to an interface parameter of 0, as depicted in Fig. 3.5(b) [116].

In summary, the energy level alignment process at substrate–molecule interfaces is complex and can be affected by a variety of processes. This complexity is increased further by the surface properties of semiconductors, with most studies having focused on the interaction with simpler metallic surfaces. This makes it challenging to predict the energy level alignment at interfaces, requiring experiments to determine it accurately. Unfortunately, experimental determination of the interface properties is challenging due to its proximity to the surface. This can lead to a strong influence of environmental parameters, limiting the reproducibility of the experiment and yielding inaccurate results. Some researchers therefore use UHV experiments to study the interface in a controlled environment. While this alleviates the issues that environmental influences can cause, it limits the relevance of the research to device development since the synthesis and application of the envisioned hybrid device renders exposure to atmospheric conditions inevitable.

3.4. Transfer Interactions of Molecular Monolayers and Semiconductors

While the previous section discussed energy level alignment and also briefly addressed the topic of charge transfer in that context, this section gives a short introduction to the transfer interactions between the molecular monolayer and the semiconductor for excited state molecules. Due to the lack of a detailed theory describing the charge or energy transfer from a semiconductor to a molecule, the presented theoretical models mainly describe charge transfer from an excited molecule to a semiconductor. These models were originally developed to understand intermolecular interactions but have been adapted to molecule–semiconductor systems by incorporating a continuous DOS to describe the semiconductor CB or VB.

The main focus of research for excited state interaction has historically been on electron transfer from molecules to oxide semiconductors, such as titanium dioxide (TiO_2). This is due to the relevance of this process for dye-sensitized solar cells, which use an organic sensitizer usually deposited on TiO_2 to enhance absorption coefficients. The excited electron from the molecule is transferred to the oxide, leading to charge separation at the molecule–TiO_2 interface. The transferred electron is usually replenished through an iodine redox couple dissolved in an electrolyte [119].

3.4.1. Marcus Theory on Charge Transfer

The prevalent theory describing charge transfer rates between molecules was mainly developed by Rudolph Marcus and is accordingly called Marcus theory [120], [121]. He was awarded the Nobel Prize for his work on the theory in 1992, underlining its important role in the description of charge transfer processes [122]. In its original form, this theory focuses on outer electron transfer, excluding major structural changes of the charge donor or acceptor molecule, especially the formation or breaking of chemical bonds. Thus, it was mainly intended to describe charge transfer processes between weakly coupled molecules. However, it has since been expanded to describe a variety of other charge transfer processes. Marcus theory is based on the Franck–Condon principle, a consequence of the vastly different timescales needed for fast electronic processes, such as absorption or transfer, and the resulting nuclear motions. During a charge transfer or absorption process, the surrounding nuclear environment cannot respond. Thus, the nuclear configuration before and after the process is identical. The Franck–Condon principle states that a process is more likely to occur if the thermodynamically ideal configurations at the start and end state are identical, thus not requiring any reorganization of the affected nuclei [123]. While this theory was developed with vibrational transitions of molecules in mind, it can also be applied to the reorganization of nuclei upon charge transfer, for example in a solvent environment.

The model is motivated by a classical electrostatic approach to investigating the charge transfer between two spheres in a polarizable solvent. Here, a charge transfer from one sphere to the other yields a polarization response, which can be split into a fast component associated with the electrons within the solvent molecules and a slow response associated with molecule rotation and reorganization. These processes can be different for solvent molecules in the direct vicinity of the sphere (inner region), which have a well-organized and complex structure, and the free solvent (outer region). Due to the long-distance interactions associated with electric fields, Marcus theory assumes that the outer region interactions dominate the overall energetics of the system since the inner sphere has a comparatively negligible volume. With these assumptions, Marcus found a parabolic dependence of the increase in free energy on the amount of charge transferred [120]–[122].

This parabolic behavior is also applicable to the microscopic picture of transferring single charges because it only describes the response of the surrounding environment and, thus, can still be described classically. Since no transfer of sub-integer charges is possible, the parabolic behavior is now interpreted as an abstract parameter that includes all influences associated with nuclear reorganization, called the nuclear configuration. In general, the donor and acceptor states of a charge transfer process are not energetically degenerate and have different energies. This is represented as a vertical shift between the parabolas of the donating and receiving states. The energy diagram describing a charge transfer process between two molecules is shown in Fig. 3.6(a), depicting the change in nuclear configuration for the equilibrium states q_i, the shift in free energy ΔE, and the so-called reorganization energy λ, which is the energy needed to reorganize the nuclear configuration to the equilibrium state from the acceptor state without any charge transfer [120]–[122].

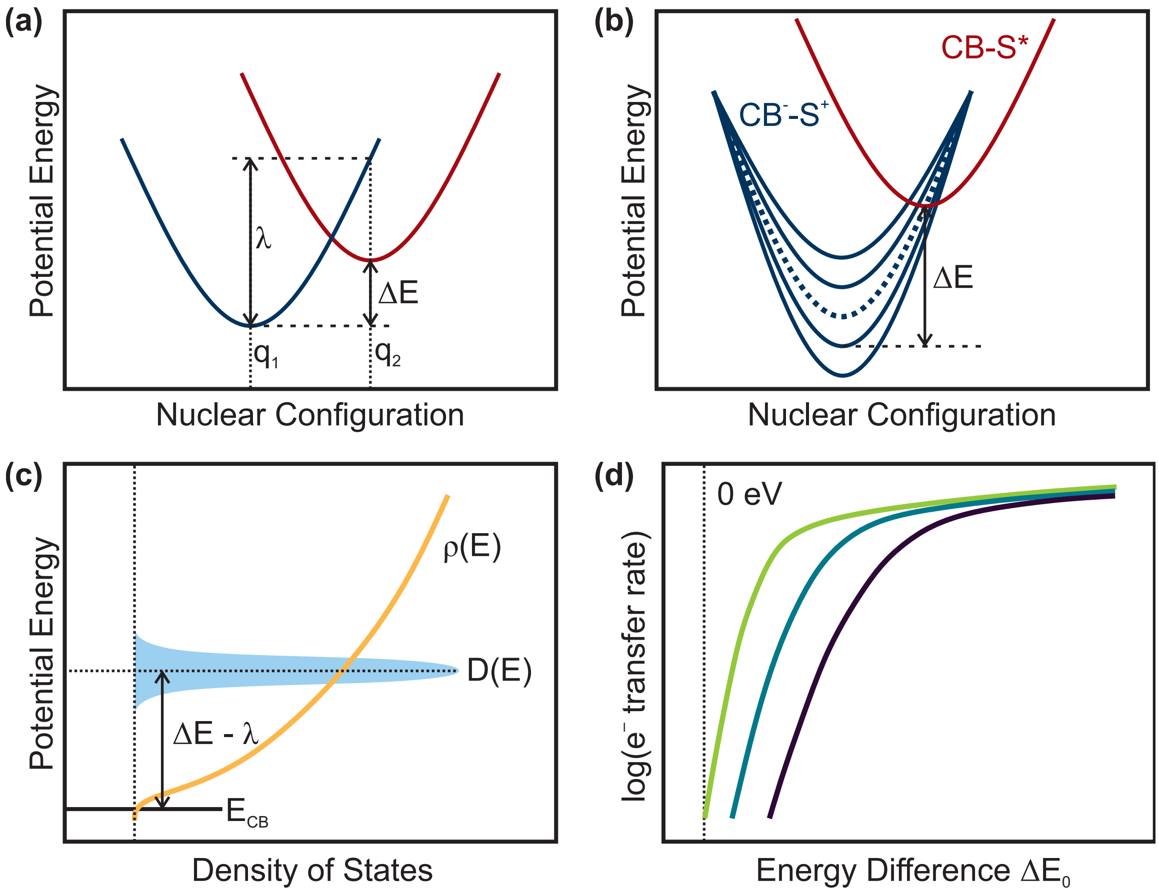

Figure 3.6 Schematic depiction of the derivation of electron transfer rates between a system with a continuous DOS and one with a single state. (a) Simplified potential landscape for the derivation of electron transfer rates in a system with two single-state entities, with the relevant parameters being the center distance, reorganization energy, and potential gradient. (b) Extension of (a) for an acceptor system consisting of a continuous DOS with the corresponding variation in potential gradient. (c) Overlap of the DOS of the acceptor system $\rho(E)$ with the energy level of the donor molecule $D(E)$, which has a significantly narrower distribution function due to its single-state nature. (d) Approximate evolution of the logarithm of the electron transfer rate for low (green) to high (purple) reorganization energies.

The electron transfer rates according to this potential landscape were derived using the Arrhenius equation [30], [124], [125]:

$$k_{ET} = k_e \nu_{eff} \exp\left(\frac{-E^*}{k_B T}\right), \tag{3.5}$$

where v_{eff} is the effective frequency of motion, k_e is the transmission factor, and E^* is the activation barrier for the electrons to cross over for charge transfer. According to the previously described theory on nuclear configuration, this activation barrier is the sum of the energy difference ΔE between the donor and acceptor states and the reorganization energy λ. The transmission factor can then be given in terms of the Landau–Zener coefficient P_0 [124], [125]:

$$k_e = \frac{2P_0}{1+P_0}, \tag{3.6}$$

where

$$P_0 = 1 - \exp\left(-\frac{|H_{if}|^2\pi^{3/2}}{h\nu_{eff}\sqrt{k_BT\lambda}}\right). \tag{3.7}$$

With H_{if} being the electron exchange energy between the donating and accepting states $H_{if} = \langle\Psi_i|H|\Psi_f\rangle$. This complex relationship can be simplified through Taylor expansion and approximation to the second order, leading to the expression for the nonadiabatic electron transfer rate for a transition from a donor state at the specific energy E [126]:

$$k_{ET}(E) = \frac{2\pi|H_{if}|^2}{\hbar\sqrt{4\pi\lambda k_BT}}\exp\left(-\frac{(E+\lambda-\Delta E)^2}{4\lambda k_BT}\right), \tag{3.8}$$

which is identical to the electron transfer rate determined through quantum-mechanical considerations. The normalized energy distribution of the donor state present in this relationship is found to be

$$D(E) = \frac{1}{\sqrt{4\pi\lambda k_BT}}\exp\left(-\frac{(E+\lambda-\Delta E)^2}{4\lambda k_BT}\right), \tag{3.9}$$

thus leading to the simplification [127]–[129]

$$k_{ET} = \frac{2\pi|H_{if}|^2}{\hbar}D(E). \tag{3.10}$$

This transfer rate describes the charge transfer from a donor state at energy E to an acceptor state offset by ΔE, and is valid for charge transfer between, for example, molecules in solution but not for charge transfer to a semiconductor system. Here, the donor state interacts with many possible acceptor states described by the VB in the semiconductor. In the diabatic case, the transfer rate can be described by the integral of transfer rates for all possible donor–acceptor states [130], [131]:

$$\begin{aligned} K_{ET} &= \tfrac{2\pi}{\hbar}|\overline{H_{if}}|^2\textstyle\int_0^\infty dE D(E)\rho(E) \\ &= \tfrac{2\pi}{\hbar}\textstyle\int_0^\infty dE\,\rho(E)(1-f(E))|\overline{H}(E)|^2\tfrac{1}{\sqrt{4\pi\lambda k_BT}}\exp\left(-\tfrac{(E+\lambda-\Delta E)^2}{4\lambda k_BT}\right), \end{aligned} \tag{3.11}$$

where $\rho(E)$ is the CB DOSs of the acceptor semiconductor, $f(E)$ is the Fermi distribution function, and $\overline{H}$ is the average electronic coupling. This is schematically depicted in Fig. 3.6(b). In the case of moderate doping, $f(E)$ is assumed to be negligible. Close to the band edge, the DOS can be approximated as [132]

$$\rho(E)dE = \frac{(2m^*)^{3/2}}{2\pi^2\hbar^3}\sqrt{E}dE. \tag{3.12}$$

The schematic distribution of states for the donor and acceptor states is shown in Fig. 3.6. Due to the low reorganization energy, estimated to be around 0.1 eV in the absence of any solvent, the distribution function $D(E)$ is very narrowly distributed around the energy $\Delta E - \lambda$. Therefore, one can assume that the DOS of the CB is approximately constant within this small energy window, yielding the relationship [128]

$$K_{ET} = \frac{2\pi}{\hbar}|\overline{H_{if}}|^2\rho(\Delta E - \lambda)\int_0^\infty dED(E). \tag{3.13}$$

Since the distribution for the molecular state is normalized, the integral equals one. This simplifies the expression even further to [128]

$$K_{ET} = \frac{2\pi}{\hbar}|\overline{H}|^2\rho(\Delta E - \lambda) = C\sqrt{\Delta E - \lambda}, \tag{3.14}$$

with

$$C = \frac{(2m^*)^{3/2}|\overline{H}|^2}{\pi\hbar^4}, \tag{3.15}$$

indicating that the charge transfer rate of an electron from the molecular excited state to the semiconductor is proportional to the square root of the energy difference between the CB and the difference of the excited state energy ΔE and the reorganization energy λ. Assuming that the reorganization energy is comparatively small and independent of the substrate, the charge transfer rate is dependent on the square root of the energy difference, as shown in Fig. 3.6(d).

The theory for the back transfer can, in principle, be handled analogously but now includes a set of donor states and a single acceptor state. However, due to charge transport, surface recombination, and charge carrier trapping in surface states, it is challenging to define the donor states. Due to the broad range of possible processes with unclear rate constants, no reliable theory has been found to describe these processes yet [30].

3.4.2. Förster Resonant Energy Transfer

In contrast to Marcus theory, Förster resonant energy transfer (FRET) is a model of energy transfer between an excited donor molecule and a weakly coupled acceptor molecule. It can be described formally as a unified simultaneous exciton recombination in the donor and an absorption process in the acceptor, as depicted in Fig. 3.7(a). While the theoretical approach used to calculate the electron transfer rates of FRET classically is based on this analogy, it is important to note that the FRET process does not involve any optical emission. Förster theory assumes dipole–dipole interaction to be the dominant interaction mechanism at play. Quantum-mechanical and classical approaches both yield the transfer rate [133], [134]

$$k_{FRET} = k_D \left[\frac{R_0}{r}\right]^6, \tag{3.16}$$

where k_D is the emission rate constant of the donor and R_0 is the Förster radius. Notable here is the characteristic r^{-6} distance dependence of the energy transfer rate. This property is often used to demonstrate FRET as a transfer mechanism in experiments.

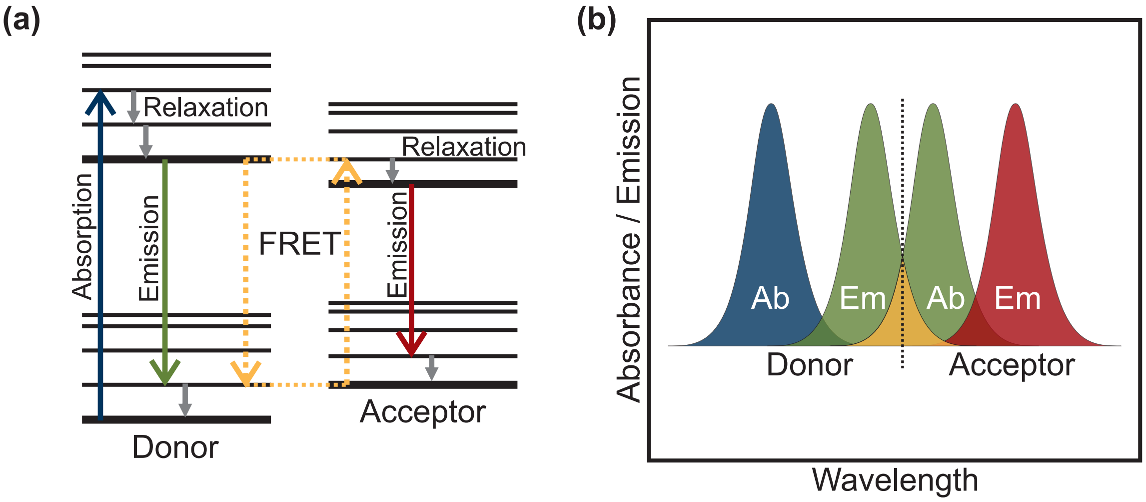

Figure 3.7 Schematic depiction of (a) the energy levels and (b) the required spectral overlap for FRET. Energy transfer is enhanced if the emission of a donor system matches a possible absorption line of an acceptor system.

The Förster radius is usually around 1 to 10 nm. It is dependent on the relative orientation κ of the dipoles, the fluorescence quantum yield Φ_D^0 in the absence of transfer processes, the refractive index n of the surrounding medium, and the spectral integral J [135]:

$$R_0^6 = \frac{9(\ln 10)\kappa^2\Phi_D^0}{128\pi^5 N_A n^4} J. \tag{3.17}$$

The spectral integral highlights the necessity for spectral overlap between the emission of the donor molecule and the absorbance of the acceptor, which is schematically depicted in Fig. 3.7(b). It is calculated to be [135]

$$J = \int d\lambda\, F_D(\lambda)\epsilon_A(\lambda)\lambda^4, \tag{3.18}$$

where $F_D(\lambda)$ is the normalized emission function of the donor and $\epsilon_A(\lambda)$ is the absorption coefficient of the acceptor. The theory for FRET has not been adapted for the interaction of a molecule with a semiconductor. However, most researchers have relied on using Förster's theory to describe the processes observed and have found the distance dependence to be true for some of these systems [136]–[139].

3.5. Hybrid Systems for Catalysis

Hybrid systems of either metallic or semiconductor substrates and organometallic catalysts have been explored in various combinations, utilizing different philosophies to achieve improved performance. The field of research is diverse due to the broad range of catalysis applications, including water splitting [140] and CO_2 reduction [15], but also other processes. In addition, some studies revolve around the development of electrocatalysts, while others rely on photocatalysis or the combination of both. The morphologies and device structures can also vary significantly. Some systems use disordered nanostructures, such as colloidal nanoparticles, to enhance the surface-to-volume ratio, while others use regular structures on extended substrates akin to photonic crystals to achieve light-guiding effects [141]. The following discussion focuses on photocatalytic processes for CO_2 reduction.

Photocatalytic systems can either be based on single-photon or multiphoton Z-scheme systems, each coming with advantages and disadvantages. These systems are generally designed to use the semiconductor as a photosensitizer, absorbing the incoming light to generate electron–hole pairs. The electron–hole pairs are split at the interface, transferring the electrons to the LUMO of the catalyst to induce reactions.

For example, graphitic carbon nitride has been successfully combined with ruthenium bipyridine molecules immobilized through a phosphonic acid head group for photocatalysis of CO_2 reduction [142]–[144]. Graphitic carbon nitride (g-C_3N_4) is a popular choice as a substrate material as it is made up of earth-abundant materials. It has a band gap of 2.7 eV and its CB position is suitable for catalysis of CO_2 reduction. Pairing a porous g-C_3N_4 substrate with *trans*(Cl)-Ru4,4'-$(CH_2PO_3H_2)_2$-2,2'-bipyridine, which is an electrocatalytically active molecule that does not exhibit a significant amount of visible-light absorption, results in a system that can catalyze CO_2 to formate with a selectivity of more than 70 % [142]–[144]. Such a system is additionally capable of exhibiting large turnover numbers (TONs) reaching around 1000 [143].

Moving from an extended g-C_3N_4 substrate to nanosheets of the material boosts its performance even further, as highlighted by Maeda *et al.* [145], who achieved selectivities of more than 90 % for formate production and TONs surpassing 5000. g-C_3N_4 is not the only substrate to be paired with this type of molecular catalyst. Other semiconductors such as ZnS/Ni or more complex sulfide variants, such as $(CuGa)_{0.8}Zn_{0.4}S_2$, $(CuGa)_{0.3}Zn_{1.4}S_2$, and $(AgIn)_{0.22}Zn_{1.56}S_2$, have been tested with limited success, reaching significantly lower TONs of around 100 while also exhibiting lower selectivities [146]. Lower performance was achieved for $CaTaO_2N$ as a substrate, which exhibited a high selectivity for formate of 98 % but a low stability, yielding a TON of only 11 [147]. A variety of other substrates, including

TiO_2, have also been tested [148], and the ruthenium catalyst is not the only molecule to be tested for hybrid performance, with other candidates being based on, for example, rhenium [149], [150], cobalt [151], or iron metal centers [152], [153].

The device layouts of these systems are mainly restricted by the available semiconductor substrates since the requirements of visible light absorption and low electron affinity limit the available substrate options. So-called Z-scheme systems were developed to alleviate this problem. Here, an additional molecule is inserted between the catalyst and the semiconductor. The energy level alignment of this molecule should allow for electron transfer from the semiconductor CB to the HOMO of this intermediate, which also exhibits visible light absorption. In addition, the intermediate molecule should have a LUMO allowing charge transfer to the catalyst. Thus, the system uses two photons instead of one to increase the energy of the electron in multiple steps. The requirement of charge transfer from the CB to the HOMO is significantly easier to reach, allowing for semiconductors with a significantly narrower band gap, which could offset the efficiency penalty of a two-photon system.

The most popular Z-scheme devices are based on a binuclear ruthenium complex, which has been combined with a variety of semiconductors including Ta_3N_5 [154], TaON [155], and GaN/ZnO [156], exhibiting similar if not slightly better TONs ranging between 100 and 750. However, the highest performances achieved with such a system are based on the previously mentioned g-C_3N_4. In this case, selectivities of up to 99 % for formate production and turnover frequencies (TOFs) reaching 33,000 s^{-1} have been achieved [143], [157]. Both device structures can also be implemented with the simultaneous application of an external bias, resulting in photoelectrochemical systems [15]. Example systems include rhenium or manganese bipyridine complexes on Si [158], [159] or copper oxide [160], [161] for one-photon processes and a ruthenium–rhenium binuclear complex on NiO or $CuGaO_2$ [162], [163].

In conclusion, a broad variety of systems and combinations have been tried in the literature. In general, these investigations have been driven by performance evaluation instead of systematic analysis. While metastudies have identified the need for a low electron affinity material to achieve high-performance devices [15], the greatly varying experimental results make a systematic comparison challenging. It is also necessary to overcome the difficulties generally associated with analyzing, for example, CO_2 reduction systems regarding product quantification and contamination.

4. The Protoporphyrin IX–Semiconductor Interface

Parts of this chapter are published in [164].

While many device-level attempts at hybrid catalytic systems have been made, most current research is exploratory rather than systematic. This chapter describes a systematic investigation of hybrid systems based on PPIX as the organic monolayer structure with various semiconductor substrates. PPIX is the free-base representative of a large, structurally and electronically similar group of molecular catalysts that also includes metalloporphyrins, which have been demonstrated in catalytic hybrid devices [21]–[23], [165], [166]. Therefore, it can serve as a stand-in for these hybrid devices and provide insights into the energy level alignment and interaction mechanisms between semiconductor substrates and molecular monolayers.

LB deposition was chosen to synthesize these model structures because this method ensures the formation of high-quality monolayers without the chemical bond formation needed for SAMs. The requirement of covalent bonding makes it significantly more challenging to form comparable SAMs on different substrates since these do not necessarily exhibit the same surface chemistry. It would, therefore, be unlikely to find a functional group that is capable of high-quality SAM formation on all surfaces. Any changes in the functional group to adapt to a specific substrate surface is likely to influence transfer and alignment processes, adding unwanted variables. LB deposition offers a viable alternative, and is also easy to use and scalable for device applications [74], [75], [167].

The investigations focused on the Langmuir layer structure of PPIX on a DI water subphase, studied using isotherm analysis. Using the insights gained, the PPIX morphology on Si substrates deposited at various surface pressures was studied, optimized, and compared to the surface morphology on other substrates. High-quality PPIX LB layers were achieved with optimized parameters on Si, GaN, AlGaN, AlN, and ZnO. These substrates were chosen to enable a systematic study of the influence of electron affinity and band gap on the system. While the band gap and the electron affinity are positively correlated in Si and the nitrides, ZnO has a significantly larger electron affinity than GaN while exhibiting a similar band gap.

The chemical structures of the substrates and the monolayer were investigated with X-ray photoelectron spectroscopy (XPS), with the results showing that the reference surfaces and the monolayer exhibit the expected chemical structure. Ultraviolet photoelectron spectroscopy (UPS) was employed to study the energy level alignment by comparing the surface electronic structure of bare substrates to substrates covered with a PPIX monolayer. Changes in the work function were determined by studying the secondary electron cut-off

(SECO) of the respective UPS spectra. In addition, changes in electronic structure due to the intramolecular interaction of the PPIX monolayer were analyzed by UV–Vis spectroscopy. Due to the luminescence properties of PPIX, molecule–substrate interactions in its excited state can be revealed by analyzing the luminescence intensity. Quenching of the luminescence was used to gauge charge or energy transfer to the substrate. Cross-referencing the energy-level alignment with the transfer rate enabled the identification of charge transfer mechanisms corresponding to Marcus theory as the dominant interaction with larger band gap substrates, but slight inconsistencies for the luminescence on Si substrates could also hint at the possibility of energy transfer processes.

The insights gained on the energy level alignment and interaction mechanisms of PPIX only give an indirect indication for possible catalytically active systems since PPIX itself does not provide any catalytic activity. To gauge the validity of these insights for organometallic systems, similar investigations on morphology, intramolecular interaction, chemical structure, and energy level alignment were performed for various metalloporphyrins. These included iron (FePPIX), zinc (ZnPPIX), and cobalt (CoPPIX) metal centers, some of which have shown catalytic activity for certain reactions [21]–[23], [165], [166]. The transfer interactions could not be investigated to the same extent due to the lack of luminescence of most metalloporphyrins. However, the other observed phenomena were comparable to PPIX. This highlights the validity of the PPIX model system as a stand-in for metalloporphyrin catalyst hybrid systems.

4.1. Protoporphyrin IX Langmuir–Blodgett Monolayer Formation

PPIX monolayers were deposited onto the substrates of interest via LB deposition. To begin with, the monolayer formation process on a DI water subphase was studied by analysis of the surface pressure–area isotherm and the accompanying compression modulus. A specified amount of molecules was deposited on the DI water subphase with known surface area, which was systematically reduced to study the increase in surface pressure relative to the MMA. As shown in Fig. 4.1, the surface pressure initially did not increase as the surface area was reduced. It slowly started to rise at an MMA of around $0.8\,\mathrm{nm}^2$. This increase in surface pressure was linearly dependent on the decrease in the MMA between $0.55\,\mathrm{nm}^2$ and $0.4\,\mathrm{nm}^2$. Below this MMA, and as the surface pressure surpassed $55\,\mathrm{mN\,m^{-1}}$, the increase started to level off significantly.

Overall, the surface pressure isotherm exhibits no major phase transitions within the observed MMA. The lack of surface pressure increase in the high MMA limit is notable: The surface pressure did not increase measurably for the initial $0.2\,\mathrm{nm}^2$ of compression. This lack of increase leads to the conclusion that the molecules deposited on the surface do not exhibit a gas-like phase, since this would cause an increase in pressure according to the ideal gas equation. This gas-like phase cannot have been surpassed by the addition of too

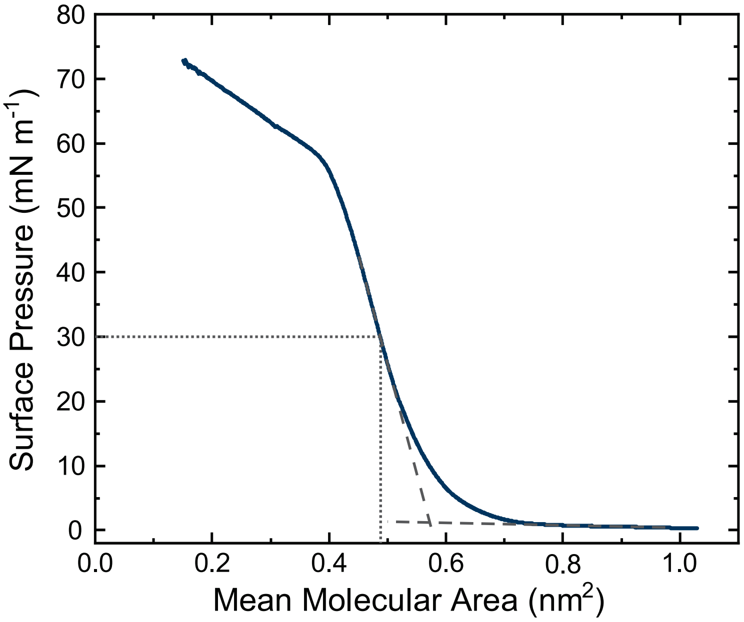

Figure 4.1 Isotherm of PPIX deposited on a DI water subphase. The dashed lines indicate the extension of the linear region of surface pressure increase to determine the mean area occupied by PPIX in the observed phase to be (0.57 ± 0.02) nm^2. The monolayer collapses as the surface pressure surpasses 55 mN m^{-1}. The dotted lines depict the surface pressure determined to be optimal for high-quality monolayers.

much PPIX either, since a surface pressure increase would accompany it during the addition of the molecule on the subphase. This strongly hints at the PPIX self-condensing into denser structures, leaving significant areas of the subphase surface without a monolayer coverage at this early stage of the compression process. After a certain area reduction, the islands start to interact with each other as the amount of unoccupied space is reduced. The subsequent close-to-linear increase in surface pressure points to the absence of any phase transitions during the compression. Therefore, the PPIX islands likely maintain their originally formed structure. The reduction in surface pressure increase beyond 55 mN m^{-1} likely arises due to the collapse of the structure and not a phase transition, since the surface pressure is already very high and approaching the theoretical limit achievable, which is the surface pressure of water at 72.8 mN m^{-1}.

Extension of the close-to-linear region toward lower surface pressures yields the surface area that a PPIX molecule occupies on average within the observed Langmuir film phase. For the phase in this isotherm, this average area was determined to be (0.57 ± 0.02) nm^2. This is significantly smaller than the surface area of a PPIX molecule along its plane, which is estimated to be around 1.5 nm^2. Therefore, the Langmuir film likely consists of close-packed molecules in a rather upright orientation. This is intuitively expected since the amphiphilic structure of PPIX, with its two carboxyl group tails and the extended π-orbital system perpendicular to the porphyrin heterocycle, would greatly favor this orientation due to free energy reduction upon interaction with the water subphase or π–π stacking with neighboring molecules, respectively. These are also likely the cause of the comparatively high stability of the Langmuir film, with high surface pressures being required to break this structure.

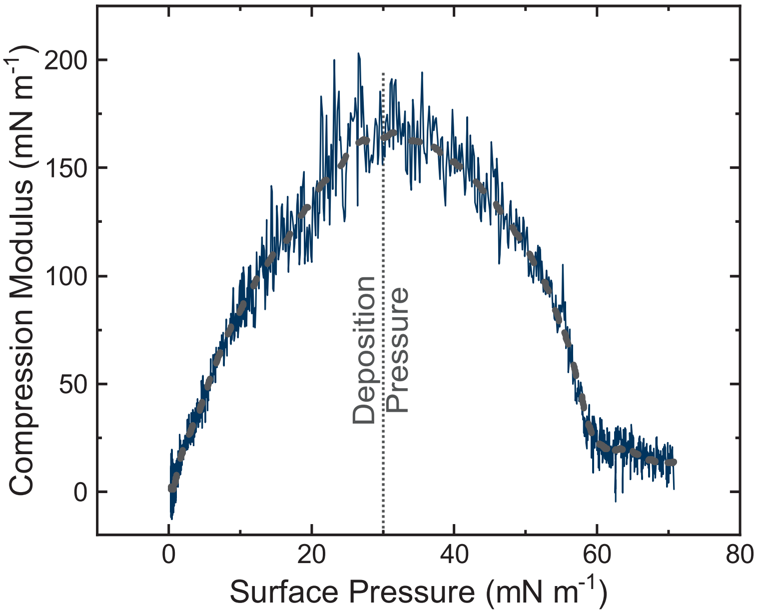

Figure 4.2 Dependence of the compression modulus of the PPIX Langmuir layer on the surface pressure, indicating a broad peak centered around roughly 30 mN m^{-1}. The maximum compression modulus of 170 mN m^{-1} is an expected value for a liquid-condensed monolayer [168]–[170]. The gray dashed line shows a running average of the data to decrease noise and increase readability.

The compression modulus of the PPIX Langmuir film can be determined from the previously discussed isotherm. The results are depicted relative to the surface pressure in Fig. 4.2. For low surface pressures, the compression modulus increases steadily before reaching a maximum of around 170 mN m^{-1} at a surface pressure of 30 mN m^{-1}. After this inflection point, it decreases rapidly as the Langmuir film collapses. The compression modulus behavior of the Langmuir film lacks local minima, which is an additional indication of the lack of phase transitions. The magnitude of the maximum compression modulus points to the PPIX monolayer either being in the liquid-condensed or solid phase [168]. The surface pressure at maximum compression modulus indicates the ideal surface pressure for LB deposition since it provides the densest molecule structure without collapse. Thus, the compression modulus curve indicates 30 mN m^{-1} to be close to the ideal LB deposition surface pressure.

4.2. Morphology of Protoporphyrin IX Langmuir–Blodgett Monolayers

While the investigation of the surface pressure and compression modulus of the PPIX Langmuir film already gave the first insights into its molecular structure and film formation process, a more in-depth analysis of the PPIX monolayer is required to understand the process fully. Therefore, LB deposition of PPIX layers was performed on hydroxylated Si substrates at surface pressures ranging from 2.5 mN m^{-1} to 40 mN m^{-1}. The samples were investigated with atomic force microscopy (AFM), including quantitative nanomechanical mapping (QNM), to obtain information on the thin film formation process and the resulting morphology.

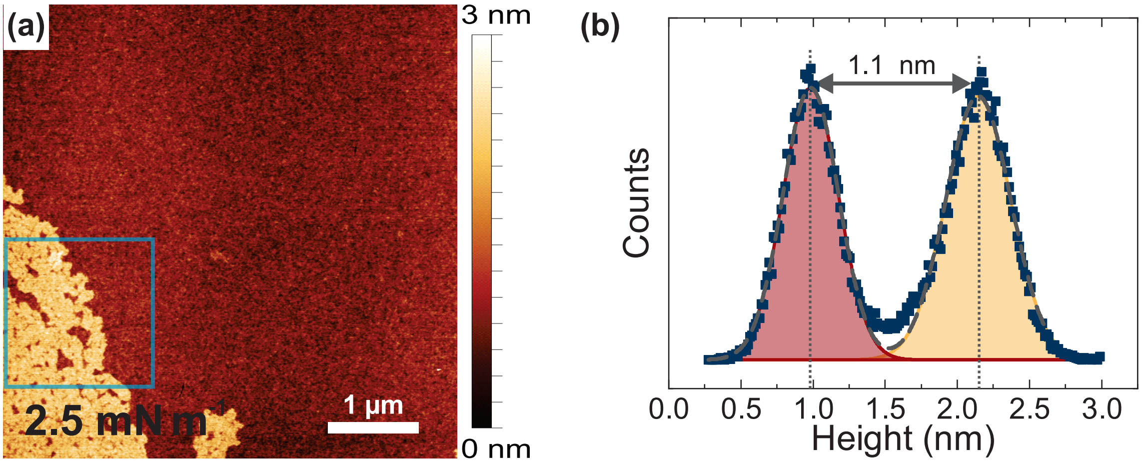

Figure 4.3 (a) AFM micrograph of a PPIX LB layer deposited on Si at a surface pressure of 2.5 mN m^{-1}, indicating an inhomogeneous partial surface coverage. (b) Height histogram of the area highlighted in (a), showing a bimodal distribution with a center distance of 1.1 nm.

An AFM micrograph showing a PPIX LB layer deposited at a surface pressure of 2.5 mN m^{-1} is depicted in Fig. 4.3(a). Two different surface regions can be identified within the micrograph. The lower region spanning the larger relative area is not covered by a monolayer. The surface morphology and its RMS roughness of 176 pm match a bare hydroxylated Si substrate. The features located in the bottom left corner of the micrograph indicate the presence of a molecular monolayer of uniform thickness that is interrupted by holes. Overall, the shape of these holes and the edges of the area covered by the monolayer appear rather irregular, thus not suggesting a long-range crystalline order, since this would result in the preferential appearance of structures with regular shapes and angles on the borders.

The height difference between the substrate and monolayer surface can be determined via statistical analysis of the height within the area marked by the blue square in Fig. 4.3(a). This region was chosen to represent both regions in a ratio of 1:1, thus yielding equal weighting for the histogram analysis. The extracted height histogram is depicted in Fig. 4.3(b) and shows a bimodal distribution in which the peak marked in red represents the height distribution of the substrate, while the yellow peak indicates the height distribution of the substrate covered with a monolayer. The substrate peak does not appear at the height of 0 nm, because the arbitrary height origin is set to the minimum value of the entire micrograph to avoid negative height values. The thickness of the monolayer can be determined to be (1.1 ± 0.1) nm from the peak distance of the height distributions. The thickness variation of the monolayer appears to be low, as determined by the moderate increase of the full width at half maximum (FWHM) from the bare substrate to the monolayer distribution from 0.45 nm to 0.53 nm.

While the irregular shape of the monolayer islands indicates a lack of long-range order along the surface plane, the narrow thickness variation points at a well-defined molecular orientation relative to the surface normal. Since the thickness of the monolayer is smaller than the molecule length in its assumed orientation, with the carboxyl group facing the subphase, the PPIX molecules likely maintain a tilted orientation within the monolayer structure. Assuming that the PPIX molecules occupy a parallelepiped volume, with the longest axis being the estimated length of the molecule of 1.5 nm, its tilt angle would be around 40° to the surface normal. This estimate implies that the PPIX maintains a flat structure, which is not necessarily the case since the tail groups could have enough degrees of freedom to induce buckling of the molecule. A precise determination of the orientation would require significantly more elaborate studies, such as near-edge X-ray absorption fine structure (NEXAFS) spectroscopy, which require synchrotron facilities and are, thus, beyond the scope of this work.

The observed tilting of the molecule is in line with previous studies on LB films of various molecules, including protoporphyrins, and is an expected behavior [171]–[173]. The tilt angle can have a significant influence on the intermolecular interaction since it influences the slip angle and, thus, the dipole–dipole interactions as well as the π-orbital hybridization of the molecules in the monolayer.

The surface coverage of the sample surface is very inhomogeneous for this low surface pressure, exhibiting bare substrate and dense monolayer simultaneously. This indicates that the LB layer self-assembles on the DI water and forms a condensed layer before compression is initiated. This is in line with the observations from the isotherm experiments discussed in the previous section, which indicated that the Langmuir film does not exhibit a gas-like phase and does not show any phase transitions. Therefore, the increase in surface pressure likely arises mostly due to the compression of the condensed structure islands within the Langmuir layer.

Increasing the surface pressure increases the relative coverage, as can be seen in the AFM micrograph of a sample deposited at 10 mN m^{-1} shown in Fig. 4.4(a). The morphology is similar to the monolayer structure observed in the bottom left corner of Fig. 4.3(a), but now spans

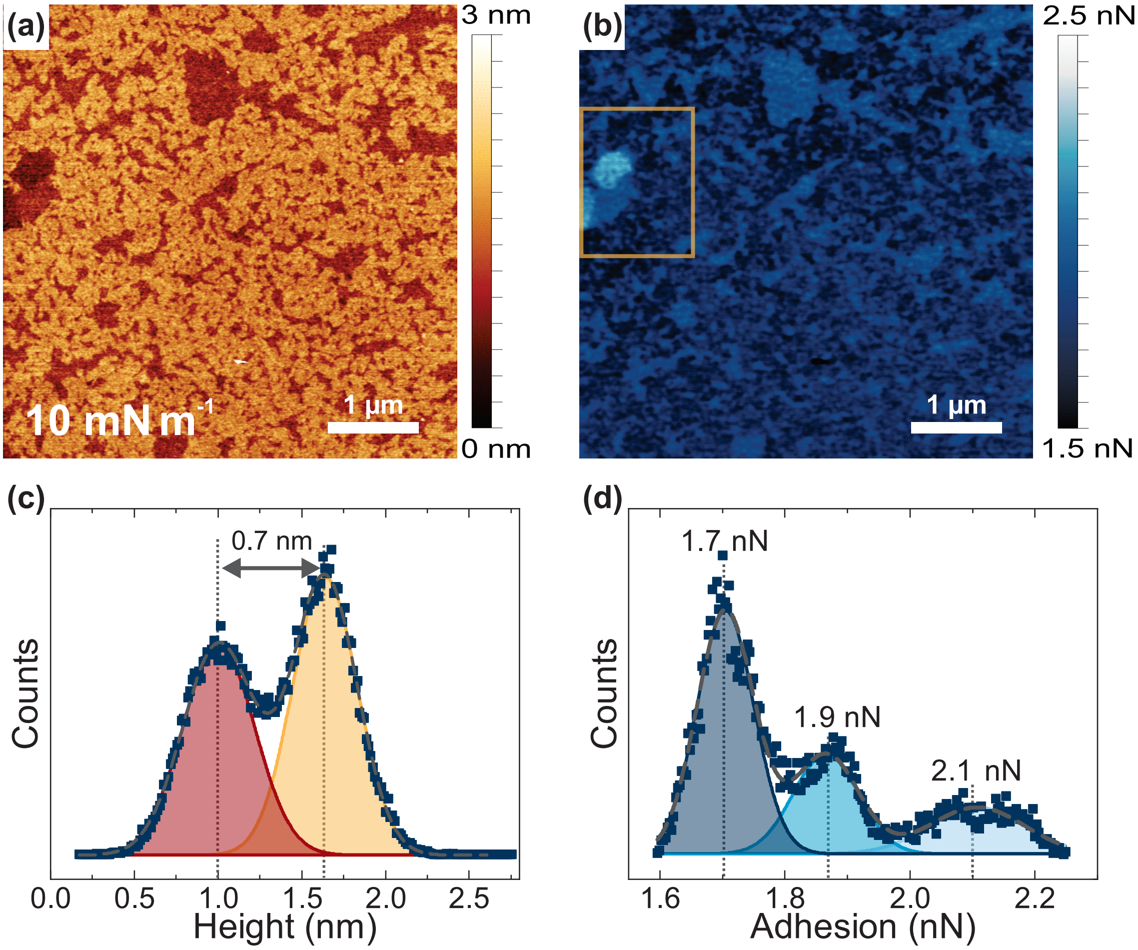

Figure 4.4 (a) AFM micrograph of a PPIX LB layer deposited on Si at a surface pressure of 10 mN m^{-1}, indicating an inhomogeneous coverage by monolayers in different orientations. (b) Corresponding adhesion map recorded simultaneously to the morphology depicted in (a), showing three distinct regions of different adhesion properties. (c) Height histogram of (a), indicating a height difference of 0.7 nm for the two most prevalent morphologies. (d) Distribution of adhesion force in the region highlighted in (b).

the whole investigated surface area. The grain structure appears to be comparable, still exhibiting mainly irregular shapes and thus not indicating a uniform horizontal aggregation. In contrast to the thickness determined for the LB layer deposited at 2.5 mN m^{-1}, the height difference between the two main structures is significantly smaller at a value of (0.7 ± 0.1) nm, as depicted in the peak distance of the bimodal distribution shown in Fig. 4.4(c). The FWHMs of the individual height distributions remain comparable at 0.51 nm and 0.46 nm. Upon closer investigation of the micrograph, a region of lower height becomes apparent at the left edge of the image. The simultaneously acquired adhesion map is shown in Fig. 4.4(b) and depicts a significantly higher adhesion at this particular region of interest. Quantitative analysis through the adhesion histogram shown in Fig. 4.4(d) shows three distinctive peaks for the region marked in orange in Fig. 4.4(b). The highest adhesion of 2.1 nN coincides with the adhesion of the Si probe tip and a hydroxylated Si surface determined via a measurement performed in immediate succession, thus indicating that this small surface area corresponds to the substrate surface. The higher adhesion forces likely arise due to the short-range interactions of the native oxide of the probe tip with the sample. Introducing a hydrophobic monolayer reduces adhesion since the terminal methyl groups of the PPIX exhibit weaker interactions with the probe tip. Therefore, most of the surface is covered in LB layers of different morphologies, one exhibiting a higher adhesion force of 1.9 nN and the other 1.7 nN. The lower adhesion force matches that for the monolayer shown in Fig. 4.3(a) and for the other samples shown throughout this section.

A possible explanation for the observed features is the existence of an intermediate monolayer structure. Its thickness can be determined via height analysis to be around (0.4 ± 0.1) nm, which indicates a completely horizontal orientation of the molecule since this thickness approaches the thickness of a monolayer of graphene, which is around 0.3 nm. Since the height difference between the thin and thick monolayer morphologies was determined to be (0.7 ± 0.1) nm, the overall thickness of the monolayer containing upright molecules matches the thickness determined previously for the sample deposited at 2.5 mN m^{-1}. The total thickness is determined to be (1.1 ± 0.2) nm.

The observation of an intermediate layer structure somewhat contradicts the previous observations made for lower surface pressures and the isotherm analysis. Due to the limited area of investigation, the existence of this intermediate structure cannot be fully excluded for the lower surface pressure samples either. The lack of any distinct features suggesting phase transitions in the isotherm data indicates that this structure has a very low stability threshold, leading to the grain compression dominating the observed surface pressure increase.

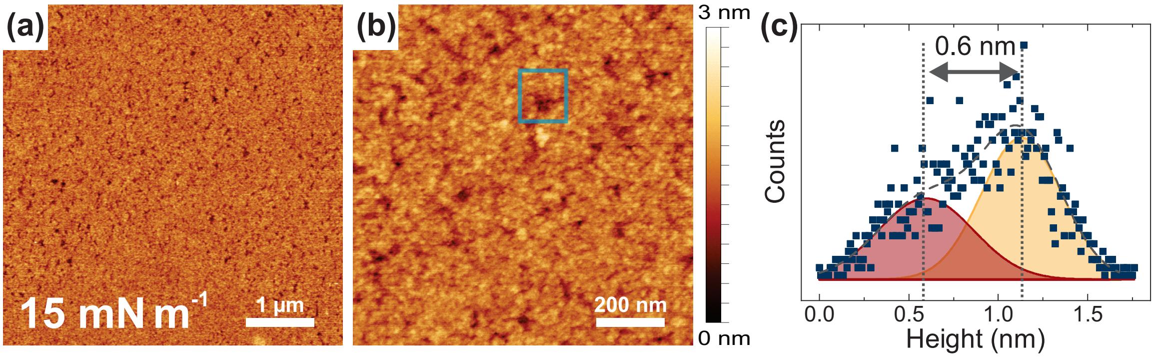

Figure 4.5 (a)–(b) AFM micrographs of a PPIX LB Layer deposited on Si at a surface pressure of 15 mN m^{-1}, with (b) recorded using a smaller scan area. (c) Height histogram for the highlighted region in (b), indicating a bimodal distribution with a center distance of 0.6 nm.

The monolayer morphology for LB layers deposited at 15 mN m^{-1} is significantly more homogeneous, as shown in Fig. 4.5(a). The surface is almost entirely covered by the LB layer.

Only small pinholes remain in the structure. These pinholes are depicted in more detail in Fig. 4.5(b), showing that their horizontal extent is at most around 50 nm. The small surface area makes an accurate estimation of the depth of these pinholes challenging, as can be seen in the significantly increased noise of the height histogram shown in Fig. 4.5 due to the smaller dataset extracted from the region marked in blue. The extracted hole depth coincides with the difference in height between the intermediate and self-aggregated layers observed at 10 mN m^{-1}, thus suggesting that the structure contains molecules with horizontal orientation.

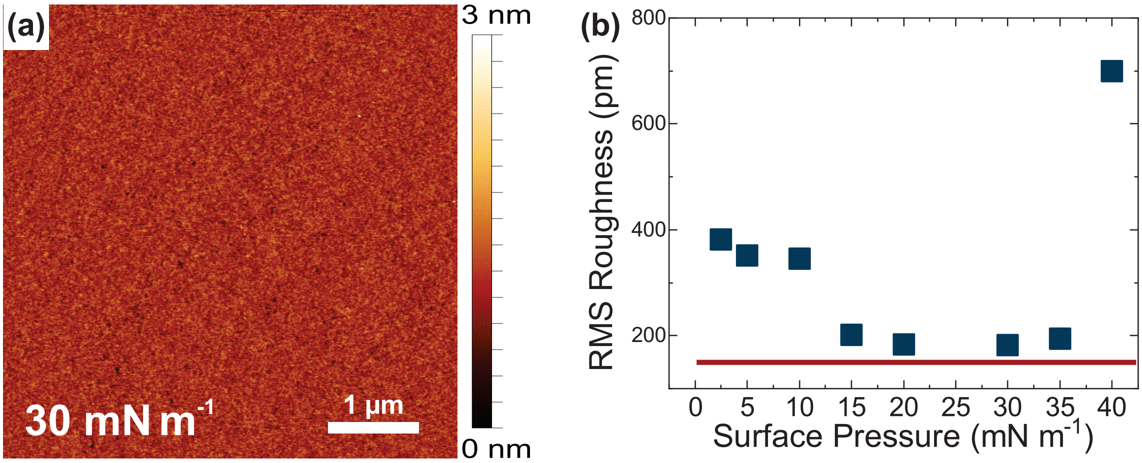

Figure 4.6 (a) AFM micrograph of a PPIX LB layer deposited on Si at a surface pressure of 30 mN m^{-1} with homogeneous surface morphology. (b) RMS roughness extracted from PPIX LB layers deposited on Si at various surface pressures. The roughness of the monolayer surface for LB layers deposited at 20 to 30 mN m^{-1} approaches the RMS roughness of the substrate indicated by the red horizontal line at 170 pm.

At 30 mN m^{-1}, the surface morphology is almost indistinguishable from a bare Si substrate, as shown in Fig. 4.6(a). The structure is devoid of any holes and exhibits a high level of uniformity, which is also highlighted by its RMS roughness of 182 pm being almost identical to the surface roughness of bare Si, 175 nm. The dependence of the RMS roughness on the deposition surface pressure is depicted in Fig. 4.6(b). The RMS roughness is slightly below 400 pm at the lower surface pressures but drops significantly as a surface pressure of around 15 mN m^{-1} is reached. Between 15 mN m^{-1} and 35 mN m^{-1}, the surface roughness remains very close to the roughness of the substrate, indicating a high monolayer quality. Compression within this surface pressure region does not yield any structural changes, indicating elastic deformation. A further increase in surface pressure leads to the collapse of the monolayer, as indicated by a drastic increase in RMS roughness for a sample deposited at 40 mN m^{-1}.

It is important to keep in mind that surface pressure does not linearly reflect the reduction in subphase surface area. The increase from 15 mN m^{-1} to 35 mN m^{-1} occurs over an MMA reduction of around 0.1 nm^2, while the increase from 2.5 mN m^{-1} to 15 mN m^{-1} required an MMA reduction close to 0.2 nm^2.

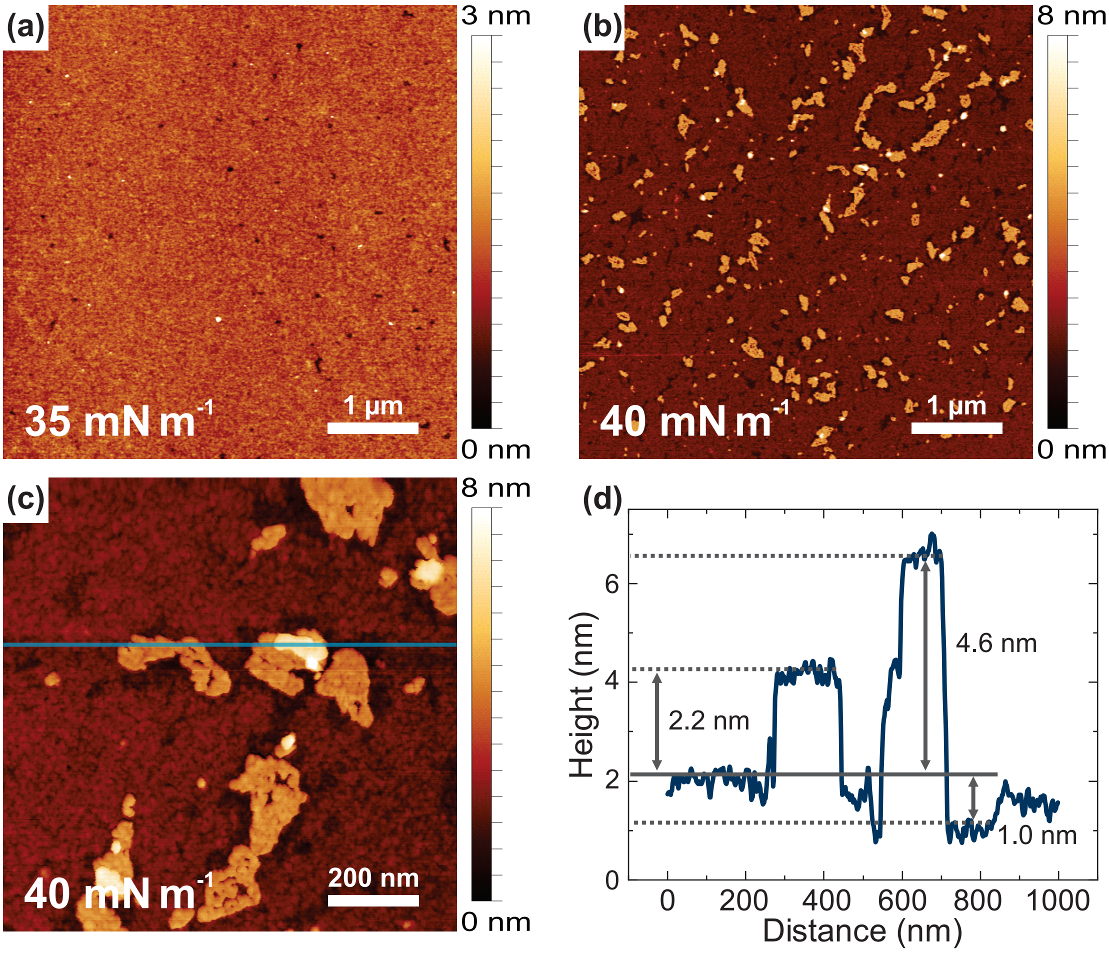

Figure 4.7 (a) AFM micrograph of a PPIX LB layer deposited on Si at a surface pressure of 35 mN m^{-1}. (b)–(c) AFM micrographs of an LB layer deposited at 40 mN m^{-1} with different scan areas, showing the formation of multilayers. (d) Line profile of the height extracted at the position highlighted in (c).

Increasing the surface pressure slightly from 30 mN m^{-1} to 35 mN m^{-1} does not result in significant changes in the morphology, as depicted in Fig. 4.7(a). Going beyond this leads to a breakdown of the monolayer structure, however. This is shown in Fig. 4.7(b) and (c), which depict AFM micrographs of an LB layer deposited at a surface pressure of 40 mN m^{-1} recorded at different magnifications. These micrographs indicate the emergence of distinct multilayer structures exhibiting a well-defined thickness, which points to the formation of an ordered multilayer structure. The multilayers appear similar in shape to the individual islands of monolayers observed at low surface pressures and are bordered by thin sections of lower height, likely arising from the integration into the multilayer of the molecules that used to reside at this position. A line-scan analysis across the horizontal line marked in blue in Fig. 4.7(c) is shown in Fig. 4.7(d), demonstrating that the most prevalent multilayer thickness extends roughly (2.2 ± 0.2) nm above the monolayer. This thickness indicates either the direct formation of trilayer structures, a bilayer structure accompanied by a straightening of the initial monolayer molecules, or the emergence of a more complex crystalline structure. Some of the multilayer structures also show a second layer appearing on top. These highest layers appear to be (2.4 ± 0.2) nm in thickness and could, thus, be a result of another layer of the same structure.

A more in-depth analysis of the crystal structure of these multilayers with, for example, X-ray diffraction (XRD) is challenging due to the small size of the islands. Therefore, a closer study would require synchrotron measurement techniques that are beyond the scope of this work.

As a consequence of this systematic investigation, the further studies presented in this work focus on LB layers deposited at 30 mN m^{-1}. This surface pressure is chosen due to the high monolayer quality of the deposited LB films. Additionally, the monolayer is at its maximum compression modulus at this surface pressure, indicating that it is densely packed and still compresses elastically. While a small increase beyond 30 mN m^{-1} does not yield significant multilayer formation according to the presented AFM micrographs, the small surface area studied with AFM cannot fully rule out a local breakdown of the layer. Therefore, a slightly lower surface pressure was chosen to ensure a safety margin to prevent a local breakdown of the monolayer structure.

The morphological studies presented so far have been obtained for Si substrates. Since the intent of this work is the comparison of electronic interactions of multiple semiconductor substrates, it is important to ensure that the insights gained also remain valid for other semiconductors. In particular, morphological differences between substrates could severely skew certain measurement results, such as determinations of the energy level alignment and transfer properties. A different molecular orientation might, for example, induce different aggregation states with vastly different luminescence properties. Therefore, the monolayer thicknesses of LB layers deposited onto GaN and ZnO were compared to those of LB layers deposited on Si, as depicted in Fig. 4.8. To this end, AFM scratching experiments were performed on samples with LB layers deposited at a surface pressure of 30 mN m^{-1}.

In contrast to the previously presented AFM micrographs, these studies were performed with tapping mode (TM) AFM, employing a significantly less sharp AFM probe and thus resulting in images of slightly lower quality. Initially, the PPIX monolayer was removed from a 1 µm^2 surface area via scratching in contact mode (CM). TM micrographs of the scratched and surrounding area were subsequently recorded, revealing the edges between scratched and pristine regions. Line profiles spanning over these edges indicate a step height corresponding to an LB layer thickness of (1.2 ± 0.1) nm for a GaN substrate, (1.0 ± 0.2) nm for ZnO, and (1.1 ± 0.1) nm for Si. These thicknesses are in good agreement with each other and with

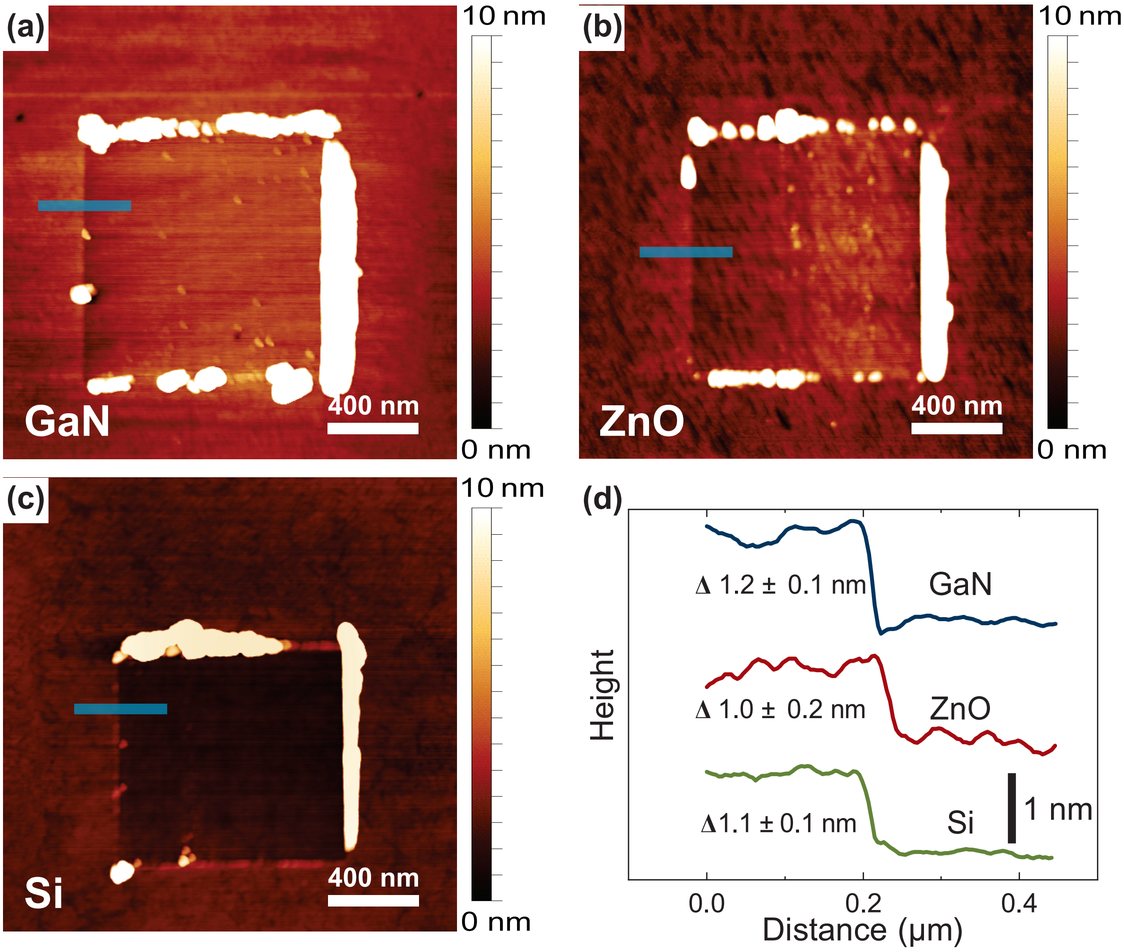

Figure 4.8 (a)–(c) AFM micrographs (recorded using TM) of a surface area for which the PPIX monolayer has been removed through contact mode scratching with the AFM tip for GaN, ZnO, and Si substrates, respectively. (d) Extracted line scans at the positions highlighted in (a)–(c), which reveal a comparable monolayer thickness for all substrate materials.

the previously determined thicknesses obtained by analyzing LB layers deposited at lower surface pressures. The insignificant differences in thickness point at comparable monolayer structures for the different substrates. This is a consequence of using LB deposition since the monolayer formation process occurs on the DI water subphase and, thus, is identical for all substrates.

4.3. Chemical Properties of Protoporphyrin IX Langmuir–Blodgett Monolayers

In addition to morphological information, it is important to gain detailed knowledge of the chemical state of the substrate and molecule. Using XPS, the elemental constituents of the near-surface regions of the LB layers and bare substrate reference samples were investigated. High-resolution spectra enabled the identification of the specific chemical environments of each identified element, yielding information on the chemical structure of reference surfaces and also of the PPIX molecule after LB deposition. In addition, the signal attenuation of the substrate-related elements gave an additional indication of the monolayer thickness. The XPS spectra shown in this chapter are limited to the Si and Au samples to enhance readability. The spectra of the other samples can be found in Fig. B.3.

High-resolution XPS spectra of the C1s, N1s, and O1s transitions for both the reference and the LB-layer Si and Au samples are shown in Fig. 4.9. All samples were thoroughly cleaned with various acids, solvents, and an oxygen plasma treatment, as described in detail in Sec. A.1. During the LB deposition process, the samples needed to stay submerged in the DI water subphase as the Langmuir film was formed by compression. This submersion could have had a significant effect on the surface properties of the samples. It could limit the comparability to a pristine reference sample that was analyzed directly after the final surface preparation step. Therefore, the submersion was mimicked for the reference samples as well. To this end, the reference samples were submerged in DI water for 30 min before the analysis.

It is important to note that both the reference and LB samples exhibit minor C1s signal intensities, as visible in Fig. 4.9(a) and (b). These arise due to carbon contamination on the surface, which is present despite the elaborate cleaning procedure. This contamination is unfortunately inevitable and cannot be prevented in the handling of *ex situ* samples, since atmospheric carbon (such as CO_2), low molecular weight carboxylic acids, and alcohols readily adsorb on the surface within a very short timeframe. Even limited exposure to the atmosphere results in significant contamination. In the case of the reference samples used in this study, the extended immersion time in the DI water likely led to more contamination accumulating on the surface. The same process would also occur for the samples during submersion before LB deposition. Thus, the studied reference surfaces are intended to exhibit comparable levels of surface contamination to the interface contamination on the semiconductor–monolayer interface. While the overall intensity is significant, it is at most 10 % of the PPIX monolayer C1s signal, indicating that the effective monolayer thickness would be around 0.1 nm if the contamination were evenly distributed over the whole surface. Such a thickness is unreasonably thin since it is significantly lower than even the thickness of monolayer graphene, suggesting that most of the surface is not covered by a monolayer of contaminating molecules.

The LB layer samples exhibit a complex C1s spectrum, which can be deconvoluted by fitting five Voigt functions to the recorded data. These fits are shown in the colored overlay in Fig. 4.9(a) and (b). The dashed lines represent the envelopes of these fits, which closely describe the data recorded. Each Voigt component can be matched to a specific chemical environment of the substituent carbon atoms within the molecular structure of the PPIX. In particular, sp2-hybridized C=C ($\sim$284.6 eV), sp3-hybridized C–C ($\sim$285.2 eV), pyrrolic C–N

($\sim$286.3), iminic C=N ($\sim$287.9 eV), and carboxylic C=O ($\sim$289.4 eV) binding states can be identified for the LB layers of all substrates [174]–[176]. A comparison of the experimentally determined stoichiometry, shown exemplarily for the Si substrate relative to the theoretical values, is depicted in Fig. 4.10 and shows a good agreement between the expected and measured C1s spectra. This leads to the conclusion that the PPIX maintains its chemical structure and does not undergo chemical changes during the deposition process. Differences between theory and experiment are apparent from the slightly higher C–C and slightly lower C–N components in the fit to the experimental data. This deviation is likely due to an imperfect deconvolution of these two peaks in the fit. The number of peaks required to describe the C1s spectra also leads to many degrees of freedom for the fitting algorithm. The fit is especially insensitive in this central spectral region, which could easily lead to a wrong estimation of the stoichiometry.

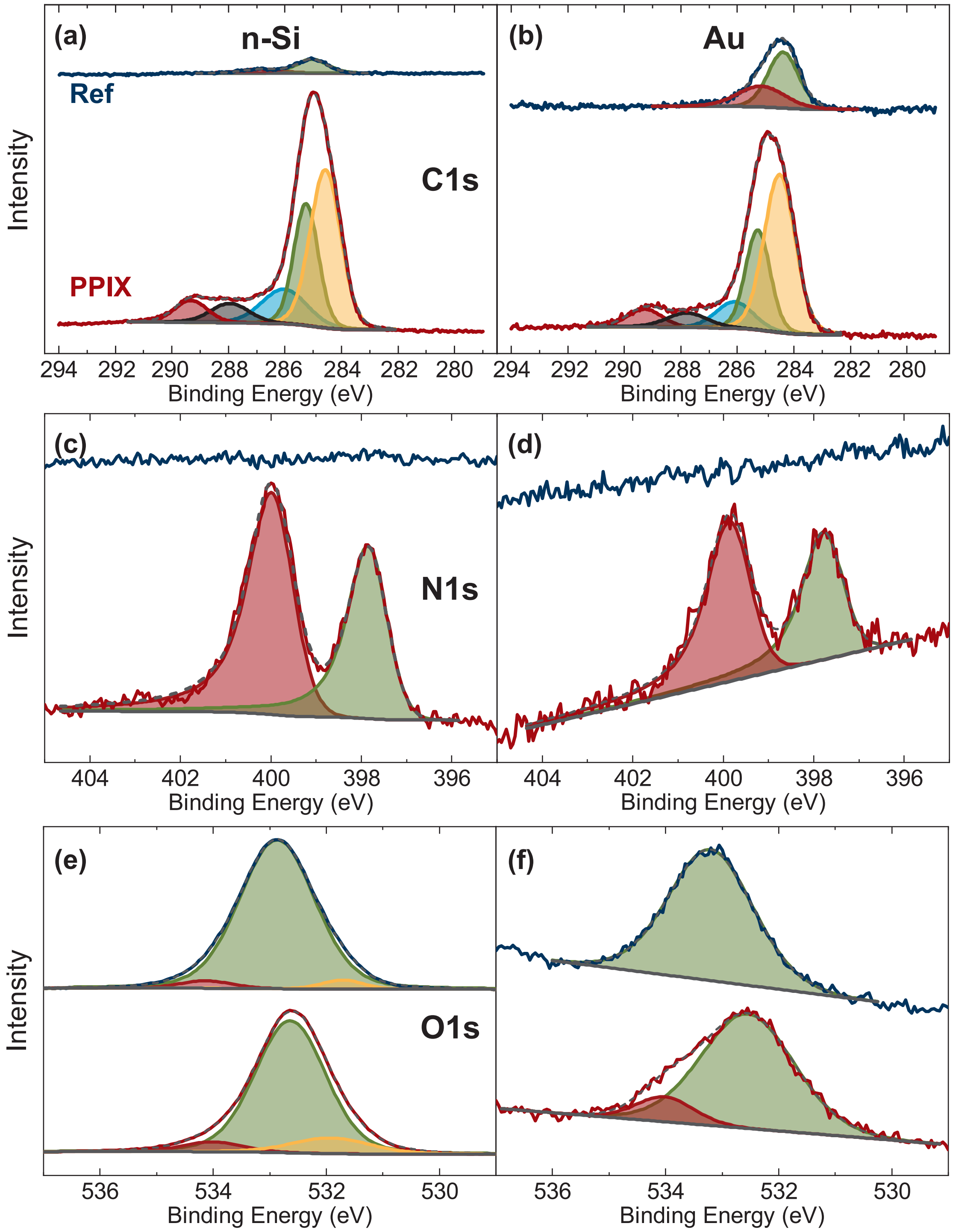

Figure 4.9 High-resolution XPS spectra for PPIX deposited on Si (left) and Au (right). (a)–(b) Top: C1s transition indicating slight but inevitable surface contamination by adventitious carbon for the reference samples. Bottom: Samples with a PPIX LB layer exhibiting a complex spectral shape that can be fitted by a set of peaks consisting of C=O (red), C=N (black), C–N (blue), C–C (green), and C=C (yellow). (c)–(d) N1s transition exhibiting pyrrolic N–H (red) and pyridinic =N– (green) states characteristic of a free-base porphyrin. (e)–(f) O1s transitions, in which the surface oxide dominates the Si substrate measurements.

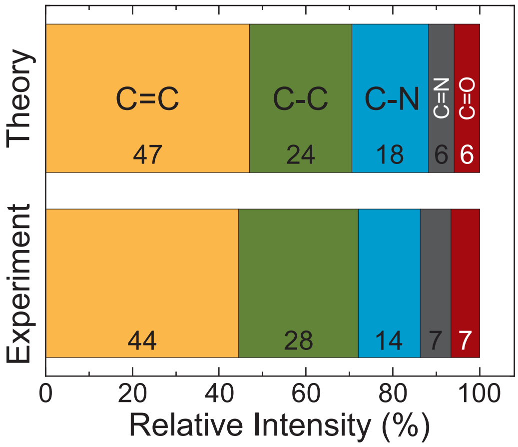

Figure 4.10 Expected and measured relative intensities of the observed carbon species, highlighting that the chemical structure of the PPIX is maintained after LB deposition.

The N1s transitions are depicted in Fig. 4.9(c) and (d) and do not show any trace of nitrogen for the reference samples. This indicates that the adventitious carbon contamination contains few nitrogen-bearing functional groups such as amines or amides. In contrast, the LB layer samples exhibit significant N1s signals from the porphyrin structure. In its free-base form, the porphyrin ring contains two iminic =N– and two pyrrolic –N– nitrogen atoms, which can be identified by their respective binding energies at 397.8 eV and 399.9 eV. Deviating from the expected 1:1 ratio, the data indicate a larger amount of protonated nitrogen across all investigated samples. The ratio changes between samples, but also between repeated experiments on identically prepared substrates. Overall, the relative peak area corresponding to protonated nitrogen appears to be 35 % to 50 % larger than the peak area corresponding to the unprotonated nitrogen. This relative intensity increase is known to occur on TiO_2 and has been investigated thoroughly using solution- and UHV-prepared monolayers (or submonolayers) of tetraphenylporphyrin and derivatives thereof [177]–[180]. Depending on the preparation method and relative surface coverage, the imbalance between iminic and pyrrolic nitrogen varies drastically, with the iminic nitrogen almost disappearing for UHV-evaporated submonolayers with low surface coverages [178], [180]. As the relative coverage increases, the pyrrolic intensity peak starts to appear, with multilayers of solution-prepared and UHV-evaporated samples approaching the expected 1:1 ratio. While the initial study of these processes performed by Lovat *et al.* [178] suggested that this protonation of the iminic nitrogen arises from hydrogen dissolved within the TiO_2 matrix, subsequent investigations agree on its origin being the deprotonation of surface hydroxyl groups. This interpretation is supported by observations of an increase in relative intensity for the protonated species in samples prepared in ethanol solution by Wechsler *et al.* [177], [179]. This increase likely occurs due to the increased concentration of the hydroxyl groups on the surface through interaction with the functional groups of the ethanol.

While this interpretation is likely at least partially valid in the case of the presented LB layer samples, the deposition method might also play a significant role in the protonation of the iminic nitrogen. It has been shown that the amount of protonated nitrogen within the porphyrin structure can be influenced by the pH of the solvent and that a fully protonated 4H diacid state can be obtained at pH values below 3 [181]. The DI water used in the presented studies was freshly prepared, but the dissolution of CO_2 due to exposure of the subphase to the atmosphere can lead to a slight lowering of the pH to around 6. This could explain the protonation of the LB layer deposited on the Au substrate, which should not exhibit any surface hydroxyl groups. However, further studies are required to determine the cause of protonation in this specific case. Protonation due to subphase interactions could be an avenue for further experiments since these interactions could yield interesting effects, such as electrostatic repulsion. Reduction of the subphase pH might, thus, have a significant impact on the intermolecular distance and could yield a possibly desirable homogeneous monolayer of PPIX with reduced molecular surface density. This might be a possible solution to the steric hindrance effects arising from the dense packing of catalyst molecules on the substrate surface.

The final atomic constituent of the PPIX molecules is oxygen. High-resolution O1s XPS spectra are depicted in Fig. 4.9(e) and (f) and indicate comparable signal intensities for the reference samples compared to the ones with the LB layer. In the case of the Si reference sample, the oxygen signal mostly stems from the surface oxide formed due to the oxygen plasma treatment and subsequent immersion in DI water over an extended amount of time. This surface oxide formation is commonly observed for non-oxide semiconductors. It is self-limiting since a thin oxide layer suffices to protect the semiconductor underneath from further oxidation through contact with oxygen and water in the atmosphere. The native oxide on Si is self-limiting at a thickness of around 2 nm, which is attained within a few hours of contact with the atmosphere [182]. Since the analyzed samples were processed in an oxygen plasma, the oxide thickness might be significantly different in this case. A more in-depth investigation of the native oxide thickness can be found in the analysis of the Si2p spectra later in this section.

Due to the low stoichiometric oxygen content of the PPIX and its location directly at the interface to the surface oxide, its signal is completely masked by the signal from the substrate. The slight deviations in the fit of the substituent components likely arise due to the low sensitivity of the fit and are not necessarily a result of the PPIX LB deposition. In the case of Au, no oxide is formed on the surface. Nevertheless, the O1s signal intensity of the reference and sample spectra remain comparable, likely due to the presence of adsorbed water stemming either from the submersion process or atmospheric humidity [183], [184]. While this signal remains for the LB layer sample, a small shoulder at the high binding energy side of the peak appears. This signal matches the binding energy expected for a carboxylic functional of around 534 eV and, thus, could arise from the PPIX functional groups. The LB deposition also led to a pronounced shift in the binding energy of the water signal. The origin of this is unclear, but it is not a consequence of charging since the Au4f spectra discussed in the following paragraphs do not show any indications of this occurring. Therefore, a possible explanation could be the change in the local environment of the adsorbed water as a consequence of the adsorbed PPIX. Hydrogen bond formation has been shown to significantly impact the binding energy of the O1s signal of DI water. Therefore, interaction with the hydrophilic hydroxyl groups of the PPIX could potentially cause such a shift [183], [185].

The ZnO, GaN, and AlGaN samples were investigated in the same manner as the Si and Au samples. The experimental results for the former set of substrates are in agreement with the above interpretation. Only the N1s spectra of the nitride samples and the O1s spectrum of the ZnO show significantly different spectral features. This is expected since nitrogen and oxygen are major constituents of the respective bulk materials.

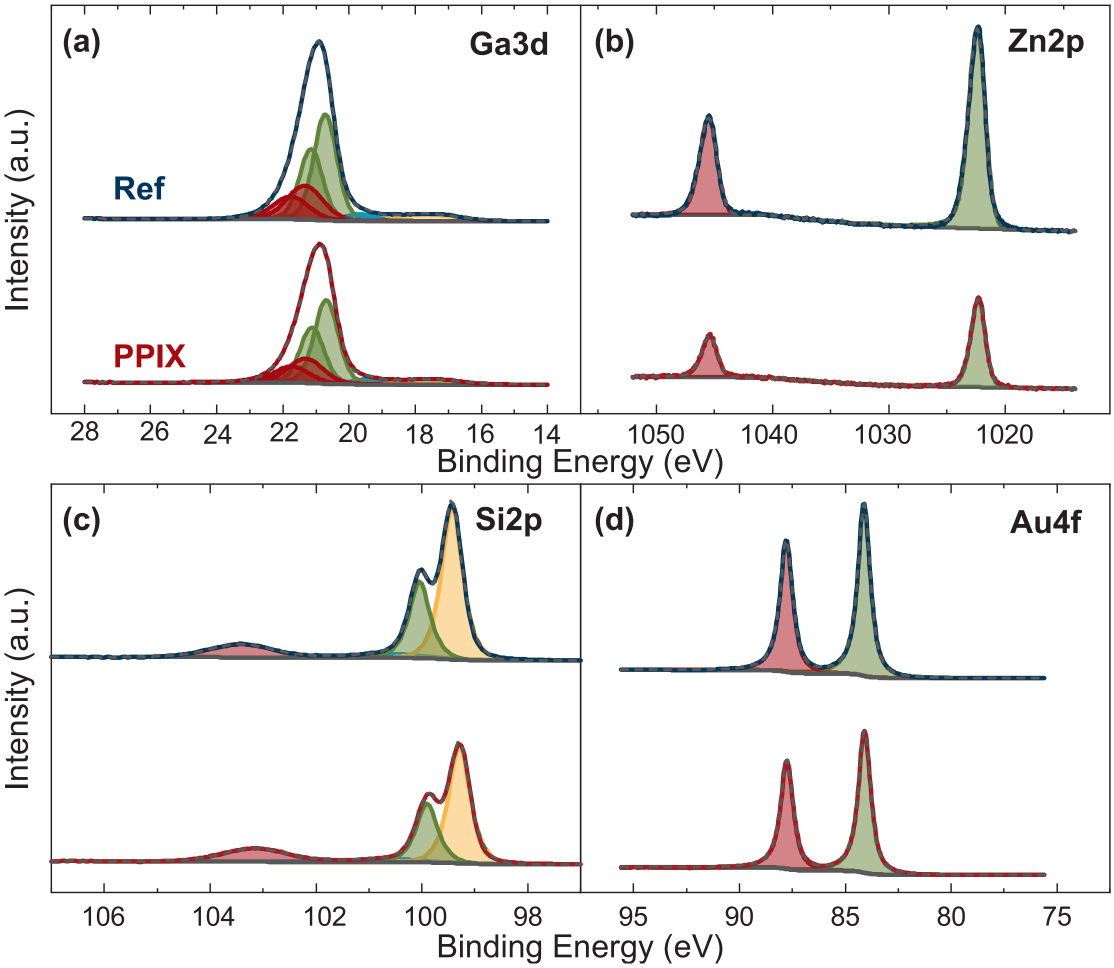

Figure 4.11 XPS spectra of the relevant elemental transitions of the respective substrate for (a) GaN, (b) ZnO, (c) Si, and (d) Au, for reference samples and samples covered by a PPIX LB layer. The monolayer thickness can be estimated through signal attenuation analysis.

In addition to the high-resolution analysis of the elemental transitions associated with PPIX, the chemical structures of the substrate constituents were investigated. The high-resolution Si2p and Au4f spectra for the substrate reference and LB-layer samples are shown in Fig. 4.11. The Si2p spectra exhibit the expected spectral features for a Si sample covered by a thin oxide layer. The two main features at 99.4 eV and 100.0 eV correspond to the spin–orbit split doublet of pure Si–Si bonds. The smaller and significantly broader peak at 103.4 eV arises from stoichiometric SiO_2, while an even smaller component in between at 100.7 eV hints at the presence of substoichiometric oxide [186]. By comparing the peak intensity of oxide- and bulk-related peaks, the thickness of the native oxide can be determined according to the method described in Sec. A.6.2. In the case of Si, after the surface preparation procedure, the oxide thickness was determined to be (1.3 ± 0.2) nm, which is slightly below the self-limiting thickness of the native oxide, which is around 2 nm. Thus, an additional oxide removal step, as described in Sec. A.11.1, was needed to ensure a minimal oxide thickness. The same analysis indicated slightly thicker surface oxides of (1.7 ± 0.2) nm for the nitride samples, independent of the Al to Ga ratio.

The LB layer thickness can be estimated by analyzing the signal attenuation of the substrate-related intensities between the reference and LB layer samples, as described in Sec. A.6.2. The LB layer thickness for the Si sample was determined to be (0.9 ± 0.2) nm. The LB layer thicknesses of most other samples were within the margin of error, ranging from (0.8 ± 0.2) nm for Au to (1.0 ± 0.2) nm for GaN, with most other samples in between. Only the analysis of the Zn2p spectra of the ZnO sample found significant deviations, indicating an LB layer thickness of (1.3 ± 0.2) nm. This difference likely arises due to an imperfect estimation of the inelastic mean free path (IMFP) of the photoelectrons. As described in Sec. A.6.2, this value is required for an accurate estimation of the overlayer thickness and was approximated using an empirical formula. The kinetic energies of the photoelectrons generated from the Zn2p core levels are significantly lower than the substrate-related photoelectrons from all other samples investigated, by around 900 eV. Therefore, imprecision of the empirical IMFP estimation over this wide energy range can easily cause skewed overlayer thickness estimations. To check this hypothesis, the LB layer thickness estimation of the ZnO samples was repeated using the O1s transition instead. The determined thickness is in line with the other samples, yielding an overlayer thickness of (0.9 ± 0.2) nm, thus supporting this assumption.

Overall, the LB layer thicknesses determined via XPS are, thus, comparable to each other, supporting the consistency of the LB layer thicknesses on different substrates already determined via AFM. Nevertheless, the average thickness determined via XPS is slightly lower than the estimates based on AFM. This could be caused by systematic errors in the empirical IMFP estimation. This factor influences the signal attenuation exponentially, meaning that even slight deviations can cause significant errors in the determined thickness. Additionally, the derivation of the IMFP relies on the SAMs mainly consisting of alkanes of varying chain length. While it is common practice to use the IMFP value obtained in this manner for all organic overlayers, its quantitative validity beyond the specific model system initially investigated might be questionable.

4.4. Electronic Interaction of Protoporphyrin IX Langmuir–Blodgett Monolayers with Semiconductors

The electronic interaction between the molecular monolayer and the substrate is of paramount importance to the catalytic performance of a potential device since all envisioned benefits of the hybrid system revolve around it. Therefore, it is imperative to gain more in-depth knowledge of the processes at play. This section focuses on understanding the energy level alignment and transfer processes at the interfaces between the mentioned semiconductors and a PPIX LB layer.

4.4.1. Energy Level Alignment of Protoporphyrin IX Monolayers

The energy level alignment at the interfaces was determined using UPS and UV–Vis spectroscopy. The data from all measurement methods individually give insight into specific properties, which are subsequently combined to obtain a complete picture of the work function, vacuum level, and energy levels of the substrate and molecule. The theoretical background required for the analysis of the presented data is described in Sec. 3.3 and 3.4.

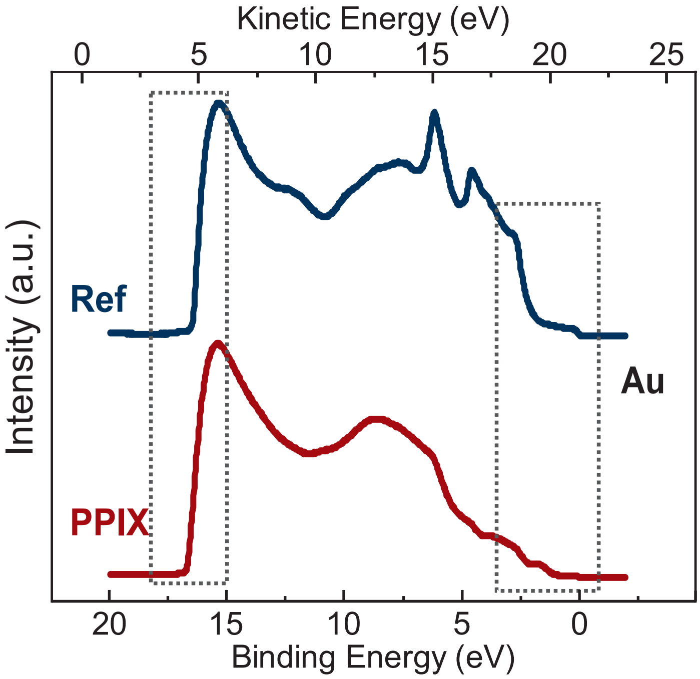

Figure 4.12 UPS spectrum of a bare Au substrate (blue) and a substrate covered with a monolayer of PPIX (red). The main regions of interest for the energy level alignment—the SECO and the low binding energy region—are highlighted by dashed boxes.

Exemplary UPS spectra of Au and of Au covered with an LB layer of PPIX are shown in Fig. 4.12 and serve as a stand-in to describe the regions of interest in the spectrum. The general measurement principles of UPS can be found in Sec. A.6.4. Comparing the spectra, it becomes evident that UPS has a significantly lower depth of information than XPS, which arises due to the lower kinetic energy of the analyzed electrons. The distinctive features present in the reference Au spectrum are strongly attenuated or not present at all for the LB layer sample, indicating that a thin overlayer of 1 nm can suffice to attenuate most of the signal. While this can be advantageous due to the enhanced surface sensitivity, it can also increase the impact of contamination.

UPS spectra make use of a significantly smaller energy range than XPS, starting at binding energies of roughly 20 eV for a He I plasma illumination source, which limits the maximum observable binding energy due to its comparatively small photon energy of 21.2 eV. Therefore, UPS spectra are often shown in their entirety since the whole scanned energy range can be recorded with a single high-resolution measurement without investing a significant amount of integration time. Within this narrow binding energy range, one can only measure very shallow core-level electrons, making UPS a very limited tool for analyzing core-level properties. Nevertheless, its superior energy resolution makes it ideal for analyzing the electronic spectrum. For example, the secondary electron cut-off (SECO) at the high binding energy side of the spectrum yields the work function of the investigated sample. The opposite side of the spectrum contains information on the low binding energy region of the sample, which might, for example, be the VB spectrum of a semiconductor. For the investigations performed in this work, the spectral shape between these two extreme cases is not of interest. Therefore, full spectra are provided in the Appendix B, and the discussion in the following paragraphs only focuses on the regions of interest marked with the dashed boxes in Fig. 4.12.

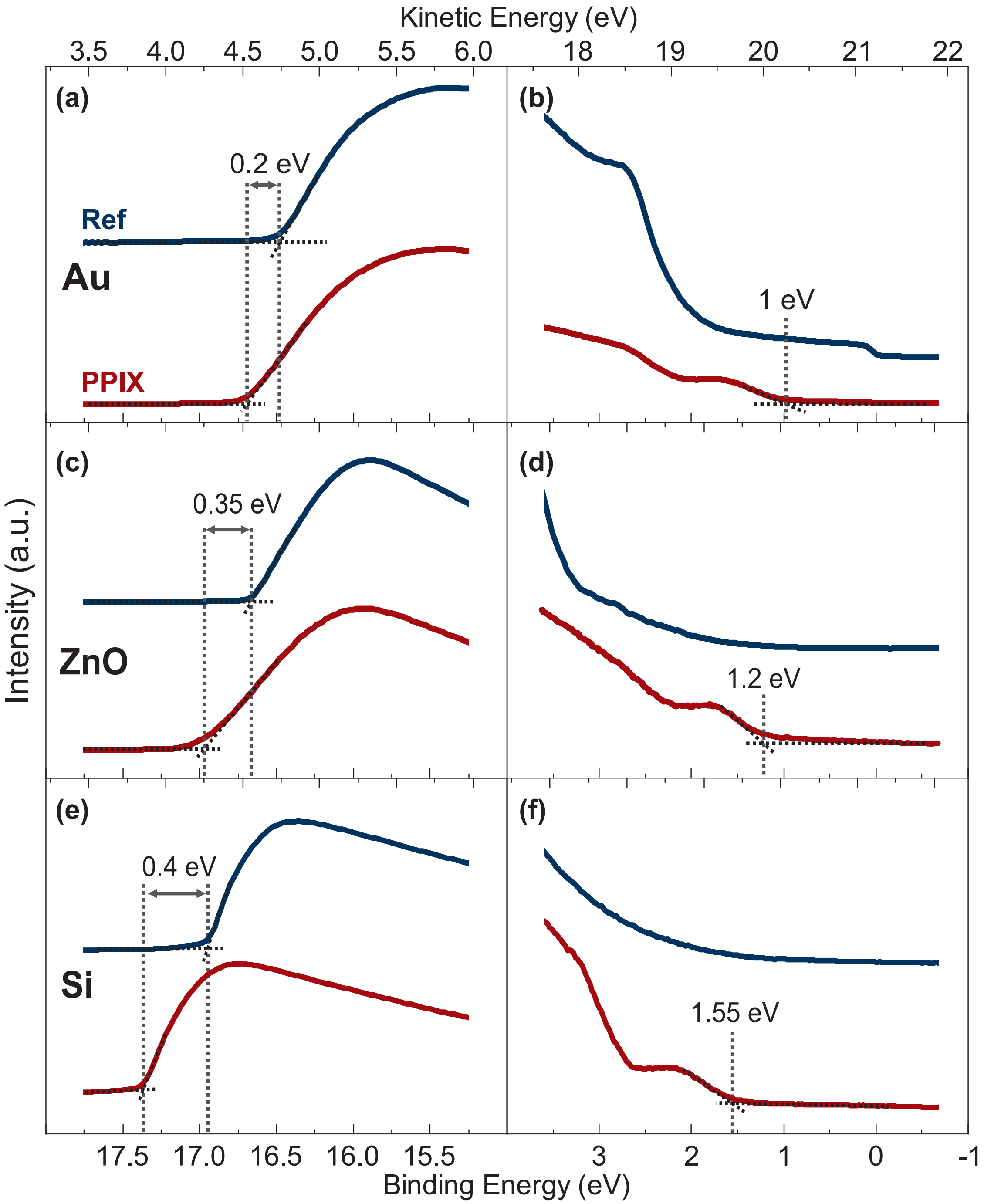

Figure 4.13 (a), (c), and (e) show the SECO region extracted from full UPS spectra for Au, ZnO, and Si substrates, respectively, which indicate interface dipole formation and the work function. (b), (d) and (f) are the corresponding excerpts from the low binding energy regions, indicating the position of the PPIX HOMO relative to the Fermi energy.

The SECO and VB regions of the UPS measurements performed on reference and LB-layer Au, ZnO, and Si samples are shown in Fig. 4.13, and the measurements for the group III–

nitrides are depicted in 4.14. Analysis of the AlN substrate was not possible due to charging of the sample arising from insufficient conductivity of the material. The process of analyzing the obtained data to extract the vacuum level shift and HOMO position is described in more detail in the remainder of this section, with Au serving as an example. The analysis of the SECO region yields the work function of the substrate through linear extrapolation of the rising signal to the background level (Sec. A.6.2). The kinetic energy at this intersection is the work function of the investigated material. In the case of Au, the work function was determined from the SECO shown in Fig. 4.13(a), yielding a value of (4.75 ± 0.05) eV. This is significantly lower than the expected work function of Au, which is reported to be larger than 5.1 eV [187], but studies on the work function after exposure to the atmosphere have found that this induces significant changes, yielding work functions similar to our observations [188]. Upon LB layer deposition, the work function is reduced abruptly by 0.2 eV, which arises due to a vacuum level potential shift through the formation of an interface dipole layer between the PPIX molecule and the Au surface, which could be a consequence of molecular dipole moments or partial charge transfer (Sec. 3.3.2).

The VB region depicted in Fig. 4.13(b) shows more complex spectral features for the reference and LB layer samples. In the case of the reference sample, a distinct potential step at a binding energy of 0 eV arises due to the metallic nature of the material. This feature represents the electron energy distribution at the Fermi level of the Au substrate, which is the reference energy for photoelectron spectra. Its appearance at 0 eV implies that the energy calibration of the system is correct and no sample charging occurs during measurement. The same feature is also visible for the LB layer sample but is drastically attenuated due to the overlayer. An additional peak arises for the LB layer samples. This feature can be attributed to the HOMO orbitals of the PPIX molecules within the layer. Through linear extrapolation of the rising edge of this feature, the onset of the HOMO orbital can be determined to be around 1 eV below the Fermi level. Since the relative difference between the vacuum level and Fermi level is known from the SECO analysis to be (4.55 ± 0.05) eV, the ionization energy can be determined to be (5.6 ± 0.1) eV.

Due to the semiconducting properties of these samples, there is no measurable Fermi edge at a binding energy of 0 eV. In addition, accurate VB analysis of the bare semiconducting samples is not possible due to the native oxide covering most semiconductor surfaces. Its thickness of 1 to 2 nm suffices to attenuate any VB signal, requiring UHV preparation, such as argon sputtering, to remove the oxide before the analysis. This could also lead to surface damage or a change in the near-surface stoichiometry, further complicating the issue and skewing the measurement results. Therefore, the VB positions used to determine the energy level alignment were extracted from the literature instead.

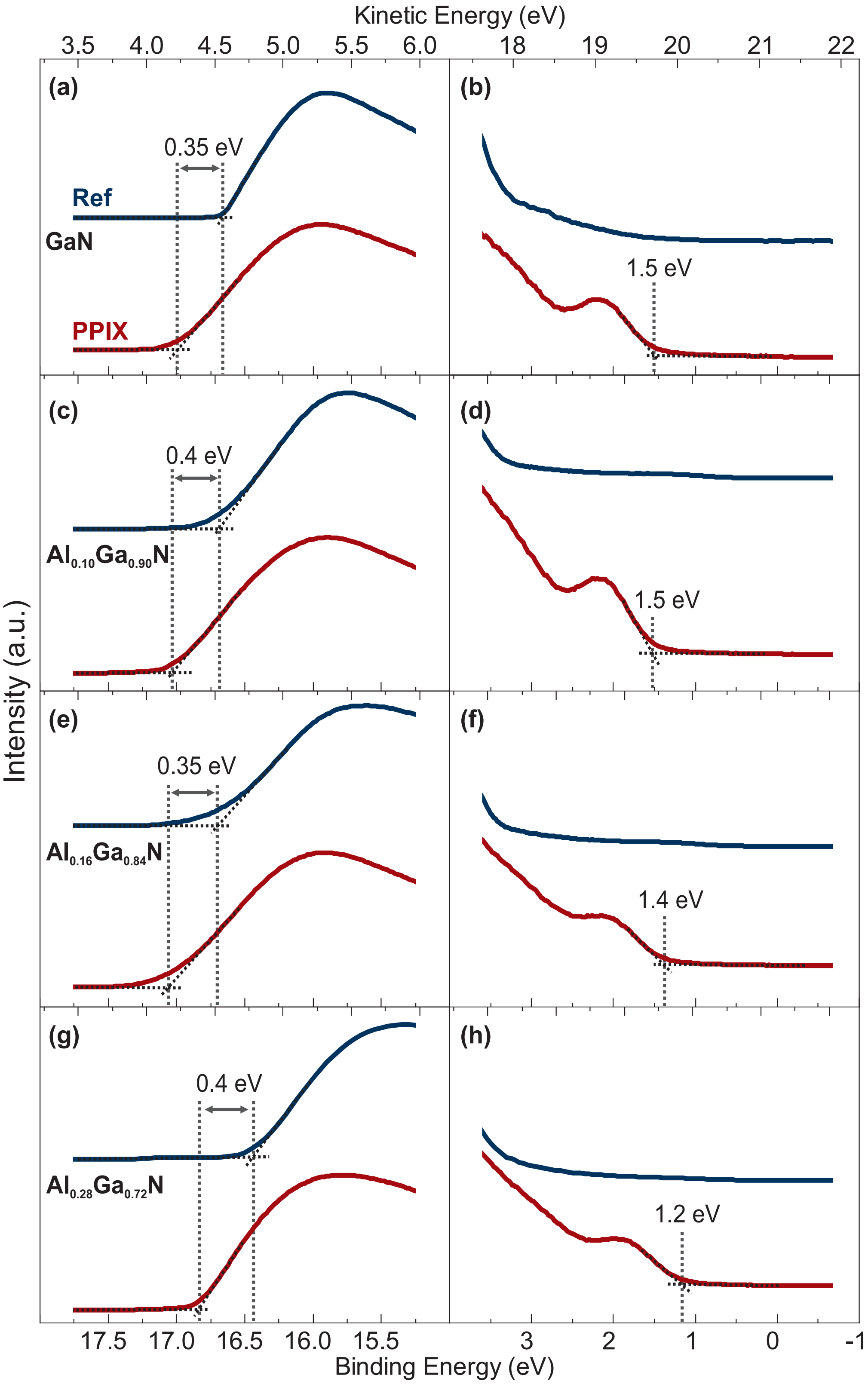

Figure 4.14 (a), (c), (e), and (g) depict the SECO region extracted from full UPS spectra for AlGaN samples of varying Al to Ga ratio. (b), (d), (f), and (h) show corresponding excerpts from the low binding energy regions, indicating the position of the PPIX HOMO relative to the Fermi energy.

The UPS spectra of all other samples exhibit qualitatively identical features. Thus, this analysis was performed analogously for the remaining samples. The vacuum level shift at the interface catches the eye in particular, since it appears to be identical (within the margin of error) for all semiconductor samples under investigation, with a value of around 0.4 eV. Similar interface dipole shifts have previously been identified for different SAMs of porphyrins on, for example, nitrides [189], [190]. The only deviating sample is the metallic Au substrate. A possible explanation for the origin of these energy shifts is the dipole moment of the molecule arising due to its amphiphilic nature, in particular, the carboxylic acid functional groups facing the substrate. These groups could interact with the native oxide or hydroxyl groups present on all substrates under investigation except for Au. The interaction of the surface with the carboxylic acid functional groups could, therefore, explain the deviation between the inert metallic substrate and the semiconductors. In addition, the free charge carriers in the Au could form an opposite mirror dipole at the interface, thereby mitigating the effectively observed dipole shift.

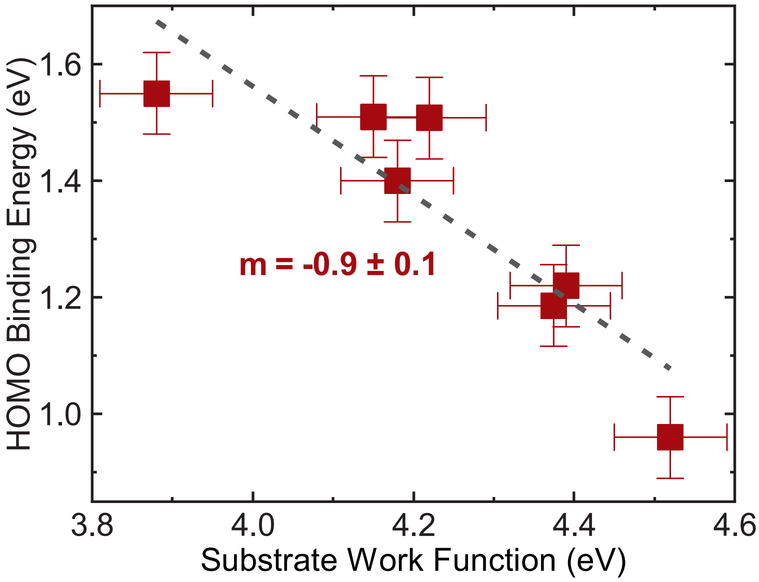

Figure 4.15 Variation of the HOMO binding energy (HOMO$-E_F$) with the work function of the substrate. The linear relationship with a slope close to −1 indicates that the HOMO binding energy aligns with the vacuum level.

Using the extracted surface properties and comparing all the acquired data yields information on the alignment pattern at the interface. Fig. 4.15 depicts the dependence of the energy difference between the HOMO and the Fermi level on the work function of the reference substrate. A linear relationship between these two parameters can be implied. The proportionality factor obtained through linear regression is close to −1, which indicates that the energy level alignment process is governed by vacuum level alignment rather than Fermi level alignment. This is supported by the low variance of the ionization energy, which is on average 5.6 eV and exhibits a standard deviation of 0.1 eV. This is within the margin of error of the value expected.

Similar results have been obtained in prior UHV studies performed with Zn porphyrins on various metals [109] and other similar interfaces [116], [117]. In addition to this observed vacuum level alignment in conjunction with a static dipole moment, many prior studies have found a shift in the alignment interactions for high work function samples when the work function approaches the ionization energy of the molecule. This has been interpreted by Greiner *et al.* [116] as being caused by a rapid increase in charged molecules on the surface, leading to an increase of the interface dipole that counteracts and pins the HOMO energy of the molecule (Sec. 3.3.2).

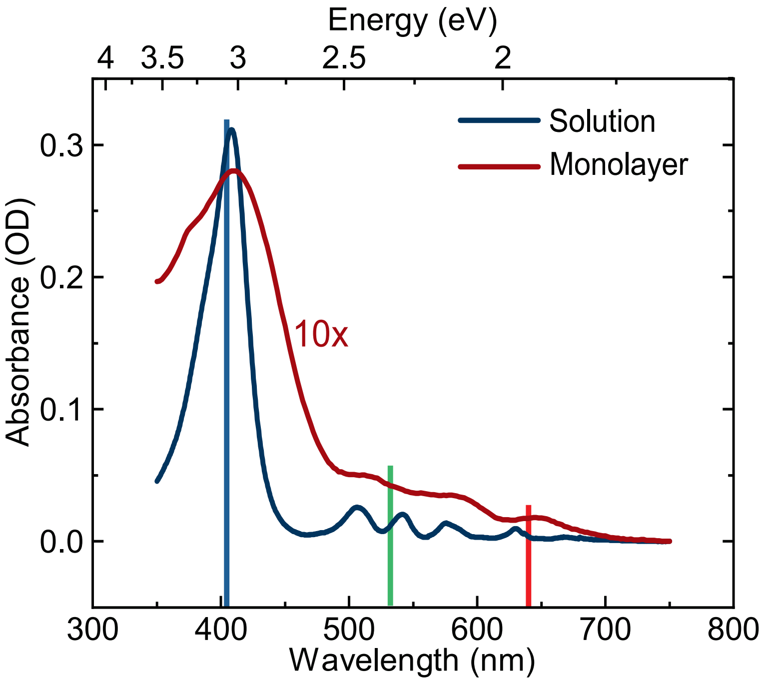

Figure 4.16 UV–Vis absorbance of PPIX as a 5 µM solution in dimethyl sulfoxide (DMSO) with an optical path length of 10 mm, and as a monolayer deposited on a microscope slide at a surface pressure of 30 mN m^{-1}. The monolayer absorbance is magnified by a factor of 10 for better readability.

UPS is only capable of analyzing occupied states. Thus, one cannot obtain any information on the LUMO position and its alignment with the CB. Its energy level alignment relative to the redox potentials of the reactions to be catalyzed, but also relative to the CB of the substrate, is crucial for the performance of a potential hybrid catalyst device. Therefore, the LUMO position of the molecules in the LB layer was determined indirectly through UV–Vis spectroscopy. With this approach, the transition energies between the HOMO and LUMO and consequently the relative energetic position of the LUMO relative to the HOMO could be determined. UV–Vis spectra of PPIX in solution and as a monolayer are depicted in Fig. 4.16. The PPIX in solution exhibits the expected Soret band (B band, transition between S_0 and S_2) at 408 nm as well as four Q bands (transition between S_0 and S_1) at 507 nm, 542 nm, 576 nm, and 630 nm [191]. These features remain similar in a monolayer of PPIX but are significantly broadened for all bands observed. While the B band peak remains at a similar position, the Q bands experience a bathochromic shift. Both the broadening and the spectral shift are hints at intermolecular interaction (see Sec. 3.3.1). Nevertheless, a full interpretation, especially with regard to the differences between B and Q bands, is beyond the scope of this work. The important parameter determining the LUMO energy level is the onset of the lowest-energy Q band at around 690 nm corresponding to a HOMO–LUMO splitting of 1.8 eV. This leads to a LUMO (S_1 state) energy level onset of 3.8 eV. The onset of the LUMO+1 (S_2 state) energy level is located at roughly 2.9 eV.

With a combination of UPS and UV–Vis, the energy level alignment was determined for all semiconductor samples under investigation. A depiction of the deduced energy level alignment can be found in the following section.

4.4.2. Energy and Electron Transfer between PPIX and Semiconductors

The investigation of transfer mechanisms at hybrid interfaces intended for catalysis can be challenging. The ideal approach to study these would be to measure the TOF of the device in an *in situ* experiment since this is the relevant figure of merit for the catalytic performance in the context of charge transfer. However, this tends to impose high requirements on the device since such *in situ* measurements can only be done if the device structure is sufficiently optimized to allow for extended measurement times. This usually involves chemisorption of the molecule, which is imperative to prevent its desorption from the surface. A desorbed molecule could act as a homogeneous catalyst, skewing the measurement results. The catalytic activity of the bare substrate could also have a significant impact. Lastly, device optimization becomes challenging for non-colloidal systems due to the low surface area. This, in combination with the low TOFs achieved in systems so far, results in very low product concentrations close to the detection limit of many product analysis techniques. This becomes even more complicated for CO_2 reduction catalysis, for which the determined product concentrations could also result from catalyst degradation at such low concentrations.

Therefore, *in situ* measurements are the ideal approach for the initial optimization of hybrid systems, which requires alternatives for faster screening in a controlled environment. The performance of a hybrid system is thought to be greatly influenced by its ability to provide the required charge to the catalytically active center while ensuring that the molecular catalyst remains in its excited state for as long as possible. The luminescence intensity of the LB layer-molecule can provide similar information on these processes. After photoexcitation, the molecule is in its excited state. Relaxation of this excited state could happen via multiple pathways, which can be characterized by their respective rate constants. An unavoidable transfer process of a luminescent molecule is its relaxation through the emission of a photon. Generally, most other transitions are “dark,” meaning that they do not emit a photon upon relaxation. This allows the luminescent relaxation rate to be compared with the transition rates of the other relaxation processes, since an increase in the dark relaxation rate has a direct impact on the observed luminescence intensity. This process is called luminescence quenching and is often used to analyze intermolecular interactions. In hybrid systems, such dark relaxation pathways might be charge or energy transfer processes, as described in Sec. 3.4.

While it is challenging to determine the absolute transfer rates of a system accurately by analyzing the luminescence intensity, this method can be used to compare the relative transfer rates if all measurements are performed under identical conditions. This enables a comparison of the interaction behavior of the substrates studied. For a real catalytic system, the intended catalytic processes usually require transfer from the semiconductor to the molecule. The proposed luminescence analysis cannot provide in-depth information on such processes, and instead yields information on the transfer in the opposite direction, from an excited molecule to the semiconductor. Thus, this technique only provides indirect information on how to prevent undesirable relaxation pathways to maximize the excited state lifetime and, therefore, the probability of a catalytic process occurring. Depending on the identified transfer processes, one could make arguments of symmetry that would invoke the idea that the prevention of transfer in one direction should enable transfer in the other direction, but is not a direct proof for charge transfer to occur in the other direction. This measurement method motivates the use of PPIX since the catalytically active protoporphyrin derivatives, such as iron and cobalt porphyrin, have very low luminescence quantum efficiency, making the luminescence detection of monolayers of these molecules challenging or impossible.

The luminescence intensity of PPIX on all substrates was investigated through excitation with three different energies, which are highlighted in the UV–Vis spectrum shown in Fig. 4.16. In the context of this study, all four Q bands are treated as LUMO levels, and the B band as the LUMO+1 level. Excitation with 640 nm light was used to probe the LUMO onset, while illumination at 532 nm was used to probe higher regions of the LUMO energy level. Finally, illumination at 405 nm was intended to provide information on the charge transfer from higher-energy molecular orbitals. The excitation power of each laser was carefully adjusted using the relative absorption obtained through the UV–Vis spectrum to ensure that the excitation rate was identical for all three illumination wavelengths. Thus, the obtained luminescence intensity can be compared across samples and wavelengths.

Exemplary photoluminescence spectra of PPIX deposited on all substrates using 532 nm and 405 nm illumination are depicted in Fig. 4.17. Compared to a luminescence spectrum of PPIX dissolved in DMSO, shown in Fig. B.9, these spectra are slightly bathochromically shifted, which likely arises due to the aforementioned hybridization that was already apparent in the UV–Vis spectrum. In addition, the relative intensities of the observed transitions drastically change upon condensation of the PPIX into an LB layer, indicating a significantly lower

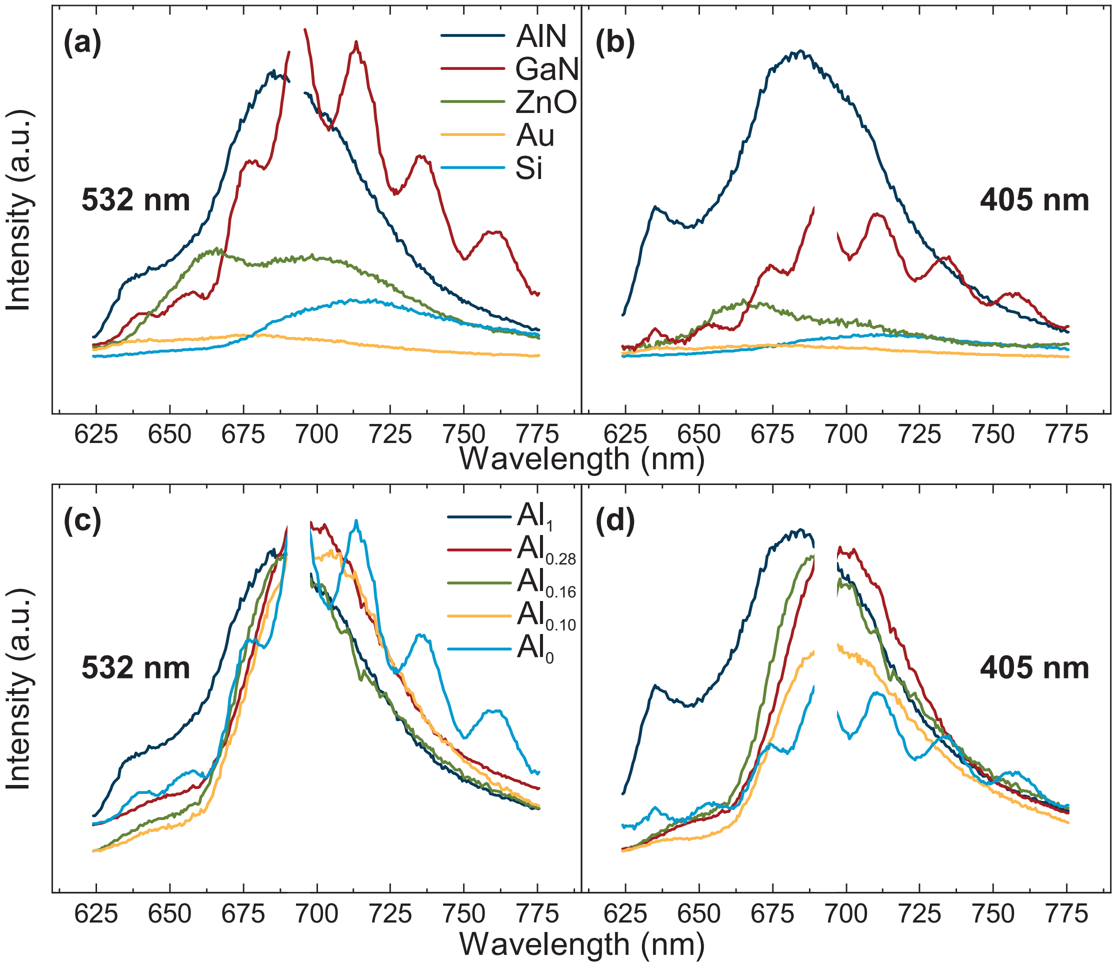

Figure 4.17 Exemplary photoluminescence spectra for (a) and (c) excitation at 532 nm and (b) and (d) excitation at 405 nm of (a) and (b) of a variety of semiconductor and metallic samples and (c) and (d) a set of AlGaN samples with various Al to Ga ratios. The region around 690 nm is excluded for all samples grown on the sapphire substrate due to the intense luminescence of the sapphire due to Cr contamination.

high-energy luminescence peak compared to the broad feature at around 700 nm. The LB layers on the different samples also exhibit slight differences in their spectral shapes. This excludes the drastically different spectra in the case of GaN, which arise due to interference phenomena of the significantly thicker and, at this wavelength, transparent GaN thin film substrate.

Due to the lack of a detailed understanding of how the spectra are affected by the substrate, an accurate interpretation of the change in spectral shape is beyond the scope of this work. Instead, the interpretation is limited to the dependence of the overall luminescence intensity on the substrate and excitation wavelength. As becomes apparent in Fig. 4.17(a) and (b), the overall intensity depends strongly on the substrate, indicating significant luminescence quenching on the majority of substrates. In the case of 532 nm excitation, the maximum signal intensity is observed for the GaN and AlN substrates. Excitation into the LUMO+1 state upon illumination at 405 nm leads to a comparative reduction of the GaN luminescence intensity. This difference has been investigated in further detail on AlGaN samples with different Al to Ga ratios, as depicted in Fig. 4.17(c) and (d). It is evident that the reduction in luminescence intensity upon excitation to the LUMO+1 state depends on the Al content in the nitride semiconductor. As already described in Sec. 2.1.2, the change in Al to Ga ratio mainly affects the energy level of the CB, leading to a reduction in electron affinity and an increase in the band gap of the semiconductor material. Assuming that transfer processes between the PPIX and the substrate are the relevant quenching mechanism, it is hard to distinguish between electron and energy transfer. For electron transfer mechanisms, the luminescence intensity would be dependent on the electron affinity of the substrate. In the case of energy transfer, the band gap is the relevant property. With the present group III–nitride material system, these parameters are strongly connected, thus not allowing for distinction between these transfer mechanisms.

This matter can be resolved by analyzing the ZnO substrate, because this material exhibits a band gap very similar to GaN while having a significantly higher electron affinity. Since PPIX on ZnO exhibits a significantly lower signal intensity than GaN for both illumination wavelengths, the predominant transfer mechanism governing the observed luminescence quenching is likely electron transfer. Fig. 4.19(a) depicts the integrated luminescence intensity for all substrates except AlGaN, normalized to the highest intensity observed on the AlN substrate, clearly showing the difference between the ZnO and GaN luminescence intensities. Also shown is the integrated intensity upon excitation with 640 nm, which closely follows the intensity observed for excitation with 532 nm.

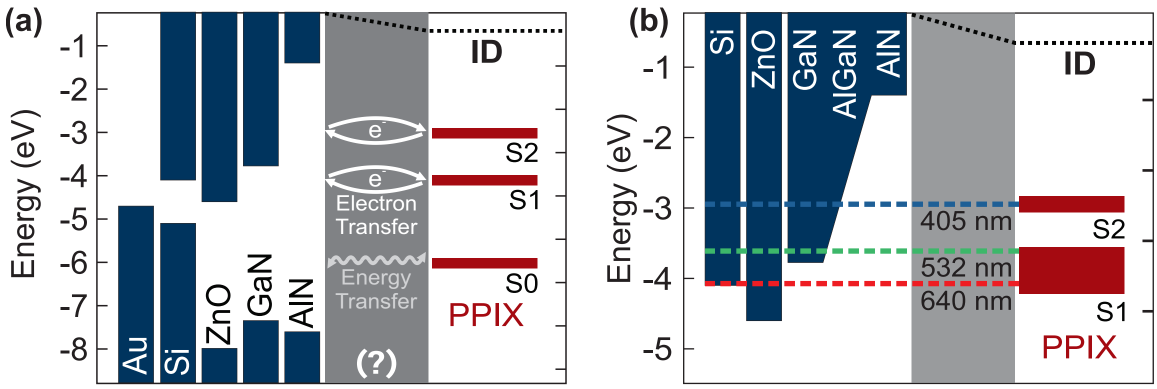

Figure 4.18 (a) Proposed band alignment and apparent interaction processes between PPIX and all substrates under investigation, including the formation of an interface dipole resulting in a $\sim$0.4 eV shift in vacuum level, the vacuum level alignment, and the fast electron transfer processes between substrate and molecule. (b) Detailed view of the semiconductor CB relative to the PPIX LUMO levels including the approximate excited state energies for excitation with the respective wavelengths.

The assumption that charge transfer processes are the dominant quenching process observed within this hybrid system is mostly supported by the energy level alignment of the LUMO and LUMO+1 levels with the substrate CBs, as depicted in Fig. 4.18. The LUMO state is positioned lower than the electron affinity of GaN. This leads to a diminished electron transfer rate compared to substrates such as ZnO, for which the potential landscape favors a transfer to the semiconductor CB. Similarly, the LUMO+1 resides above the CB of GaN, which allows this transition to occur at a significantly faster rate, leading to a decrease in photoluminescence intensity. Both excited states are significantly lower in energy than the electron affinity of AlN, prohibiting an electron transfer to the substrate, as indicated by the increased photoluminescence intensity. The highest potential gradient is observed for Au since unoccupied states are present directly above the Fermi level at around 4.75 eV.

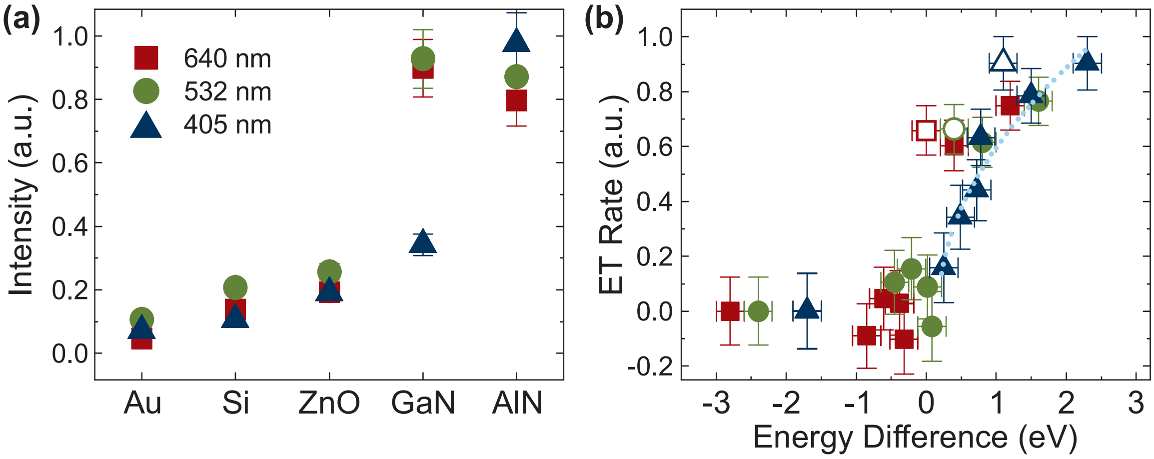

Figure 4.19 (a) Normalized integrated intensity of PPIX photoluminescence upon excitation with 405 nm, 532 nm, and 640 nm wavelength light for all samples except the AlGaN samples. (b) Dependence of derived estimates of the relative electron transfer rate from the excited state of PPIX to the substrate on the energy difference between the excited state and substrate CB. Open symbols refer to the Si substrate. The dotted blue line is a fit of the data acquired with 405 nm excitation according to Marcus theory (see Sec. 3.4).

The dependence of luminescence quenching on the potential energy gradient required for charge transfer to occur is depicted in Fig. 4.19(b). Here, an arbitrary measure for the electron transfer rate is calculated, assuming full quenching (and, thus, a value of 1) for the Au substrate and no quenching (a value of 0) for AlN. A positive energy difference denotes favorable energetic alignment for charge transfer from the molecule to the semiconductor. Negative values indicate an upward potential gradient. Here, it becomes evident that the transfer rate rises significantly as soon as the potential gradient changes direction. Applying the charge transfer theory explained in detail in Sec. 3.4 to fit the data for excitation with 405 nm light yields a good agreement between fit and data, thus suggesting that the process involved in the luminescence quenching can be modeled using Marcus theory with a reorganization energy of around (0.2 ± 0.1) eV. Similar analyses are impossible for illumination with the two other wavelengths, since the number of samples exhibiting a positive potential difference is significantly lower. This behavior has been observed for other molecules and quantum dot systems before, leading to similar conclusions being drawn regarding Marcus theory and charge transfer [30], [128], [192].

Additionally, the large differences in behavior between excitation into the LUMO+1 state and the LUMO state are interesting due to their implications for determining the charge transfer rates, since the thermalization rates of LUMO+1 to LUMO are known to be fast, resulting in lifetimes of a few femtoseconds [193] for PPIX in solution. While charge transfer processes on the order of a few tens to hundreds of femtoseconds are regularly observed in monolayer samples [30], [194]–[196], it is not certain what the specific timescale would be for the investigated systems. Attempts to experimentally determine the relaxation time constants of a PPIX monolayer using transient absorption spectroscopy were unsuccessful due to the low signal intensity of a single monolayer and sample degradation. Thermal relaxation could, for example, be significantly slower due to changes in the vibrational properties associated with intermolecular interactions. Nevertheless, even a significantly lower thermalization rate would still be significantly faster than any electrochemical process, for which the required timescale is in the millisecond range. This highlights the importance of energy level alignment and charge transfer mechanisms at the interface, since these processes would severely diminish the performance of a hybrid device based, for example, on a ZnO substrate.

The electron transfer rates for excitation to the LUMO state also show qualitative deviations from the previously discussed charge transfer theory, especially for the narrower band gap semiconductor Si, which is depicted with empty symbols in Fig. 4.19(b). Here, the electron transfer rate is significantly higher than the expected value, in particular since the energy difference resulting from excitation with 640 nm wavelength light is negligibly small. A possible explanation for this could be that a smaller reorganization energy is needed for the electron transfer process from the lower LUMO state compared to the higher energy states. Energy transfer processes might also have a significant influence on this narrower band gap semiconductor substrate, which has been observed in previous studies on the distance dependence of this quenching behavior [138], [197]. Energy transfer to the bulk states is not possible in all the other semiconductors due to the lack of spectral overlap of luminescence and excitation. Further investigations with a more exhaustive set of narrow band gap semiconductors would be necessary to clarify the cause of this outlier and confirm the occurrence of energy transfer.

The given interpretation of energy and charge transfer processes in the investigated hybrid systems is based on a rather simplified picture of the energy landscape at the interface. In addition to the semiconductor bulk properties, defect states on the semiconductor surface located within the band gap may also facilitate transfer. While the expected surface state density is around 2 orders of magnitude lower than the PPIX molecule density ($1 \times 10^{12}\,\mathrm{cm}^{-2}$ surface states [198] compared to $\sim 2 \times 10^{14}\,\mathrm{cm}^{-2}$ molecules), these may still have an impact on the formation of, for example, localized hybrid excitons at the interface. Metalloporphyrins have been found to very effectively passivate surface defects of both GaN and AlN photodetectors [189], [190], highlighting the possibility of interaction between surface states and molecular orbitals. In addition, surface band bending could play a significant role for all these samples due to its influence on electron drift after charge transfer, which is closely related to transfer processes from the VB to the unoccupied HOMO state. The energy level alignment suggests that electron transfer from semiconductor to molecule could only occur for Si because the VB energy of all other wider band gap semiconductors is far below the HOMO. This could possibly lead to accelerated degradation of the molecular catalyst since many catalytic molecules are found to be most prone to degradation in their oxidized state. Thus, it may be possible to use the time evolution of the luminescence signal to study the effect of the energy level alignment of the VB and HOMO on molecule degradation.

4.5. Influence of the Introduction of Metal Centers on the Interface

The previous sections of this chapter focused on PPIX LB layers, assuming that their properties at hybrid interfaces are representative of catalytically active molecules too. While this assumption is likely to be valid due to the structural similarities to metalloporphyrins, it is evaluated in more detail in this section to increase the confidence level. This includes analyses of the morphology and energy level alignment similar to the previously performed studies on free-base PPIX. Luminescence studies were not carried out, because the luminescence quantum efficiency of the catalytically active molecules is significantly lower than for the free-base PPIX, making its detection significantly more challenging. The impact of metal centers was studied for iron (FePPIX), cobalt (CoPPIX), and zinc (ZnPPIX), of which the cobalt metal center has seen the most use in catalytic applications, such as electrocatalytic CO_2 reduction [21], [199]–[204]. While the ZnPPIX does not require charge stabilization, CoPPIX and FePPIX are only commercially available in their chlorine-coordinated form, since the Fe III and Co III oxidation states are generally more stable than their II counterparts. Thus, the metal centers of these samples are axially coordinated with a chloride ion.

4.5.1. Morphology

The Langmuir films of the molecules studied were initially investigated via isotherm analysis to compare the Langmuir film formation process, film stability, and mean occupied surface area per molecule in the condensed phase. The isotherms for all three investigated PPIX derivatives are shown in Fig. 4.20, exhibiting an overall shape comparable to the previously investigated free-base PPIX. All isotherms initially started at a surface pressure of $0\,\mathrm{mN\,m^{-1}}$ and rose to surface pressures of about $50\,\mathrm{mN\,m^{-1}}$ upon full compression, and did not exhibit any phase transitions or previously unobserved features.

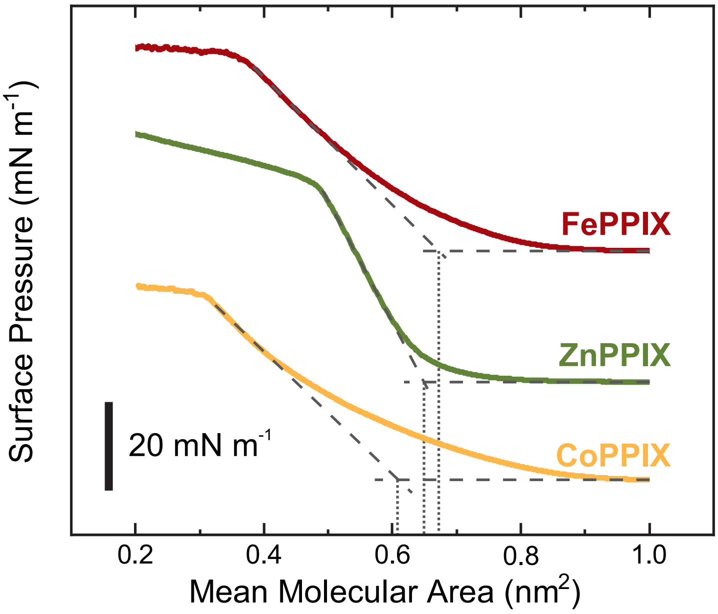

Figure 4.20 Isotherms of PPIX metallized with either Fe, Zn, or Co deposited on a DI water subphase. The dashed lines indicate the extensions of the linear regions of surface pressure increase for the determination of the MMA of 0.67 nm^2 for FePPIX, 0.65 nm^2 for ZnPPIX, and 0.61 nm^2 for CoPPIX. Notable are the significantly lower compression moduli of CoPPIX and FePPIX, apparent from the lower slopes. All the Langmuir films exhibited breakdown beginning at a surface pressure of around 45 mN m^{-1}.

While these isotherms qualitatively are similar in most respects, CoPPIX and FePPIX exhibit lower compression moduli, which are apparent from the significantly lower rates of pressure increase in the presumably liquid-condensed phase. The average occupied area of these films, thus, is challenging to determine, since no clear linear region can be found for these molecules. Nevertheless, extrapolation from the steepest slope yields comparable occupied areas for all metalloporphyrins, which are slightly larger than for the free-base counterpart. The molecular area in the liquid-condensed state is determined to be (0.61 ± 0.05) nm^2 for CoPPIX, (0.68 ± 0.05) nm^2 for FePPIX, and (0.65 ± 0.02) nm^2 for ZnPPIX. While the reason for the different behavior of CoPPIX and FePPIX compared to ZnPPIX cannot be found with isotherm analysis, the differences likely arise due to the coordinated chlorine (Cl), either because it is still coordinated to the metal center or because of the induced charged molecular state. Despite the influence of the coordinated Cl, all molecules appear to establish dense Langmuir films and should therefore allow the deposition of dense LB layers.

The morphology of the metal–PPIX layers was studied analogously to the free-base PPIX but was limited to a smaller set of deposition surface pressures, comparing monolayers deposited at 2.5 mN m^{-1} and 30 mN m^{-1}. AFM micrographs of LB layers deposited at low surface pressures are shown in Fig. 4.21. The metalloporphyrins exhibit self-assembly behavior comparable to free-base PPIX, and similarly show dense monolayer structures and bare sub-

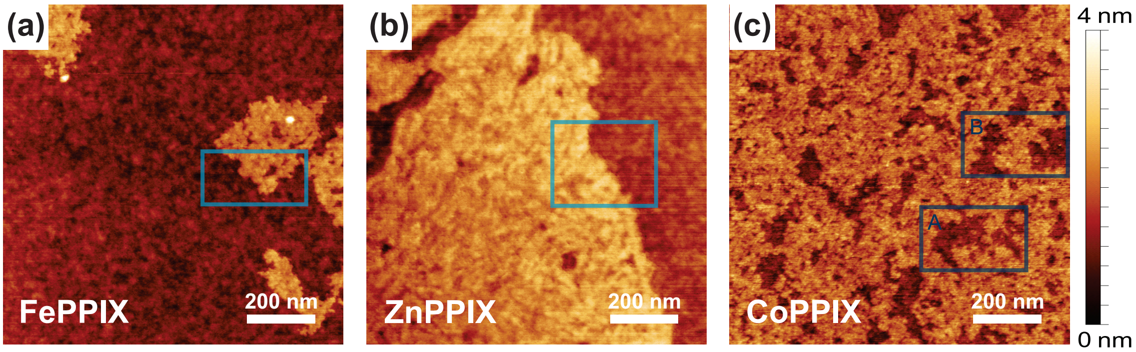

Figure 4.21 AFM micrographs of Si substrates with LB layers of PPIX derivatives deposited at a surface pressure of 2.5 mN m^{-1}, showing partially covered surfaces similar to those observed for PPIX.

strate surface areas simultaneously. The observed relative surface coverage is misleading since the investigated area is small compared to the overall surface of the sample. As apparent in an exemplary micrograph of the ZnPPIX sample at lower magnification in Fig. B.1, the relative coverage is strongly dependent on the specific surface region under investigation, requiring a significantly larger scan size or analysis of more spots to achieve statistical significance. The monolayer heights of the structures depicted in Fig. 4.21 were investigated via height histogram analysis of the marked regions in the case of FePPIX and ZnPPIX, or by averaging over the entire micrograph in the case of CoPPIX. The extracted histograms are shown in Fig. 4.22 and exhibit bimodal distributions, which can be analyzed by fitting two Gaussian distributions. While the center distance and, thus, the monolayer thickness is (0.8 ± 0.1) nm for the CoPPIX sample, it is significantly larger for FePPIX and ZnPPIX, both exhibiting a monolayer thickness of (1.1 ± 0.1) nm. Similar thicknesses were observed for the free-base PPIX, indicating that the observed thickness for CoPPIX is an outlier. A smaller thickness was previously determined to be due to the thickness variation of the molecule in an upright orientation compared to a horizontal orientation for free-base PPIX.

This leads to the conclusion that the CoPPIX sample exhibits a second monolayer morphology with the CoPPIX molecules oriented horizontally. To validate this theory, the adhesion properties of CoPPIX, depicted in Fig. 4.23, were analyzed in more detail. Similar to what has been observed previously with PPIX, some areas of the regions of lower height indicate significantly higher adhesion contrast compared to others. The absolute values acquired in this micrograph are, unfortunately, only loosely comparable to the adhesions determined for the PPIX sample, because the absolute adhesion can be strongly influenced by the AFM probe parameters. Comparing height histograms corresponding to areas of lower and higher contrast shows slightly different height differences, with the high-contrast regions indicating a thickness of (1.0 ± 0.1) nm, which matches the previously determined thicknesses within the margin of error. The smaller thickness of (0.7 ± 0.1) nm is also in good agreement with the previously determined thickness for the intermediate layer, which again exhibits a thickness

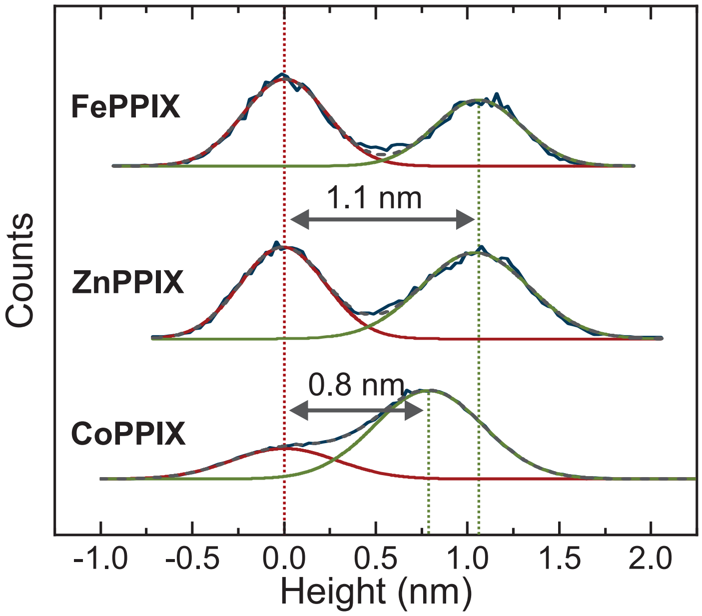

Figure 4.22 Monolayer thickness determination via analysis of the bimodal distributions extracted from height histograms of the AFM micrographs depicted in Fig. 4.21. Due to differences in local coverage, the extracted height histograms of (a) FePPIX and (b) ZnPPIX are extracted from subsections marked in light blue in Fig. 4.21.

of 0.3 nm. It is likely that similar morphologies of horizontal orientation exist for the ZnPPIX and FePPIX, but they were not present in the small areas under investigation.

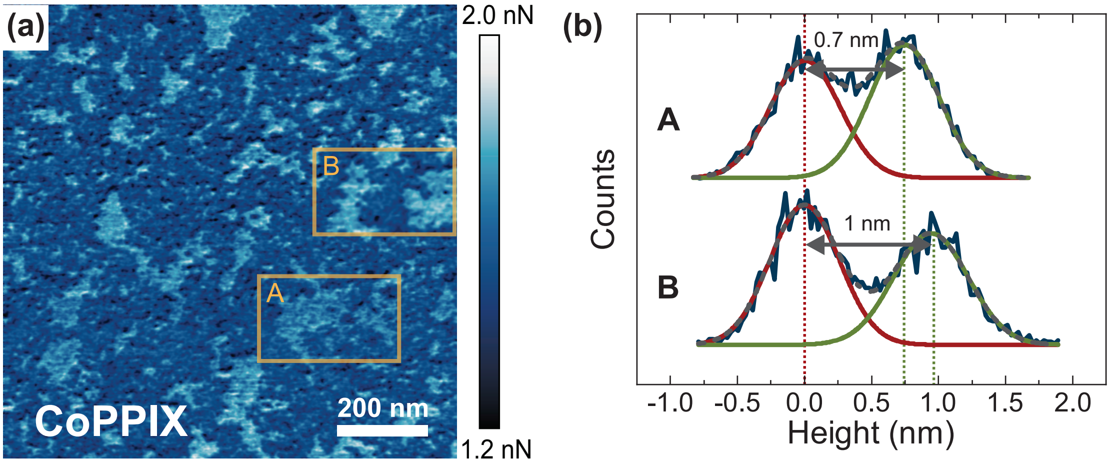

Figure 4.23 (a) Adhesion map simultaneously acquired with the morphology of a CoPPIX LB layer deposited at 2.5 mN m^{-1}, which is depicted in Fig. 4.21(c). (b) Height histograms extracted from the respective regions marked in (a) and Fig. 4.21(c) of two subsections with slightly different adhesion.

Increasing the surface pressure to 30 mN m^{-1} leads to denser monolayer structures, as depicted in Fig. 4.24. Compared to the free-base porphyrin LB layers deposited at this surface pressure, however, the monolayer quality is overall worse. In particular, the FePPIX LB layer (Fig. 4.24(a)) already appears to exhibit the first signs of monolayer breakdown, indicated by an increase in RMS roughness to 482 pm and the occurrence of small multilayer features. The surface of the sample deposited with an LB layer of CoPPIX, depicted in Fig. 4.24(c), shows streaks that might arise due to minute variations in the LB layer thickness, which could be an indication of a less ordered film. This thickness variation leads to a slightly increased RMS roughness of 270 pm. The ZnPPIX LB layer, shown in Fig. 4.24(b), exhibits the highest quality of the three metalloporphyrins under investigation, with a morphology closely matching the bare substrate and previously deposited PPIX LB layers. This is supported by the surface roughness, which is significantly lower for the ZnPPIX LB layer, approaching the roughness of PPIX LB layers and of the substrate.

Similarly to what has already been observed for the isotherms, the morphology studies indicate slightly worse monolayer formation properties for CoPPIX and FePPIX. Similarly to the isotherms, these effects are likely caused by the coordinated Cl, which could induce steric hindrance from its axially oriented coordination site, or through the induced charge upon dissociation in the Langmuir film. Nevertheless, optimizations of the deposition properties, and in particular the surface pressure, could result in significant quality improvements. Since the LB layers of these metalloporphyrins are only employed here for comparison to the PPIX LB layers, this optimization is not within the scope of this work.

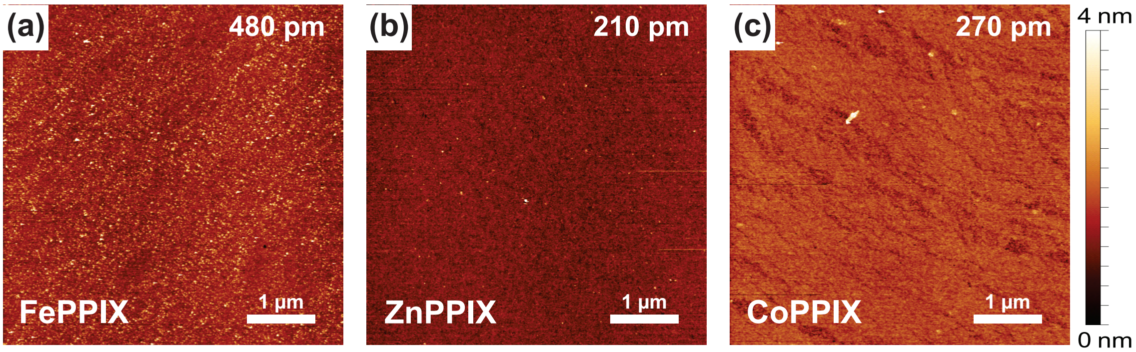

Figure 4.24 AFM micrographs of Si substrates with LB layers of PPIX derivatives deposited at a surface pressure of 30 mN m^{-1}, showing closed monolayers of varying quality. The metal porphyrins coordinated with an axial chloride ion (FePPIX and CoPPIX) in particular indicate increased surface roughness, hinting at monolayer breakdown and, therefore, reduced stability of the compressed monolayer phase.

4.5.2. Chemical Properties

The chemical structures of the metalloporphyrin LB layers were studied using XPS, measuring the same elemental transitions as for the free-base PPIX. Since the free-base protoporphyrin showed no significant differences between the investigated substrates, the XPS studies of the metallized LB layer samples were limited to Au substrates only. The analysis was performed analogously to maintain consistency and comparability to the free-base LB layer. In addition to the organic elemental transitions C1s, N1s, and O1s, the respective metal components were also investigated. These high-resolution spectra are depicted in

Fig. 4.25. While the C1s and O1s spectra are similar to the free-base PPIX LB layer spectra, the N1s transition is significantly different. This is a consequence of the metal center coordinating with the four nitrogen atoms in the ring structure, equalizing the differences between the pyrrolic and the iminic nitrogen. Due to the metal center, the N1s transitions become energetically degenerate and, thus, indicate one major transition, which is slightly shifted toward higher binding energies. This energy shift and only a single peak are expected for metalloporphyrins, demonstrating that the LB deposition preserves the metal centers within the molecules [180], [205]–[209].

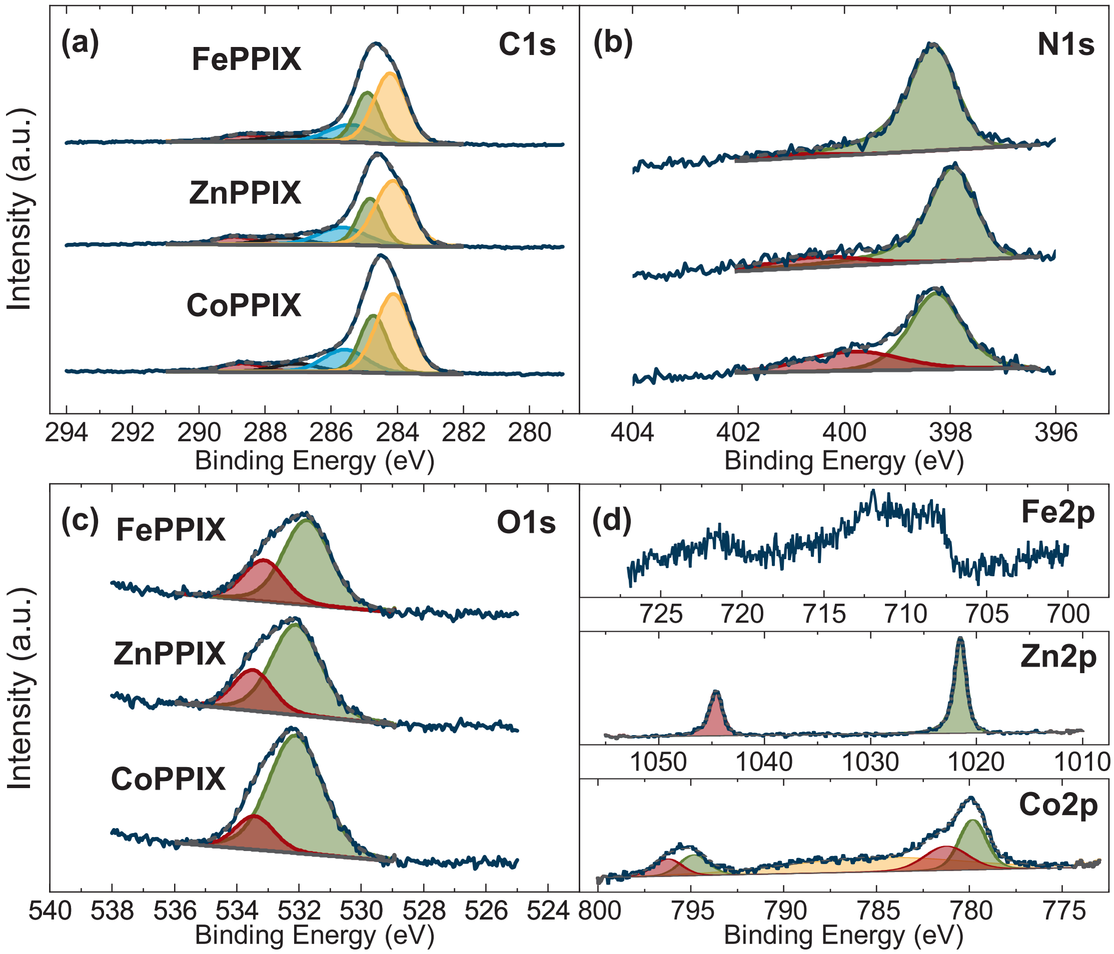

Figure 4.25 High-resolution XPS spectra of the relevant elemental transitions for the metalloporphyrin LB layers deposited at 30 mN m^{-1} on Au substrates. (a) C1s transitions exhibiting the expected similarity to free-base PPIX, including the elemental transitions of C=O (red), C=N (black), C–N (blue), C–C (green), and C=C (yellow). (b) N1s transitions, dominated in this case by a single peak associated with the metal-coordinated nitrogen atoms (green). A small peak at higher binding energies (red) could indicate the presence of residual free-base porphyrin. (c) O1s spectra highlighting the presence of two transitions, one of which likely arises due to surface-adsorbed water. (d) Respective elemental transitions for the metallic centers of each porphyrin.

In addition to the high-resolution spectra of the organic constituents, the metallic centers can be analyzed. The respective spectra of the Fe2p, Zn2p, and Co2p transitions are depicted in Fig. 4.25(d). After the same integration time, the Fe2p signal from the FePPIX sample is significantly smaller than the Zn2p and Co2p signals from the other samples. While the relative sensitivity differs slightly between the elemental transitions, this difference does not explain the smaller signal. Due to the N1s transition of the FePPIX monolayer exhibiting only one peak, the reduced Fe2p signal is unlikely to arise from degradation of the FePPIX to free-base PPIX as it is exposed to the DI water subphase or the oxygen in the atmosphere. Therefore, possible explanations for this phenomenon could potentially be explained by metal center substitution from contaminants in the liquid subphase or experimental error. Further measurements would be required to confirm its origin. The low signal-to-noise ratio (SNR) does not allow for in-depth analysis through the deconvolution of the Fe2p transition.

In contrast, the Zn2p and Co2p signals can be analyzed in detail to extract the metal center oxidation states. In the case of ZnPPIX, the Zn exhibits only one chemical state, resulting in two peaks due to spin–orbit coupling. These transitions, located at 1021.5 eV and 1044.6 eV, are in agreement with previously performed XPS studies on Zn porphyrins [210] and suggest that the Zn is in the expected II oxidation state. Therefore, it is probable that the Zn maintains its coordination in the PPIX ring, preserving the overall structure during LB deposition. The Co2p signal appears to be slightly more complex, indicating the presence of multiple transitions. To begin with, the two major transitions exhibit the expected spin–orbit splitting of 15 eV. Limiting the discussion to the 3/2 spin transitions, peaks at 779.8 eV and 781.2 eV can be identified. A broad feature centered around 785.0 eV is also present. While the transition at 779.8 eV points at the presence of Co III, the transition at 781.2 eV in conjunction with the presence of a possible satellite peak at 785 eV points at the presence of Co II [211]–[213]. Due to the coordination with Cl, the expected oxidation state of the Co within the CoPPIX is II, which suggests that the CoPPIX partially loses its Cl coordination through interaction with either the substrate, the subphase, or the atmosphere, leading to the formation of the Co II oxidation state. Similar studies of the Co oxidation states have been performed by Zhu *et al.* [214], who reported the presence of only Co III upon SAM formation, using a solution-based technique. Nevertheless, a closer analysis of the high-resolution spectra shown in their report suggests a false assignment of the respective oxidation states and the presence of Co II.

In conclusion, the origin of the oxidation states of the Co metal center remains unclear, and further studies are necessary to identify the processes at play. For example, adding small amounts of HCl in the subphase could create an abundance of Cl^- ions in the subphase and, thus, influence the dissociation process of Cl from the CoPPIX. Similarly, investigating LB layers deposited on different metals and semiconductors could yield further insight into the influence of the substrate. Despite the differences in oxidation states, the N1s peaks suggest that the CoPPIX molecule remains intact. Since the oxidation state of the metal center will be altered in a catalytic environment, the influence of an initially mixed oxidation state might be negligible for catalytic applications.

4.5.3. Energy Level Alignment

The energy level alignment on Au substrates was determined for the metalloporphyrins to examine any qualitative differences from the more thoroughly investigated free-base protoporphyrin. The obtained UPS spectra are depicted in Fig. 4.26, showing the SECOs and low binding energy regions of the respective samples. Due to the measurements presented being acquired at a significantly later time compared to the other measurements on PPIX, the Au reference measurements were repeated with this sample set to improve the comparability between reference and sample. Like the free-base PPIX, the LB layer induced a vacuum level shift at the interface. The magnitude of this shift is identical to what has been observed for free-base PPIX layers. For the CoPPIX and the ZnPPIX, the vacuum level shifts by (0.20 ± 0.05) eV, while the shift of the FePPIX is (0.25 ± 0.05) eV.

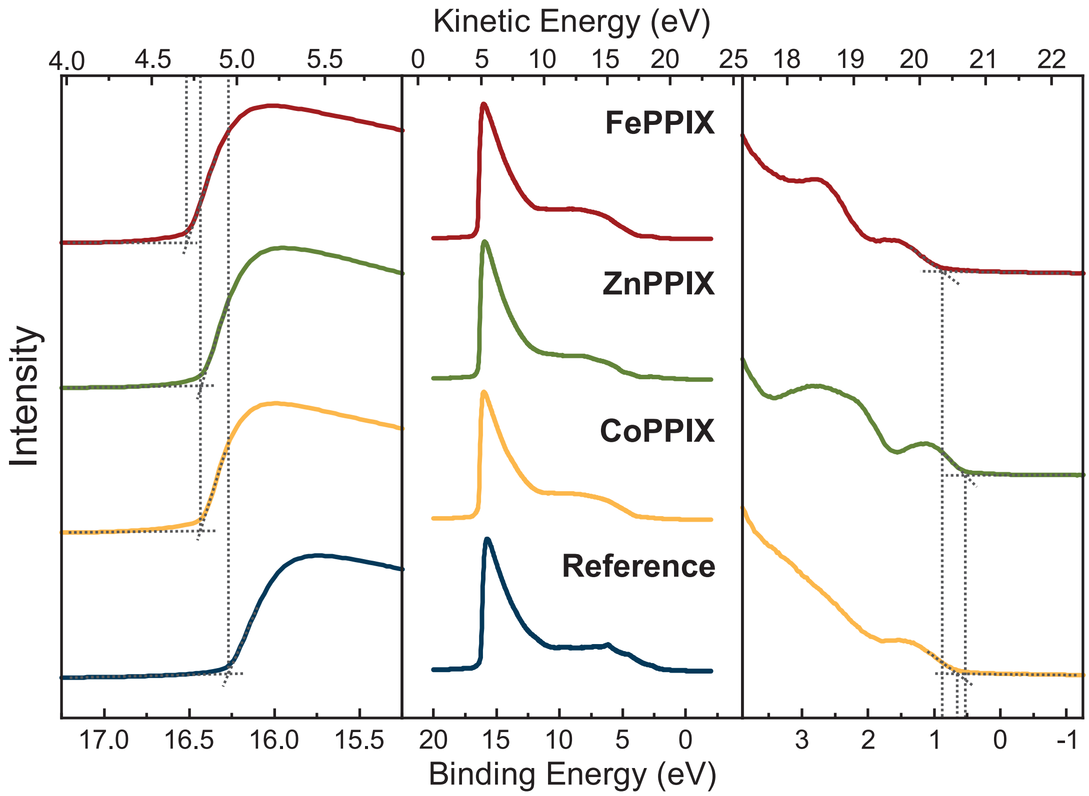

Figure 4.26 UPS spectra of metalloporphyrin LB layers deposited at 30 mN m^{-1} on Au substrates in comparison to a reference spectrum with enlarged views of the SECO and low binding energy regions on the left and right side, respectively. While the SECO exhibits a shift similar to free-base PPIX, the HOMO region exhibits slight differences, especially for the lower molecular orbitals shifted toward higher binding energies.

The observed HOMO features also exhibit similarities to the free-base PPIX, with the HOMO levels being (0.89 ± 0.05) eV, (0.52 ± 0.05) eV, and (0.65 ± 0.05) eV below the respective Fermi levels of FePPIX, ZnPPIX, and CoPPIX. Thus, the ionization energies were determined to be (5.59 ± 0.07) eV, (5.27 ± 0.07) eV, and (5.40 ± 0.07) eV for FePPIX, ZnPPIX, and CoPPIX, respectively. While the energy level alignment exhibits slight differences from the free-base porphyrin, their magnitude of 0.3 eV underlines that it is indeed viable to apply the approach used for the free-base PPIX analysis to obtain insights into the energy level alignment of metalloporphyrin semiconductors. The spectral shape of the HOMO appears to be similar to the free-base PPIX for all samples, but differences arise for the lower molecular orbitals, as clearly visible in the more pronounced peaks associated with the higher binding energy molecular orbitals for FePPIX and ZnPPIX.

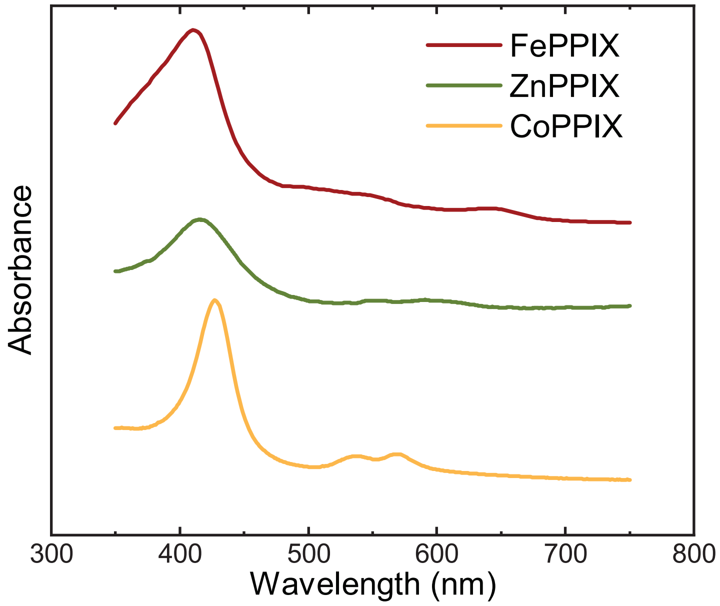

Figure 4.27 UV–Vis absorbance of metalloporphyrins as monolayers deposited on microscope slides at a surface pressure of 30 mN m^{-1}. The respective spectra of the molecules in solution are depicted in Fig. B.2.

Analogously to the free-base PPIX, the UV–Vis absorption spectrum of each monolayer was measured to determine the HOMO–LUMO splitting and, thus, infer the position of the LUMO relative to the vacuum level via the known HOMO position. The respective UV–Vis spectra of the metalloporphyrins are shown in Fig. 4.27 and share close similarities with the spectrum of the free-base variant. All spectra have a dominant absorption peak located between 400 and 450 nm, accompanied by smaller peaks at higher wavelengths. In comparison to the respective spectra of molecules in solution, depicted in Fig. B.2, all monolayer absorption features appear to be shifted towards longer wavelengths and are broadened, similar to the absorbance features of free-base PPIX. Through the onset of the lowest-energy transition observed for each molecule, the HOMO–LUMO splits are determined to be 1.8 eV, 1.9 eV, and 2.1 eV for FePPIX, ZnPPIX, and CoPPIX, respectively.

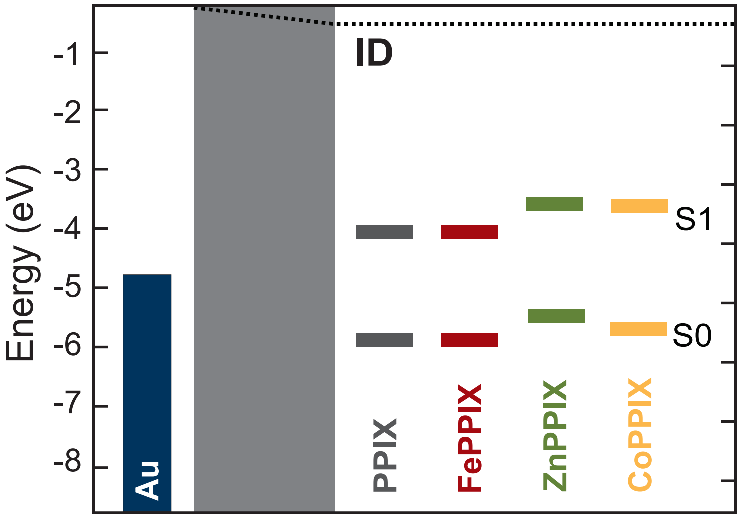

Figure 4.28 Energy level alignment diagram of the free-base PPIX and metalloporphyrin monolayers relative to an Au substrate. It is evident that the metal center in the PPIX molecule has a relatively small influence on the HOMO–LUMO splitting and the alignment properties of the junctions.

The combination of all the acquired data yields a complete picture of the energy level alignment on an Au substrate, shown in Fig. 4.28. The effect of the metal centers of the metalloporphyrins on the HOMO–LUMO splitting and the energy level alignment is relatively small, as evident from the minimal differences between the molecules relative to each other and compared to the free-base PPIX. This suggests that the influence of the respective metal center on the frontier orbitals is small, which is in agreement with theoretical and experimental studies in the literature [215]–[217]. Thus, one can conclude that the insights on the charge transport phenomena observed for free-base PPIX likely remain accurate for many relevant metalloporphyrins, underlining their relevance for catalytic devices employing a porphyrin-based catalytic layer.

5. The Mabiq–Semiconductor Interface

While porphyrins and similar molecules are prominent representatives of molecular catalysts, there are many others, some of which likely have superior molecular structures. Therefore, this chapter focuses on the energy level alignment of a different type of molecular catalyst called Mabiq. In contrast to most other organometallic catalysts, the molecular structure of Mabiq, depicted in Fig. 5.1, can accommodate metal centers at two coordination sites. This allows greater tunability of its catalytic properties, since the included metals can be chosen to enable intramolecular synergy and could, thus, open pathways to, for example, the catalysis of CO_2 to complex, long-chain carbohydrates. In addition, the interaction of two metal centers could enhance the TOF of a catalytic process.

While research into these compounds is in its early stages and is mostly limited to Mabiq compounds with only a single metallic center [26], [27] and, thus, not fully exploring the capabilities of the molecular structure, the initial results are promising for catalytic applications such as CO_2 reduction [26]. In addition, initial studies of bimetallic compounds have given the first indication of the desired intermetallic interaction, highlighting the potential of Mabiq [25], [218].

Similar points have been made regarding inorganic heterogeneous catalysis. In this context, researchers have found that alloying two or more elements in bulk or nanoparticle samples led to an increased specificity, efficiency, or activity of the surface [219]–[224]. This approach has been pushed close to the maximum by the use of high-entropy alloys, which are a combination of at least five different metallic elements in a structure with near equimolar stoichiometry [225]. Most of these structures have in common that their surface structure is either affected by phase separation or exhibits a stochastic distribution of nearest neighbors. Phase-separated structures can arise either due to the natural properties of the alloy or by being created in an intentional synthesis process, such as the growth of core-shell wire structures [222]. This leads to comparatively low coverage of the surface with the desired bimetallic structure since the surface is mainly structured in uniform domains of a single element. In contrast, structures like high-entropy alloys do not follow any order, meaning that the distribution of nearest-neighbor elements is, on average, uniform but essentially random for a specific site. Thus, both of these approaches lack the ability to tune the bimetallic interaction actively. Here, bimetallic organic compounds like Mabiq have an advantage because the specific elements and their interatomic distances are defined and maintained through the molecular structure. Therefore, a hybrid approach of an inorganic substrate and a bimetallic organic compound could increase these benefits even further.

This investigation closely follows the measurement procedure established for PPIX, ensuring the comparability of the results. The Mabiq molecules used in the following studies were exclusively the free-base variant and, thus, do not include any catalytic metal centers. All attempts at LB deposition of metallo-Mabiqs were unfortunately unsuccessful because the coordination groups necessary to stabilize metal centers generally led to a significant increase in solubility in the DI water subphase, thus preventing the formation of a Langmuir layer.

5.1. Morphology of Mabiq Langmuir–Blodgett Monolayers

The Mabiq molecules were deposited using LB deposition, similar to the process previously described for PPIX. In contrast to PPIX, the molecular structure of Mabiq (depicted as an inset in Fig. 5.1) does not exhibit hydrophilic functional groups. Therefore, the amphiphilic properties of the Mabiq molecules are not directly apparent, making a prediction of the molecular orientation from the molecular structure difficult.

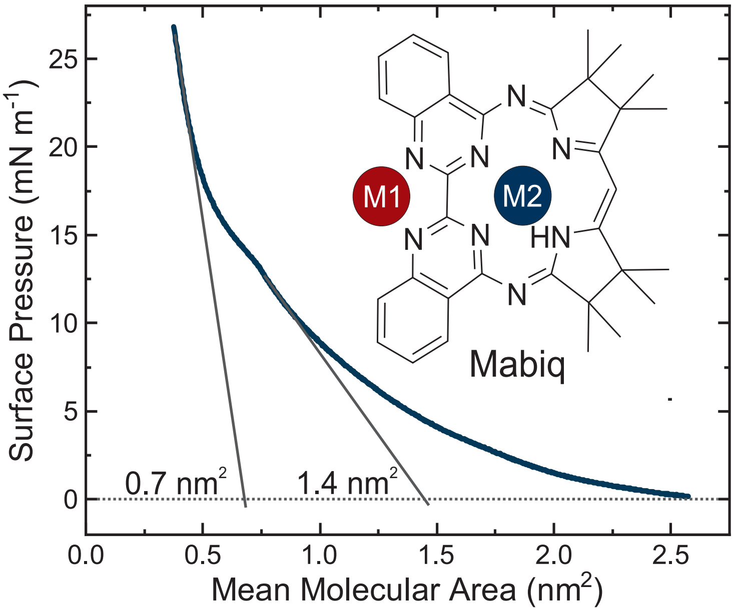

Figure 5.1 Isotherm of Mabiq deposited on a DI water subphase. The dashed lines indicate the extensions of the linear sections used to determine characteristic MMAs of 1.4 nm^2 and 0.7 nm^2. Due to the limited compression range of the trough and the low compression modulus of the Mabiq LB layer, a decrease in surface pressure indicating a breakdown could not be observed.

To begin with, the properties of the Mabiq Langmuir films on a DI water subphase were investigated by recording a surface pressure–area isotherm, shown in Fig. 5.1. The surface pressure only increases slowly upon compression, which leads to difficulties for the isotherm analysis with the given Langmuir trough size. Nevertheless, carefully adjusting the number of molecules deposited on the surface allowed for the recording of a complete isotherm. The surface pressure initially increases comparatively slowly and does not exhibit a distinctly linear region. A decrease in slope at a surface pressure of just below 15 mN m^{-1} is visible upon close inspection. Extension of the nearly linear region just below and above this feature leads to the extraction of two average molecular areas, possibly corresponding to two distinct Langmuir film phases, with the lower and higher surface pressure phases exhibiting average molecular areas of (1.4 ± 0.2) nm^2 and (0.7 ± 0.1) nm^2, respectively. The low surface pressure region, therefore, could correspond to a near-horizontal molecular orientation of the Langmuir film, while the smaller average area could correspond to a phase change to a molecular structure with a more upright orientation.

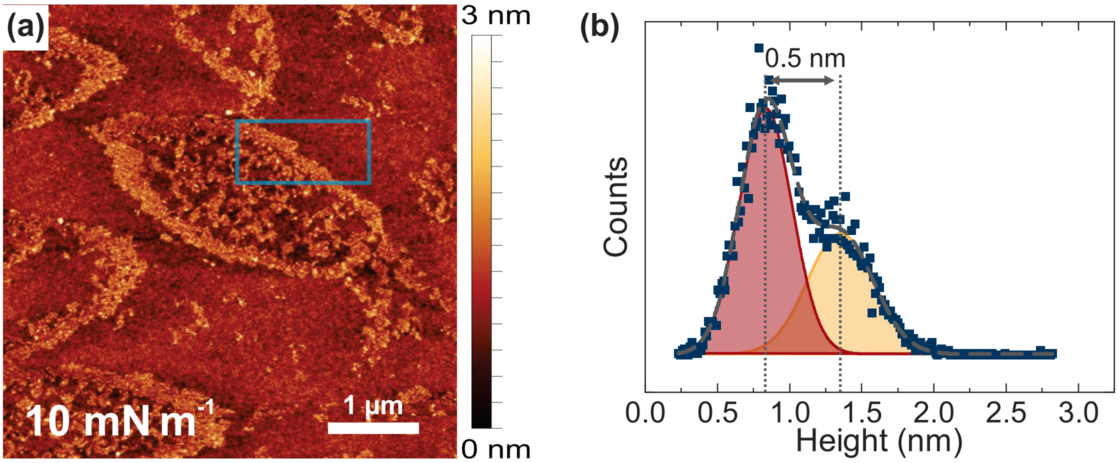

Figure 5.2 (a) AFM micrograph of a Mabiq LB layer deposited on Si at a surface pressure of 10 mN m^{-1}, indicating an inhomogeneous partial surface coverage. (b) Height histogram of the highlighted area in (a), showing a bimodal distribution with a center distance of 0.5 nm and, thus, indicating a mostly horizontal orientation of the molecular structure.

This postulated molecular orientation change upon surface pressure increase was validated through AFM, by analyzing the morphological properties of LB layers deposited on hydroxylated Si surfaces at different surface pressures. An AFM micrograph of a Mabiq LB layer deposited at 10 mN m^{-1} is depicted in Fig. 5.2(a) and shows a molecular layer with incomplete coverage on the surface. A distinct shape with lanceolate contours and pointed ends emerges in the submonolayer features. These features have a relatively closed structure at their edges but exhibit significantly less partial coverage towards the center. The thickness of this layer was determined via height histogram analysis, as shown in Fig. 5.2(b), which yielded a comparatively small thickness of only (0.5 ± 0.1) nm. Since this thickness approaches the interlayer distance of graphite, the molecular monolayer is likely to be made of molecules with a mostly horizontal orientation. Compared to horizontally oriented PPIX, these layers appear to be slightly thicker, which could be a consequence of a slight buckling of the molecular structure.

An increase in surface pressure to 15 mN m^{-1} leads to the formation of a nearly closed monolayer film comprising nanoscoping islands of molecule coverage, as visible upon a close investigation of the morphology depicted in Fig. 5.3(a). This also becomes apparent for the

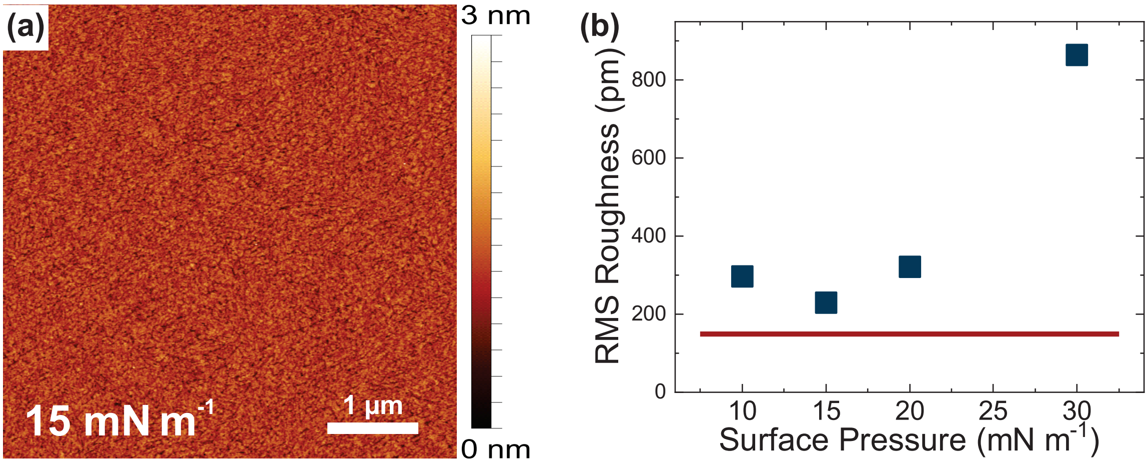

Figure 5.3 (a) AFM micrograph of a Mabiq LB layer deposited on Si at a surface pressure of 15 mN m^{-1} showing a homogeneous and flat surface morphology. (b) RMS roughness of Mabiq LB layers deposited on Si at various surface pressures. The roughness of the monolayer surface for LB layers deposited at 15 mN m^{-1} approaches the RMS roughness of the substrate indicated by the red horizontal line at 170 pm, but remains slightly above the roughness achieved for PPIX.

RMS roughness, extracted from all recorded micrographs and shown in Fig. 5.4, which highlights that the surface roughness of the 15 mN m^{-1} LB film is minimally but slightly higher than both the expected substrate roughness and the lowest roughness achieved for PPIX LB layers, with a value of 230 pm. Therefore, while this appears to be the optimal structure for monolayer coverage with the given molecular phase, it is still lacking in packing density compared to PPIX LB layers.

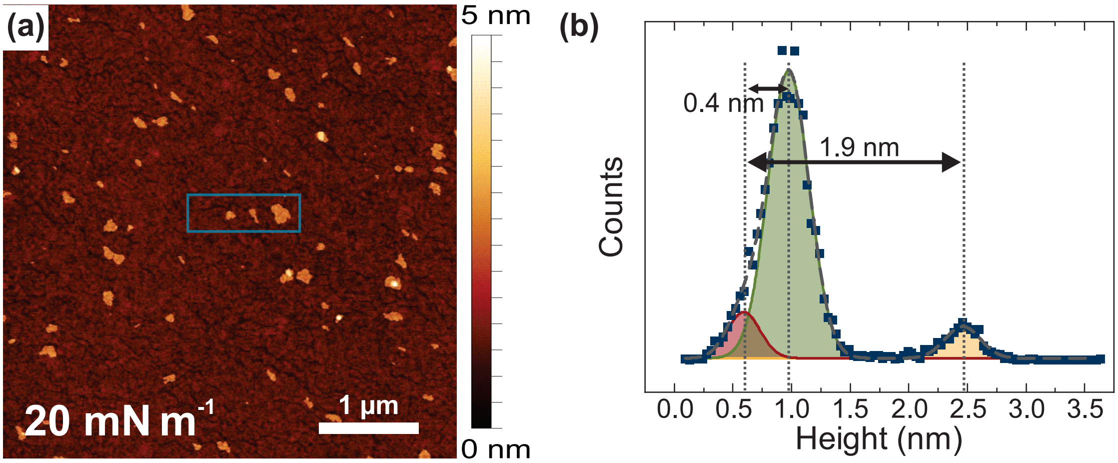

Figure 5.4 (a) AFM micrograph of a Mabiq LB layer deposited on Si at a surface pressure of 20 mN m^{-1}, which exhibits partial coverage with a different LB layer phase. (b) Height histogram extracted at the position of the marked region in (a). The height of the established new layer is 1.5 nm.

A further increase of surface pressure to 20 mN m^{-1} does not reduce the surface roughness but instead leads to the formation of a new LB layer phase, as shown in Fig. 5.4(a). This is indicated by the appearance of small features of uniform thickness, which appear in irregular shapes scattered randomly over the surface. At this surface pressure, the new LB layer phase covers only a small portion of the surface, allowing for the thickness to be measured by histogram analysis, which was limited to the area marked by the blue rectangle in Fig. 5.4(a) and is depicted in Fig. 5.4(b). A clear bimodal distribution is visible again, indicating the height difference between the previously established monolayer and the newly established phase to be around (1.5 ± 0.1) nm. In addition, a tail toward lower heights originating from a peak around (0.4 ± 0.1) nm below the dominant peak indicates that uncovered substrate remains. Thus, the total thickness of the emerging phase is around (1.9 ± 0.1) nm. Due to a lack of contrast in the adhesion properties of the individual layers and the substrate, the obtained data are insufficient to provide a definitive deconvolution of the established molecular structures and orientations. While the majority of the surface remains covered by a close to horizontally oriented LB layer of Mabiq, the new phase could consist of a variety of structures. Its total thickness suggests that this film cannot comprise a single layer of Mabiq with vertical orientation since the molecular dimensions are insufficient to provide a thickness of nearly 2 nm. Thus, the layer likely has a multilayer structure. It could consist of the originally established horizontally oriented layer, followed by a newly established structure of possibly more upright molecular orientation. The multilayer formation could also be accompanied by a change in molecular orientation of the initially horizontal LB layer. In addition, while it is likely that the structure is established as a bilayer, more complex multilayers could be established. Due to the low surface coverage and small grain size, a detailed analysis of this structure is challenging and likely requires analysis methods such as in-plane XRD with synchrotron sources.

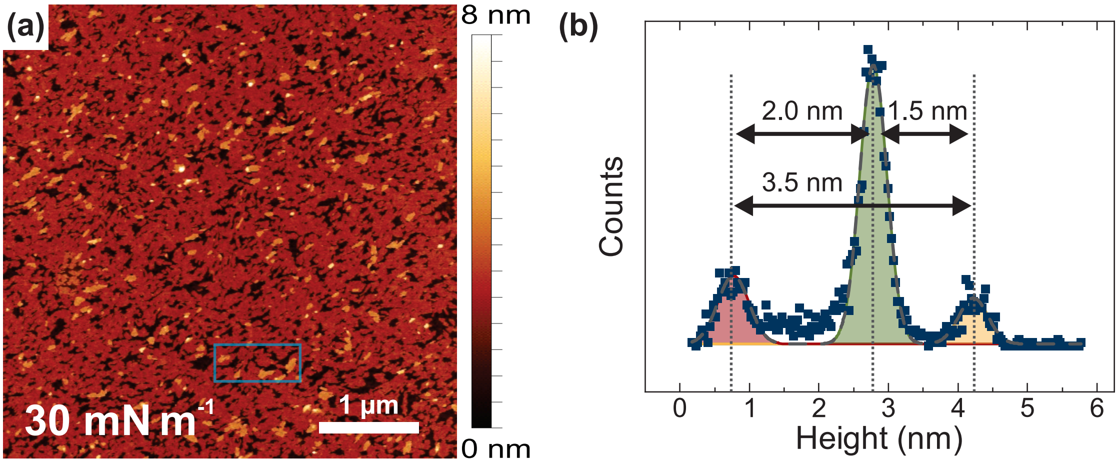

Figure 5.5 (a) AFM micrograph of a Mabiq LB layer deposited on Si at a surface pressure of 30 mN m^{-1}, showing that multilayer structures are established. (b) Height histogram extracted at the position of the marked region in (a). The heights of the two observable layer structures are 2.0 nm for the lower layer and 1.5 nm for the upper layer. It is unclear whether the observed baseline is a monolayer or the bare substrate.

An increase in the surface pressure to 30 mN m^{-1} leads to almost complete coverage with the layer structure initially observed at 20 mN m^{-1}, as shown in Fig. 5.5(a). An additional layered structure can be observed on top of this multilayer structure, further increasing the three-dimensionality of the system. This third layer again emerges in small grains scattered across the surface. Height histogram analysis of the area marked in the blue rectangle indicates a trimodal distribution, as shown in Fig. 5.5(b). The thickness of the now predominant multilayer structure is determined to be (2.0 ± 0.1) nm, which is an indication of the lowest level observed in the AFM micrograph not being covered by a molecular monolayer. The subsequently emerged additional layer extends (1.5 ± 0.1) nm beyond the initial multilayer, thus indicating a total thickness of (3.5 ± 0.1) nm. The absence of a monolayer structure could be due to condensation, which might arise if the multilayer structure possesses an overall lower free energy. A straightforward comparison of the layer thicknesses imposes the following interpretation: The initially observed multilayer structure consists of the originally observed monolayer (thickness $\sim$0.5 nm) covered by a vertically oriented layer of molecules (thickness $\sim$1.5 nm). Additional layers stacked on this bilayer have a similar orientation to the second layer, thus having the same interlayer spacing of roughly 1.5 nm. While this interpretation is plausible, the aforementioned in-depth analysis using, for example, synchrotron techniques would be necessary for validation.

Bare substrate surface areas are common for all substrates despite the establishment of multilayers. This indicates that the initial monolayer structure has an unstable equilibrium that can be easily disturbed, leading to multilayer formation before the monolayer is fully compressed. This is additionally highlighted in an analysis of the monolayer structure at the optimal surface pressure of 15 mN m^{-1} compared to one deposited at 20 mN m^{-1}, shown in Fig. 5.6. Here, the observed structure and the obtained surface roughness, excluding regions of multilayer structures, indicate that the monolayer coverage is greater for the higher surface pressure sample. Nevertheless, similar structures and regions lacking monolayer coverage of the substrate surface remain. This can be attributed to the lack of a distinctly amphiphilic structure, which could stabilize the monolayer due to beneficial interaction with the subphase.

In conclusion, an adequate monolayer structure of Mabiq was achieved through LB deposition at a surface pressure of 15 mN m^{-1}. The monolayer comprises horizontally oriented molecules, a qualitatively different structure from the previously analyzed PPIX molecules. Further increasing the surface pressure leads to slightly higher relative coverage but fails to produce a closed monolayer before breaking down into a complex multilayer system.

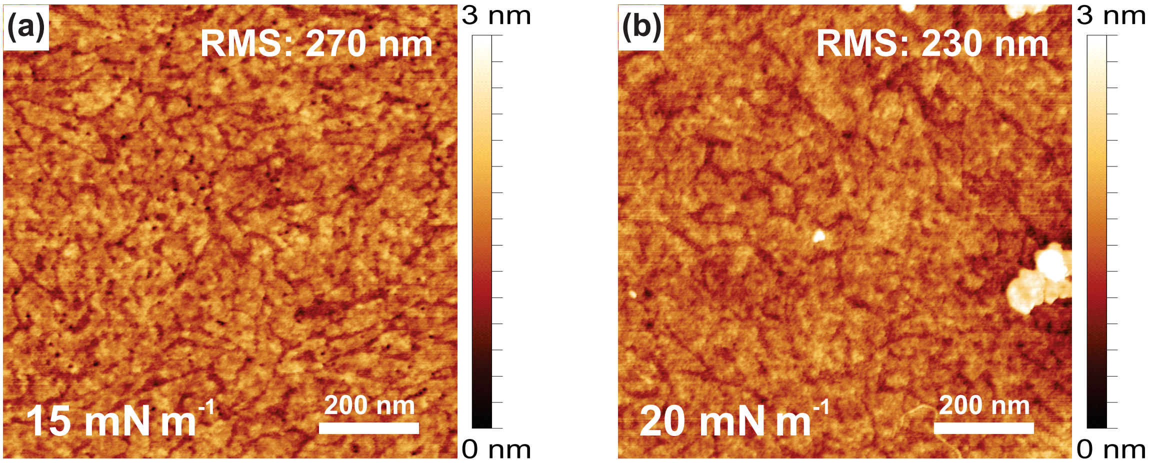

Figure 5.6 (a)–(b) Small scan range AFM micrographs of Mabiq deposited on Si at surface pressures of 15 mN and 20 mN, respectively. At this higher magnification, a microscopic structure becomes apparent for the monolayers at both surface pressures. This structure appears to be reduced at higher compression ratios since the RMS roughness of the higher surface pressure layer is slightly lower after excluding the multilayer structures.

5.2. Chemical Properties of Mabiq Langmuir–Blodgett Monolayers

The chemical structures of Mabiq monolayers deposited on Au and Si substrates at a surface pressure of 15 mN m^{-1} were analyzed with high-resolution XPS of the relevant elemental transitions. To begin with, spectra of Au substrate samples with and without a Mabiq LB layer are depicted in Fig. 5.7(a) and (b). Similar to the previous studies on PPIX, one can observe contamination of the bare Au substrate. In this case, however, the level of contamination appears to be higher, indicating significant levels of carbon and nitrogen of unknown origin. This could be caused by, for example, slightly slower sample transfer times for this particular sample.

Nevertheless, the sample spectra with the Mabiq monolayer indicate an increase in the expected carbon and nitrogen peaks and a slight increase in the O1s signal. The C1s spectrum exhibits a spectral shape that can be deconvoluted into two transitions, one corresponding to carbon coordinated with two nitrogen atoms, centered at around 286.9 eV, and the other component encompassing all remaining chemical environments of carbon, centered at 285.1 eV. While other fitting approaches introduce two additional components to deconvolute this transition further, the acceptable increase in FWHM of around 0.2 eV and the accurate description of the data with only two peaks led to the decision to describe these peaks in a simpler manner [226]. The measured relative content of 18 % for the high energy state closely matches the expected 18.75 % deducted from the stoichiometric ratio of 6:26 for a single molecule, thus suggesting that the Mabiq molecule remains in its original chemical state.

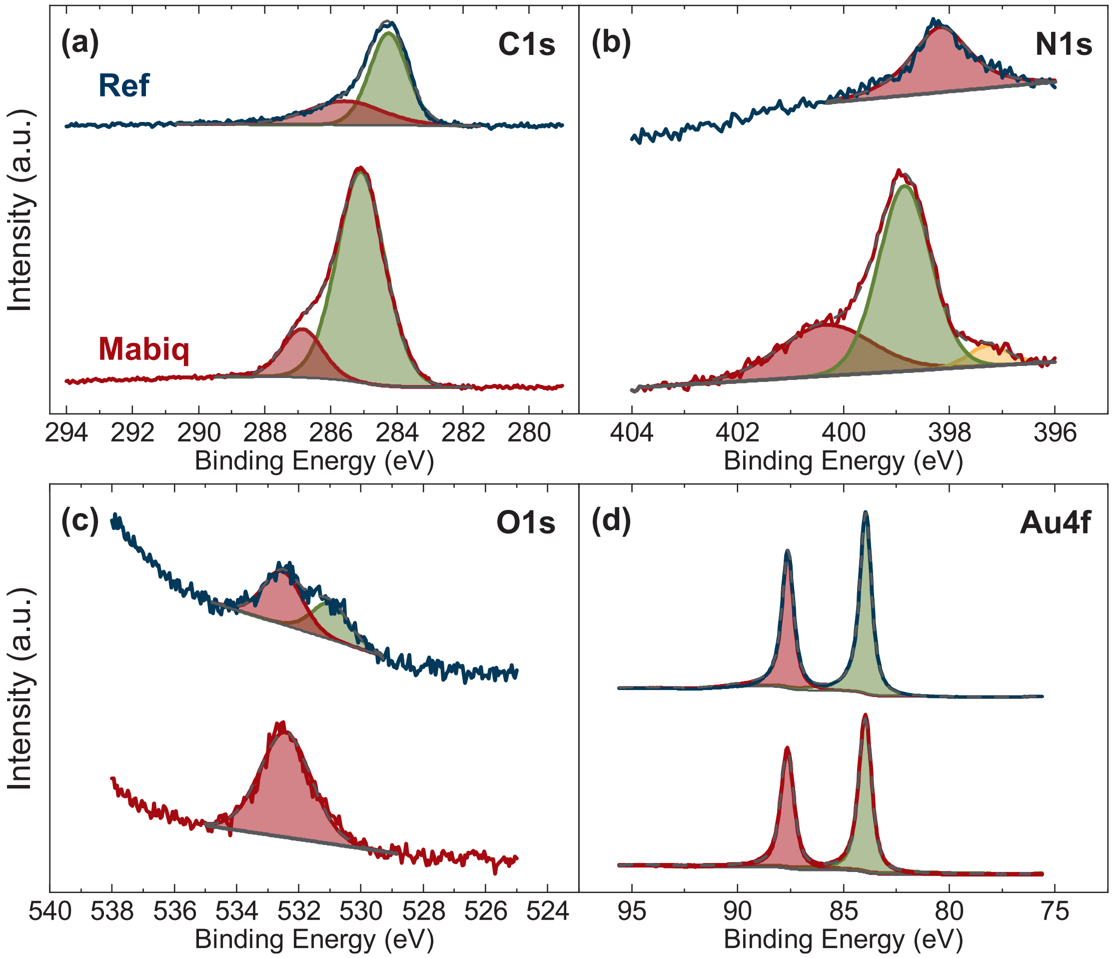

Figure 5.7 High-resolution XPS spectra of the relevant elemental transitions for Mabiq LB layers deposited on a Au substrate. (a) C1s transition for reference (top) and Mabiq (bottom) samples consisting of pyridinic (red) and a combination of all remaining chemical carbon states (green). The limited resolution does not allow the differentiation of all chemical states individually. (b) N1s transition for a reference sample (top) indicating slight nitrogen contamination and a Mabiq sample with the expected pyrrolic nitrogen (green), but also an unidentified component possibly arising from coordination of the open Mabiq coordination site with water and slight residual contamination (yellow). (c) O1s transition showing residual oxygen on the surface for the reference sample (top) but even more unexpected water for the Mabiq sample (bottom), which again could arise from coordinated water on the surface. (d) Au4f transition indicating a significant attenuation of the signal for the Mabiq sample (bottom) compared to the reference (top).

Analysis of the high-resolution N1s spectrum of the LB layer is performed via deconvolution using three transitions. The lowest binding energy transition, located at around 397.1 eV, is of unknown origin, possibly arising from the contamination already observed on the reference sample. It might alternatively arise due to the coordination of a Au atom with one of the Mabiq coordination sites. A similar process has been observed at room temperature for PPIX [205] and at elevated temperatures for Mabiq [227] on single-crystalline samples under UHV conditions. The other two transitions located at around 398.9 eV and 400.6 eV corre-

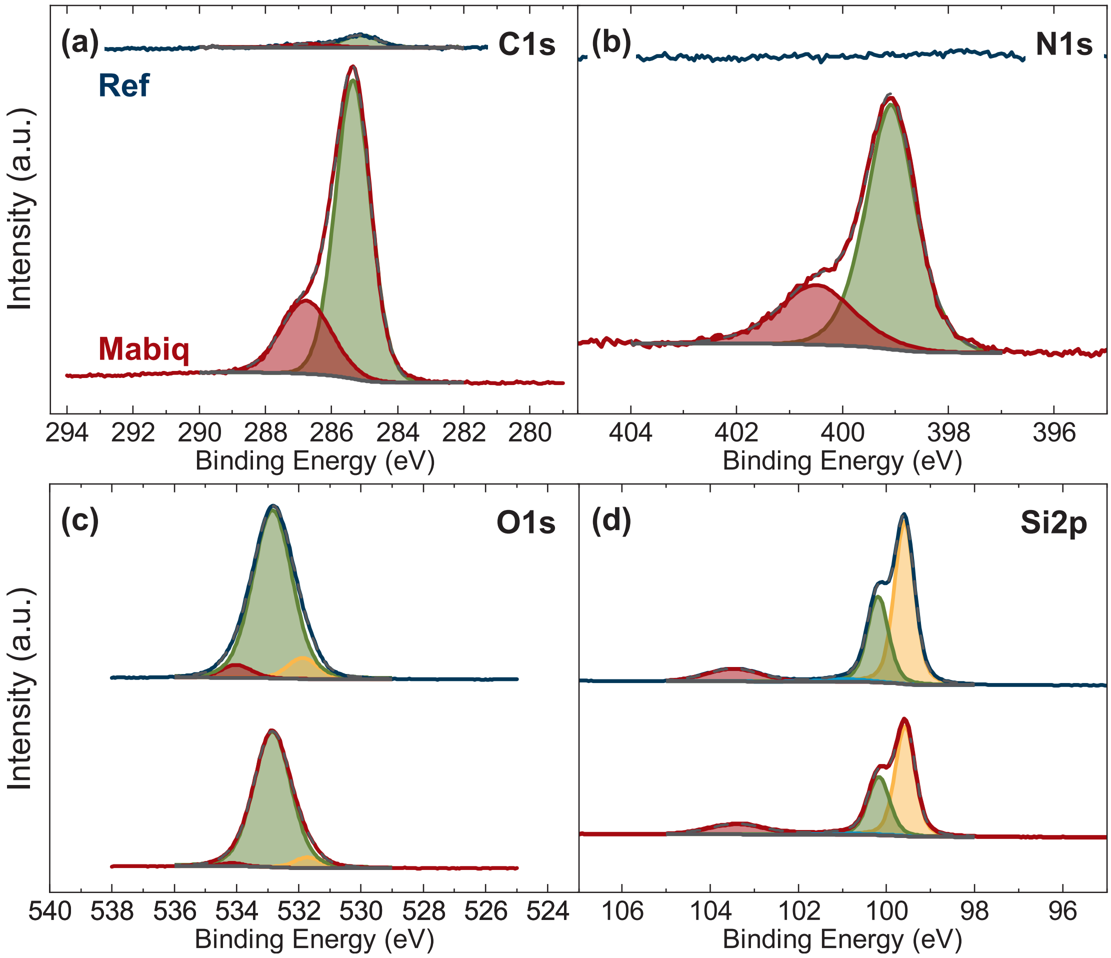

Figure 5.8 High-resolution XPS spectra of the relevant elemental transitions for Mabiq LB layers on a Si substrate. (a) C1s transition for reference (top) and Mabiq (bottom) samples. (b) N1s transition for a reference sample and a sample with a Mabiq LB layer. (c) O1s transition, which is mainly dominated by the surface oxide of the Si substrate. (d) Si2p transition indicating the presence of oxide but also exhibiting signal attenuation due to monolayer coverage.

spond to the iminic and aminic nitrogen present in the Mabiq molecule, respectively [226], [227]. Interestingly, the peak ratios observed do not match the expected ratio, with the aminic peak expected to exhibit a relative prevalence of 12.5 %, corresponding to a ratio of 1:7, being significantly overrepresented with a relative peak area of 25 % and a ratio of 2:6.

An increase in aminic nitrogen could result from the interaction of the Mabiq molecule with, for example, the water subphase or the substrate, leading to proton transfer to one of the iminic nitrogen groups. This could be associated with the slight acidity of the DI water resulting from CO_2 dissolution and carbonic acid formation. Therefore, this process could be investigated by systematic control of the substrate pH through the introduction of buffering agents. Another possible explanation is direct coordination with the H_2O molecules themselves, which might arise through coordination with the M1 site marked in Fig. 5.1. This would likely result in a stoichiometric ratio of 3:5, however, leading to the conclusion that only half the Mabiq molecules would be coordinated in such a manner. By themselves, the XPS data do not distinguish between the stoichiometry of single molecules but are averaged over the whole surface, making an accurate determination of the coordination impossible with the given tools. Interestingly, a pairwise organization of Mabiq on surfaces has been observed in previous studies, which observed shared coordination at the M1 site with substrate metals [226], [227]. Thus, a similar structure might be established in a Langmuir layer with a water molecule occupying this coordination site, thus leading to the observed effect. The given data do not yield a conclusive explanation for the microscopic ordering of the Mabiq molecules on the surface. Thus, this theory cannot be confirmed with these data and would require more in-depth microscopic studies using single-crystalline surfaces and atomic-resolution scanning tunneling microscopy.

Fig. 5.7(c) and (d) depict high-resolution O1s and Au4f spectra acquired on the same substrate. The O1s signal increases after LB deposition, indicating the presence of additional oxygen, which likely originates from surface-adsorbed water [183], [184], [228] and could also arise from the hypothesized coordinated water molecules. The attenuation of the Au4f signal yields an organic overlayer thickness (determined in the same way as in the PPIX analysis) of (0.6 ± 0.2) nm and is, thus, in good agreement with the monolayer thickness determined via AFM. These results were replicated with the Si substrates, shown in Fig. 5.8. The high-resolution C1s and N1s spectra are comparable in shape but lack the low binding energy signal in the N1s spectrum present for Au substrates. In contrast to Au, the native oxide of the Si substrate dominates the O1s signal, thus making the observation of surface-adsorbed water challenging. Similar considerations for the organic overlayer yield an LB layer thickness of (0.5 ± 0.2) nm, which is also comparable to the Au substrate and AFM results. The high-resolution spectra of Mabiq on GaN and ZnO, shown in Fig. B.4 and Fig. B.5, respectively, also show strong similarities.

The Mabiq molecule appears to maintain its chemical structure during LB deposition. Slight deviations from the expected stoichiometry and previous UHV experiments for the ratio of aminic to iminic nitrogen could result from coordination with single molecules of the DI water subphase. The cause of these variations could not be conclusively determined with the available data.

5.3. Electronic Interaction of Mabiq Langmuir–Blodgett Monolayers With Semiconductors

The energy level alignment of Mabiq with Au, Si, GaN, and ZnO samples was studied analogously to the PPIX samples using a combination of UPS and UV–Vis spectroscopy to determine the HOMO and LUMO positions relative to the energy levels of the respective bulk substrates. The SECOs and low binding energy regions of all investigated samples are depicted in Fig. 5.9.

As is visible from the SECOs of the spectra depicted in the left column of Fig. 5.9, the potential shift upon LB deposition of a monolayer of Mabiq at a surface pressure of 15 mN m^{-1} is around 0.75 eV for all samples, with slight differences likely arising from uncertainties associated with the *ex situ* influence of atmospheric interactions or prior illumination history. This value is significantly larger than the potential shift for the PPIX samples, which is around 0.4 eV. The origin of this increased potential shift could either be a partial charge transfer between molecule and substrate or a larger dipole moment of the molecule. While such a dipole moment is not evident from the molecular structure itself, substrate interactions could lead to a buckling of the molecule, thus effectively inducing a dipole moment via the resulting asymmetry. This large potential shift is beneficial for inducing charge transfer from substrate to molecule and could positively affect the performance of catalytic reduction processes.

The low binding energy region of the UPS spectra, depicted in the right column of Fig. 5.9, indicates the emergence of additional features upon deposition of the Mabiq monolayer. These are likely caused by electrons in the HOMO and lower molecular orbitals. The onset of the additional peak emerging at the lowest binding energy determines the HOMO offset relative to the Fermi level, which exhibits pronounced variations similar to those previously discussed for PPIX samples. Such large changes in the HOMO position relative to the Fermi level indicate vacuum level alignment yielding an average distance from the HOMO to the vacuum level of 6.3 eV. The vacuum level alignment process is shown in Fig. 5.10, which depicts the dependence of this difference relative to the substrate Fermi level. A linear regression of the determined onset positions yields a function with a slope close to −1, which is a strong indication of vacuum level alignment. The same behavior has already been shown for PPIX and, thus, together with prior results [116], suggests that this alignment process is the predominant one for samples with HOMO energies significantly below the substrate Fermi level. The molecule itself appears to play only a minor role, being mostly responsible for the shift in potential energy and the HOMO position relative to the vacuum level. It does not have a significant impact on the alignment process itself.

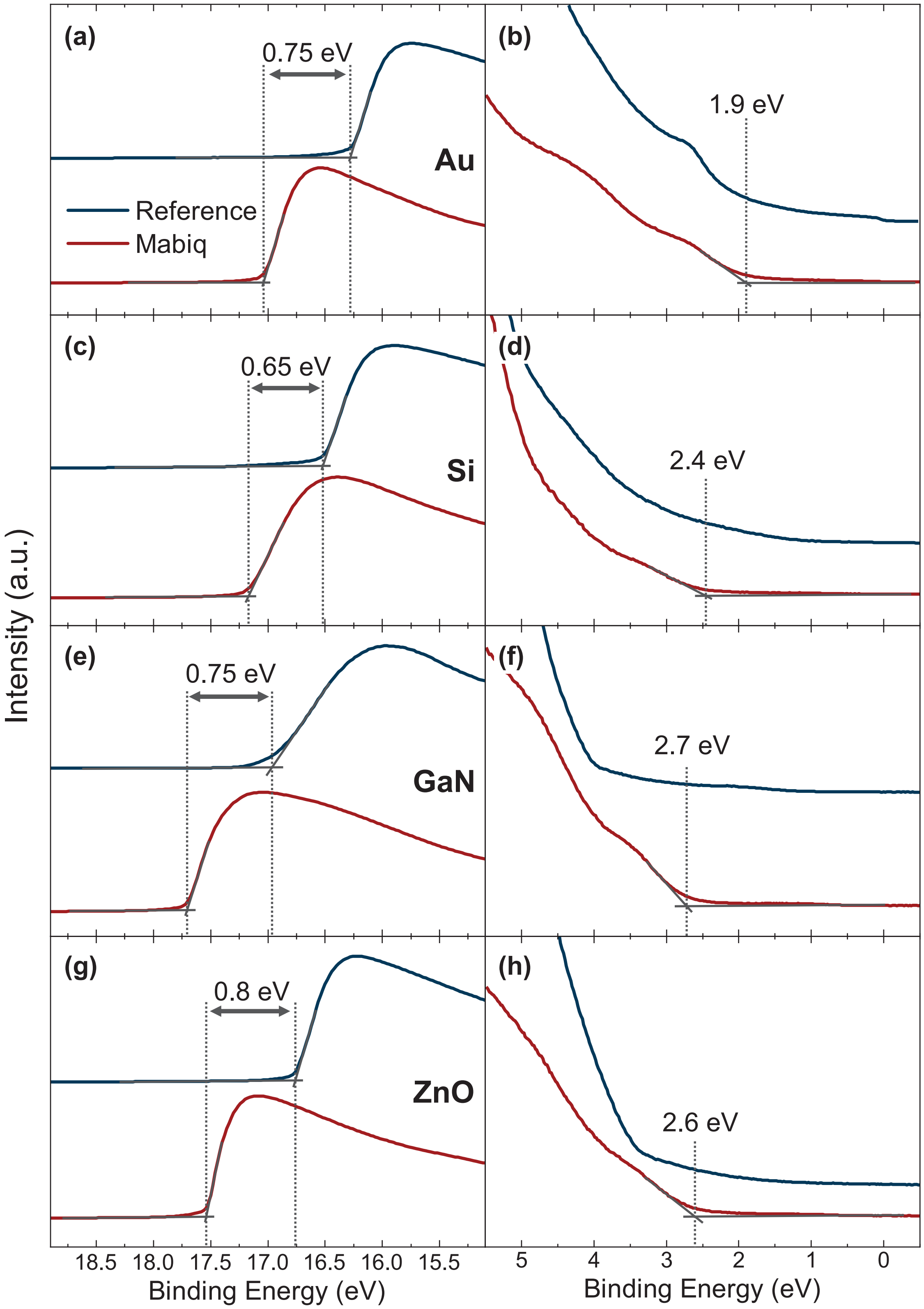

Figure 5.9 Magnified view of the SECO (left) and low binding energy region (right) for all samples under investigation. The SECO exhibits a shift of around 0.75 eV upon coverage with a Mabiq monolayer. The binding energy of the HOMO exhibits significant differences between the measured samples.

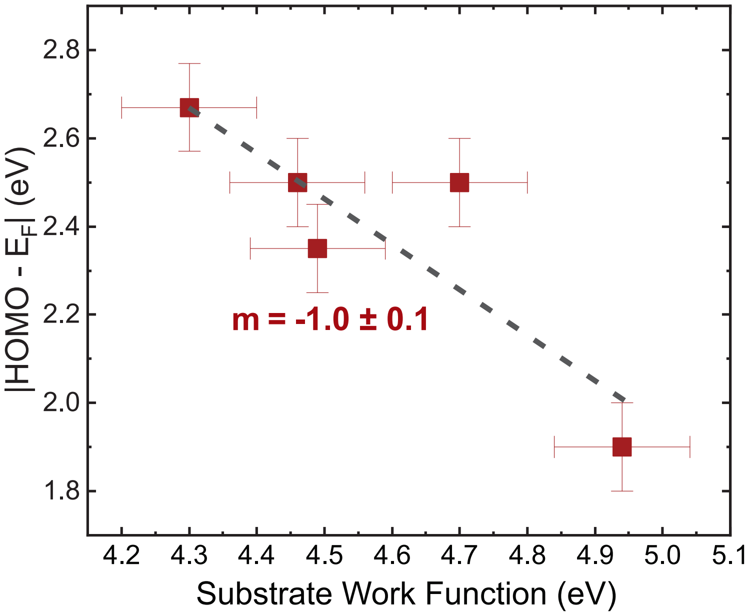

Figure 5.10 Variation of the HOMO binding energy, relative to the absolute Fermi energy of the substrate (HOMO$-E_F$), with the work function. The linear relationship with a slope close to unity indicates that the HOMO binding energy aligns with the vacuum level instead of exhibiting Fermi level alignment.

The influences of the intermolecular and substrate–molecule interactions were studied by comparing the UV–Vis spectra of low-concentration Mabiq dissolved in dichloromethane with monolayer samples. Compared to PPIX, the spectrum of Mabiq in solution exhibits no distinct peaks and mainly consists of an increase in absorption at around 490 nm, which monotonically continues as the wavelength is reduced toward the UV range. Similar to the observations made using PPIX, Mabiq monolayers exhibit a bathochromic shift in monolayer conformation. Here, the absorption onset is located at around 520 nm, corresponding to a reduction of the HOMO–LUMO splitting by around 0.15 eV. The HOMO–LUMO splitting of the monolayer samples of around 2.4 eV can be used to retrace the LUMO position to the vacuum level in conjunction with the insights gained from UPS. By this method, the LUMO is found to be located around 3.9 eV below the vacuum level. While this value is comparatively high and would likely hinder, for example, the electron transfer process from Si to the molecule, there is a large potential shift at the interface. Taking this into account, the LUMO level might align with substrate CBs as low as 4.65 eV. It would, thus, allow electron transfer processes from various narrow band gap semiconductors, such as Si. A schematic overview of the energy level alignment is shown in Fig. 5.12, highlighting the comparatively high electron affinity of the Mabiq considering the potential shift at the interface.

Comparison of the HOMO–LUMO splitting and the HOMO binding energy additionally leads to the conclusion that the LUMO is positioned close to or even below the Fermi level of the system for all substrates except Au, which could result in partial occupation of the LUMO

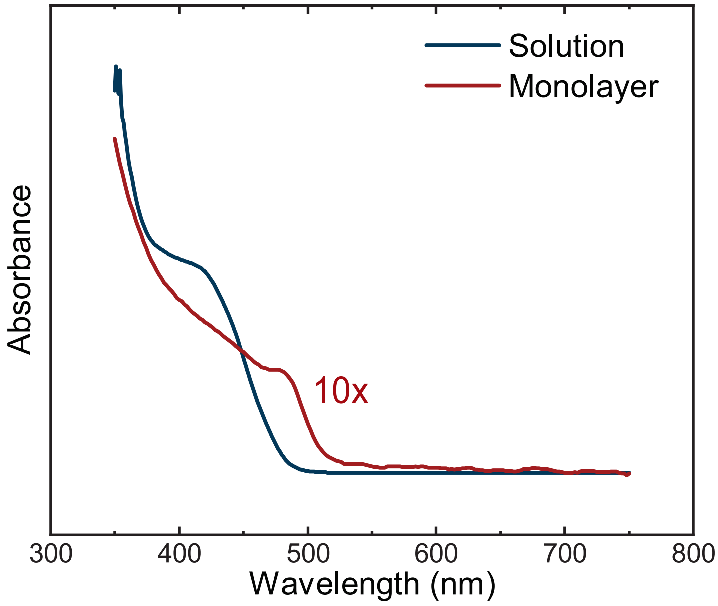

Figure 5.11 UV–Vis absorbance spectra of 5 µM Mabiq dissolved in dichloromethane compared to a monolayer adsorbed on a glass surface. The absorbance of the monolayer is depicted at 10 × magnification to enable comparison of the qualitative shapes of the spectra.

states. An enlarged view of the very low binding energy region is shown in Fig. B.8. In particular, the Mabiq samples deposited on GaN and ZnO show a small peak at the expected binding energy with an onset of 0.3 to 0.4 eV, which could be an indication of a partially occupied LUMO. For Si, this peak is significantly less pronounced but is also positioned at a similar binding energy. Since the peak for Si should be positioned at even lower binding energies and due to the very low peak intensities observed, these data need to be interpreted cautiously. The origin of such low-intensity peaks could also lie in different properties or could be a measurement artifact. Nevertheless, their presence is an initial hint at the possibility of a partially occupied LUMO, which would be highly interesting for catalytic applications.

In summary, Mabiq was deposited as a monolayer using LB deposition at surface pressures of 15 mN m^{-1}. Higher surface pressures led to multilayer formation before a fully dense monolayer coverage could be achieved. LB layers deposited on Si, Au, ZnO, and GaN substrates showed comparable chemical properties, highlighting that the Mabiq molecule remains largely unchanged during the process. Slight deviations in the peak ratios of the N1s transitions could not be fully resolved but are likely a consequence of interaction and coordination with H_2O molecules from the DI water subphase. The energy level alignment studies performed with UPS indicate a comparatively stronger potential shift of around 0.75 eV, which could enable successful charge transfer even from narrow band gap semiconductors to the vacuum level–aligned Mabiq molecules deposited on the substrate surface. These investigations suggest that Mabiq could be a promising candidate for hybrid catalytic devices, not

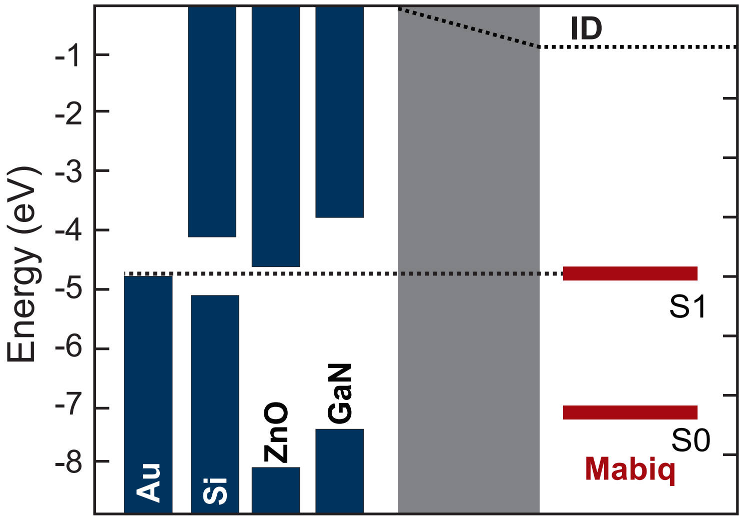

Figure 5.12 Schematic depiction of the energy level alignment of Mabiq monolayers deposited on Au, Si, ZnO, and GaN. Due to the potential shift caused by the interface dipole, the energy level alignment is favorable for electron transfer to the Mabiq molecule. Compared to the alignment of PPIX, the LUMO of Mabiq is positioned well below the CB of Si and even slightly lower than that of ZnO. Thus, the alignment of Mabiq is promising for applications in reduction catalysis.

only because of its bimetallic functionality but also due to its beneficial interface properties.

6. Modification of Silicon–Mercury Schottky Junctions With Protoporphyrin IX Interlayers

The previous chapters discussed energy level alignment and charge transport in the context of catalytic applications. However, these phenomena are also highly relevant to other applications of hybrid devices, especially in molecular electronics. In this context, hybrid systems could be used to modify electronic devices by manipulating the properties of, for example, Schottky junctions [229]–[231]. The similarities between the device structures used for catalysis and electronics have led to the cross-pollination of analysis techniques between the two fields, yielding additional insight into the behavior of semiconductor properties such as band bending. The information gathered through the analysis in previous chapters could also help understand the properties of a hybrid Schottky junction with an organic interlayer.

Therefore, experiments regarding surface or interface band bending, as well as the influence of PPIX LB layers on a Si–Hg Schottky junction, are analyzed in this chapter. PPIX was chosen due to the prior knowledge obtained and presented in Chapter 4. Si was chosen due to its widespread prevalence in electronic devices. While the previous chapters were mostly limited to the analysis of the immediate interface and the molecular monolayer, the electronic measurement methods used in this chapter allow for a more in-depth investigation of the near-interface regions in the substrate. The analysis here also extends to the influence of doping type and concentration.

The methods used include the determination of the surface band bending in the absence of a metal contact through surface photovoltage (SPV) studies with and without a PPIX monolayer, the analysis of UI curves of Si–Hg Schottky junctions, and the extraction of the barrier height at the interface through temperature-dependent UI curves. The results of these measurements can be combined with the insights previously obtained from UPS and photoluminescence measurements to acquire a more accurate model of the band alignment, which includes the surface band bending at the interface.

Modification of a metal–semiconductor interface with a molecular monolayer is challenging due to its thickness being a single layer of molecules, which could exhibit pinholes and might also be easily penetrable by a metal deposited on top. This is especially true for commonly used physical vapor deposition (PVD) techniques, such as evaporation or sputtering. In these methods, the metal particles approach the surface with significant excess energy. Radiative heating or heating through the plasma could also result in elevated sample temperatures. This leads to an increased diffusivity of metal ions and molecules and could increase the number of pinholes in the monolayer. These pinholes represent shortcuts in the envisioned device, since the junction within them exhibits the known properties of a standard Schottky junction between the metal and semiconductor materials [232], [233]. The effect of the monolayer is, thus, diminished or even completely annihilated. This behavior can be mitigated through prevention of increased substrate temperatures, reduction of the thermal energy of the arriving metal, and choice of low-diffusivity metals such as lead [234]. These processes result in a significant overhead, however, since they require special PVD setups that enable the evaporation of such materials at larger source-to-sample distances, lower deposition rates, and controlled substrate temperatures, possibly down to cryogenic conditions.

Since the research questions to be answered in this chapter are of a general nature and are not concerned with specific Schottky junctions, this overhead can be circumvented by using liquid metals for the contacts. Hg is an interesting contact material for substrates covered with LB layers since it is liquid at room temperature. Thus, it is suitable for a gentle deposition method at low temperatures that avoids exerting mechanical stress on the sample. This method of soft contact formation has therefore been widely adopted in research of sensitive thin films and monolayers, but has also been used to form temporary contacts for quality control and failure analysis in large-scale semiconductor manufacturing [235]. Due to the health concerns associated with Hg, alternative liquid metal contacts have been developed recently. These are usually based on gallium and indium, which can form a eutectic mixture that is liquid at room temperature and can be used similarly to Hg [236]. Due to the availability of a well-tested measurement setup, this work focuses on Hg as the contacting metal.

6.1. Influence of Protoporphyrin IX on the Surface Photovoltage Characteristics

To begin with, the surface band bending of the semiconductor substrates and the influence of deposited LB layers were investigated through contact potential difference (CPD) and surface photovoltage (SPV) studies. Moderately doped Si substrates (with a resistivity of 7.5 Ω cm for both doping types), with ohmic contacts on their backsides, were mounted into a Kelvin probe measurement system to determine their work functions. Without external illumination, the Fermi level at the surface is generally pinned close to the middle of the band gap. Sufficiently powerful illumination with an external light source asymptotically shifts the Fermi level at the surface to the bulk value, as described in more detail in Sec. 2.2.

Fig. 6.1 depicts SPV measurements of moderately doped n- and p-type Si treated to achieve different surface terminations. For the measurements shown in Fig. 6.1(a) and (b), the samples were prepared by etching in HF to remove the native oxide, leaving a H-termination on the surface. Fig. 6.1(c) and (d) depict the same samples after subsequent treatment with an oxygen plasma followed by immersion in DI water for 30 min. The data were recorded by pulsed illumination, starting in dark conditions followed by three pulses of illumination using 405 nm, 554 nm, or 880 nm light. While these wavelengths are all well above the band

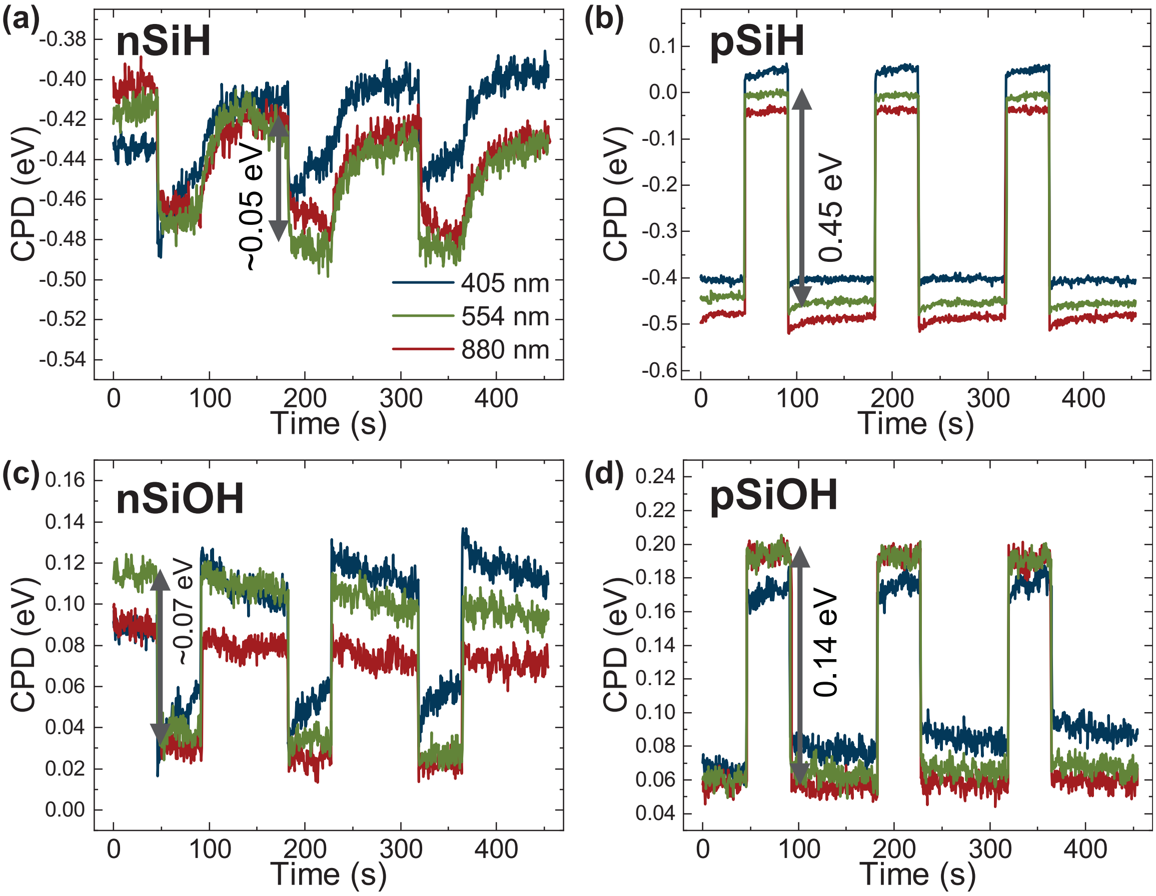

Figure 6.1 SPV measurements of (a) and (c) n-type and (b) and (d) p-type Si for (a)–(b) H-terminated surfaces and (c)–(d) surfaces treated by short exposure to oxygen plasma. The SPV was analyzed under illumination by 405 nm, 554 nm, and 880 nm LEDs, which were turned on periodically for 45 s after an initial dark measurement of 45 s. A dark period of 90 s between illuminations allows investigation of the SPV relaxation.

gap of Si, they were chosen with regard to the PPIX LB layer to be deposited on the surface in mind. As highlighted in Chapter 4, the PPIX LB layers exhibit no absorption in the near-infrared (NIR) wavelength range of the 880 nm LED. In the range of the 554 nm LED, the Q bands, corresponding to the absorption from the HOMO to the LUMO, are absorbing. Approaching the UV region, the 405 nm LED corresponds to the transition from the HOMO to the LUMO+1 state of the PPIX.

The SPV measurements of the H-terminated (SiH) and the oxygen plasma-treated (SiOH) samples do not exhibit significantly different behavior for the different illumination wavelengths. This suggests that the impinging light provides sufficient power to achieve near-complete saturation of the SPV, especially since the LEDs were not adjusted to normalize the illumination intensity.

Comparing the behavior of the n- and p-type SiH samples depicted in Fig. 6.1(a) and (b), clear differences in the amount of SPV become apparent depending on the doping type. The CPD at the surface is nearly identical for both samples with a value of around −0.5 to −0.4 eV. The negative sign indicates measured work functions smaller than the electrode work function, which was determined to be 4.8 eV, as described in Sec. A.5 in the Appendix. Illumination led to a small SPV for the n-type sample of roughly −50 meV. In contrast, the SPV of the p-type sample is determined to be 0.45 eV. The sign of the SPV indicates the direction of the surface band bending. A decrease points at upward band bending, as is expected for an n-type semiconductor. In the case of the p-type sample, the positive SPV indicates the expected downward band bending. The differences in the amount of band bending can be explained by the Fermi level pinning. The CPD of both samples in the dark indicates Fermi level pinning close to the bulk Fermi level of the chosen moderately doped n-type Si, which is expected to be around 4.3 eV, given its doping concentration of around 6×10^{14} cm^{-3} calculated from the specific resistivity. Therefore, the amount of band bending is significantly lower than for the p-type sample, for which the bulk Fermi level position relative to the vacuum level is expected to be around 4.9 eV, as extracted from the doping concentration of around 2×10^{15} cm^{-3}. The expected difference of bulk Fermi levels of 0.6 eV for the given samples closely matches the experimentally determined difference of the CPD under illumination for SiH samples, which is 0.5 eV. This highlights that the illumination intensity is sufficient to reach flat band conditions for both materials.

The slight differences in the CPD without illumination of up to 0.1 eV are likely a consequence of prior influences, changes in the local environment, or sample aging. The illumination experiments were performed in series, beginning with the highest-wavelength light and moving toward shorter wavelengths. This was done intentionally to start with the lowest-energy photons and prevent the influence of persistently excited electrons from higher-energy photons on lower-energy measurements. Nevertheless, the prior illumination could yield a slight change in the occupation of the surface states that persists at longer timescales than the waiting time between measurements. The waiting time was kept at a few minutes to reduce the influence of other factors: Due to the measurements being performed in ambient conditions, longer waiting times could result in changes in the local environment, including humidity, temperature, or air contamination. These influences could yield slight changes in the recorded CPD, for example, due to varying degrees of water adsorption on the surface. The H-terminated samples were freshly prepared and measured minutes after HF etching. Due to the metastability of the H-termination, it is prone to oxidation on a timescale of hours. Thus, the measurement times need to be kept as short as possible to minimize the effects of reoxidation.

Shifting attention to the SiOH substrate data shown in Fig. 6.1(c) and (d), one can identify qualitatively similar behavior regarding the direction of band bending. The CPD appears to be significantly shifted, however, since it is now corresponding closely to the Fermi level position of bulk p-type Si for both samples, being around 0.05 to 0.1 eV. This shift probably arises due to the change in surface states originating from the thin oxide layer formed during the synthesis procedure. The native oxide results in the formation of interface states at the semiconductor–oxide interface and new surface states associated with the oxide material. Due to the small thickness of the oxide, these states are in close proximity to each other and could exhibit significantly different properties from the SiH surfaces. The band bending of the p-type sample is significantly reduced to around 0.14 eV, resulting in a measured CPD under illumination of 0.2 eV. This value corresponds to a bulk Fermi level of 5.0 eV and is, thus, slightly larger than the expected work function of 4.9 eV. This is likely due to the influencing factors discussed previously. Some of the deviation could also be due to electrostatic interactions, such as an interface dipole of the surface hydroxyl groups or adsorbed water on the hydrophobic surface, or a slight charging of the native oxide due to the plasma treatment.

In contrast, the n-type measurements shown in Fig. 6.1 (c) exhibit unexpected behavior. Judging from the bulk work function of the sample and the measured CPD of 0.1 eV, one would expect an SPV of at least 0.5 eV, but the measurements indicate a significantly lower value of around 0.07 eV. The origin of this deviation is unclear. It might be caused by a significant change in surface recombination rate due to the surface oxide, which could affect the number of free holes present at the surface upon illumination of an n-type semiconductor. This would result in the need for significantly higher illumination power to reach saturation. However, the similarity of the behavior at all illumination wavelengths points against this explanation.

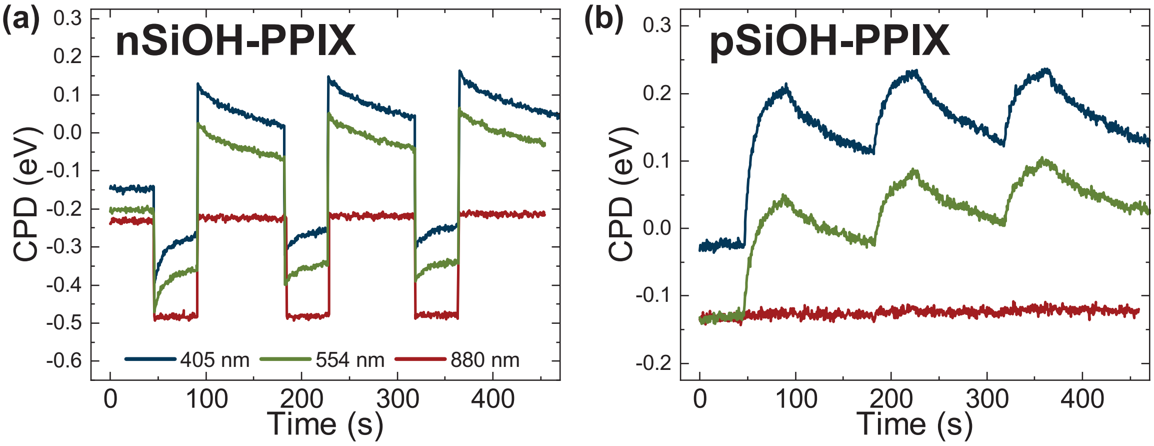

Figure 6.2 SPV measurements of (a) n-type and (b) p-type Si after oxygen plasma treatment covered with a PPIX LB layer using the same illumination sources and measurement intervals as in Fig. 6.1.

The SPV data acquired for the SiOH samples covered with an LB layer of PPIX are shown in Fig. 6.2. Both the n- and p-type samples exhibit a shift toward more positive CPDS relative to the previously determined reference SiOH surfaces. This shift is around 0.3 eV in magnitude, resulting in dark work functions around 4.6 eV, as previously discussed in Sec. 4.4 based on UPS spectra. In addition to determining this shift, which is likely caused by interface dipole formation, the SPV measurements enable the analysis of the response of these hybrid surfaces to external illumination.

As alluded to previously, the wavelengths of the illumination sources were chosen either to solely excite the Si (880 nm) or to excite the PPIX molecule to its first (554 nm) or second (405 nm) excited state. The measurements for the n-type sample shown in Fig. 6.2(a) indicate major qualitative differences from the SPV measurements of the bare substrate. In contrast to the low SPVs observed for the reference sample, the PPIX sample exhibits a significantly higher SPV of 0.27 eV when excited at 880 nm. Similar photovoltages were also observed for the shorter wavelengths, but the measurement spectra additionally exhibit a more complex temporal evolution than what was observed for previous samples. While illumination in the NIR, which excludes excitation of the PPIX, results in a near stepwise behavior, higher photon energies lead to the appearance of significant decay features, both under illumination and in darkness. This decay occurs over seconds and is most pronounced at the beginning of the experiment. After the first illumination step, the CPD increases significantly to around 0.1 eV, marking a jump significantly larger than both the initial SPV and the SPV measured under NIR illumination. The CPD becomes more negative during the time spent in darkness until the next illumination cycle is started. While the SPV remains at a similar magnitude from this point onward, the CPD appears to shift to higher values with increasing illumination duration. This is also visible across measurements with 405 nm illumination, which exhibits a slightly more positive CPD than the prior two measurements. While this behavior appears to decay over time in darkness, it is unclear whether it is fully reversible. Due to the long time constants associated with this phenomenon, it is difficult to distinguish between the relaxation process and drift due to the aforementioned environmental influences, especially as the CPD approaches its initial value and changes become slow.

The p-type sample also exhibits significantly different SPV properties, as shown in Fig. 6.2(b). Interestingly, there was no measurable SPV under illumination with 880 nm, indicating flat band conditions after LB deposition of PPIX. In contrast, excitation of the PPIX molecule leads to a significant SPV. The SPV are the highest upon initial illumination, ranging from 0.15 eV for the 554 nm illumination to 0.25 eV for the 405 nm illumination. In contrast to the time evolution of the n-type sample, which exhibited an initial spike with subsequent decay, the CPD for the p-type sample exhibits a slower build-up. The decay behavior appears to be comparable, however.

Due to the complexity of the changes observed for both samples, developing an accurate model is challenging. Multiple processes are at play simultaneously, complicating the analysis. These include degradation of the PPIX monolayer due to exposure to the atmosphere, photodegradation as a result of the external illumination, surface recombination rates and possible influences on the surface recombination kinetics by the PPIX, charge transfer processes from molecule to semiconductor and vice versa, and lastly changes due to dark or photoinduced adsorption or desorption of contaminants. The time constants associated with all these processes are unknown, making it impossible to discern between them based solely on SPV measurements. Nevertheless, the qualitative differences for the LB layer samples, which only occur upon excitation of the PPIX, are a promising indication of charge transfer interactions between the materials. A more elaborate investigation in a controlled environment, for example, under UHV conditions, could provide valuable information on the interaction between PPIX and Si of different doping types. Ideally, this investigation could be combined with XPS and UPS studies with additional external illumination to provide spectral information on the processes at play.

6.2. Influence of Protoporphyrin IX on the Voltage–Current Characteristics

Schottky junctions to the substrates were established by placing a droplet of Hg on the substrate surface. They were evaluated through UI analysis, measuring the current density through the interface relative to the applied voltage. These measurements were performed on the same substrates used in the previously described SPV measurements and additionally for samples with much higher doping concentrations bordering on degenerate doping (resistivities below 0.01 Ω cm), marked by an additional "+" sign in the sample name. The resulting UI curves are shown as semilogarithmic plots in Fig. 6.3, depicting measurements of both doping concentrations for both types of reference samples and LB layer samples. The reference measurements were performed on the substrate after oxygen plasma treatment and submersion in DI water for 30 min, analogous to the reference samples used in the previous chapters.

The reference samples show the expected behavior for the respective Schottky junctions established. To begin with, the samples with high doping concentrations show a rather symmetric behavior, indicating only slight differences depending on the polarity of the applied voltage in this logarithmic plot. The polarity of the measurement is defined to be positive for forward voltages of junctions with n-type samples. The differences in forward and reverse bias become significantly more apparent for the substrates with lower doping concentrations, with a larger current passing through the junction for forward bias. This difference can be explained by the probability of charge carriers tunneling through the Schottky barrier at the interface, which corresponds to the depletion layer width in the semiconductor. As described in Sec. 2.3, high doping concentrations lead to a significant reduction in depletion layer width, resulting in high tunneling probability and, therefore, high tunneling current density. This reduces the influence of the Schottky barrier height, resulting in a loss of the rectifying behavior of the Schottky diode. Similar processes establish ohmic contacts with semiconducting samples. Due to the significantly larger depletion layer width for the samples with moderate doping concentrations, the tunneling probability is significantly lower, leading to a pronounced

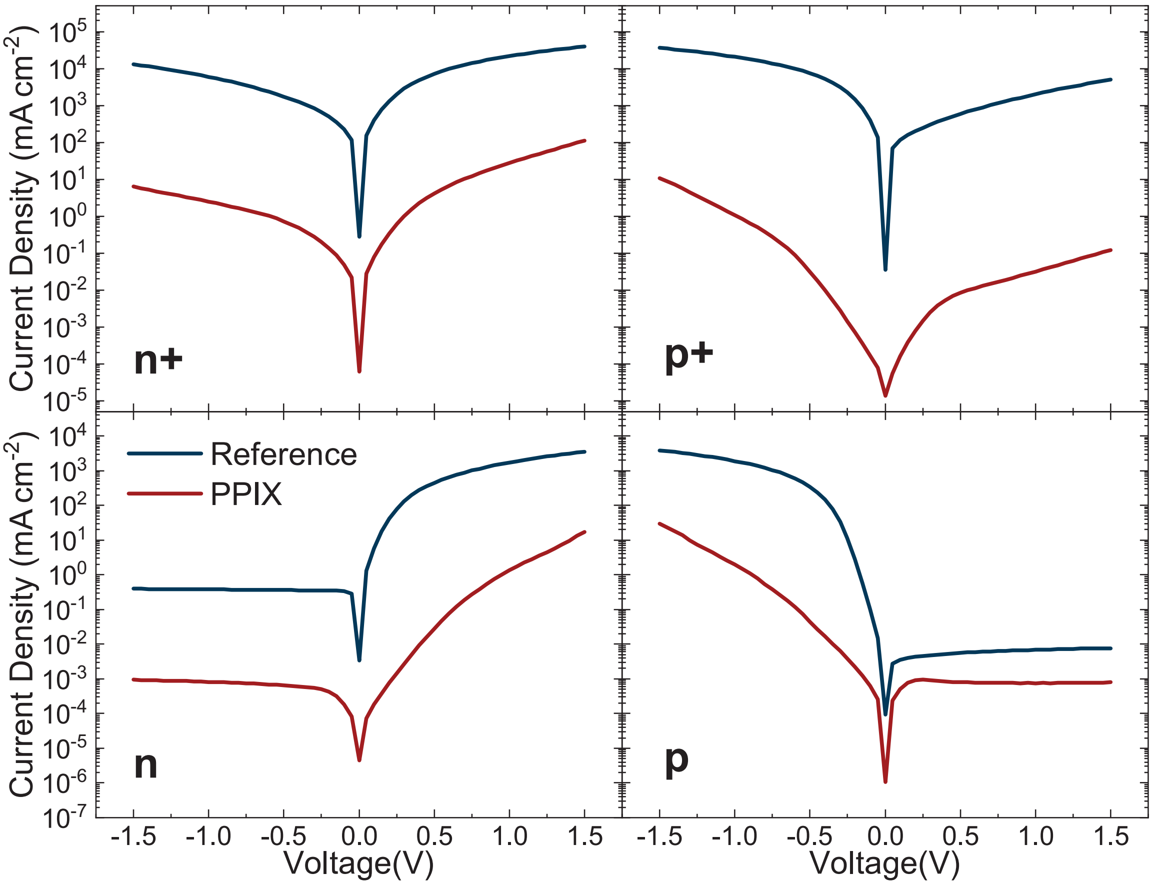

Figure 6.3 UI curves for n-type (left) and p-type (right) Si of high (top) and medium (bottom) doping concentrations, for pristine samples and samples covered with a PPIX LB layer. The metallic top contact is established by a liquid Hg droplet deposited on the surface. The UI characteristics are significantly changed for all samples, exhibiting a significant reduction in current density across the junction due to the PPIX monolayer.

influence of the Schottky barrier and thermionic emission dominating the transport through the interface.

The introduction of LB interlayers to the Schottky junction leads to a sizable reduction of three to four orders of magnitude in current density for all samples. This suggests that the LB layer remains intact after Hg droplet deposition and shows that the effect of a PPIX interlayer is not negligible due to short-circuiting through pinholes. Simultaneously, the reduction in current density implies that the PPIX interlayer introduces a significant resistance to charge carriers crossing the interface. This indicates that the PPIX molecular orbitals are either energetically unable to participate in charge transfer or that the charge transfer rates are a bottleneck. Interestingly, the current density reduction is not homogeneous across the voltage range and across samples. This leads to changes in the UI curve shape, especially for the moderately doped samples and the highly doped p-type sample. These changes can be described as an overall flattening of the curves, which show a significantly smaller current density increase at low forward and reverse potentials compared to the reference samples, which might, for example, originate from a reduced ideality factor.

Table 1 Rectification ratios of Schottky junctions with of reference junctions and junctions with PPIX interlayer as extracted from the endpoints of the UI curves shown in Fig. 6.3. While the moderately doped n-type sample shows a comparatively low influence of the PPIX interlayer on the rectification ratio, its influence on the other samples is significantly higher.

	n+	n	p	p+
Reference	3.0	9.0×10^3	5.0×10^5	7.3
PPIX	17.7	1.8×10^4	3.7×10^4	89.0

These differences also lead to a change in the rectification ratio for some of the samples, as depicted in Tab. 1. While the rectification ratio of n-type Si remains in the same order of magnitude, both highly doped samples exhibit an increase in rectification ratio of around an order of magnitude upon the addition of a PPIX interlayer. In contrast, the rectification ratio of p-type Si decreases upon adding PPIX. This indicates an influence of the PPIX that goes beyond introducing a charge transfer barrier since this would likely induce a consistent change independent of the doping type. To better understand the effect of the PPIX interlayer, the ratios of the UI curves of the reference samples and the PPIX samples are depicted in Fig. 6.4 for the moderately doped substrates. Here, the previously discussed variation in UI curve shapes becomes even more apparent as pronounced dips in the low forward bias regime for both samples arise. For increasingly higher forward bias, the ratio between the reference and PPIX sample becomes linearly smaller. While high reverse biases lead to no change in the current density ratio, the behavior in the low reverse bias range is distinctly different for n- and p-type Si. For the n-type sample, the ratio slowly approaches saturation. In contrast, the ratio of the p-type sample exhibits a small peak for small reverse biases. Upon closer investigation of the respective UI curve in Fig. 6.3, this small increase in current density for low reverse biases is a consequence of the increased current density from the PPIX sample in this range.

The dips in the current density ratio are located at 0.25 V and −0.4 V forward potentials for n- and p-type Si, respectively. The difference in the potentials of these dips coincides with the difference of PPIX HOMO-LUMO splitting and the band gap of Si, which was determined to be around 0.7 eV in Chapter 4. This could be interpreted as an initial hint for the participation of a PPIX molecular orbital in the charge transfer process across the interface. An increasing potential applied to the junction could shift alignment and enable participation of the LUMO respectively HOMO in majority carrier transfer from semiconductor to metal at the

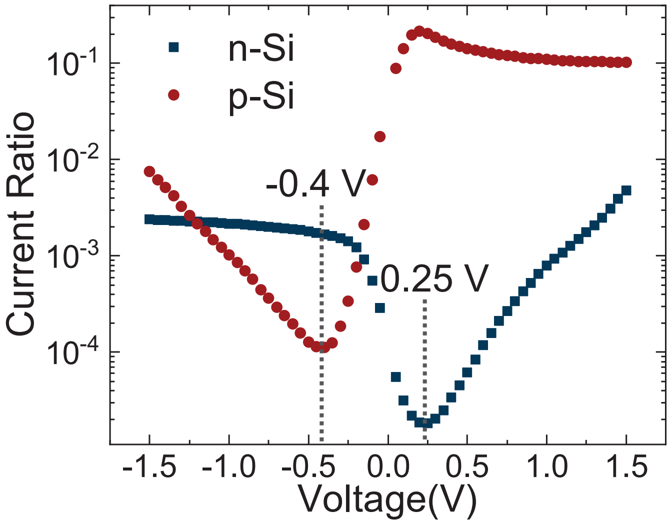

Figure 6.4 Ratio of the UI curves of Schottky junctions with PPIX interlayer compared to reference measurements. While the ratio remains rather constant at increased voltages in the blocking direction of the junction, the reduction of current upon interlayer introduction is most apparent for small forward voltages.

straddling junction between Si and PPIX. While these values do coincide, the limited understanding of the charge transfer processes at such interfaces and the lack of data supporting this interpretation means that this is limited to being a working theory.

An enlarged view of the reverse bias part of the UI curves is shown in Fig. 6.5 on a linear scale. Both samples exhibit differences depending on the scanning direction. While scans toward the forward bias direction result in the expected characteristics, the p-type sample in particular exhibits a pronounced local current increase when scanning toward more rectifying potentials. The peak is located at around 0.2 V and leads to an apparent negative resistance when scanning past it. While it might be theoretically possible that a resonance between a molecular orbital and the VB could lead to such a behavior, it is more likely that the decrease in current is a result of the scan speed: It could result from filling or emptying molecular orbitals that become available as the potential is scanned. This explanation is supported by the behavior of the p-type sample for negative biases, for which the current behavior is reversed. The enclosed areas for forward and reverse bias are within 15 % of each other, thus suggesting that the stored and extracted charge are comparable. The experimental setup did not allow for a precise definition of the scan rate, and therefore, an accurate quantification of the stored charge could not be made.

Schottky junctions are commonly analyzed by fitting the forward bias behavior with the Shockley equation to extract many parameters, including the barrier height and ideality factor, with a single fit. While this is a valid approach for well-understood systems for which it is known which processes are relevant or negligible, a fit of the present Schottky junctions would not yield a greater understanding of the system. This is due to the limited information on the

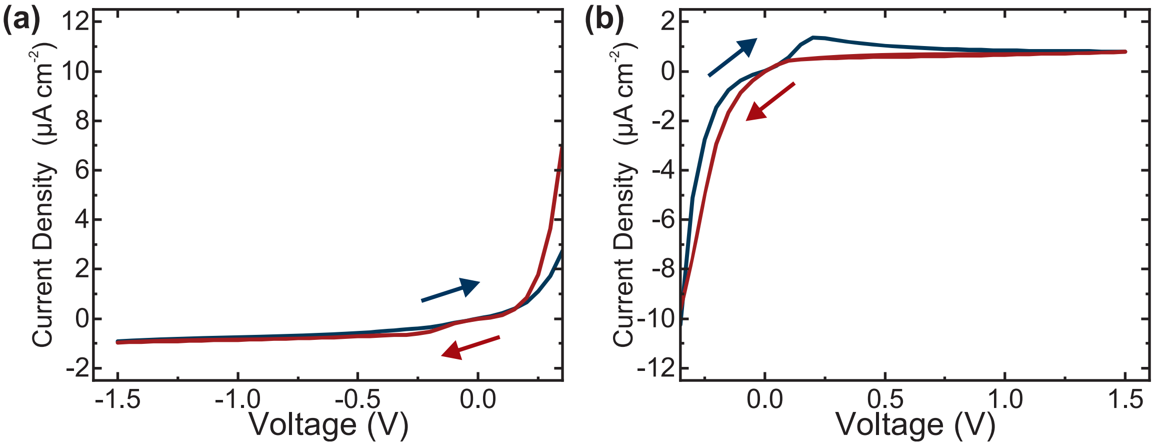

Figure 6.5 Enlarged view of current density measured at reverse biases with different scan directions for (a) n-type and (b) p-type Si with a PPIX LB layer. An increase in current can be observed for the p-type sample when the voltage is scanned toward positive voltages, which could arise due to interaction of the PPIX HOMO with the VB of Si.

charge transfer processes at play, which could render the interpretation of a fit with the Shockley equation invalid. Instead, the analysis of the UI curves of the samples was extended to a wider parameter range by temperature variation to enable more accurate statements about the influence of PPIX on the junction.

6.3. Changes of Barrier Height with Protoporphyrin IX Monolayers

So far, the analysis of the Si surface and Hg–Si Schottky junctions has been limited to room temperature. By studying the influence of temperature on the UI characteristics of the investigated Schottky junctions, more in-depth knowledge of the processes at play can be obtained. This investigation is limited to the moderately doped samples because the significant tunneling current of the highly doped samples would severely influence the measurement, limiting the value of the obtained data. To this end, temperature-dependent analysis of the UI curves of moderately doped Si samples was performed by adding a thermoelectric cooler to the measurement setup. This allowed for a temperature variation between −10 °C and 30 °C. Lower temperatures were not achievable in the setup. A significantly lower temperature would have been impractical anyway, due to the freezing of the Hg droplet at around −38 °C. UI curves recorded at different temperatures within this range are shown in Fig. 6.6. The setup did not include an active temperature control, and the reverse side of the thermoelectric element was not held at a constant temperature. Therefore, the temperatures could only be coarsely adjusted, but were measured accurately to ensure high data quality.

For the reference samples, the measurements exhibited close to no change in current density at a large forward bias but exhibited a significant change at reverse bias. This points to thermionic emission being the dominant charge transfer process for these Schottky junctions, which is expected since this is the major charge transfer mechanism relevant for most systems. The intricacies of thermionic emission are described in Sec. 2.3, in which the expected dependence of the current on the junction temperature is derived for small forward and reverse biases. This behavior is similar to the n-type sample with a PPIX monolayer and is the first indication of the relevance of thermal excitation for the charge transfer. Interestingly, the UI curve of the p-type PPIX sample exhibits close to no change with temperature, which could either indicate that thermionic emission is not the driving force in this sample or that the Schottky barrier height is relatively small.

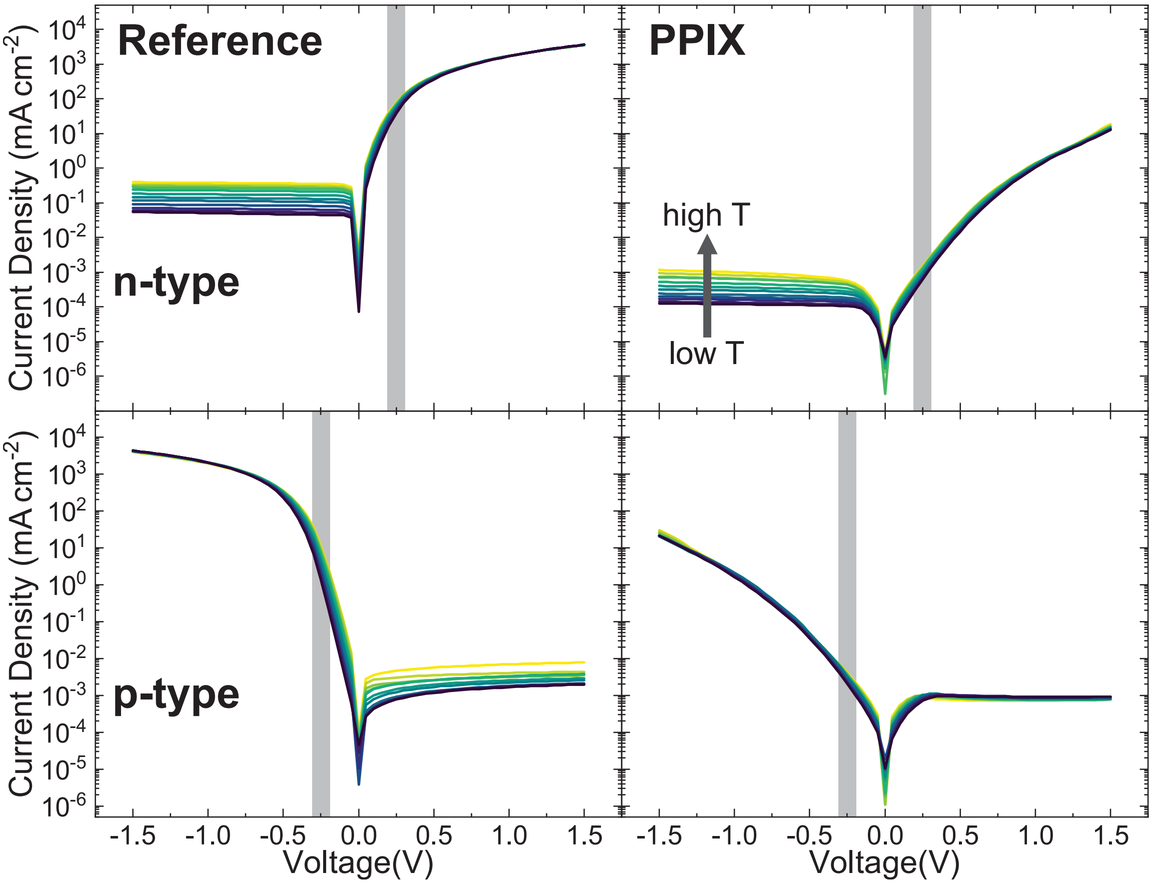

Figure 6.6 Temperature-dependent UI curves for n-type (top) and p-type (bottom) Si of pristine reference samples (left) and samples covered with a PPIX LB layer (right) in a temperature range from roughly −10 °C to 25 °C. The temperature mainly influences the current density for small forward and reverse bias.

A Richardson plot analysis was performed to determine the validity of the thermionic emission theory for the given junctions and is shown in Fig. 6.7. The saturation currents were extracted from the UI curves and averaged over forward and reverse directions through exponential fits at low forward bias. These were linearized according to the Richardson equation to determine the thermionic emission current. The Richardson plots indicate linear behavior for all samples, validating the thermionic emission theory for these Schottky junctions and their

PPIX-modified versions. The Schottky barrier height can be extracted from the slope of the linear fits of these datasets, as marked by the gray dashed lines in the figure. The slopes of the reference samples indicate barrier heights of 0.31 eV for the n-type sample and 0.72 eV for the p-type sample. The sum of these barrier heights is 1.13 eV, which closely matches the expected value, the band gap of Si. For the Schottky junctions with a PPIX interlayer, both samples exhibited a reduction of the barrier height to 0.17 eV or 0.18 eV for n- and p-type Si, respectively. This indicates a moderate reduction for the n-type sample and a significant reduction for the p-type sample, which is an unexpected behavior, since the introduction of the potential shift induced by the PPIX interlayer is expected to shift the interface potentials, leading to a reduction of the barrier height for one doping type and an increase for the other.

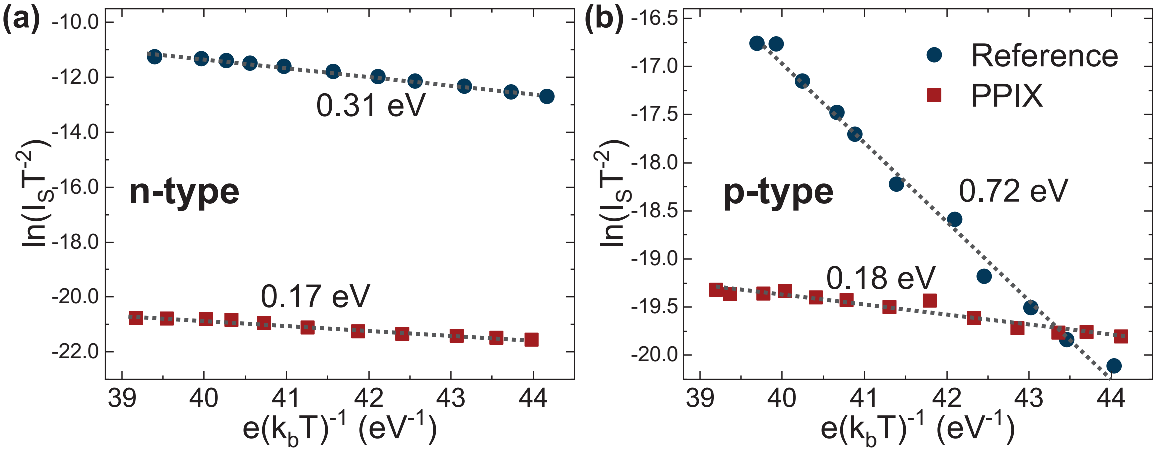

Figure 6.7 Richardson plots extracted from current densities at a forward bias of 250 mV for moderately doped n-type (left) and p-type (right) reference samples and samples covered by a PPIX interlayer. An approximately linear relationship indicates that the thermionic emission theory is valid. A reduction in work function was observed upon introduction of the PPIX interlayer in both case. While this effect appears to be moderate for n-type Si, it is significantly more pronounced for p-type Si.

In the case of the p-type sample, the behavior can be interpreted as a result of the interface potential shift due to dipole layer formation upon the LB deposition of PPIX. The reduction and direction coincide with the magnitude and direction of this potential shift determined in Sec. 4.4. For the n-type Si, however, the observed behavior does not match this potential shift. This unpredicted behavior coincides with the behavior exhibited by the n-type sample during the SPV measurements, complicating the interpretation of the acquired data.

6.4. Energy Level Alignment and Influence of Protoporphyrin IX Interlayers

The interaction of the semiconductor surface with the PPIX LB layer is unexpectedly complex, making it difficult to draw clear conclusions. The main challenge is the occasional appearance of unexpected behavior of unknown origin during selected measurements. This makes it hard to discern between variations caused by, for example, environmental factors and interaction phenomena between the two systems. In addition, the surface properties of Si by itself are already challenging to analyze. Nevertheless, an attempt to draw a conclusion from the measured data is shown in Fig. 6.8.

The measurement data are significantly easier to summarize in a model for the p-type SI than for the n-type Si. The reference Schottky junction is characterized by an energy barrier that indicates Fermi level pinning close to the middle of the Si band gap, leading to the formation of significant band bending in the Si. The interface dipole shift due to the PPIX LB layer is the same as observed on n-type Si, with a magnitude of 0.4 eV, leading to a downward shift of the vacuum potential towards the Hg contact. This potential shift leads to the Hg and the p-type Si work function already being well-aligned. The significantly reduced barrier height is a consequence of this interface dipole but also indicates that the interface states have been passivated by the PPIX monolayer. This is in line with the observed SPV presented in Sec. 6.1, indicating a passivation of the surface states and a significant reduction in surface band bending in the case of the monolayer-covered p-type Si. For small forward voltages, the PPIX layer acts as an insulator due to the straddling alignment with the PPIX posing a significant potential barrier. As increasingly higher potentials are applied to the junction, the HOMO of the LB layer could aid in the conduction of holes from Si to Hg. This becomes apparent in the dip in the current ratio observed in Fig. 6.4. While the respective potentials of the dips do not exactly align with the HOMO–VB distance (0.9 eV for p-type Si and 0.1 eV for n-type Si, including interface dipole), the location might be skewed by, for example, thermionic emission. Additionally, the precise location of the HOMO regarding the interface dipole is uncertain since the interface dipole shift and the HOMO position can only be determined in conjunction. Thus, the position of the potential shift concerning the extent of the molecular orbitals cannot be determined accurately. The increased current observed in the reverse scanning direction at slightly rectifying potentials shown in Fig. 6.5 could be explained similarly. Its origin could be the ionization of the PPIX molecules due to electron transfer from the HOMO of the molecule to the Hg as the potential is scanned in the negative direction. The empty states could be refilled as the polarity switches, causing the increased current at low forward potentials. The reason why this was not observed for the n-type Si could be that the potential barrier between the Si CB and the PPIX HOMO is too high.

The reference Schottky junction for the n-type Si exhibits the expected behavior. The Schottky barrier height is compatible with the barrier height of the p-type sample since the sum of both barriers is comparable to the band gap of Si, as expected. This indicates that the Fermi level is pinned at the same potential for both doping types. Introduction of the identical 0.4 eV interface dipole should, therefore, induce an increase in barrier height if the effect is solely electrostatic, as observed for the p-type sample. On the contrary, the Schottky barrier height for n-type Si is reduced to a similar value. For the LB layer samples, the sum of the Schottky

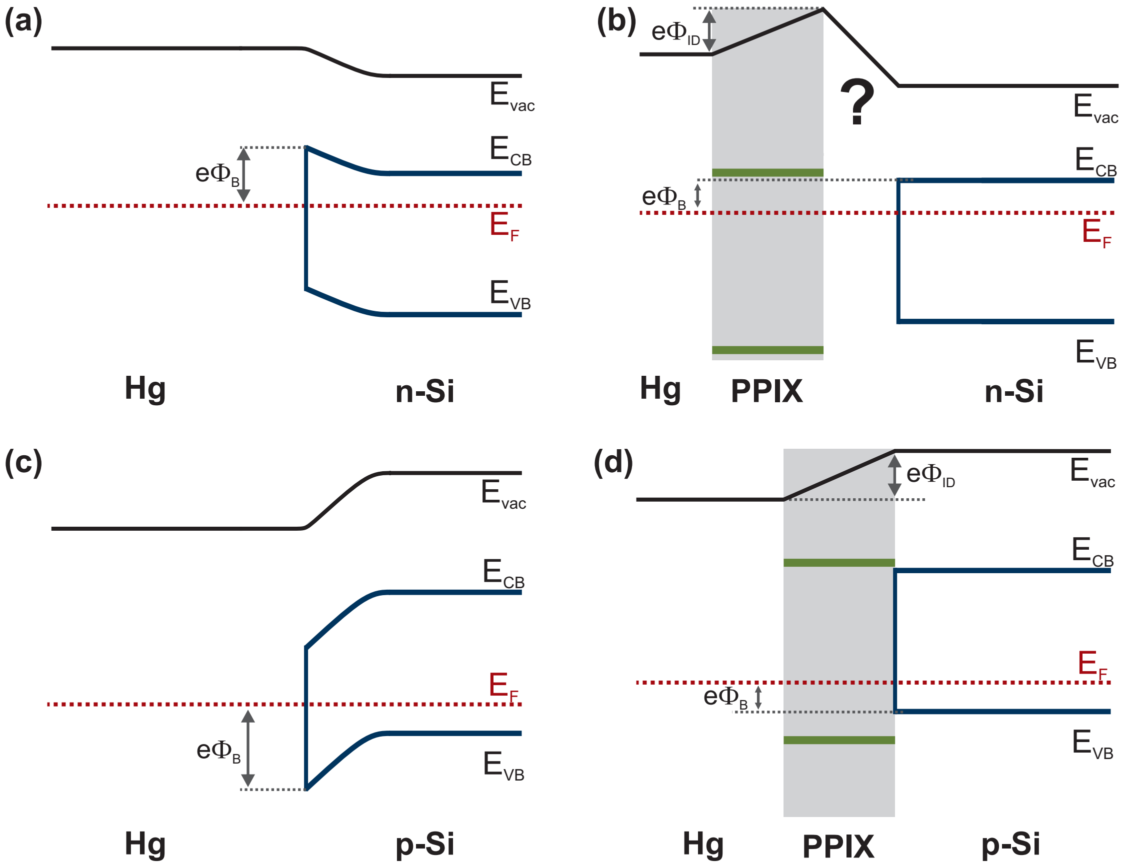

Figure 6.8 Schematic depiction of the proposed band alignment of the PPIX-modified Hg–Si Schottky junctions. Reference Schottky junctions with moderately doped (a) n-type and (c) p-type Si. (b) and (d) Schottky junctions of n-type and p-type Si with a PPIX interlayer, indicating the presence of an interface dipole layer shifting the band alignment and the positions of the HOMO and LUMO levels of the PPIX.

barriers is, thus, significantly different from the band gap of the Si, being only 0.35 eV. This indicates an additional, unknown effect influencing the alignment in the case of the n-type Si. This could, for example, be caused by a different or additional interface dipole formed through the interaction of the three components of the hybrid junction. In addition, the pinning of the Fermi level could be significantly changed. The low observed barrier height suggests that the band bending in the n-type Si is also negligible. Thus, the depiction in Fig. 6.5(b) suggests the presence of an additional interface dipole.

This is only one possible interpretation of the data. The observed low potential barrier might also be a measurement artifact. While the potential barrier was measured for multiple samples, systematic errors in sample preparation and the small number of samples tested leave open the possibility of a false measurement. Therefore, a conclusive model for the n-type Si would require additional measurements. Additional insight could, for example, be gained by impedance spectroscopy and capacitance–voltage analysis. This would reveal the built-in voltages of the junctions. Photoconductivity analysis and measurement of the open circuit potential upon external illumination could yield insights into the interaction of the PPIX monolayer with the metal and the semiconductor. Further understanding could also be gained by systematically varying the metal contact material and studying the effect of the metal work function on the hybrid junction. While impedance spectroscopy analysis of the given samples was attempted, the experimental setup did not allow for the acquisition of conclusive data. The lack of electromagnetic shielding and excessive stray capacitances associated with a measurement setup optimized for low-level direct current measurements, rather than alternating current studies, caused noisy and skewed impedance spectra. External illumination is impossible with a liquid Hg contact since frontside illumination is obstructed by the macroscopic thickness of the top contact. While other contact materials are theoretically possible, the requirements to avoid short-circuiting the monolayer are challenging to meet.

7. Chemisorption of Protoporphyrin IX Langmuir–Blodgett Films

Previous chapters were focused on the investigation of electronic interactions between physisorbed monolayers and various substrates. Such hybrid systems are, in general, not well-suited for catalytic applications because the weak adhesion forces enable the possibility of monolayer desorption during operation. This creates an additional deactivation pathway, reducing the longevity of the device. When the catalytic application involves a solvent that the monolayer is soluble in, complete desorption can occur within seconds, thus rendering the device completely unusable. Forming a stable chemical bond between substrate and molecule would prevent this issue. As discussed in Sec. 3.2, SAMs generally rely on chemisorption to establish a self-limiting monolayer structure of well-ordered molecules. Various interface chemistries have been investigated, with the main differences being in the functional groups that bind to the substrate surface. One of the better-explored approaches is silanization, which uses silane functional groups to establish a chemical bond to a hydroxylated oxide surface.

7.1. Proposed Mechanism for Amide Bond Formation

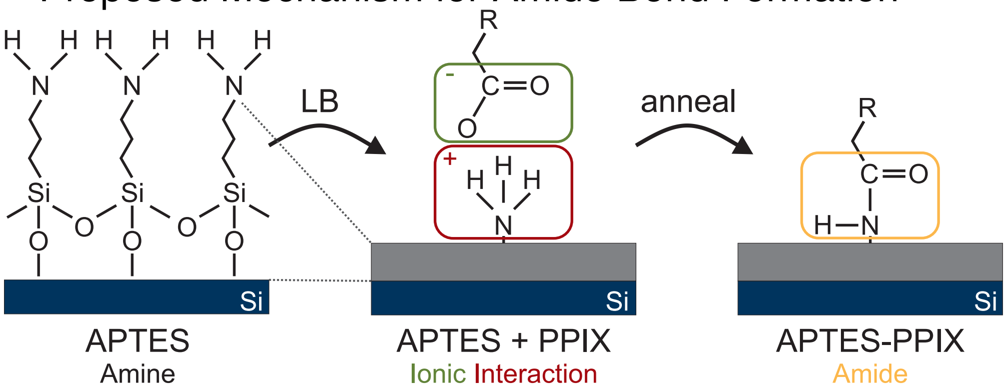

Figure 7.1 Schematic view of the attempted process to achieve covalently attached PPIX on a Si surface. The process is initialized by the formation of an amine termination through functionalization of the surface with APTES. After the introduction of the PPIX through LB deposition, the amine groups should be adjacent to the carboxylic acid functional groups of the PPIX. Amide bond formation can then be initiated via thermal activation.

Using silanization to establish a two-step functionalization approach, this chapter explores a possible method to establish chemisorbed monolayers of PPIX using LB deposition on Si substrates. A diagram of the overall process is shown in Fig. 7.1. This method involves an initial surface functionalization using APTES, which establishes a chemical bond to the surface and offers an amine tail group. A more in-depth description of this functionalization process can be found in Sec. A.3. LB deposition of PPIX onto this amine-terminated surface should result in ionically bound PPIX molecules, since a proton transfer from the carboxyl to the amine functional group is likely [237]. The amine can establish an amide bond with a carboxylic acid group of the PPIX at elevated temperatures by expelling a water molecule, thus covalently bonding the PPIX to the surface. Similar reactions have been performed using APTES monolayers before, but these have employed solution-based functionalization processes adapted from biochemistry, including the introduction of an activated intermediary, such as the formation of an *N*-hydroxysuccinimide (NHS) ester [238]–[240]. Another approach involves initially combining APTES and PPIX and functionalizing the surface through solution-based silanization processes [241].

The formation of an APTES SAM is associated with its own challenges. One of the major ones is the prevention of polymerization, as previously described in Sec. 3.2. The combination of a comparatively short backbone of only three carbon atoms paired with an amine functional group further complicates the formation of a dense layer. The short backbone limits intermolecular van der Waals interactions, which could lead to a lower surface density of APTES molecules. In addition, the amine functional group can interact with the hydroxylated surface. This creates ionic interactions through proton transfer from the hydroxyl group to the amine group, binding the molecule in the opposite orientation to that intended [95], [242]–[244]. Different functionalization techniques have been developed to circumvent these problems, ranging from vapor phase functionalization [96], [245], [246] to various wet chemical methods, either under anhydrous conditions in solvents such as toluene [96], [243], [247], [248] or with a controlled amount of water [96]. Since these methods have been extensively explored in the literature, and since silanization has only been used in an exemplary manner to provide amine groups for the investigation of the subsequent reaction, this work makes use of an established method that provides high-quality monolayers.

So far, an attempt to obtain amide bonds through LB deposition has not been reported in the literature. Therefore, this investigation is intended as a proof of concept to ensure that LB deposition can yield a covalently bound molecular monolayer. While amide bond formation is a well-understood process for molecules in solution, the applicability to the given structure involving two solid-state layers could be limited. In particular, steric hindrance could be a major influencing factor since both reaction partners are fixed in space and are not free to rotate. This proof of concept is likely not the optimal way to achieve chemisorbed monolayers. Other surface chemistries, such as phosphonic acids, could be used to obtain higher resistance to desorption. Additionally, the PPIX carboxylic acid extensions, in addition to the APTES interlayer and the native oxide, add up to a thickness greater than 2 nm, which results in diminished electronic interaction between molecule and semiconductor.

7.2. Annealing of Stacked Layers of (3-Aminopropyl)triethoxysilane and Protoporphyrin IX

The amide bond formation process can be understood in more detail via an *in situ* annealing study. To this end, the chemical bond formation was investigated with high-resolution XPS spectra of the N1s, C1s, O1s, and substrate Si2p transitions.

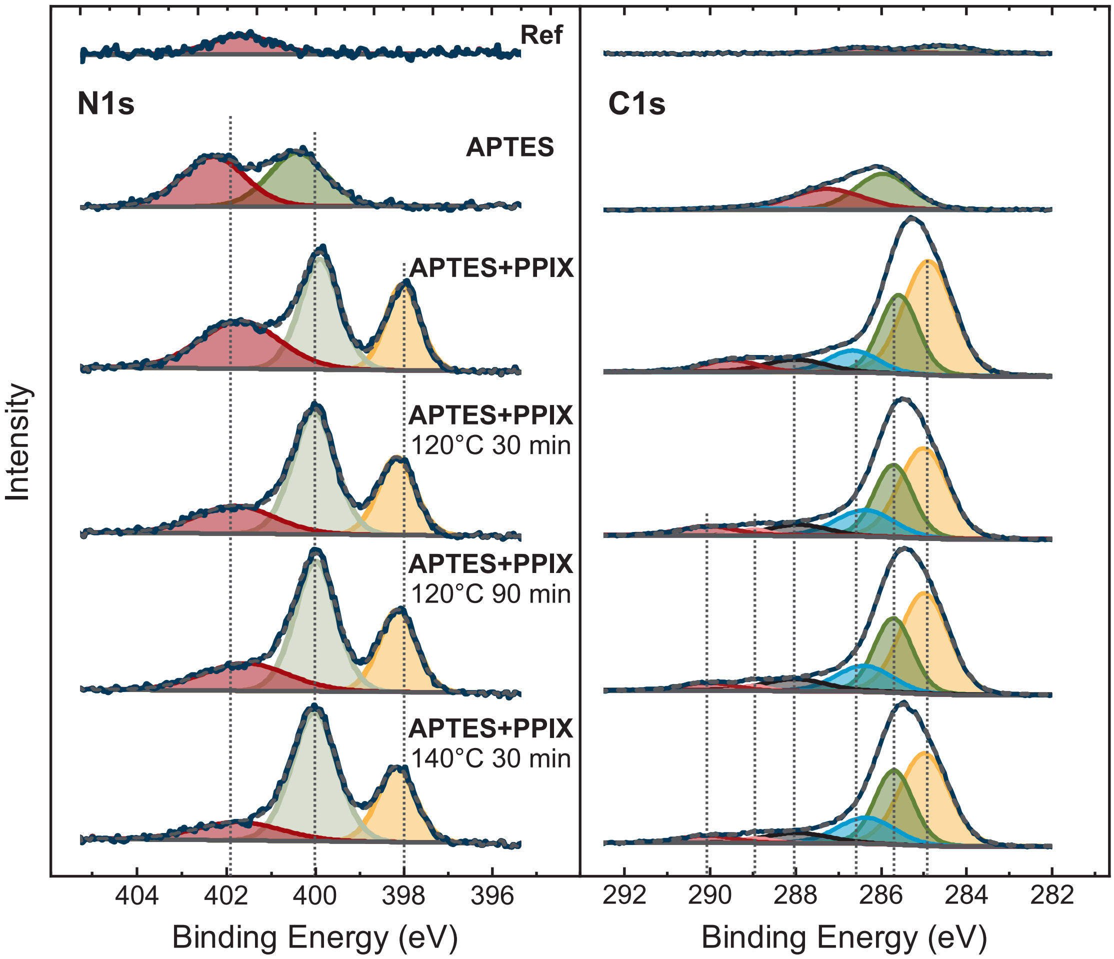

Figure 7.2 High-resolution XPS spectra of the N1s (left) and C1s (right) transitions of the reference surface, an APTES-functionalized surface, and samples of all further intermediate processing steps. While the PPIX features are similar to those discussed for pure PPIX monolayers, the features associated with the N1s transition of APTES indicating partially ionized NH_3^+ molecules (red), as well as the expected amine groups (green), are clear signs of successful amide bond formation.

The high-resolution spectra of the elements intended to establish the chemical bond are displayed in Fig. 7.2. The upper part shows spectra of a reference sample and a sample covered with a monolayer of APTES. The reference sample contained minute amounts of carbon and nitrogen, likely arising from atmospheric contamination. In contrast, the N1s and C1s spectra of the APTES samples show significantly higher intensities. Interestingly, the

N1s peak indicates the presence of two chemical nitrogen species with respective binding energies of 400.6 eV and 402.7 eV and a peak ratio of roughly 1:1. The peak at smaller binding energies likely arises from the expected amine termination [174]. The peak at higher binding energies is commonly observed for APTES-functionalized surfaces and has been reported extensively in the literature. While some studies suggest that this peak corresponds to an APTES molecule in the opposite orientation [249] or occurs due to amide bond formation [250], the vast majority of reports support a partial protonation of the amine group, forming NH_3^+ groups [247], [251]–[255]. The origin of these groups is somewhat uncertain, but it is likely that they are a consequence of interaction with, for example, carboxylic acids from the environment or in solution [256]. It has been shown that the ratio of these two chemical states can be tuned through acid or base treatment after functionalization, which supports this theory of external influence through acidic interaction [257].

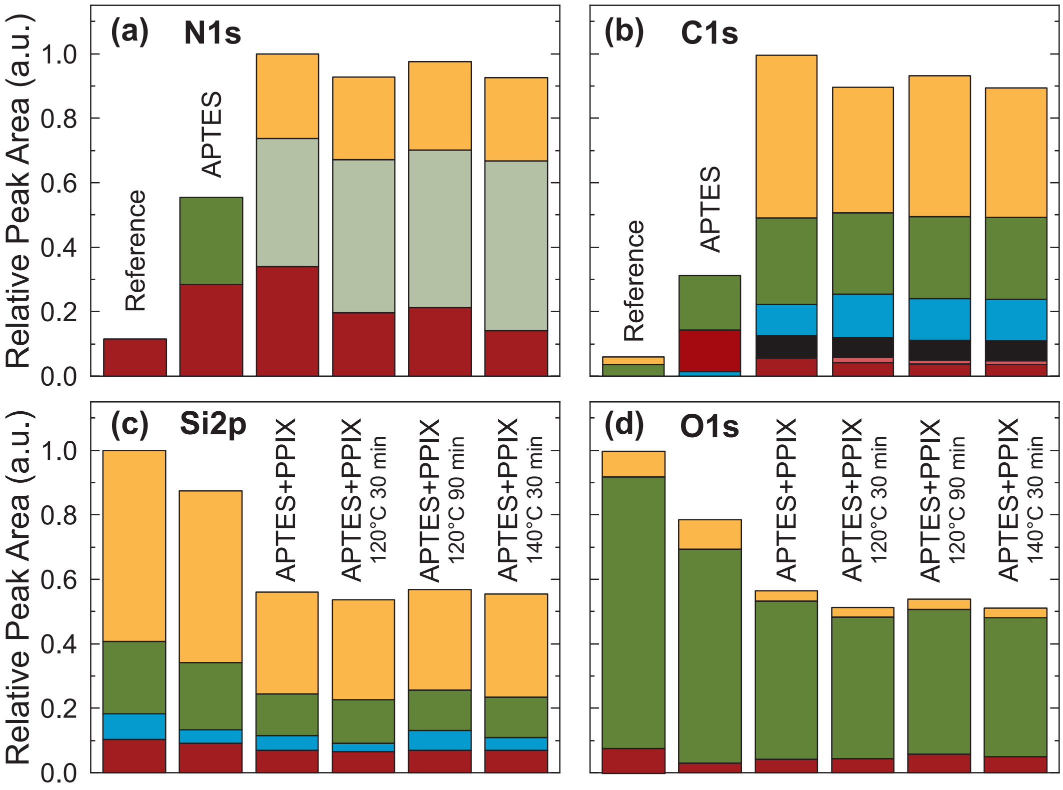

Figure 7.3 Integrated peak areas for all chemical states identified through high-resolution XPS. (a) N1s peak areas indicating a partially charged APTES monolayer after APTES functionalization. Upon introduction of PPIX, the relative amount of ionized amine groups significantly increases but falls again upon annealing. (b) C1s peaks that initially arise in the expected ratio. Upon annealing, an additional peak toward higher binding energies, which could be associated with amide bond formation, emerges. (c) Si2p peaks, which are attenuated by increasingly thick overlayers but do not exhibit any changes in total thickness with annealing. (d) O1s peaks, which exhibit a similar behavior to the Si2p.

Upon the addition of the PPIX overlayer via LB deposition at a surface pressure of 30 mN m^{-1}, the complexity of the spectra increases. For the C1s spectrum, the observed transitions are nearly identical to the previously shown high-resolution spectra of PPIX deposited on bare substrates. The N1s spectrum indicates variations in the spectral shape induced by the pyrrolic and iminic nitrogen from the PPIX. The peak corresponding to pyrrolic nitrogen exhibits a large spectral overlap with the amine peak of the APTES. Therefore, these two species cannot be resolved individually.

Nevertheless, the relative contribution of amine nitrogen can be estimated by analyzing its peak area ratio to the iminic nitrogen transition. The relative peak intensities of the observed chemical species are shown in Fig. 7.3(a). Studies of PPIX on bare substrates suggest a ratio between 1.35:1 and 1.5:1. The ratio observed for the multilayer system is within this range, being 1.45:1, pointing at negligible amounts of signal from the NH_2 peak. In addition, the NH_3^+ signal intensity increased. Without intermolecular interaction, the attenuation from the PPIX overlayer should lead to a signal reduction. Therefore, the observed N1s signal is not a superposition of the individual spectra of APTES and PPIX but indicates that most amine groups on the surface have been protonated and have formed NH_3^+ functional groups. This is a consequence of the interaction with the carboxylic acids from the PPIX, leading to an ionic bond between protonated amine and deprotonated carboxyl groups.

This sample was subsequently annealed *in situ*, meaning that it remained in UHV conditions for the full procedure to prevent any effects arising from contamination. This process was aimed at providing sufficient thermal energy for amide bond formation between the amine and carboxyl groups, which is expected for an elevated temperature of around 150 °C [258], [259]. Initially, the sample was annealed at 120 °C for 30 min, and the XPS analysis was repeated. As shown in Fig. 7.2, the annealing led to significant changes in the N1s spectrum. The intensity of the peak corresponding to the NH_3^+ chemical species is now significantly reduced, while the peak corresponding to, among others, pyrrolic nitrogen has increased in intensity, now exhibiting a ratio close to 2:1 to the iminic nitrogen, as can be seen in Fig. 7.3(a). This suggests a change in the interface chemistry between the amine and carboxyl functional groups. If an amide bond were established, this would also exhibit a significant overlap with the pyrrolic N1s transition, being located at around 399.7 eV. Thus, the decrease in NH_3^+ intensity and the increase of the peak located at around 400 eV is a strong indication of amide bond formation at the interface. Increasing the annealing duration to 90 min or increasing the temperature to 140 °C led to a further increase in the intensity of the 400 eV peak at the expense of the protonated amine signal, suggesting that an increasing number of amide bonds are formed.

The expected density of amine functional groups in an APTES monolayer is, according to the literature, between 2.1 and 4.1 nm^{-2} [260], [261]. The area covered by one PPIX molecule (MMA) in the Langmuir film at the deposition pressure is around 0.5 nm^2, as determined from the surface pressure isotherm described in Sec. 4.1. Thus, the surface density of carboxyl groups is similar to the maximum achievable amine coverage, at 4 nm^{-2}. The stoichiometry at the interface should match, resulting in a complete conversion of NH_3^+ groups to amide bonds. As apparent for the samples annealed for longer and at higher temperatures, the amount of NH_3^+ decreases significantly to about a third of the initial intensity. While extended annealing and elevated temperatures might result in higher reaction yields, a full conversion can likely not be achieved due to steric hindrance resulting from the forced lateral alignment during LB deposition. Further optimization of the reaction conditions to increase the yield is beyond the scope of this work.

In addition to the N1s spectra, the C1s spectra shown in Fig. 7.2 indicate qualitative changes in intensity. These changes are less pronounced since only a relatively small proportion of the carbon atoms inside the molecular structure partake in the interface interactions. To begin with, the C1s high-resolution spectrum of the multilayer structure exhibits slight differences from the spectrum of PPIX deposited on bare Si, especially concerning the position of the peak associated with the carboxyl functional group depicted in red. Compared to PPIX on bare Si, this peak is shifted by 0.4 eV towards lower binding energies, likely due to proton transfer to the amine moieties. After annealing, the spectral features indicate qualitative changes that necessitate the introduction of an additional peak to describe the data fully. Now, the peak associated with the carboxyl groups is split in two, with one shifted towards higher binding energies at 289.7 eV and the other towards lower binding energies at 288.5 eV. The origin of this qualitative change is difficult to determine, especially due to the comparatively low signal intensity, which leads to the fit being highly sensitive to the starting conditions. These features might result from a structural change in the monolayer associated with a rotation of one of the carboxyl groups away from the surface. Still, the limited amount of data means that the origin of these changes cannot be definitively identified. Other than these changes on the high binding energy side, the C1s spectra remain the same upon annealing, as can be seen from the lack of changes in relative peak area in Fig. 7.3(b). This suggests that the monolayers stay on the surface and do not form extended agglomerates upon possibly increased diffusion due to elevated temperatures.

The high-resolution Si2p and O1s spectra of the same samples are depicted in Fig. 7.4. An overview of the relative intensities of the respective peaks can be found in Fig. 7.3(c) and (d). Qualitatively, the spectral shapes of all substrate-related spectra remain unchanged upon the addition of APTES and PPIX. Due to signal attenuation, the overall intensity is reduced. Using the approach described in Sec. A.6.2, the APTES monolayer thickness and the layer thickness of the APTES PPIX multilayer structure were determined to be (0.6 ± 0.2) nm and (2.3 ± 0.3) nm, respectively. While the APTES thickness is in good agreement with the literature [95], the thickness of the combined layer is significantly larger than expected since the PPIX LB layer thickness on a bare substrate was determined to be around 1 nm in Sec. 4.2.

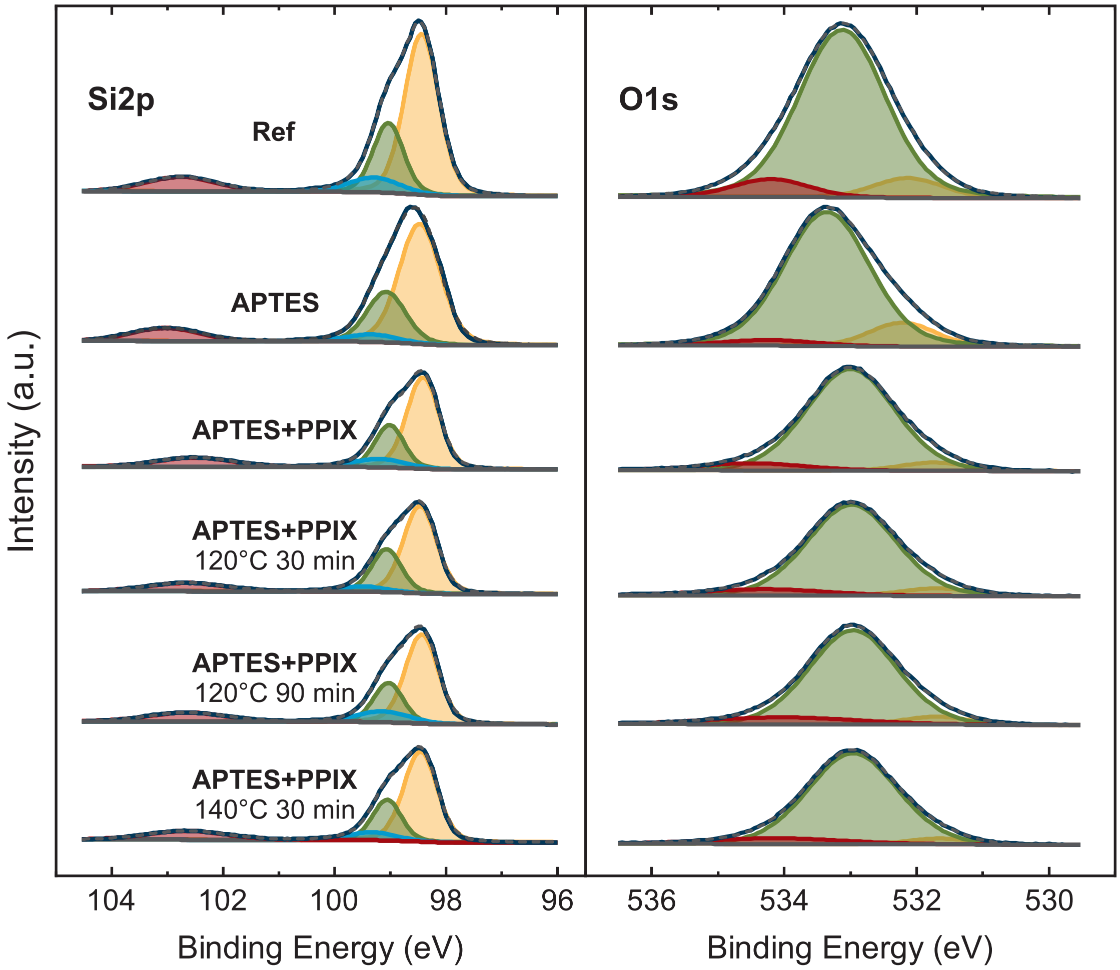

Figure 7.4 High-resolution XPS spectra of Si2p (left) and O1s (right) peaks recorded at intermediate steps of the functionalization process. While the initial molecule application steps result in a significant attenuation of the substrate signal, subsequent annealing steps do not affect the spectra.

Here, the PPIX layer appears to be (1.7 ± 0.4) nm, indicating that the PPIX molecules are oriented fully upright. This change in molecular orientation might be a consequence of proton transfer and subsequent ionic interaction between the molecules, but it could also be a consequence of the significantly higher SCA of an APTES-covered sample surface compared to hydroxylated surfaces. Applying the same analysis to the attenuation of the O1s signal yields a more reasonable total layer thickness of (1.5 ± 0.2) nm, which contradicts the layer thickness found from the Si2p attenuation. This might result from a wrong estimation of the IMFP for the given structure, which has already been observed for the Zn2p signal in Sec. 4.3.

Fig. 7.5 shows AFM micrographs of the APTES monolayer and the multilayer structures before and after UHV annealing at 140 °C for 30 min. The low RMS surface roughness of 150 pm for the sample covered in a SAM of APTES indicates a high-quality monolayer with-

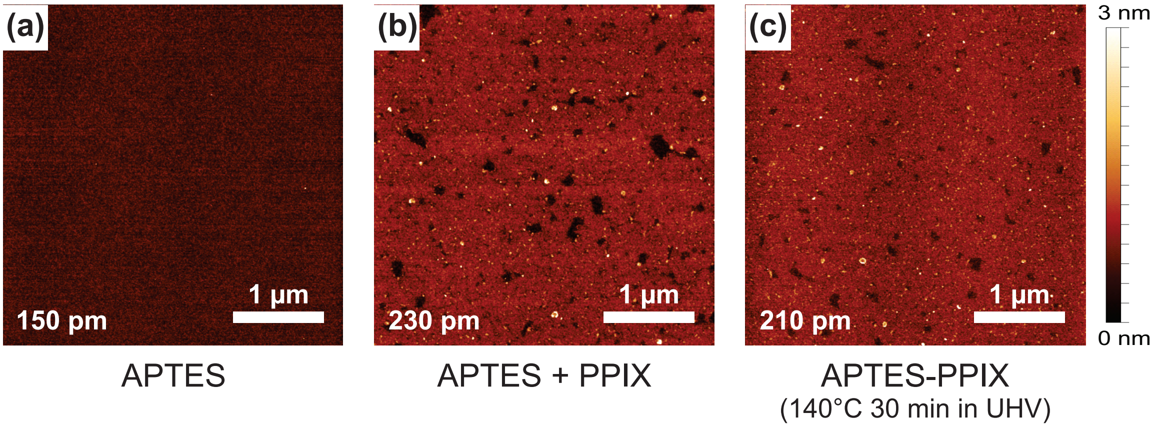

Figure 7.5 AFM micrographs of (a) APTES-functionalized Si, (b) APTES-functionalized Si with a PPIX LB layer deposited at 30 mN m^{-1}, and (c) the same sample as in (b) after annealing in UHV. While the APTES monolayer exhibits a high quality with low surface roughness, the PPIX LB layer in (b) indicates a reduced quality compared to PPIX on a bare Si substrate. This likely arises due to the more hydrophobic amine-terminated surface hindering the transfer process. After annealing, the monolayer does not exhibit significant changes in its morphology.

out any multilayer structures or agglomerations. Despite being deposited at the same surface pressure as the dense monolayers described in Sec. 4.2 at 30 mN m^{-1}, the surface morphology after LB deposition contains holes and a significant amount of agglomerations. These could result from the deposition on an APTES monolayer. The holes likely arise due to the increased SCA of the APTES samples, as described in the next paragraph. This higher SCA impedes transfer from the DI water subphase to the sample and can result in defects in the monolayer. This could also be the cause of the additional agglomerations, but these are just as likely the result of APTES desorption due to the immersion in DI water, which is necessary for LB deposition. Silane SAMs are known to desorb from the surface upon exposure to DI water for hours [96]. The duration of immersion for LB deposition of about 30 min might suffice to desorb parts of the monolayer, which could then readsorb to the surface upon substrate withdrawal from the subphase, resulting in the formation of agglomerates. The holes and agglomerations lead to a slightly increased surface roughness of 230 pm. The surface structure after annealing and XPS analysis remains unchanged, still exhibiting the same agglomerations and holes. This shows that the increased temperature does not lead to excessive diffusion along the surface, as indicated in the XPS analysis.

Interestingly, the holes present in the LB layer do exhibit a thickness significantly lower than the layer thickness determined via XPS of (1.7 ± 0.4) nm, being only 0.9 nm thick. This could indicate a PPIX double layer forming during LB deposition since the thicknesses are roughly split by a factor of two. However, this idea does not agree with the C1s to Si2p ratio, which only increases by a reasonable 16 % over the ratio determined for a PPIX LB layer on hydroxylated Si. In conclusion, a clear explanation for the unexpected attenuation of the Si2p signal cannot be provided with the present data. A more in-depth analysis of the layer thickness using, for example, X-ray reflectivity, ellipsometry, AFM scratching, or NEXAFS spectroscopy could give a more conclusive answer regarding the PPIX orientation in the presented structure.

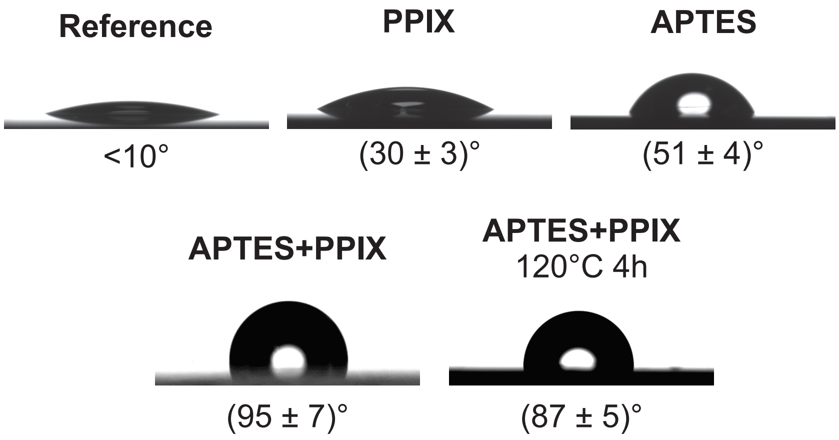

Figure 7.6 SCA of DI water droplets on sample surfaces measured at intermediate steps of the functionalization process. The introduction of APTES between PPIX and Si increased the observed SCA significantly compared to a Si surface only covered with PPIX (top, middle). This is an indication of stronger interaction between the amine and carboxylic acid groups that prevents monolayer desorption.

The SCAs of samples at different steps in the functionalization process are shown in Fig. 7.6. After the surface cleaning and hydroxylation procedure, the SCA is well below 10°. Upon the addition of PPIX, the SCA only increases slightly to around (30 ± 3)°. This low SCA likely arises due to immediate desorption of the PPIX monolayer as the surface gets into contact with the water, so that the resulting increase in SCA is significantly diminished. A surface functionalized with an APTES monolayer exhibits a SCA of (51 ± 4)°, which is expected for an amine-terminated SAM [96]. Subsequent deposition of PPIX on the APTES layer leads to a significant increase in SCA, reaching the hydrophobic regime with a SCA of (95 ± 7)°. Here, the ionic bond formed after proton transfer likely results in higher adhesion forces, which cannot be overcome by the interaction with the DI water. After the annealing procedure for 30 min at 140 °C in UHV, this SCA remains within the margin of error at (87 ± 5)°, again indicating that the structure remains intact during annealing.

In conclusion, *in situ* XPS studies of multilayer structures comprised of APTES SAMs and PPIX LB layers showed that chemisorption of a carboxylic acid LB layer onto an amine-terminated surface is possible by the implementation of a low-temperature annealing process, resulting in monolayers of reasonable quality. This reaction only serves as an example. Many other combinations of functional groups could likely yield similar results. There should also be substantial scope for optimizing the annealing temperature and duration and the LB deposition process to improve the monolayer quality and reaction ratio. In addition, this procedure could be simplified by using a suitable molecule with a hydrophilic functional group known to bond with surface hydroxyl groups, such as phosphonic acids.

8. Time-Resolved *In Situ* FTIR Spectroscopy of Electrochemical Interfaces

Parts of this chapter are published in [262].

Analyzing the catalytic processes occurring on the surface of hybrid devices poses many experimental challenges. To begin with, such devices suffer from stability issues, with many systems degrading over minutes to hours. This creates time pressure, making it difficult to apply common electrochemical analysis techniques such as cyclic voltammetry (CV) and electrochemical impedance spectroscopy. Degradation can be caused by unwanted chemical deactivation pathways or catalyst desorption. In addition, the processes relevant for catalysis occur within a monolayer of molecules on the surface, necessitating surface-sensitive techniques with sub-monolayer sensitivity to accurately determine catalytic processes and deactivation pathways. Lastly, the unoptimized performance of such catalytic devices makes evaluation of the product challenging since the amount of material produced is often below the detection limit of commonly used analysis methods, such as gas chromatography. This is especially true for the well-ordered sample structures presented in this work since a significant amount of gas or electrolyte is needed in an experimental setup housing a limited amount of molecules due to the comparatively low surface-to-volume ratio. Nevertheless, these well-ordered systems allow for a significantly more controlled environment compared to, for example, a colloidal system, making them especially valuable for basic research.

These factors all create challenges for experimental optimization, which have been largely circumvented in this work so far by analyzing the *ex situ* properties of the hybrid structures. Nevertheless, applying the knowledge gained to catalysis is necessary to prove the validity or find possible mitigating influences in process environments. To this end, the method of *in situ* attenuated total reflection Fourier transform infrared (ATR-FTIR) spectroscopy was chosen to solve many of the aforementioned experimental challenges because it offers sub-monolayer sensitivity in an *in situ* environment, probing the vibrational features of the catalyst, educt, and product. This technique could, therefore, deliver valuable information on catalytic processes occurring at the interface, enabling further insights by cross-referencing with the previously acquired knowledge on energy level alignment and transfer processes. Compared to other vibrational spectroscopy geometries, the ATR measurement geometry offers inherent surface sensitivity, ease of use, and the ability to circumvent any issue that might arise due to the strong infrared (IR) absorption of the electrolytes involved. Unfortunately, the setup, optimization, and validation of this measurement technique were associated with many challenges, delaying the process and preventing the execution of *in situ* analysis of hybrid devices within the available timeframe. Nevertheless, the optimization and validation led to significant scientific insights, which are highlighted in this chapter.

8.1. Attenuated Total Reflection Surface-Enhanced Infrared Absorption Spectroscopy for *In Situ* Investigations of Hybrid Catalysts

In situ ATR-FTIR spectroscopy is an emerging technique mainly used to study processes in the near-surface regions of heterogeneous catalysts. It offers sensitivity to molecular vibrations, which enables the identification of specific chemical bonds at the interface. This is especially relevant for the observation of catalytic processes involving organic molecules, such as CO_2 reduction catalysis [263], [264]. Such measurements can be performed by either placing an internal reflective element (IRE) closely above the surface under investigation (the Otto configuration [265]) or by using the IRE itself as the substrate (the Kretschmann configuration [266]). Aside from differences in the magnitude and origin of signal enhancement, the Otto configuration offers higher flexibility due to the separation of the IRE structure and the surface under investigation. This comes at the cost of geometrical influences arising due to the narrow gap (around 1 µm) between the IRE and the sample surface, which can have a significant influence on, for example, mass transport. This leads to deviations between the *in situ* conditions and the true operating conditions.

Therefore, recent developments and setups are mainly based on the Kretschmann configuration. Here, the IRE has the dual purpose of serving as a light-guiding crystal for the IR probing light and as the working electrode (WE) under investigation. This poses a unique engineering challenge because the materials chosen and the layer structure have to provide sufficient transparency in the desired mid-IR wavelength range while maintaining a surface structure that is representative of the device under investigation. In addition, the inherent surface sensitivity of the ATR geometry often does not provide a strong enough signal to study the generally low density of catalytic sites on a heterogeneous catalyst, thus requiring further surface enhancement. This can be achieved by introducing nanostructured, metallic systems, which provide local field enhancement and plasmonic enhancement [267]. The combination of such surface-enhancing structures with an ATR geometry is called ATR surface-enhanced infrared reflection-absorption (ATR-SEIRAS) and provides a strong increase in signal intensity within the immediate vicinity (<10 nm) of the nanostructure [267].

Due to this complexity and the necessity of including metallic nanostructures in the surface morphology, most studies so far have investigated metallic surfaces that were modified to provide the desired enhancement. By far the most common surfaces studied are Au thin films [33], [34], [268], [269]. These structures can be deposited with thicknesses below 50 nm to provide sufficient transmission in the mid-IR range and additionally exhibit a high chemical stability due to the chemical inertness of Au.

These thin films are usually deposited onto Si or germanium (Ge) IREs using various techniques and surface conditioning treatments to provide a desirable nanostructure with the highest achievable surface enhancement. Commonly used techniques include the electroless deposition of Au nanoparticles [33], [36], [270], [271], electrodeposition [34], colloidal self-assembly [272], and PVD [268], [273], [274]. These techniques are sometimes accompanied by electrochemical surface roughening [269], [275]. While Au is the element most commonly used to synthesize ATR-SEIRAS surfaces, other materials, such as a variety of platinum group metals [276], [277], silver [278], and copper [279] have been used successfully.

Unfortunately, all these materials exhibit a low adhesion to Si. This leads to sample destruction since the metallic thin film can easily delaminate from the IRE, especially in an aqueous environment. The delamination is difficult to reproduce and occurs spontaneously, possibly during measurement but certainly when the sample is removed from the electrochemical measurement cell. This can lead to imprecise measurement results since the delamination cannot be immediately recognized and might cause variations in the measurements, including in the observed enhancement. The sample, therefore, is single-use at best and has a high probability of failing prematurely, requiring a significant amount of labor and necessitating a high sample throughput. This, together with enhancement variations naturally caused by the difficult-to-reproduce synthesis methods, makes analysis with this sample tedious and impossible to perform under more challenging conditions.

A variety of alternatives have been developed to alleviate this issue. In the semiconductor industry, the predominant solution is the introduction of a chromium or titanium sticking layer between the Si and the Au. In our studies, a titanium sticking layer led to a significant signal reduction, completely negating the surface-enhancing effect of nanostructuring and, thus, defeating the purpose of implementing the metallic layer. Similar results have been reported by Andvaag *et al.* [34], while other groups have reported the successful use of such a thin film structure [275].

Transparent conductive oxides (TCOs) have also been introduced as adhesion-promoting layers. These additionally provide a conductive layer on the IRE surface, which enables electrodeposition techniques to be used to deposit metal nanostructures on the surface [34], [280], [281]. Electrodeposition could also be enabled through degenerate doping of the Si IRE, but this would also induce a significantly higher free carrier absorption, reducing the IR transmission. Nevertheless, a thin surface doping would likely provide the possibility of electrodeposition on the Si IRE; however, it would not solve the adhesion problems. TCOs can provide solutions to both problems while maintaining significant IR transmissivity, but they also exhibit limited chemical stability. They can easily degrade under the application of an external potential in electrochemical environments, thus reintroducing a degradation pathway that was circumvented previously by introducing inert metals. The nanostructured morphology achieved through the specific, pulsed electrodeposition technique necessary for sufficient surface enhancement exhibits significant porosity and therefore enables contact between the TCO and the electrolyte. This limits the accessible surface potential range to roughly $-0.3\,V_{RHE}$ to $+2.7\,V_{RHE}$ for the most commonly used TCOs, indium tin oxide (ITO), indium zinc oxide (IZO), and fluorine-doped tin oxide (FTO) [282]–[284].

This limitation led us to the development of an alternative surface structure to improve the adhesion of a Au layer on the substrate surface. The Si IRE is nanostructured using a black Si etch before the deposition of the Au nanoparticle film. These nanostructure etching methods can be performed through directional reactive ion etching or a wet chemical process involving nanoparticle catalysts. These were originally developed for Si solar cells, in which the resulting needle-like surface structure effectively reduces the surface reflectivity and can, thus, improve the conversion efficiency [35], [285], [286]. This additional nanostructure enhances adhesion through closer contact with the metal nanoparticles.

One key performance indicator in the analysis of such surface structures is the surface enhancement, which translates to the ability of the system to detect minute changes in surface properties. Since the number of active sites on a surface is generally hard to determine, it is difficult to define surface enhancement through an *in situ* catalytic process. Therefore, benchmarking techniques involving the adsorption and desorption of monolayers of molecules such as 4-dimethylaminopyridine [270], [287] or MOP [36] have been established as a standard to compare the surface enhancement of different surface structures. These molecules can be adsorbed or desorbed from a Au surface via a change in potential applied to the WE, and their adsorption to the surface is self-limiting. Thus, the signal generated by a monolayer of molecules can be accurately determined and compared across various sample morphologies.

In the following sections, the signal enhancement of the newly developed black Si-based nanostructures is compared to established Au thin film structures. In addition, time-resolved FTIR measurements are implemented in this *in situ* technique.

8.2. Time-Resolved *In Situ* FTIR Spectroscopy of Electrochemical Systems

While steady-state *in situ* FTIR of catalytic surfaces can provide some insight into the reaction mechanisms at the surface, time-resolved studies offer the possibility of providing more detailed information. Such studies could be performed to investigate the response of a catalytic system to a pulsed potential or the reaction kinetics under external illumination for photocatalytically active systems. Analyzing the time evolution of the reaction mechanisms can help to identify reaction intermediates and, in particular, rate-limiting steps in reaction cycles. Addressing these rate-limiting steps can greatly improve the TOF of the catalytic device. Thus, it is imperative to identify and understand the particular processes involved in a full catalytic cycle.

Time-resolved IR spectroscopy can be performed using various methods, each with advantages and disadvantages. The most straightforward method is to acquire spectra in rapid succession. The achievable time resolution is given by the mirror speed of the interferometer and so is mechanically limited to above 10 ms [288].

Faster acquisition therefore requires alternative methods to achieve a better time resolution. One method is based on a completely redesigned source, relying on two mid-IR frequency comb lasers with a known difference in frequency spacing that produces heterodyne beating at exactly that frequency difference. By choosing this beating to be in the MHz frequency range, it can be resolved sequentially using a high-frequency detector and, thus, can be used to deconvolute the spectrum. This system is entirely based on solid-state devices and so can acquire spectra significantly faster, with a time resolution of around 1 µs. The major disadvantage of this technique is the limited spectral bandwidth due to the frequency comb laser source. This constrains the overall measurement bandwidth to around 60 cm^{-1} per source and, thus, can require frequently changing the source and repeating the measurement to cover a wider spectral range [289], [290]. Therefore, this measurement technique was not implemented in this work.

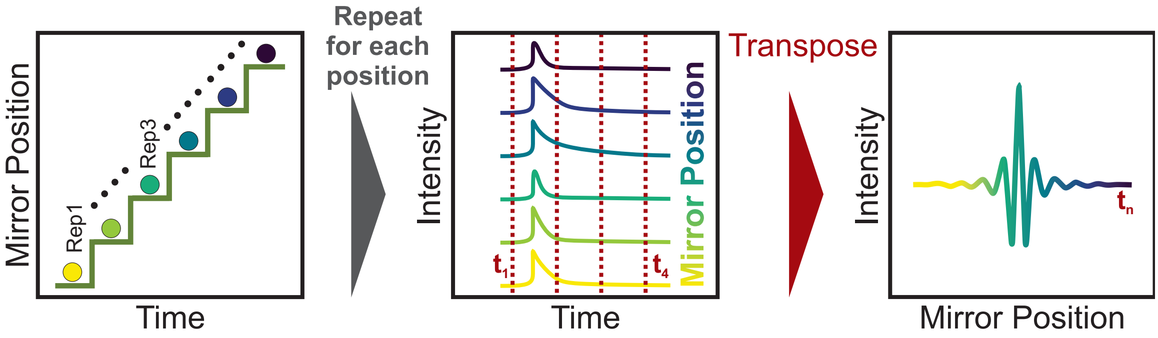

Figure 8.1 Schematic depiction of the step scan method, which allows the acquisition of FTIR spectra at a nanosecond resolution, without the need for fast interferometer movement, by stepping the mirror position and acquiring the temporal evolution of the interferogram at a specific point before repeating the experiment at the next interferogram position.

Lastly, a better time resolution could also be achieved with a standard FTIR device by recording in a stepwise manner. In this method, the interferometer position is fixed during a repetition of the experiment, as depicted on the left-hand side of Fig. 8.1. The time evolution of the signal at the interferogram position corresponding to this fixed mirror position is measured using a high-speed detector and read-out electronics, as shown in the center of Fig. 8.1. After the measurement is finished for this specific mirror position, the mirror is moved to the next position and the measurement is repeated. Therefore, This method requires at least as many repetitions of the experiment as there are interferogram points to be recorded, which could easily reach multiple thousands. After the time evolution at the last interferogram point has been recorded, a full dataset containing the time evolution of the IR intensity at each mirror position has been acquired. The dataset is then transposed to form a complete interferogram for each measurement time, as shown on the right-hand side of Fig. 8.1.

Due to this method solely relying on the speed of the detector and read-out electronics, the time resolution can be extended down to the nanosecond range. The major drawback is the time needed for the large number of repetitions, often resulting in a measurement time of multiple hours. The system must remain unchanged during this period. Any change in the sample that causes differences in the IR absorption properties due to, for example, delamination, would render the dataset useless. This is because the method groups points from the very beginning of the measurement to the last measurement in every interferogram. The measurement points can be recorded hours apart in real time, but the Fourier transformation only yields reliable spectra if all interferogram points have been recorded under identical conditions [288].

In the experiments discussed within this chapter, data acquisition was performed by combining this stepwise technique with the rapid mirror movement technique discussed previously. Within the framework of the measurement device used, these techniques are called step scan and rapid scan, respectively.

Time-resolved FTIR measurements have so far mostly been performed on longer timescales over the course of seconds to minutes. Lower-timescale studies in the range of milliseconds or faster are significantly harder to find and mainly rely on IREs with electroless or PVD metallic thin films [291]–[293]. While these might suffice for rapid scan measurements, their questionable stability due to the low adhesion renders them unsuitable for step scan applications. Instead, the aforementioned ITO interlayer method has been employed, resulting in successful measurements in the low millisecond range [294]. Approaching these timescales, a new limitation emerges for electrochemical systems due to their RC time constant $\tau = R{\cdot}C$. This is an inherent property of an electrochemical cell, governed by the electronic properties, including the resistance of all current-passing components R and the capacitance of the electrode surfaces C. The major factors influencing the RC time constant are the resistance of the electrolyte, the resistance of the WE sample, and the capacitance at the interface between the WE and electrolyte [295].

Using the ITO-based sample structure, initial attempts to reduce the RC time constant were made by Morhart *et al.* [295] by miniaturizing the WE area. The authors argue that a smaller electrode area reduces the capacitance and, thus, leads to a reduced RC time constant. While this is theoretically correct, the practical implementation of this idea also leads to a significantly increased series resistance, thus partially negating the desired effect. In addition, a miniaturized WE induces additional measurement challenges with standard laboratory devices since the spot size of the IR beam becomes substantially too large for the sample. Therefore, this work focuses on lowering the series resistance to reduce the RC time constant and, thus, improve the time resolution of this *in situ* technique. Fortunately, the newly developed sample exhibits superior conductivity, especially compared to the ITO-based samples, thus providing similar capabilities without the need for small electrode surfaces.

8.3. Nanostructured Gold Films for Surface Enhancement

As discussed in the previous sections, a variety of thin film deposition techniques and morphologies have been developed over the years, all of which come with advantages and disadvantages. The newly developed black Si-based structure is intended to alleviate some of the difficulties experienced with existing approaches, with an emphasis on improving adhesion properties and transverse conductivity.

The intention for these films is to serve as WEs in a home-built *in situ* spectroscopy setup, which is schematically depicted in Fig. 8.2(a). The main component is a three-electrode electrochemical cell. This cell has a volume of around 4 mL and is designed to allow light to reach the sample from both the top and the bottom. The bottom pathway is intended for IR spectroscopy in ATR geometry, which is enabled by a wafer-based IRE (Irubis). The top window was not used in this work but could facilitate the excitation of a semiconductor WE through, for example, a pulsed laser. A more in-depth description of the setup can be found in Sec. A.11.

With the aforementioned requirements in mind, two variants of a black Si surface morphology were synthesized and compared to established morphologies. Electroless-deposited Au nanoparticles and electrodeposited Au on an ITO thin film were chosen as benchmark systems to make comparisons of the morphology and surface enhancement. Schematic depictions of these surface structures can be found in Fig. 8.2(b). In the first variant of the black Si-based structure, the metal thin film consists solely of an electroless-deposited thin film. The other variant adds a thin Au layer on top of this structure, which is evaporated via PVD to enhance the transverse conductivity and possibly increase adhesion. While the nanoparticles and their distribution on the surface are depicted similarly in the diagram for all synthesized structures, this does not inherently have to be the case.

The different deposition methods and surface structures of the samples can lead to different nanoparticle shapes and sizes and can influence the arrangement of particles on the surface. Therefore, morphological analysis was performed on all structures using scanning electron microscopy (SEM) and AFM. The resulting micrographs are shown in Fig. 8.3. To enhance readability, the samples will henceforth be referred to by abbreviated names. The sample structure A, depicted in Fig. 8.2(b) will from now on be referred to as flat Si gold (FSG), B as ITO layer gold (ILG), C as black Si gold (BSG), and D as black Si gold evaporated (BSGE).

As is clearly visible in the SEM images in Fig. 8.3(a)–(d), the Au deposition processes successfully resulted in Au nanostructures on the respective surfaces. The two surfaces created

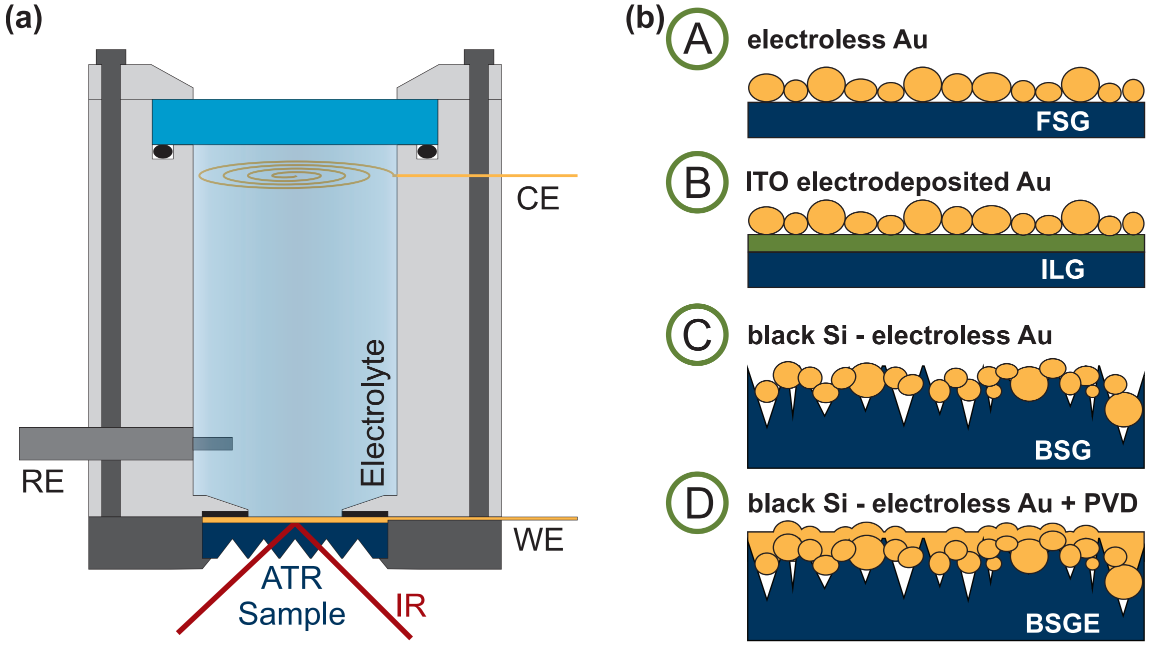

Figure 8.2 (a) Schematic depiction of the electrochemical cell used for the experiments presented in Sec. 8.3 and Sec. 8.4. The ATR IRE serves the secondary purpose of functioning as the WE of an electrochemical cell, allowing surface-sensitive measurements of the WE surface and its direct vicinity. (b) Surface structures investigated with the aim of enhancing the surface sensitivity of the IRE by plasmonic and lightning rod effects through the introduction of Au nanostructures. FSG: Si samples with electroless-deposited Au. ILG: Si samples with a sputtered ITO layer and electrodeposited Au. BSG: Black silicon-etched Si samples with electroless-deposited Au. BSGE: Black silicon-etched Si samples with electroless-deposited Au and subsequent evaporation of Au.

by electroless deposition (FSG and BSG), shown in Fig. 8.3(a) and (c), share the strongest similarities, consisting of particles with an average size of (28 ± 5) nm, as estimated by analyzing 40 randomly chosen particles from each micrograph. This deposition method led to a porous layer, leaving a relatively large surface area of the substrate exposed. For FSG, around 9 % of the substrate surface is exposed. For BSG, this value is significantly higher, with 40 % of the projected surface area showing bare substrate. This difference likely arises due to a more three-dimensional structure of the surface, resulting in stacked nanoparticles. In the case of the FSG sample, the nanoparticles are arranged side-by-side, while the arrangement for the BSG sample exhibits significantly more overlap and stacking. Additionally, the electroless-deposited samples exhibit irregularly occurring larger agglomerates, as can be seen in Fig. B.12. These agglomerates may be leftover Au particles from the prior black Si etching process, as they were present before the electroless deposition was performed.

Compared to the electroless-deposited surfaces, the electrodeposition on ITO yields a significantly different surface morphology, as can be seen in Fig. 8.3(b). While the average size of the smaller particles is comparable, being around (25 ± 4) nm, larger particles also appear

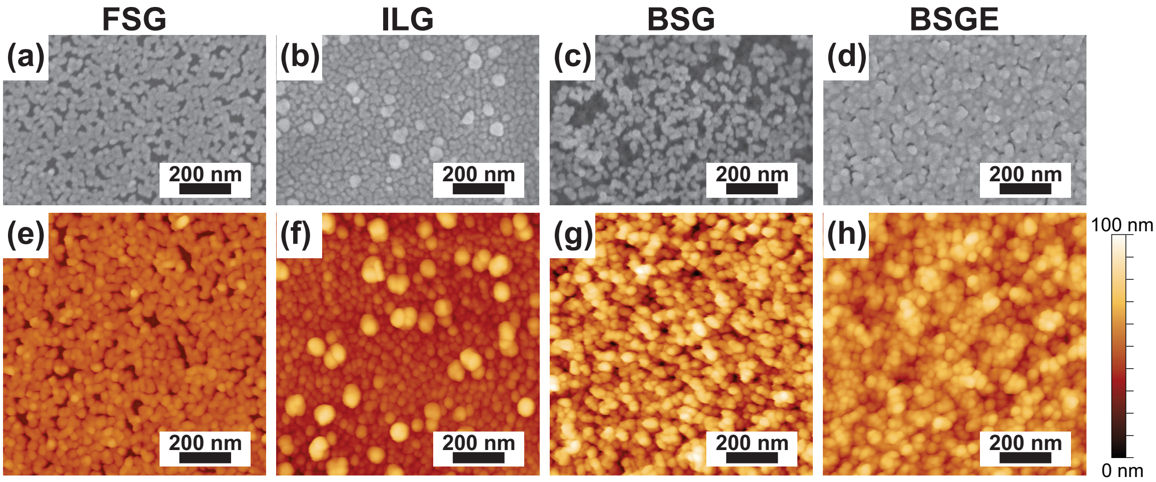

Figure 8.3 SEM (top) and AFM (bottom) micrographs of the structures under investigation: the reference structures (a) and (e) FSG (b) and (f) ILG, and the two newly developed structures (c) and (g) BSG and (d) and (h) BSGE. While all samples exhibit Au nanostructures on comparable scales, the individual coverage and relative orientation of nanoparticles differ between synthesis methods.

on the surface. These have more than twice the diameter around (57 ± 8) nm, and appear at a significantly lower frequency. The amount of exposed substrate is around 20 %, with the nanoparticles appearing to be significantly less interconnected than on the other surfaces. For ILG, the nanoparticles are arranged in smaller agglomerates of a few particles separated by a border of the exposed substrate, yielding an overall more disconnected Au layer morphology. In comparison to the other samples, the electrodeposition process used for the ILG samples requires establishing contact with the front surface in an electrochemical cell, therefore inevitably yielding regions of the surface that have not been in contact with the electrolyte. These surface areas are not covered by a Au thin film.

The final synthesized sample structure is based on BSG, with the addition by PVD of a 20 nm Au layer after electroless deposition. An exemplary BSGE sample is shown in Fig. 8.3(d) and exhibits a significant reduction of the exposed surface area to around 2.5 %. The Au thin film appears significantly more homogeneous and exhibits more interconnectivity of the individual nanostructures. Nevertheless, the traces of the Au nanoparticles underneath remain visible.

Unlike the SEM analysis, AFM allows the quantification of height information, thus facilitating the analysis of surface roughness and total surface area. AFM micrographs of all four samples are depicted in Fig. 8.3(e)–(h). The additional features from the etched nanostructures and the lack of contrast between the Au and Si substrates affect the appearance of the micrographs of the black Si samples (BSG and BSGE). While the AFM probes used have a comparatively small tip radius of 2 nm and a small front plane half angle of 10°, they still have a significant impact on the micrographs due to the exceptionally sharp features imaged.

Compared to polished Si, which has an RMS roughness of 0.15 nm, the FSG sample exhibits a significantly increased roughness of 6.2 nm due to the deposited nanoparticles. These also lead to an increased overall surface area, which exceeds the geometric area under investigation by 22 %. Due to the side-by-side arrangement of the nanoparticles, their height could be determined to be (25 ± 3) nm, which is within the margin of error of the previously determined horizontal particle diameter, indicating that the aspect ratio of the deposited nanoparticles is close to one in all dimensions. The larger nanoparticles are visible in the AFM micrograph of the ILG sample. For these, the aspect ratio also appeared to be close to one across all dimensions, making them comparable in shape but significantly larger. The RMS roughness of the entire surface was determined to be 9.3 nm, but excluding the larger structures yielded a significantly lower roughness of 3.3 nm for the surface in between. The surface area is 30 % or 16.5 % larger than the projected area, including or excluding the larger particles, respectively. The more discontinuous surface morphology of the smaller nanoparticles could not be identified in the AFM micrograph, likely because the extended dimensions of the AFM tip limited its resolution for these high aspect ratio features.

The aspect ratio of the BSG-based samples also makes it challenging to conduct an AFM analysis and identify their features. Nevertheless, statistical analysis can be performed for both sample structures. The RMS roughness was determined to be 13.3 nm and 9.1 nm for the BSG and BSGE samples, respectively, thus indicating that the black Si etch does yield a significantly rougher surface structure. PVD reduces the roughness due to its anisotropic coating behavior, which results in a faster deposition rate in the trenches of the surface compared to the sidewalls, thus reducing the height of the structures. The large increase in roughness is also accompanied by a surface area significantly larger than the geometric area, with a 70 % increase for the BSG surface and a 28 % increase for the BSGE surface. The almost twofold increase in the effective area of the BSG sample could be the cause of the comparatively low relative surface coverage determined from the SEM micrographs. Since an identical electroless deposition process was used to create the FSG and BSG samples, the reaction rate could have been a limiting factor in the case of the significantly larger BSG sample, thus possibly requiring a longer deposition time for the BSG sample to achieve a similar coverage.

In addition to the morphological analysis, the samples were compared regarding their surface-enhancing capabilities in the context of monolayer sensitivity for *in situ* electrochemical spectroscopy. To this end, the samples were mounted in the previously described electrochemical cell filled with an electrolyte containing 100 mM of the marker molecule MOP. Through the application of an external potential, a MOP monolayer was adsorbed or desorbed from the sample surface. In particular, the potentials applied to the WE were $-0.9\,\mathrm{V_{Ag/AgCl}}$ to achieve full MOP adsorption and $0.3\,\mathrm{V_{Ag/AgCl}}$ for complete desorption. Comparing the spectra of these two measurement conditions yields a difference spectrum corresponding

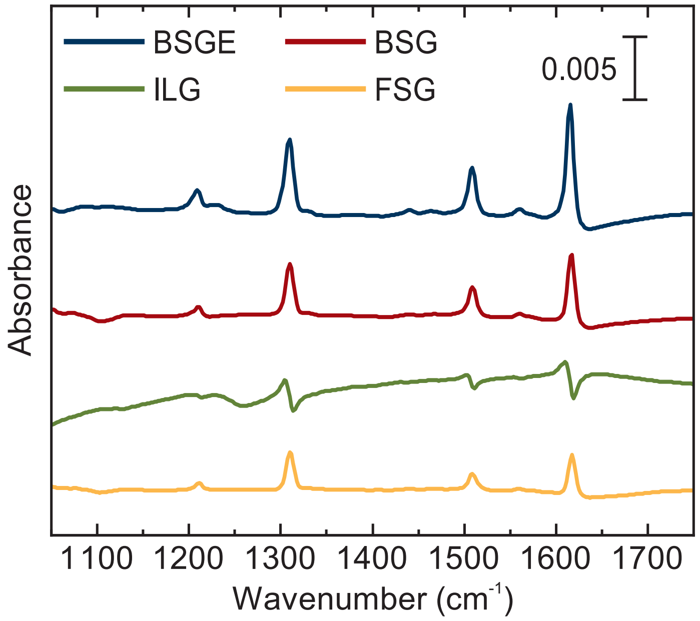

Figure 8.4 Steady-state IR spectra of a monolayer of MOP for all samples under investigation. Significant differences from the liquid MOP measurement (Fig. 8.5) arise due to the directional orientation of the MOP on the surface and the present selection rules preventing some vibrational transitions.

to the absorption of the MOP molecule. The fingerprint regions of the spectra recorded with all four samples are shown in Fig. 8.4, indicating six medium-to-strong characteristic peaks associated with a MOP molecule. These peaks have previously been ascribed to a MOP monolayer on a polycrystalline Au surface [34]. The signals at 1615 cm^{-1}, 1562 cm^{-1}, 1509 cm^{-1}, and 1211 cm^{-1} can be attributed to the υ_{8a}, υ_{8b}, υ_{19a}, and υ_{9a} ring vibrations, respectively [280]. The asymmetric C–O–C stretching vibration of the methyl group is responsible for the 1308 cm^{-1} signal. The signal at 1030 cm^{-1} can be attributed to an in-plane ring breathing vibration υ_{12} of the MOP [280].

By evaluating the dipole moments of these transitions and comparing them with the peak intensity, a qualitative estimation of the orientation of the MOP molecules on the surface can be made. This is possible because the SEIRAS effect only works with p-polarized light and, thus, can only interact with transition dipole moments normal to the Au surface. While a horizontal orientation of MOP on Au has previously been observed and attributed to π-orbital interactions on Au nanoparticles [296], other studies have found a vertical orientation when it is adsorbed through an applied potential [36]. Here, the molecules are expected to coordinate to the surface via a σ-type bond between the Au surface and the nonbinding electron pair of the ring nitrogen [36].

Based on results obtained by Quirk *et al.* [36], the transition dipole moments of the three most intense signals at 1615 cm^{-1}, 1509 cm^{-1}, and 1308 cm^{-1} share a small angle (<25°) with the principal molecular axis, while the band at 1562 cm^{-1} is significantly off-axis. Comparison to

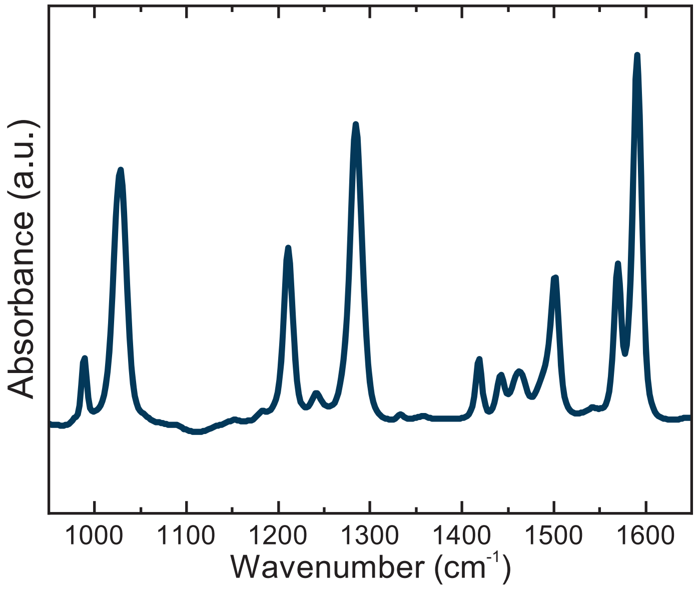

Figure 8.5 Reference IR absorption spectrum of liquid MOP on a pristine IRE exhibiting all vibrational modes, regardless of orientation, due to the homogeneous distribution of orientations in the liquid.

the reference IR spectrum depicted in Fig. 8.5 of randomly oriented, pure MOP clearly shows that these peaks maintain a high intensity in monolayer conformation, while others appear significantly attenuated. This insight, combined with theoretical results from Quirk *et al.* [36] confirms a vertical orientation for the MOP molecules on the surface of all morphologies investigated in the presented experiments. The small amplitude of the out-of-plane methyl bands in the 1450 cm^{-1} region further supports this conclusion. The relative ratios between the signal amplitudes of the three most prominent MOP peaks at 1615 cm^{-1}, 1509 cm^{-1}, and 1308 cm^{-1} remain comparable for all sample structures under investigation. This indicates a very similar MOP orientation in the adsorbed monolayer on the SEIRAS-active areas of all four samples.

The negative feature centered around 1650 cm^{-1} exhibited by the electroless Au samples indicates that the adsorption of the MOP monolayer to the Au surface displaces water molecules previously present nearby, since the 1650 cm^{-1} signal corresponds to the H_2O scissoring vibrational mode. This feature is not visible for the ILG sample, likely due to a comparatively strong background. The FSG and BSG samples also exhibit a small band at 1100 cm^{-1}, which is in the Si–O–Si asymmetric stretching vibration region. Therefore, this feature might occur due to slight changes in the surface oxide thickness. The higher relative coverage in the case of ILG and BSGE samples significantly reduces the interaction of the Si surface with the electrolyte, thus likely reducing the electrochemical oxidation.

The spectra of the four samples share many similarities but exhibit differences in signal intensity and peak shape. The ILG sample shows the most variation in peak and background shape. The broad background is most likely a consequence of broad plasmonic resonances induced by the IR light in the supporting ITO layer [297]. The asymmetry in the peaks could be, for example, the result of nanostructuring through the electrodeposition process [34], [297]. This explanation was initially proposed by Agrawal *et al.* [297], who observed similar peak shapes and postulated a potential coupling between localized plasmon resonances of ITO nanocrystals and the molecular vibrations. This nanostructuring is hard to investigate since the ITO layer is largely buried underneath the electrodeposited Au layer. Still, a partial dissolution and restructuring of the surface is not unlikely, considering the limited electrochemical stability of TCOs. Another possible explanation is based on effective medium considerations and correlating asymmetric peak shapes with the extent of percolation of the metal particles on the sample surface. The Au nanostructure on the ILG samples shows qualitative differences from the structure of the electroless samples, as discussed above. In a recent work by Andvaag *et al.* [298], a change in the interfacial reflectivity partially explains the derivative-like peak shapes depending on the percolation of the electrodeposited Au particles on the ITO layer. The percolation threshold is given as a critical point for the appearance of these peak shapes. Its intensity is comparable to the other well-established FSG morphology.

Both samples based on the black Si-etched Si IRE share symmetrical peak shapes and a flat spectral background with the FSG sample. While the BSGE sample exhibits a closed Au layer, the amount of percolation for the BSG sample is difficult to quantify accurately. AFM and SEM analysis suggest an interconnected Au nanoparticle system and, therefore, hint at the Au structures being above the percolation threshold for this sample type. As described by Andvaag *et al.* [298], SEIRAS films with a continuous metal layer exhibit significantly smaller peak asymmetries than TCO support layer samples even at similar percolation. Therefore, the conclusion is that all samples aside the ILG sample, in this context, more closely resemble a continuous Au layer than a percolated particle film if the origin of asymmetric peak shapes indeed originates from these properties.

The black Si-based samples exhibited larger signal amplitudes than the SEIRAS samples prepared according to literature methods. Signal-to-noise ratios (SNRs) were calculated as the mean amplitudes of the five most prominent MOP peaks compared to the noise in the region between 1750 cm^{-1} and 2000 cm^{-1}. The signal amplitudes were determined after subtracting a linear background in the vicinity of the peak. Since determining the signal strength for the ILG sample is more challenging due to its more complex shape, the peak-to-peak value was used as the amplitude. The electroless Au-treated geometries share similar SNRs of 258 for the FSG sample and 242 for the BSG sample. The ILG sample exhibited the worst SNR at 194. With an SNR of 310, the BSGE sample performed the best out of the four tested sample geometries. Nevertheless, the enhancement is subject to large sample-to-sample variations that likely arise due to the limited reproducibility of the fabrication processes. A significantly larger dataset would be needed to compare the surface enhancement of each morphology accurately.

In conclusion, the surface enhancement and morphological properties of the newly developed nanostructured Si IREs make them promising candidates for *in situ* FTIR, especially due to the comparatively high signal enhancement, low background distortion, and symmetric peak shapes. Therefore, the BSGE structure was chosen as the surface morphology for further analyses, especially for time-resolved studies.

8.4. Adsorption and Desorption Kinetics of 4-Methoxypyridine on Gold

The previously described experimental challenges are even more relevant for time-resolved measurements, since the time axis adds another variable that can be affected by an improper measurement technique. Therefore, it is important to verify the method used to measure the time evolution, in particular because the extracted time constants can depend strongly on the electrochemical setup. For faster timescales, the asynchronous step scan measurement technique may also have an unpredictable effect on the acquired data, requiring further validation.

As briefly mentioned in the introduction of this chapter, one of the major influencing factors of the kinetics of a system under an externally applied potential is the RC time constant arising due to the finite capacitance and resistance of the system. Aside from miniaturization of the electrode to reduce the overall capacitance, which has already been attempted [295], reducing the transverse resistance of the WE is the most viable approach to reducing the RC time constant. Due to the previously mentioned limitations of miniaturization in the context of standard FTIR systems, this work aims to investigate resistance reduction as a possible pathway towards the analysis of faster kinetics at the WE.

The previously described MOP molecular system was chosen for validation since this is an established method for the evaluation of such steady-state measurement techniques. In addition, prior work on the adsorption kinetics on ITO-based samples exists for comparison [295]. To this end, the adsorption and desorption kinetics of MOP on the BSGE surface were analyzed through rapid scan and step scan analysis. For the rapid scanning, a potential was applied to the WE to ensure full desorption of the MOP monolayer, as shown in Fig. 8.6(a). A reference steady-state measurement was then performed. Subsequently, the rapid scan measurement was started and the potential was changed to enforce adsorption of MOP at a defined time, as shown in Fig. 8.6(b). Spectra were acquired throughout the complete procedure, resulting in the occurrence of absorbance features corresponding to the MOP vibrational modes, schematically depicted in Fig. 8.6(c). Due to the limited time resolution of

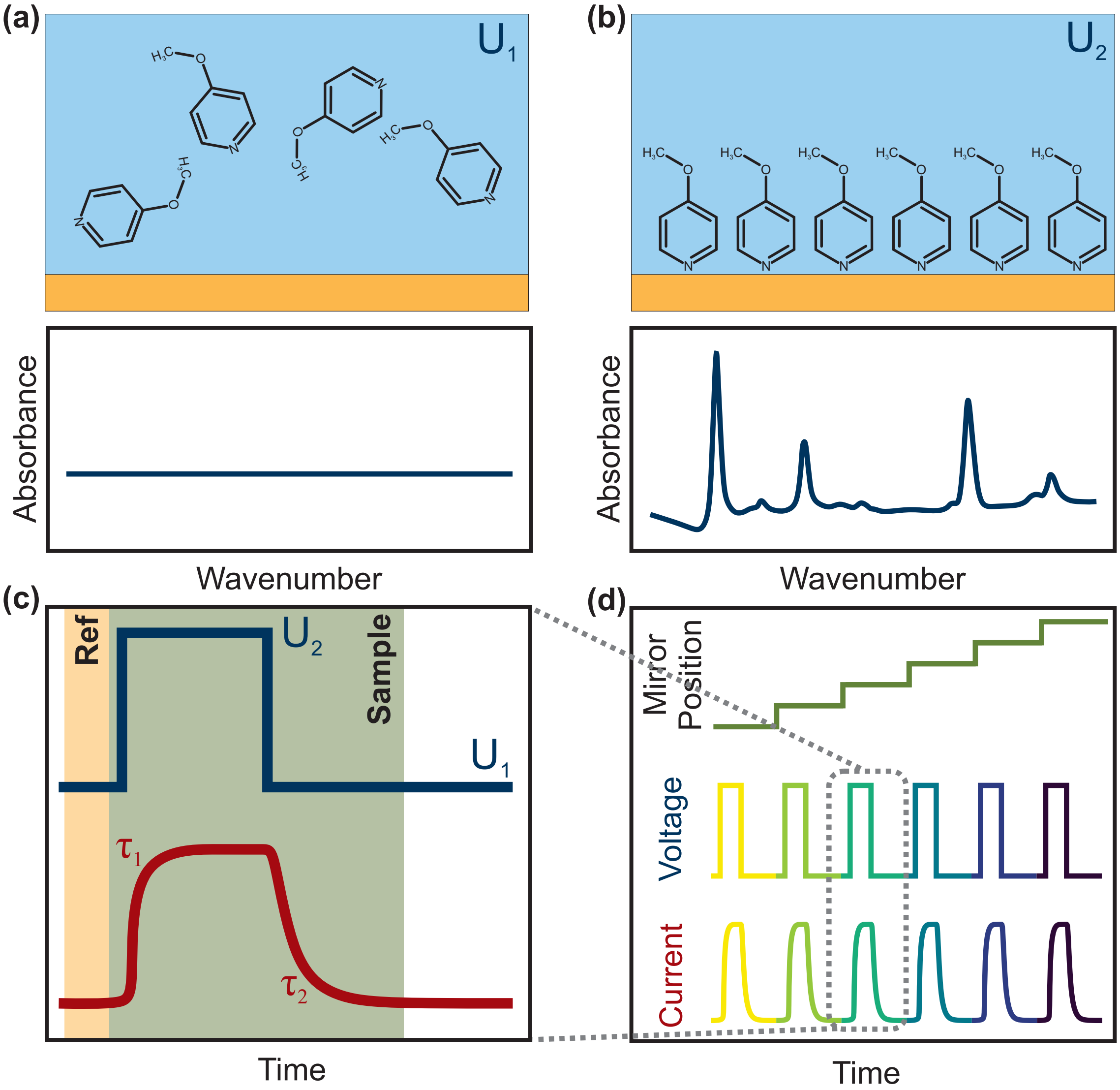

Figure 8.6 Measurement procedure for analyzing the performance of the BSGE nanostructures. The surface sensitivity is determined by periodically changing the potential of the WE. The time evolution of the IR signal is recorded for a voltage pulse at each mirror position (step scan). (a) At low potentials, the MOP introduced to the electrolyte is completely desorbed from the surface. This is used to record reference spectra. (b) At increased potentials, the MOP adsorbs in a self-limiting monolayer and the characteristic vibrational modes can be observed in the spectrum. (c) Schematic depiction of the evolution of the observed signal during a rapid scan measurement. (d) The repetition of this experiment at multiple mirror positions yields a step scan acquisition.

this method, faster processes were recorded by step scanning. This involved repeating the measurement procedure for each mirror position, as depicted in Fig. 8.6(d).

These measurement procedures were repeated for different concentrations of MOP in the supporting electrolyte, ranging from 66 µM up to 100 mM, to investigate the influence of concentration on the adsorption and desorption kinetics. The lower-concentration experiments exhibited slower adsorption time constants in the range of multiple seconds, enabling rapid scanning. For higher concentrations, the time constants to be measured necessitated step scanning. The enhanced stability of the black Si-based samples allows such step scan measurements to be performed over multiple hours without degradation of the sample surface.

The employed measurement technique can acquire a large dataset in a single experiment, since the whole mid-IR spectrum is acquired at every measured point in time. To keep the presented data as understandable as possible, these large datasets are simplified to the integrated areas of chosen peaks of interest. However, a two-dimensional step scan measurement of the fingerprint region of MOP adsorption from a 1 mM solution is depicted in Fig. 8.7 to demonstrate the concept. The brighter, yellow regions indicate the peak positions previously observed in the steady-state spectrum, thus showing that the step scan measurement yields comparable spectra as soon as equilibrium is reached. Shortly after the changes in potential are applied, the spectra indicate slight differences, evolving with an increasing signal as the MOP adsorbs or a decreasing signal as it desorbs. First, the evolution of the signal increase and decrease will be described in greater detail. Subsequently, the changes in peak positions and shape will be discussed.

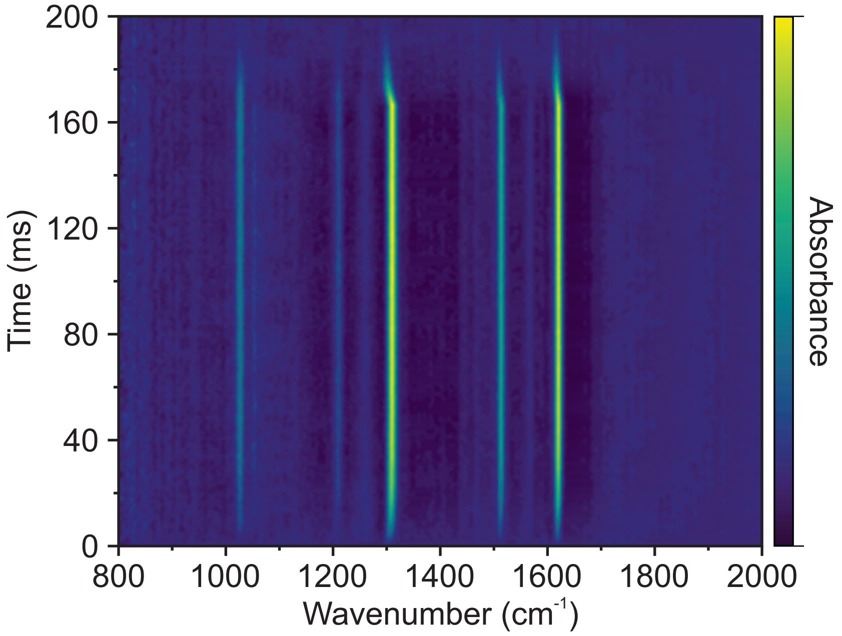

Figure 8.7 Multidimensional representation of the evolution of a MOP adsorption and desorption experiment with a MOP concentration of 1 mM carried out using a BSGE sample. The features of these time-resolved spectra match the steady-state spectra, but small shifts of the peaks become apparent during adsorption and desorption shortly after changes in the potential.

Fig. 8.8 shows exemplary plots of the normalized time evolution of the 1615 cm^{-1} peak area in rapid scan measurements of the processes of MOP adsorption and desorption from low-concentration electrolytes. Equivalent plots for higher MOP concentrations, recorded by step scanning, are depicted in Fig. 8.9. Throughout these experiments, a clear trend is visible for the adsorption kinetics, which seem to be significantly faster as the MOP concentration increases. In contrast, the desorption kinetics do not appear to vary with concentration. In the case of the rapid scan measurements, the desorption kinetics are below the achievable time resolution, but the step scan measurements do not show a significant dependence on concentration either. A step scan measurement of the lower concentration samples is impractical because this would require performing the measurement repeatedly for around 3000 interferogram points at a very low repetition rate due to the slow adsorption kinetics. A suitable repetition rate of around 0.05 Hz would lead to measurement times exceeding the capacity of the detector's liquid nitrogen cooling vessel by multiple hours.

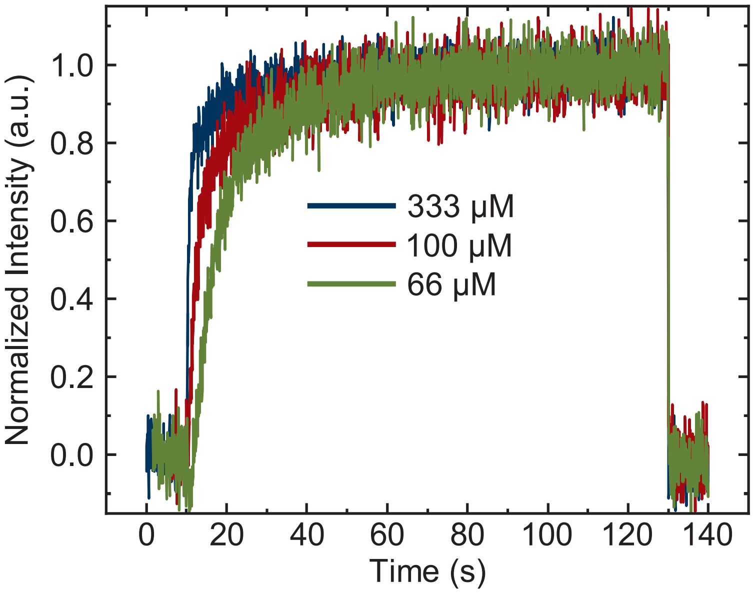

Figure 8.8 Normalized rapid scan traces depicting the intensity of the vibrational transition at 1615 cm^{-1} for various lower concentrations of MOP in the electrolyte. The adsorption time constant varies with the MOP concentration for lower concentrations. The desorption time constant cannot be resolved due to the limited time resolution of the rapid scan technique.

Only the highest concentration resulted in a slightly altered time constant for the step scan measurements. However, this could be an artifact of the experimental setup, because the measurement frequency was increased in an effort to reduce the overall measurement time to minimize the strain on the sample. All measurements were performed with the same sample, with this being the last measurement after roughly 12 h of near-constant use with frequent potential changes. Therefore, the risk of sample failure at this stage of the experiment was high. This change in frequency could have the unfortunate side effect of leaving insufficient time to establish a complete equilibrium for adsorption and desorption. This is difficult to judge since the measurements implicitly assume that the signal directly before the next measurement cycle is reduced to zero. If not, this could result in a faulty measurement since the monolayer is never fully desorbed, and the measurement data will be referenced to a surface partially covered with MOP.

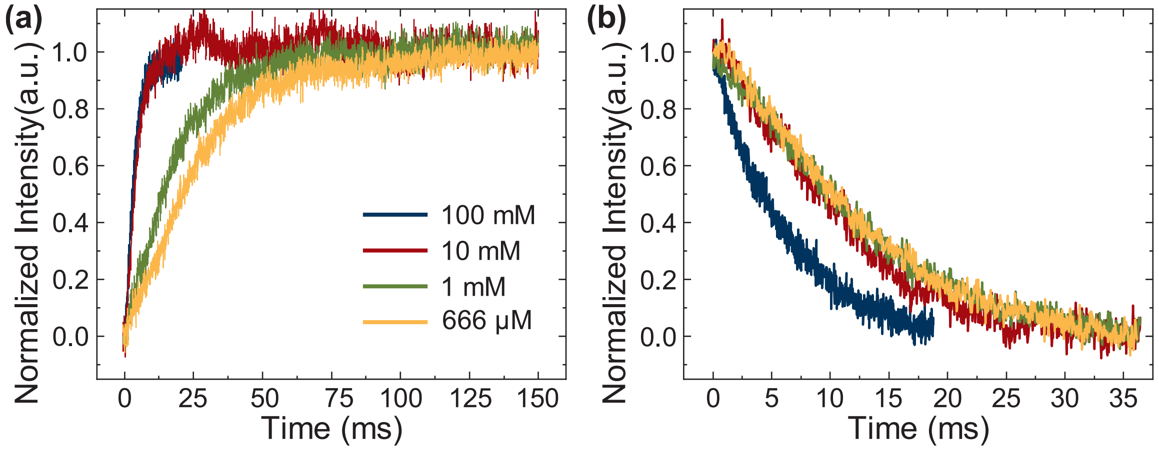

Figure 8.9 Normalized step scan traces depicting the intensity of the vibrational transition at 1615 cm^{-1} for various concentrations of MOP in the electrolyte, for (a) the adsorption of MOP and (b) the desorption process. While the adsorption process indicates that the adsorption time constant depends on the MOP concentration, the desorption time constant seems to be independent of the concentration. Slight deviations for the 100 mM desorption could have been caused by the slightly faster adsorption and desorption potential pulses applied.

A double logarithmic plot in Fig. 8.10(a) depicts the half-lifetime of the adsorption and desorption intensity and the position of the 1615 cm^{-1} peak. This discussion first focuses on the evolution of peak intensities. The previously observed dependence of the adsorption process on the concentration is readily apparent, while the desorption intensity half-lifetime remains independent of MOP concentration. The most likely cause of this change in kinetics is the limited transport toward the surface of the MOP in the electrolyte. Since the MOP is expected to be charge neutral, no attractive force is expected to be present during the adsorption. Therefore, the adsorption kinetics should follow the Langmuir–Schaefer equation, which describes the time required to reach a given surface coverage for a diffusion-limited system:

$$t = \frac{\pi}{4D}\left(\frac{\Gamma}{C}\right)^2 \propto \frac{1}{C^2}. \tag{8.1}$$

Here, D represents the diffusion constant, Γ the amount of adsorbed molecules, and C the adsorbent concentration in the surrounding liquid [299], [300]. Similar considerations have been reported in the literature, focused on how fast a MOP molecule diffuses away from the surface after desorption [295]. With the assumption that the peak intensity increases linearly with the amount of adsorbed MOP molecule, the applicability of this equation to the present context can be confirmed by validating the expected C^{-2} proportionality. To this end, a linearization was attempted by plotting the inverse square root of the half-lifetime against the MOP concentration, as shown in Fig. 8.10(b). While the assumption of diffusion limitation does not seem to be valid for MOP concentrations significantly higher than 1 mM, a C^{-2} dependence is clearly shown for lower concentrations in the figure inset. Therefore, the diffusion limitation seems to be valid only for longer time constants or lower concentrations. The most likely explanation for the deviation at shorter timescales or higher concentrations is a rate-limiting factor independent of concentration. The RC time constant is a plausible explanation of this limitation, especially because the measured half-lifetime at higher concentrations approaches values around 4 ms, which are plausible time constants for our specific electrochemical system assuming average specific capacitances of the Au electrodes.

For the low concentration range, which exhibits the expected adsorption behavior, the Langmuir–Schaefer equation provides additional insight. By applying the diffusion constant of $1.06 \times 10^{-5}\,\mathrm{cm^2\,s^{-1}}$ reported for MOP in water elsewhere [296], and the slope acquired through linear regression, as depicted in the inset of Fig. 8.10(b), the approximate density of MOP molecules on the Au electrode surface can be estimated using

$$\frac{1}{\sqrt{T_{1/2}}} = \frac{4}{\Gamma}\sqrt{\frac{D}{\pi}} \cdot C = m \cdot C, \tag{8.2}$$

with $T_{1/2}$ being the half-lifetimetime, resulting in the slope m corresponding to the total surface coverage Γ via

$$\Gamma = 4\sqrt{\frac{D}{\pi}} \cdot \frac{1}{m}. \tag{8.3}$$

This calculation, corrected for the previously determined surface increase due to roughness, yields an estimated surface density of MOP molecules of around $(3.6 \pm 0.3) \times 10^{14}\,\mathrm{cm^{-2}}$ in a fully established MOP monolayer. This corresponds to a reasonable MMA of $(0.28 \pm 0.03)\,\mathrm{nm^2}$.

The high-concentration measurements yield the first indications of setup limitations occurring as the time constants approach the single-digit millisecond range. Therefore, the RC time constant of the BSGE electrode system was investigated more closely by comparing it to the other systems previously used for steady-state analysis. The current responses of the BSGE and ILG samples, using the same $LiClO_4$ electrolyte excluding MOP, were recorded for the potential steps applied during the experiment. These are shown in Fig. 8.11. The RC time constant implies an exponential decay of the signal. Thus, the half-lifetime of this response was extracted for both current traces to ensure comparability with the previously determined time constants of MOP adsorption. As already alluded to, the half-lifetime of the current response is very similar to the shortest determined time constant of MOP adsorption, being 3.6 ms for the BSGE sample. Therefore, the measured MOP time constant is almost certainly limited by the current response that the system is capable of. The ILG sample, which has been used in the literature for time-resolved measurements, exhibited a time constant of 7.5 ms, around twice as long. Since the electrolyte–electrode interface and the electrode

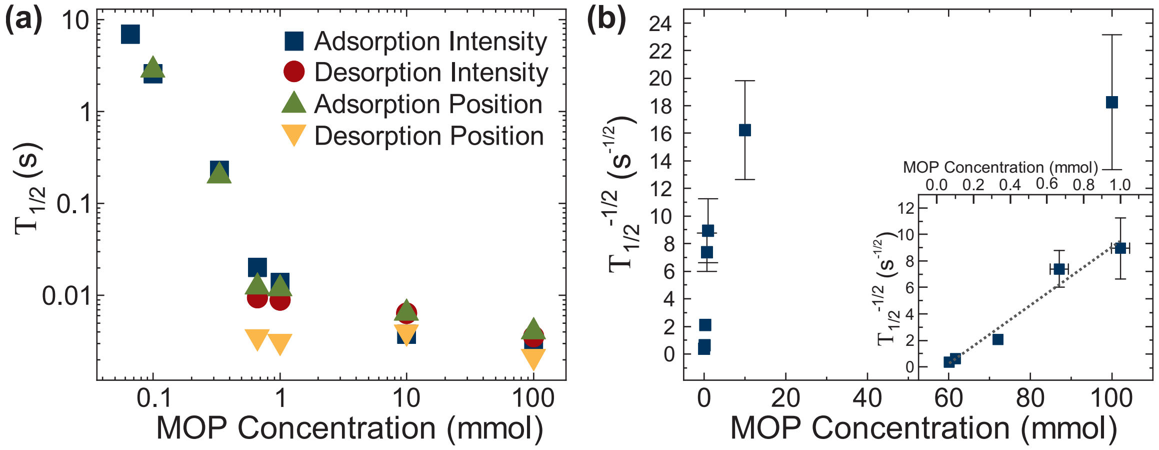

Figure 8.10 (a) Half-lifetimes of the MOP adsorption and desorption intensity and the precise peak position, during adsorption and desorption of the 1615 cm^{-1} peak, on a double logarithmic plot against the concentration of MOP in the electrolyte. (b) Attempted linearization by plotting the inverse square root of the half-lifetime of the 1615 cm^{-1} adsorption intensity against the MOP concentration to test the applicability of Langmuir–Schaefer diffusion. While the behavior appears nonlinear for higher concentrations, the time constant adheres to the Langmuir–Schaefer diffusion theory for lower concentrations (inset).

area are identical for both samples, this is likely a result of differences in the sheet conductivity of the electrode materials.

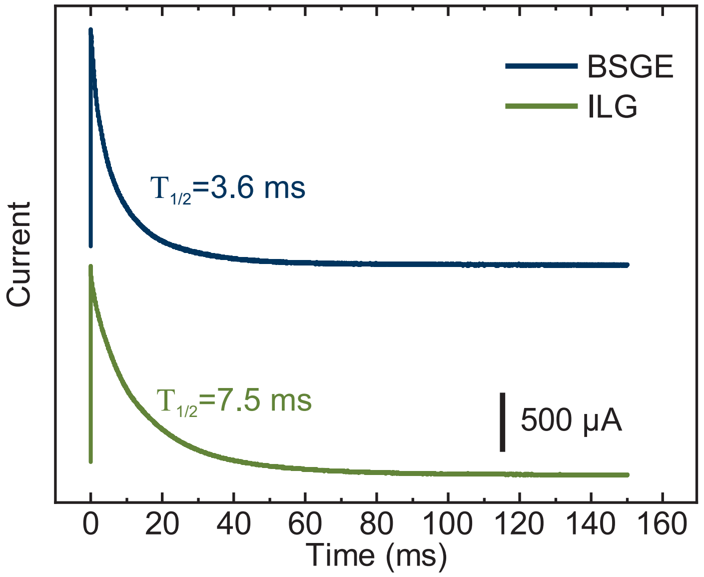

Figure 8.11 Time constants of BSGE and ILG samples for a potential step from −0.9 $V_{Ag/AgCl}$ to 0.3 $V_{Ag/AgCl}$ mounted to the electrochemical cell used for *in situ* measurements. A 100 mM $LiClO_4$ electrolyte was chosen to keep the parameters identical to later measurements of MOP adsorption and desorption.

The sheet resistances of the samples investigated in this work are depicted in Fig. 8.12(a) and highlight the increased conductivity of the BSGE sample compared to the electrodeposited sample. This in-plane conductivity increase results from the more continuous Au film created through thermal evaporation. The nanostructured morphology of the other samples reduces their in-plane charge transport capability due to the introduced potential barriers, since charges need to transfer across nanoparticle boundaries, negatively impacting the ability to deliver charges to the electrochemical interface quickly enough. The supporting Si IRE substrate generally does not add to electronic conduction because its low doping concentration leads to high specific resistances. While the ITO adhesion layer of the ILG samples also serves the purpose of increasing electrical conductivity, its specific conductivity depends on the chosen synthesis parameters and is, in general, below (by roughly two to three orders of magnitude) the specific conductivity of Au, especially for films of thicknesses below 100 nm [301]–[303]. Using this information in conjunction with the obtained half-lifetimes of the current responses of the systems, an estimation can be made of the resistance of the ILG and BSGE samples, judging the influence of the sample as well as other factors within the system and cross-checking for the reliability of the acquired data.

The acquired half-lifetimes can be converted to RC time constants by dividing them by $\sqrt{2}$, yielding 5.2 ms for the BSGE and 10.8 ms for the ILG sample. Assuming a typical specific capacitance of 20 µF, the series resistances of the systems are estimated as 2.1 kΩ and 4.3 kΩ, respectively. This difference in resistance is as expected for the given geometry and the acquired sheet resistances. Nevertheless, the series resistance of the measurement with the BSGE sample is high, pointing at other series resistances influencing the measurement. One of these is the electrolyte resistance. While the resistance between the reference electrode (RE) and the counter electrode (CE) is compensated by the potentiostat, the resistance between the WE and the RE adds to the series resistance. In addition, the resistances of cables and contacts will have an impact on the overall series resistance. In particular, the contact with the WE can cause significant additional resistance because the design of the electrochemical cell necessitates establishing electrical contact using Au leaf sheets. These are difficult to apply and could result in high contact resistances to the WE. In conclusion, further reduction of the series resistance can be achieved by optimizing the electrochemical cell design. Reducing the distance between the RE and WE and improving the WE contact could have a significant impact on the achievable time constants.

The effect of added external series resistances in the circuit is additionally highlighted in Fig. 8.12(b), which depicts the impact on the measured half-lifetime of MOP adsorption from a 100 mM solution. A linear relationship is clearly visible, confirming that the RC time constant directly influences the adsorption kinetics.

So far, the analysis of the FTIR spectra has been limited to the intensity of the 1615 cm^{-1} transition. As already mentioned in the discussion of the steady-state spectra, the relative ratio of the vibrational peaks can yield insight into the orientation of the molecule. Therefore, the intensities of three additional, readily identifiable transitions were analyzed to indicate

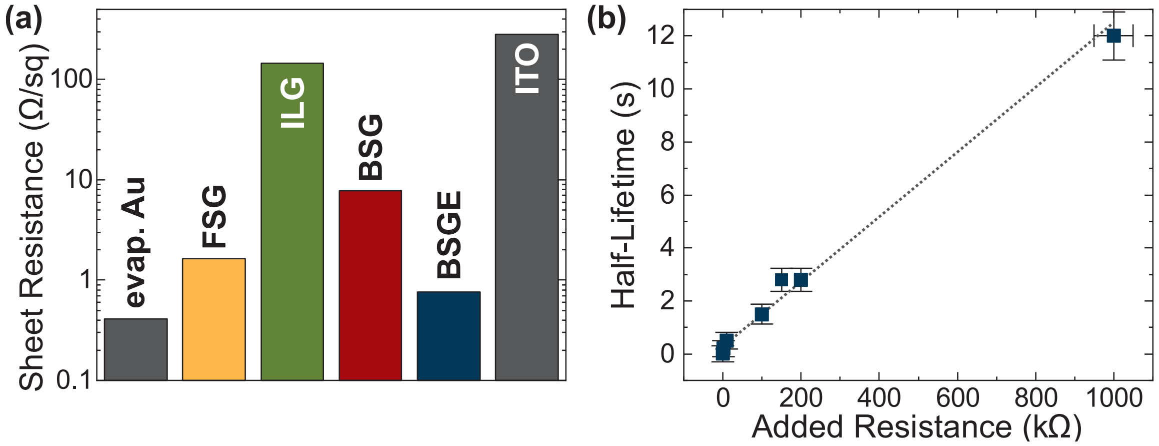

Figure 8.12 (a) Sheet resistance for the surfaces under investigation as well as a 100 nm thick Au layer evaporated on a thin Ti adhesion layer (evap. Au) and a bare ITO layer before electrodeposition. (b) Extraction of the half-lifetime for the adsorption of MOP from a 100 mM electrolyte onto a BSGE sample with additional resistance added in series to the WE, indicating the linear influence of resistance as expected from the time constant for capacitive charging.

the adsorption mode and possible changes in molecular orientation as the MOP adsorbs on the surface. The ratios calculated for a BSGE measurement of 1 mM MOP electrolyte are depicted in Fig. 8.13(a). Running averages are shown as dashed lines to enhance readability. At the beginning of the experiment, the calculated values are very sensitive to any changes in the ratio, as the peak intensities in the numerator and denominator are close to zero. As the signal increases with more MOP molecules adsorbing, this noise is reduced. Throughout the adsorption and desorption process, no definitive trends indicating a change in molecular orientation become apparent. Especially for the very low coverages, however, the noise in the signal could easily hide smaller changes in peak ratios. Significantly more measurement time would need to be allocated for additional averages to enhance the SNR and definitively characterize any minute changes in orientation at the beginning of the adsorption process.

In addition to analyzing the peak intensities, their positions can yield important information. A shift in vibrational transition frequencies generally corresponds to intermolecular interaction, which could take the form of substrate–molecule, molecule–molecule, or molecule–electrolyte interactions in the presented samples. While the spectral features are largely identical to the previously shown steady-state spectrum, the regions around the potential changes show deviations. These shifts are depicted in Fig. 8.13(b), indicating the time evolution of the peak shift relative to its steady-state position. As the MOP adsorbs on the surface, a spectral shift from lower to higher wavenumbers can be observed for the three main transitions located at 1615 cm^{-1}, 1509 cm^{-1}, and 1308 cm^{-1}. A similar but more pronounced shift is observed for the desorption. Selected spectra extracted at 2 ms time intervals for adsorption and desorption are shown in Fig. 8.14(a) and (b), respectively, which visualize the evolution of these peaks over time. Other peaks could not be analyzed reliably due to the noise in

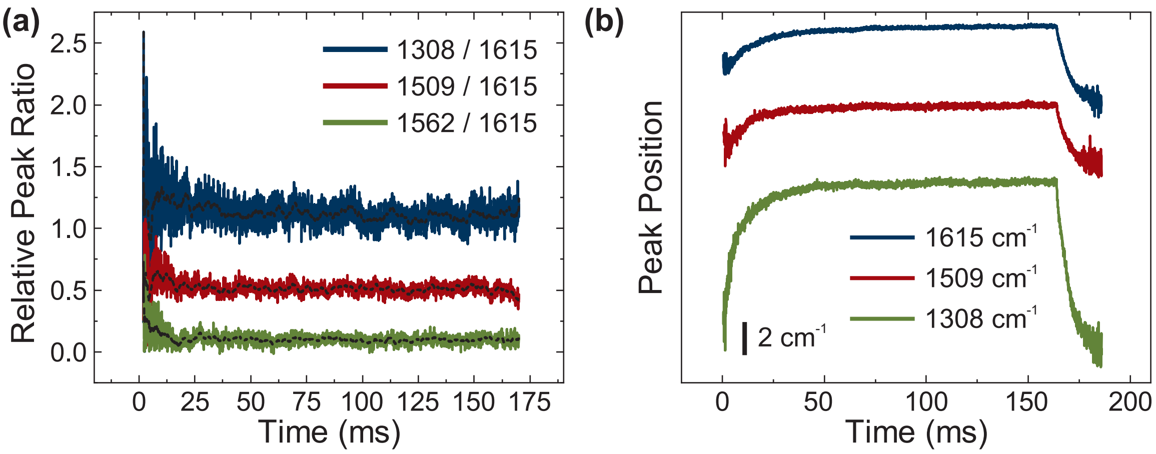

Figure 8.13 (a) Time evolution of the ratio of the intensity of various vibrational transitions to the 1615 cm^{-1} peak intensity from a measurement of MOP adsorption and desorption at a concentration of 1 mM on a BSGE sample. Dashed lines represent running averages for better readability. The lack of apparent changes in peak ratios indicates that no changes in relative molecular orientation occur during the adsorption and desorption processes. (b) Peak positions from the same measurement plotted against time. Positions were determined by fitting the relevant spectral regions with a Gaussian function to determine the peak center. Pronounced peak shifts are especially apparent for the 1308 cm^{-1} peak.

the acquired spectra resulting in issues with peak fitting and consistency in determining an accurate position.

Similar to the observations of the potential-dependent peak shift made by Quirk *et al.* [36], the C–O–C stretch mode at around 1308 cm^{-1} experiences the largest shift of all the vibrational modes under investigation. This likely arises due to dipole interactions occurring at the tail end of the molecule facing away from the surface. Such dipole interactions could either result from interactions with neighboring MOP molecules or with the electrical double layer. Interpreting these time dependencies is challenging since both the intermolecular interaction and the time dependence of the adsorption have a significant influence on the time evolution. Therefore, the influence of surface coverage cannot be fully decoupled from the adsorption and desorption kinetics.

Comparing the time constants of adsorption and desorption for the 1615 cm^{-1} peak, as depicted in Fig. 8.10(a), indicates a strong correlation between these two parameters. In contrast, the position half-lifetime for adsorption appears to be slightly longer than for the desorption processes. This could point at qualitative differences between the adsorption and desorption processes but could also result from a measurement artifact associated with the data analysis. The determination of time constants for these processes is hindered by the low SNR, especially at the beginning of adsorption and at the end of desorption, which prevents an accurate determination of the peak position. Thus, the identification of peak positions is not reliable at these stages of low coverage. This issue is compounded by the number of data

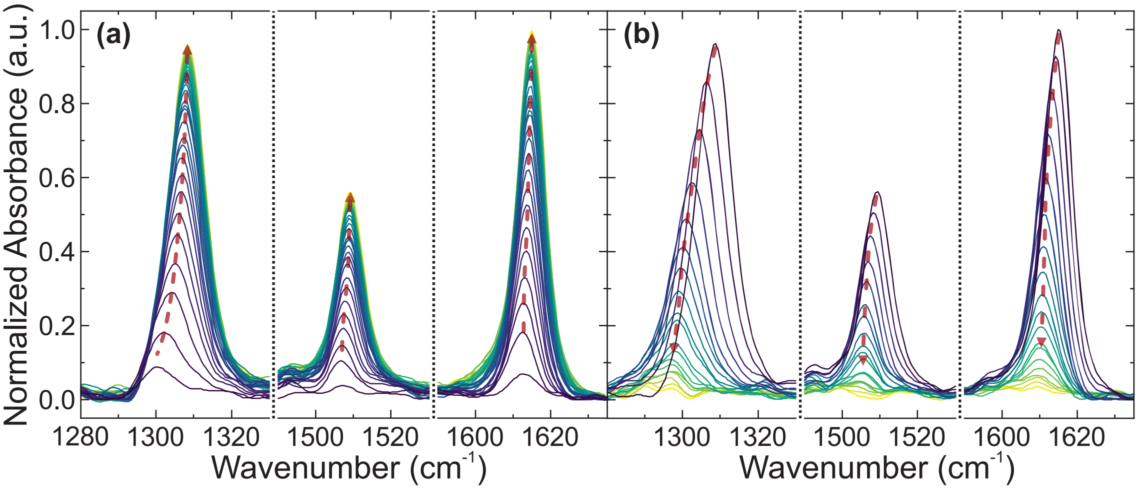

Figure 8.14 Exemplary spectra of the three major vibrational transitions of MOP extracted every 2 ms from (a) the adsorption and (b) the desorption process for a MOP concentration of 1 mM and a BSGE sample.

points present in the low-coverage state of the adsorption, which is significantly smaller due to the faster change in coverage at this stage compared to the tail of the desorption. Therefore, the number of spectra available to identify peaks is significantly reduced, which could result in an inaccurate determination of the peak position at the beginning of the adsorption.

In summary, the newly developed BSGE samples were successfully used to analyze the kinetics of MOP adsorption and desorption on an Au electrode surface. The surface enhancement of these samples is on par with, if not slightly better than, the established methods. In addition, the thin film exhibits sufficient adhesion to perform measurements for a full day, allowing multiple experiments without repeated sample change and synthesis. The superior conductivity improves the RC time constant, allowing for measurements in the single-digit millisecond range without additional equipment or sample miniaturization. These advantages were demonstrated using a MOP model system to study the kinetics of adsorption and desorption. For adsorption, the system was found to be diffusion-limited, following Langmuir–Schaefer behavior. In contrast, the desorption kinetics remained unaffected by changes in concentration. The average area per molecule in a fully established monolayer was determined to be 0.28 nm^2. The successful application of the newly developed surface morphology demonstrates its viability for *in situ* studies, but further optimizations need to be made for it to become a viable option for catalysis research. Especially problematic is the restriction in electrode material. With the given surface structure, analysis of other materials is fairly challenging. While metallic systems might be added on top by depositing thin layers of 20 nm or less, implementing semiconducting materials will be challenging. The developments necessary for full integration of the previously analyzed hybrid catalysis device with these surface-enhancing electrodes will take significant additional research.

9. Summary and Outlook

This work revolved around gaining basic insights into the electronic processes at interfaces between semiconductors and molecular monolayers. In addition, a method was developed to acquire in-depth insights into catalytic processes at surfaces via time-resolved *in situ* FTIR spectroscopy.

In the work presented in Chapter 4, molecular monolayers of PPIX were deposited on various semiconductor substrates using LB deposition. These were intended as model systems to investigate interactions between semiconductors and molecules. The morphologies of PPIX LB layers were determined at varying surface pressures. PPIX tends to self-assemble on the subphase interface, creating dense structures even at low surface pressures and exhibiting a monolayer thickness that indicates a rather upright orientation. By optimizing the surface pressure, dense monolayer structures, which were free of defects at the micrometer scale, could be deposited on the substrate surfaces. These LB layers were deposited onto Si, GaN, AlN, AlGaN, ZnO, and Au surfaces to analyze the chemical composition via XPS. The organic elemental transitions did not show any dependence on the substrate materials, indicating that the substrate does not chemically influence the LB layers.

UPS measurements revealed a shift in the vacuum potential at the interface between the substrate and monolayer, which arises due to the formation of an interface dipole layer, either due to the static dipole moment of the molecule or due to (partial) charge transfer. In addition, the HOMO level relative to the vacuum level could be determined. In combination with UV–Vis absorption measurements, a complete picture of the energy level alignment at the interface was acquired, indicating vacuum level alignment for the analyzed samples. Depending on the semiconductor substrate, its CB is either located above or below the LUMO level. The potential gradient at the interface was correlated with the photoluminescence intensity of the PPIX, which is an indicator of charge or energy transfer from the excited state of the molecule to the semiconductor CB. This analysis confirmed that Marcus theory could be used to describe the charge transfer for all samples except the narrow band gap Si. In this case, energy transfer processes might also be involved. Expanding this analysis to metalloporphyrins, including Co, Fe, and Zn as metal centers, resulted in similar HOMO and LUMO positions relative to the vacuum level. This underlines the applicability of the acquired insights to real catalytic systems.

The presented data only yield a lower limit for the kinetics of the charge transfer process from the PPIX to the substrates. The determination of its lifetime could help to characterize charge transfer rates and compare them with the potential gradients present at the interface. This would require a form of pump-probe spectroscopy, such as transient absorption spectroscopy, and could yield further clues regarding the slightly deviating Si sample. Due to the limited stability of the sample and the long measurement times required to measure a full transient spectrum, this measurement could be challenging to carry out. Additionally, insight into the back transfer of charges to the PPIX monolayer would be of great interest, especially regarding reduction catalysis.

Chapter 5 expanded on the studies described in Chapter 4, focusing on the LB layers of Mabiq. This molecule can contain two metal atoms simultaneously, possibly enhancing catalytic performance due to the synergies achieved by combining different metals. The analysis was performed analogously to Chapter 4 to make the results comparable. The morphology of the Mabiq LB layers is different from PPIX: they do not self-assemble and are less mechanically stable. They form multilayer structures at lower pressures than observed for PPIX. The significantly lower thickness of the deposited monolayer indicates a horizontal orientation of the main molecular axis on the substrate surface, which likely arises due to the lack of an amphiphilic structure. LB layers were deposited on Si, GaN, ZnO, and Au. The chemical stoichiometry of the layers and their respective binding environments was close to the expected ratios, except for N. In this case, interaction with the surface hydroxyl groups or the water subphase before deposition could result in partial coordination of a water molecule or OH group with one of the binding sites. The energy level alignment determined with UPS exhibited the same qualitative behavior as was observed for PPIX, but showed a significantly higher potential shift at the interface. This could result from the molecular orientation leading to greater orbital overlap between the Mabiq molecule and the substrate. Prior scanning tunneling microscopy studies of Mabiq found that the molecule buckled slightly when adsorbed to single-crystalline metal surfaces. This symmetry break, and a potentially accompanying dipole moment, could also explain the formation of the observed potential shift. Luminescence studies could not be performed on Mabiq, because its luminescence intensity was insufficient to determine the intensities accurately.

Unfortunately, LB deposition of metal-coordinated Mabiq moieties was not achieved due to the slight but nevertheless too high solubility of the molecule in the DI water subphase. It may be possible to prevent this by modifying the subphase, for example, by controlling its pH. Otherwise, Mabiq has been shown to coordinate with metal atoms when introduced to a single-crystalline surface in UHV [226], [227]. Therefore, it could be viable to try similar metallization processes with LB layers by deposition on a metal surface, or by introducing metal ions after LB deposition, for example, via subsequent evaporation or submersion in an ion-containing liquid.

Further insight into junctions between Si and PPIX was acquired using electronic characterization methods, as described in Chapter 6. The methods employed, such as SPV and UI characteristics, are significantly more sensitive to surface recombination rates and band bending in the Si compared to the photoelectron-based methods used up to this point. SPV studies using substrates with both n- and p-type doping revealed a significant influence of the PPIX monolayer on the surface properties. Aside from the expected shift in CPD due to the interface dipole already observed in UPS spectra, illumination revealed that the surface band bending is different from that of a bare sample. This leads to the absence of SPV for the p-type sample upon monolayer deposition. UI analysis was performed via a Hg droplet top contact to analyze the influence of the PPIX monolayer on the Schottky junction. All investigated samples experienced a significant reduction in current density, and the p-type sample additionally showed a reduction in the rectification ratio. Lastly, temperature-dependent UI analysis was performed to measure the barrier height of the Schottky junctions. While the p-type sample exhibited an expected reduction in barrier height upon deposition of PPIX, the barrier height of the n-type sample remained close to unchanged. This unexpected behavior hints at other processes that are beyond the scope of this work. This discrepancy and other ambiguous results involving the surface properties of the studied samples require more in-depth studies in well-controlled (ideally vacuum) conditions to decrease environmental influences.

A viable hybrid catalyst system requires covalent bonding between the molecules and substrate to prevent device degradation through catalyst desorption. While most systems use SAM formation with phosphonic acid head groups, an alternative method to establish covalent bonds using LB deposition was explored in Chapter 7. A two-step approach was chosen to validate the possibility of amide bond formation in a multilayer system, using APTES as a base layer SAM providing amine terminal groups on a Si surface. The SAM was established using a wet chemical technique, resulting in dense monolayers with low surface roughness. After subsequent LB deposition of PPIX, the formation of amide bonds between the carboxylic acid functional groups of the PPIX and the amine of the APTES was studied via *in situ* annealing and XPS measurements, which characterized the transition to amide bonds after annealing. AFM measurements before and after annealing do not indicate a morphological change. Still, they show that the monolayer quality is slightly diminished, with slight multilayer formation and defects in the monolayer that lead to an increase in surface roughness over what has been observed for a protoporphyrin monolayer on bare substrates. This is likely a consequence of the increased SCA after APTES deposition.

Establishing covalent bonds is not limited to the presented amide bond formation. In principle, other bond formation processes, such as esterification, should also be possible. Therefore, the concept could be expanded upon, widening the scope toward various chemical reactions that could immobilize LB layers with covalent bonds. Another possibility would be direct bond formation, omitting an intermediate SAM. This requires functional groups that establish bonds with OH-terminated surfaces. For example, the chemisorption of phosphonic acids via LB could be a promising process to establish stable and well-ordered monolayers without the need for elaborate SAM formation procedures.

Chapter 8 revolves around the development of a measurement technique intended for studying hybrid catalytic systems via time-resolved *in situ* FTIR measurements. This technique uses Au for surface enhancement combined with ATR geometries to achieve the signal enhancement necessary to measure with (sub-)monolayer sensitivities. These structures often suffer from a lack of adhesion, which leads to inconsistencies in sample stability and frequent delamination of the metallic thin film. Since time-resolved measurements with a high resolution require measurement times of multiple hours, such sample structures are unsuitable for this purpose. A novel morphology based on black Si-etched surfaces with electrodeposited and PVD Au thin films was therefore developed to improve adhesion. In addition to better stability, these samples exhibited a low surface resistivity. The potential-dependent adsorption and desorption of MOP were used to benchmark the newly developed structures against established morphologies, indicating a slightly improved signal enhancement for the black Si-based samples. Time-resolved measurements were performed with the newly developed structure to verify the system and determine the effective time resolution for potential-dependent measurements, which is limited by the RC time constant of the electrochemical cell. Concentration-dependent adsorption transients acquired for varying concentrations of MOP in the supporting electrolyte indicated a strong dependence of the adsorption time constant on the concentration. For sufficiently low concentrations, the behavior could be modeled with Langmuir–Schaefer adsorption kinetics, indicating that the diffusion of the molecule is the rate-limiting step. For higher concentrations, the behavior changed as the measured time constant reached the low millisecond range. This is likely due to the aforementioned RC time constant creating a lower limit. Using the Langmuir–Schaefer equation, the density of MOP adsorbed on the surface could be determined.

While the morphologies developed here are an improvement over the established device structures, there is still room for optimization. Due to the sensitive nature of the surface enhancement, the reproducibility of the enhancement factor remains uncertain. This could be alleviated by replacing the wet chemical surface structuring with reactive ion etching. This would allow for fine-tuning of additional parameters, thus providing a larger parameter space to tune the morphology of the black Si precisely. In addition, multiple process steps could be performed in the same machine without exposing the sample to the atmosphere, potentially yielding higher reproducibility due to the reduced chance of contamination. In addition, it might be viable to omit the electroless deposition process entirely through morphology optimization of the black Si, yielding greater reproducibility and possibly also allowing for the introduction of adhesion layers to improve the device stability. It would likely be difficult to improve the response time of the system significantly. While optimization of the geometry of the electrochemical cell and a reasonable reduction of the WE resistance would improve the response time slightly, significant progress toward microsecond resolutions will likely not be possible with the given setup. So far, most substrate designs make use of metallic layers for surface enhancement. This makes analyzing semiconducting catalytic systems more difficult, requiring further geometric optimization.

In conclusion, this work yields insights into the basic mechanisms of substrate–molecule interactions, which are relevant for hybrid catalytic applications. Patterns identified in the energy alignment and charge transfer processes could help guide further developments concerning the choice of substrates and catalysts to maximize synergetic effects and, therefore, improve device performance. The applicability of the observed processes to real devices is yet to be demonstrated, providing an avenue for the next steps to be taken. Measuring the performance of such devices in a well-defined system can be challenging. Thus, *in situ* SEIRAS could provide the necessary information due to its submonolayer sensitivity. Therefore, a measurement setup was developed in this work to provide the means of acquiring relevant data on hybrid devices under operating conditions. New surface-enhancing substrate morphologies with enhanced adhesion and slightly improved surface enhancement were developed and validated in time-resolved measurements.

This measurement technique can be adapted to verify the relevance of the basic knowledge gained on the interfaces of molecular catalysts and semiconductor surfaces. To this end, the first steps have been made to provide covalently bound molecules deposited via LB deposition. With this, significant improvements to the major components for an in-depth *in situ* study of hybrid devices have been developed. The basic knowledge acquired could thus be tested and the presented models refined to provide an in-depth view of the mechanisms at the interface between semiconductor and molecule, but also of the catalytic cycle of the molecule itself, paving the way for high-performance catalytic hybrid devices.

A. Experimental Methods

The following sections give a detailed overview of the working principles and procedures used to synthesize the samples and acquire the data presented in this work.

A.1. Substrate Cleaning and Surface Hydroxylation for Monolayer Studies

A consistent and thorough sample-cleaning procedure is imperative to minimize the influence of surface contaminations, since these can easily surpass the signals generated by a monolayer of molecules. All glassware and sample holders that were used for sample cleaning or other preparation techniques were thoroughly cleaned using aqua regia (a 1:3 molar ratio of nitric acid and hydrochloric acid; Sigma-Aldrich) to remove metallic contamination and piranha solution (a 3:1 volume ratio of concentrated sulfuric acid and 30 wt.% hydrogen peroxide; Sigma-Aldrich) to remove organic contamination before their first use. Each piece of equipment was used for a single purpose only and underwent the above cleaning procedure regularly every few weeks. Handling these solutions poses great risks due to their highly corrosive properties and requires elaborate safety precautions.

Samples were degreased by ultrasonication at 400 W for 10 min each in acetone and then isopropanol (both ultra-large semiconductor integration [ULSI] grade; Microchemicals) while fixed in an upright orientation using an in-house-designed polytetrafluoroethylene (PTFE) sample holder. Any remaining contamination was removed from the surface by 200 W oxygen plasma treatment in a 0.4 mbar oxygen (5N purity, Linde) environment using a microwave plasma generator (Diener Electronics) for 30 min. This leads to the growth of a surface oxide for all samples except the oxide-based ones. An appropriate wet chemical process removed the oxide depending on the substrate: For Au samples, the oxide was reduced upon immersion in ethanol for at least 20 min and dried under a stream of nitrogen. The Si, AlGaN, and AlN samples required immersion in 5% HF for at least 1 min to remove the surface oxide [304], [305]. Due to its ready intake through human skin, corrosive properties, and high neurotoxicity, HF poses a great risk and should be handled with the utmost care. The process was similar for GaN, but its native oxide could also be removed with the much safer option of 30% hydrochloric acid (HCl) [304].

After the oxide removal, a thin layer of controlled oxide was regrown to achieve the desired hydrophilicity necessary for the subsequent processing steps. This was achieved by another oxygen plasma treatment using the same conditions for a significantly reduced time of 30 s. After this final step, the samples were either immediately used for LB deposition or, for the reference samples, were immersed in DI water for 60 min to simulate the immersion step necessary for LB deposition.

All measurements on reference or LB layer samples were performed immediately after the described preparation technique. This usually meant the measurement was performed within a few hours of preparation. Longer storage times would lead to increased surface contamination and reduced reproducibility. Samples were reused after carrying out the full cleaning procedure again.

A.2. Langmuir–Blodgett Isotherms and Deposition

The LB isotherm measurements and deposition procedures were performed on a commercial LB setup (KSV NIMA) equipped with a 98 cm^2 PTFE trough, polyoxymethylene (POM) barriers, a z-axis manipulator for sample immersion and extraction, and a microbalance equipped with a Pt Wilhelmy plate to measure the surface pressure. The whole setup was in an enclosure with thick noise insulation to reduce the influence of air currents and environmental vibrations, which could disturb the water surface. Before initiating a measurement, all surfaces in contact with the subphase were thoroughly cleaned with isopropanol and lint-free wipes to remove any adsorbed surface contamination. Drying the parts with a stream of nitrogen ensured that they were completely dry before use. In addition to the brief cleaning procedure immediately before every experiment, the surfaces were regularly cleaned using a moderately concentrated potassium hydroxide solution every few weeks.

After cleaning, the barriers were put in place and the trough was filled with fresh, ultrapure DI water. This was added outside the trough area enclosed by the barriers to ensure that any dirt floating on the surface of the water or the sidewalls of the container remained outside the area of interest. The trough was filled to slightly above the highest point of the sidewall, which is possible due to the surface tension of the water and the high hydrophobicity of the PTFE. After filling, the Wilhelmy plate was flame annealed using a slightly oxygen-rich butane torch and was added to the microbalance for surface pressure determination. The surface was cleaned at least three times by full compression of the barriers and subsequent removal of surface contaminants using a PTFE suction nozzle on the surface. This slightly lowered the water level in the trough, which was refilled to the appropriate level from the side. Next, the samples intended for deposition were mounted to the z-axis manipulator using a POM clamp and were immersed into the DI water so that the clamp was just above the water level. Isotherm experiments did not require the addition of the sample and were carried out using only the Wilhelmy plate.

The molecule to be deposited on the sample surface was now introduced to the DI water surface of the trough with fully extended barriers. This was done using a solution with a molecule concentration of 50 µM. In the case of PPIX (98 %, Frontier Scientific) and all metalloporphyrins (Fe: 96 %, Sigma-Aldrich; Zn: 95 %, Sigma-Aldrich; Co: 95 %, Frontier Scientific), the solution contained 20 vol.% DMSO (99.9 %, anhydrous, Sigma-Aldrich) and

80 vol.% dichloromethane (99.5 %, Selectophore, inhibitor-free, Merck) to balance the solubility of the porphyrin molecules while ensuring the solvent mixture was sufficiently volatile [171]. For Mabiq, the molecule was dissolved in pure dichloromethane. It was of critical importance that the dichloromethane solvent was inhibitor-free. Experiments using amylene-stabilized dichloromethane yielded drastically lower monolayer quality, which could be a result of complexation to the molecule to be deposited or residual amylene on the surface impeding the self-assembly process. The prepared solution was added dropwise through a small-volume precision syringe to ensure that it floated on the surface of the water and did not sink to the bottom of the trough. The volume of solution added strongly depended on the molecule and procedure used. In general, isotherm experiments required around 150 µL and LB deposition around 300 µL.

After a waiting period of 20 min to ensure that the solvent was fully evaporated, the experiment was initiated by compressing the barriers at a rate of 4 mm min^{-1}. In the case of isotherm measurements, the compression was continued until the barriers were fully compressed, while simultaneously recording the evolution of the surface pressure with respect to the barrier position. For LB depositions, the compression was carried out until a set surface pressure was reached. The system was allowed to equilibrate for another 15 min while the control software maintained the surface pressure by continuously adjusting the barrier position. After this waiting time, the sample was extracted from the subphase at a speed of 1 mm min^{-1} while the control loop maintained a constant surface pressure with variations of at most 0.2 mN m^{-1}. The deposition process was stopped after the sample was removed entirely from the subphase. It was left for 5 min to enable the remaining DI water to dry before removing the sample from the clamping mechanism and drying it under a stream of nitrogen.

A.3. (3-Aminopropyl)triethoxysilane Monolayer Formation

The formation of APTES SAMs was performed according to a wet chemical method developed by Yadav *et al.* [96]. This involved the preparation of a stock solution containing 50 % methanol (99.8 %, anhydrous, Sigma-Aldrich), 47.5 % APTES (98 %, Sigma-Aldrich), and 2.5 % DI water. This solution was aged for roughly 24 h before it was used for SAM formation. The Si substrates were cleaned and prepared according to the procedures outlined in Sec. A.1, finishing with an oxygen plasma treatment for 30 s to establish a hydroxylated surface. Next, the samples were transferred to a PTFE reaction vessel equipped with a sample holder that ensured they remained in an upright orientation. A 20 mL reaction solution was prepared by diluting the aged stock solution with methanol in a 1:500 ratio and was added to the container. The container was then closed, allowing the reaction to proceed at room temperature in darkness for 30 min. Afterwards, the samples were washed by submersion in pure methanol, followed by a methanol rinse and drying under a stream of nitrogen. Them, the samples were immediately annealed in a nitrogen atmosphere at 140 °C for 1 h. The obtained amine-terminated samples could not be stored due to the reactivity of the amine groups and the possibility of contamination. Therefore, any experiments or deposition processes were carried out without delay.

A.4. Atomic Force Microscopy

AFM was employed to analyze the surface morphology, monolayer thickness, surface roughness, and adhesion properties of reference samples and samples covered with various monolayers. Measurements were performed with a Multimode 8 (Bruker) AFM using an upgraded Nanoscope V controller module (Bruker) under ambient conditions and at room temperature. While peak force quantitative nanomechanical mapping (PF-QNM) was used for almost all AFM studies in this work, the scratching experiments required a fallback on older and more established techniques such as contact mode (CM) and tapping mode (TM).

A.4.1. Scratching Experiments

Scratching experiments were used to accurately determine the monolayer thickness of a fully established monolayer of PPIX. These experiments involved the successive use of CM and TM. To begin with, CM was used to remove the monolayer from a defined area of the sample surface. The probe tip (NSG30, tip radius 6 nm, force constant $40\,\mathrm{N\,m^{-1}}$, resonance frequency $\sim$320 kHz, NT-MDT) was dragged across the surface while monitoring the cantilever deflection by tracking the position of the reflection of a laser diode off the cantilever backside. The force applied can be controlled approximately by setting a deflection setpoint. The monolayer can thus be removed with a moderate setpoint force (0.4 V) while moving the cantilever at a speed of $1\,\mathrm{\mu m\,s^{-1}}$ over a $1\,\mathrm{\mu m^2}$ surface area.

Subsequent analysis of the height steps between scratched and pristine surface area was possible via TM, for which the contact between the sample and probe is significantly lower. In TM, the cantilever is actuated to oscillate close to its resonance frequency. If the probe starts to interact with a sample surface, the frequency response of the cantilever shifts slightly, which results in a change in oscillation amplitude. Controlling this change in amplitude via a feedback loop while scanning the surface area ($1\,\mathrm{\mu m\,s^{-1}}$) allows for accurate determination of the sample height.

The AFM probes required for meaningful PF-QNM experiments are, as described in the next subsection, significantly more delicate than those used for TM. Since scratching experiments require material removal from the surface, the probes used for PF-QNM can easily be damaged in the process and are thus not suited for such experiments.

A.4.2. Peak Force Quantitative Nanomechanical Mapping

PF-QNM is a technique that uses an active feedback loop to poll the cantilever deflection in real time as it interacts with the sample surface. Thus, the forces between the sample and cantilever can be controlled very precisely, down to tens of pN, allowing for imaging of very soft or otherwise mechanically sensitive materials.

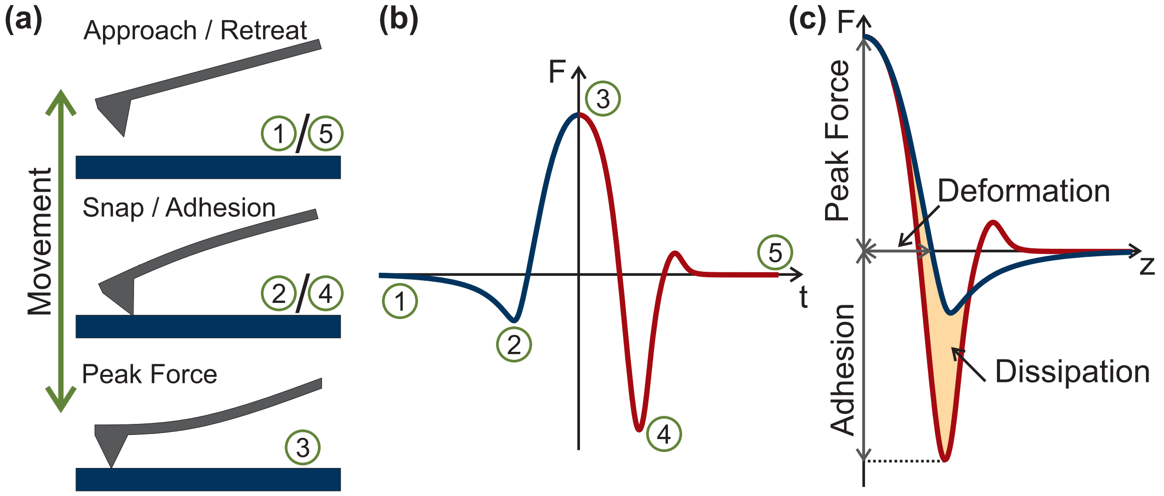

Figure A.1 Schematic depiction of the process of acquiring quantitative nanomechanical mapping data by peak force tapping. (a) Diagram of the interaction and relative position of the tip and substrate during the measurement cycle carried out at each data point/pixel of the micrograph. (b) Time evolution of the involved forces as the tip approaches, interacts with, and releases from the sample surface. Forces can be extracted by measuring the bending of the cantilever and determining its spring constant. (c) Extraction of various mechanical properties from the recorded force data used for visualization.

Due to the need for real-time polling in this method, the cantilever is actuated at a significantly lower frequency, far from its resonance frequency, at rates in the kHz regime and is set to scan at lower speeds of $0.5\,\mu\mathrm{m\,s^{-1}}$. At each point to be imaged, the cantilever probes the surface as shown in Fig. A.1(a). During the initial approach, the distance between the cantilever and the sample is reduced until the tip snaps into contact through attractive forces, such as van der Waals interactions, leading to a downward deflection of the cantilever. As the distance is reduced further, the cantilever returns to its neutral position before deflecting in the opposite direction. The distance between the sample and the cantilever is reduced until a set deflection is reached. The cantilever is retracted but remains in contact with the sample beyond the neutral point due to the attractive forces. At some point, the spring forces of the cantilever surpass the adhesion, and the cantilever detaches from the surface.

After calibrating the system to accurately determine the amount of deflection of the cantilever relative to the photodiode signal, and after calibration of the cantilever force constant, the arbitrary deflection values can be translated into forces. The typical time evolution of the force for a single measurement cycle is illustrated in Fig. A.1(b). The numbered features relate to points of interest in the cycle. Fig. A.1(c) depicts the corresponding force–distance curve, which can be used to extract various material parameters. The primary value of interest in this work is the adhesion, since this parameter exhibits a high contrast between sample areas covered with a monolayer and bare regions.

This contrast likely arises due to the change in hydrophobicity on the surface. The AFM probes used (Scanasyst Air, Bruker) are made of sharp Si tips, which experience higher adhesion forces with a bare Si substrate compared to the hydrophobic tail groups of the monolayers of molecules used in this work. Scanasyst Air probe tips additionally have the advantages of being comparatively sharp (tip radius 2 nm) and being attached via low force constant Si nitride cantilevers (force constant $0.4\,\mathrm{N\,m^{-1}}$), which make them especially useful for delicate materials such as physisorbed monolayers.

A.5. Contact Potential Difference and Surface Photovoltage

Both CPD and SPV measurements rely on the same principle, which makes use of an oscillating probe (Kelvin probe) that is brought into the vicinity of a surface to determine its work function via a feedback loop. A schematic depiction of such a measurement setup is shown in Fig. A.2(a). It consists of the aforementioned Kelvin probe, which is brought close to a sample and is electrically connected to it. A variation in the electronic work function between the Kelvin probe and the sample results in a flow of charges to achieve Fermi level alignment, as depicted in Fig. A.2(b). The reorganization of charges leads to an electric field between the Kelvin probe and the sample.

The setup now resembles a charged parallel plate capacitor and can be manipulated by periodic variation of the distance between the Kelvin probe and the sample. The charge, voltage, and geometry of a simple plate capacitor follow the relation

$$C = \epsilon_r \epsilon_0 \cdot \frac{A}{D} = \frac{Q}{U}, \tag{A.1}$$

where C is the capacitance of the plate capacitor, ϵ_r is the relative permittivity of the dielectric separator, ϵ_0 is the vacuum permittivity, A is the area, D is the distance, Q is the charge, and U is the potential difference between the plates. A change in distance of D thus requires a change in charge to maintain the potential difference fixed by the difference in work functions. Minimizing this current by applying a potential between the sample and probe yields the difference in work function because the capacitor is not charged if the external potential completely cancels the difference in work function.

While CPD measurements are carried out without external illumination, SPV measures the response of the sample work function to light. The CPD and SPV measurements presented in this work were carried out using a commercial Kelvin probe system (KP Technologies) with

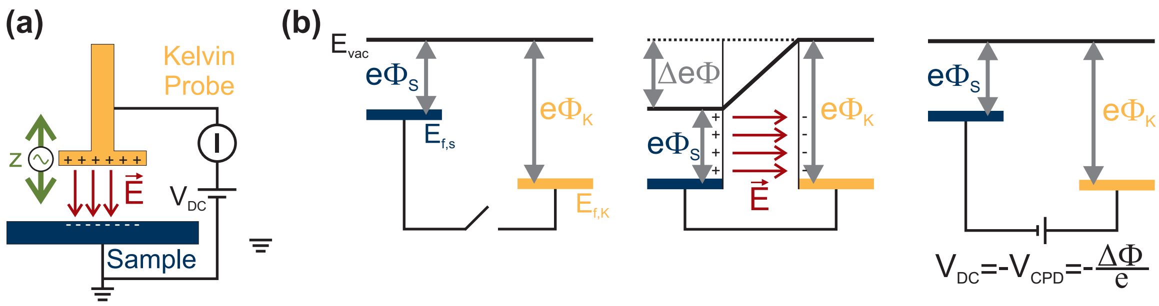

Figure A.2 (a) Schematic depiction of the setup used to measure the CPD between a Kelvin probe with known work function and a sample with unknown work function. (b) Representation of the energy level alignment occurring between the Kelvin probe and sample as they are electrically connected. The resulting electric field leads to charge accumulation on the electrode and the sample surface, which can be compensated by applying an external voltage.

a Au probe under ambient conditions using illumination with high-power LEDs. Data were acquired at a rate of 2 Hz. CPD values were averaged over at least 120 measurement points; SPV measurements are presented as time traces without averaging.

The work function of the Kelvin probe was determined to be 4.8 eV through calibration with a pristine highly oriented pyrolitic graphite (HOPG; assumed work function: 4.7 eV) sample prepared by removing the surface layer via the Scotch tape method. Even though this method has been found to produce the most reliable standard, there are considerable deviations in literature values for HOPG, between 4.5 eV and 5.0 eV [306]–[310]. Any relative changes in the SPV remain unaffected by these calibration uncertainties. Because this method is highly sensitive to changes in the atmospheric environmental conditions, comparative studies were performed immediately after sample preparation and with the shortest possible delay between samples. Illumination for SPV required a shallow angle of incidence due to the close proximity of the solid Kelvin probe with the sample, which was counteracted by high-power LEDs (M405L2, MINTL5, M880L2, Thorlabs) operating at maximum power to ensure saturation.

A.6. Photoelectron Spectroscopy

Photoelectron spectroscopy is useful for analyzing the chemical composition, binding states, and band structure of the near-surface regions of solid-state samples. Simplified schematic depictions of the experimental setup and measurement principle are given in Fig. A.3(a) and (b), respectively.

The process involves the excitation of core or VB levels in a sample by a narrow linewidth photon source with known energy. The electron is released from its state if the photon energy is higher than the binding energy of the state it occupied. It can now move freely and has

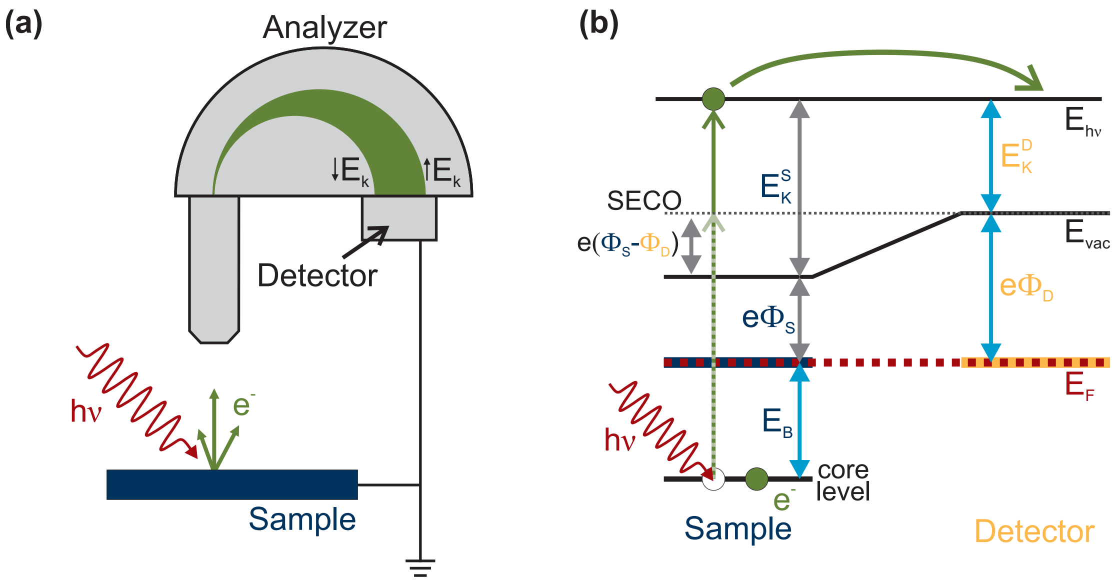

Figure A.3 Schematic depiction of the measurement principle of photoelectron spectroscopy. (a) Simplified measurement geometry depicting an excitation that leads to the emission of electrons from the sample with characteristic kinetic energy. Electrons collected by the analyzer are forced onto a circular path through a magnetic and electric lens system. The kinetic energy is measured by analyzing the radius of the circular path. (b) Visualization of the energy levels involved in the measurement including a core level that is the source of the expelled electron to be analyzed in the detector. The grounding of the detector and sample ensures Fermi level alignment between them. The kinetic energy of the electron and, thus, the binding energy can be found if the detector work function is known. In addition to core-level electrons, VB electrons can also be analyzed. The energy of the exciting photon differentiates XPS from UPS.

a certain probability of exiting the sample structure without inelastic scattering. The measurement system is evacuated and nearly void of any gaseous molecules, which reduces the scattering probability as soon as the electron has left the sample. An analyzer collects the released electrons and determines their kinetic energy by forcing them on a circular path through the electromagnetic lens system and measuring the radius with a position-sensitive detector.

Fig. A.3(b) depicts the potential landscape of this process. The sample and detector are placed in equilibrium by short-circuiting them. As illustrated with the light blue arrows, the binding energy of the core level under investigation can then be calculated as

$$E_B = h\nu - E_K^D - e\Phi_D, \tag{A.2}$$

where $h\nu$ is the excitation energy, E_K^D is the kinetic energy of the electron at the detector, and $e\Phi_D$ is the detector work function. Calibrating the kinetic energy and detector work function with a known sample thus allows for accurate determination of the binding energy. The prerequisite of Fermi level alignment between sample and detector is not a given and deviations are especially relevant for insulating samples. Most samples used in this work did not exhibit any charging effects, and, thus, no charge correction was necessary. The only exception was the AlN sample, which exhibited significant charging and was therefore not measurable.

A.6.1. Determination of Sample Work Function via the Secondary Electron Cut-Off

The majority of XPS and UPS studies involve the analysis of electrons that have not been inelastically scattered and so maintain the information of the binding energy from their state of origin. Nevertheless, inelastically scattered electrons also bear information of interest. In particular, the SECO, which determines the kinetic energy of the lowest-energy electrons reaching the detector, yields information on the work function of the sample. This is a consequence of the Fermi level alignment between the sample and detector resulting in the formation of an electric field. This process is described in more detail in the previous section on CPD measurements. The potential difference that has to be overcome by the electrons traveling from the sample to the detector is the difference between the work functions. The slowest electron that can pass over this potential gradient has a kinetic energy equal to this difference, as depicted in Fig. A.3(b). Therefore, determining the sample work function is possible by calibrating the detector work function.

The SECO is usually measured with an additional bias potential applied. This accelerates the electrons toward the detector, which allows the measurement of work functions smaller than the detector work function. In addition, unbiased measurements are superimposed with the signal from photoelectrons generated by electrons impinging on the chamber walls and lenses of the analyzer, creating a signal that corresponds to the analyzer work function. The application of an external bias decouples this signal from the sample signal [311].

A.6.2. Determination of Overlayer Thickness

Most electrons excited by the impinging photons do not exit the sample without any inelastic interaction. The probability for an electron to be released without inelastic scattering depends on the inelastic mean free path (IMFP) in the material and generally decreases exponentially with increasing escape depth. This results in an inherent surface sensitivity of the technique. The IMFP depends on the kinetic energy of the electron and the density of the overlayer material. A general rule of thumb for the depth of information is 10 nm for XPS and 2.5 nm for UPS.

This exponential dependence of the escape probability of electrons on depth can be used to determine the thicknesses of very thin layers, if the sample structure is known to be composed of two layers with distinguishable spectral features. In this case, the attenuation of the spectral features belonging to the substrate beneath the overlayer can be used to determine its thickness if the IMFP length of electrons is known for the overlayer material. This parameter is empirically determined to follow the relation

$$\frac{\lambda_{org}}{\text{nm}} = 0.9 + 0.0022\frac{E_K}{\text{eV}} \tag{A.3}$$

for organic overlayers such as molecular monolayers [312]. Here, λ_{org} is the IMFP in nanometers and E_K is the kinetic energy of the electron in electronvolts. Using this knowledge, the overlayer thickness can be determined using

$$d_{org} = \lambda_{org} \cdot \ln\left(\frac{I_{org}}{I_{ref}}\right), \tag{A.4}$$

where d_{org} is the thickness of the thin film, I_{org} is the intensity of the substrate's peak with the overlayer present, and I_{ref} is the intensity of a pristine reference [312], [313].

The situation becomes more complicated if the substrate and overlayer data are entangled, which is the case when a native oxide covers the semiconductor surface. In this case, the elements of the semiconductor are also present in the native oxide, which requires a more complicated approach derived by Strohmeier *et al.* [314] using the equation

$$d_{ox} = \lambda_{ox} \cdot \ln\left(\frac{N_{SC}\lambda_{SC}I_{ox}}{N_{ox}\lambda_{ox}I_{SC}} + 1\right), \tag{A.5}$$

where d_{ox} is the thickness of the native oxide, λ_{ox} and λ_{SC} are the IMFPs of the oxide and semiconductor, N_{ox} and N_{SC} are the volumetric densities of the oxide and semiconductor, and I_{ox} and I_{SC} are the peak intensities of the elemental transitions corresponding to the oxide state and the chemical state of the element in the semiconductor, respectively. The IMFPs used in this work have been gathered from the literature and from the National Institute of Standards and Technology (NIST) IMFP database [315]–[317].

A.6.3. X-Ray Photoelectron Spectroscopy

XPS measurements were carried out using a modular photoelectron spectroscopy setup including an electron-beam sample heater, a Phoibos 150 hemispherical analyzer including a charge-coupled device (CCD) detector, and an XR50-M monochromatic X-ray source equipped with a Focus500 monochromator (all parts obtained from SPECS Surface Nano Analysis). The analysis chamber of the system was kept at pressures below 5×10^{-10} mbar during measurements and maintained at a base pressure of 2×10^{-10} mbar in standby.

All XPS measurements presented in this work were obtained using Al Kα radiation from the monochromatic source with the power set to 300 W and at an acceleration voltage of 12 kV. The system was calibrated using the Ag3d transition of a reference silver sample and validated using the core-level transitions and the Au Fermi level position obtained throughout the experimental procedures performed in this work. The instrumental broadening caused by the detector resolution and the FWHM of the excitation source was determined to be 0.4 eV through analysis of the Au Fermi edge.

The samples were mounted within minutes after finishing their preparation and were evacuated in a load-lock chamber for around 1 h before a measurement was started. The sample position was optimized by maximizing the secondary electron background signal before each measurement. Initial survey spectra were recorded to verify the absence of significant contaminations and to confirm that the system was set up correctly. Afterwards, high-resolution spectra were recorded at a band-pass energy of 10 eV using the medium area lens mode by running multiple passes over the elemental transitions of interest. The take-off angle was held at 90° for all experiments. Integration time strongly depended on the signal strength and was adjusted accordingly.

The system's sample holder was equipped with an electron-beam heater, which allows for annealing procedures under UHV conditions. A thermocouple mounted directly on the sample surface was used by the device's closed-loop control, allowing for accurate temperature measurements with temperature stability of ± 2 °C. Annealing was performed in the preparation chamber, and the pressure was increased to 5×10^{-8} mbar for the highest annealing temperatures.

A.6.4. Ultraviolet Photoelectron Spectroscopy

UPS is analogous to XPS except for the difference in excitation source. For UPS, a differentially pumped helium plasma source generating He I emission ($h\nu$ =21.2 eV) was used to generate photoelectrons. This source was mounted to the same system as the X-ray source and all UPS measurements used the same analyzer setup. The He I emission line is significantly narrower than the characteristic X-rays generated during XPS, allowing for significantly improved energy resolution. An energy resolution of 0.044 eV was achieved with these settings, as determined by analysis of the Au Fermi edge of a reference sample.

UPS and XPS measurements were generally performed on the same sample for the energy level alignment studies with PPIX and Mabiq. Since UPS measurements generally take only a few minutes, these measurements were carried out before the XPS studies. Test measurements of XPS before and after UPS were performed for both molecules and did not show changes induced by beam damage of the UV light. Recording the SECO of the spectra required the application of an external bias of −10 V (using a Keithley 2400 source-measureme unit [SMU]) between the sample and detector. Spectra were recorded using the low angular dispersion lens mode and a reduced slit width to protect the detector from the high electron flux generated by the UPS source.

A.7. Ultraviolet–Visible Spectroscopy

UV–Vis measurements were carried out in transmission geometry using a 10 mm Suprasil cuvette for liquid samples or quartz samples for monolayers. Data acquisition was carried out by a Cary 5000 spectrophotometer (Agilent Technologies) with a 2 nm spectral resolution and an integration time of 1 s. Measurements on dissolved molecules were carried out in DMSO (99.9%, anhydrous, Sigma-Aldrich) or dichloromethane (99.5%, Selectophore, inhibitor-free, Merck) for PPIX and Mabiq samples, respectively. The molar concentration was adjusted for a high absorption while maintaining enough transmission for accurate measurements at adequate integration times.

A.8. Photoluminescence Spectroscopy

Photoluminescence spectroscopy was carried out using an in-house-built setup with multiple excitation laser sources (405 nm, iBeam Smart, Toptica; 532 nm, Torus, Laser Quantum; 640 nm, M Series, Dragon Lasers), a shared microscopy stage equipped with a flow cryostat (Microstat He, Oxford), and a spectrometer including a CCD camera (550 mm focal length, 300 mm^{-1} grating, iHR 550, Horiba) with a liquid nitrogen-cooled CCD camera (Symphony II, Horiba) set to a spectral binning factor of 2. A schematic depiction of the whole setup is shown in Fig. A.4

The excitation sources were combined into a single beampath using short-pass dichroic mirrors, with the beams added in stages from low to high wavelengths. Each source could be blocked individually by an in-house-built high-speed shutter based on hard disk drive actuators, as described in [318]. The excitation light passes through a 20× objective (Olympus LUCPlanFL N, 0.45 NA). It excites the sample housed in the cryostat, which is mounted using a micrometer XYZ stage to ensure accurate positioning and focus. Luminescence is collected through the same objective and reaches the spectrometer via a beamsplitter system. Appropriate long-pass filters block residual excitation light.

The measurement process was designed to require as little manual intervention as possible to ensure comparable data. An Arduino microcontroller performs all actions necessary for measurements using the three excitation sources in succession. The microcontroller opens and closes the shutter of each excitation source automatically while simultaneously triggering the CCD to acquire a spectrum with a given integration time to ensure minimal light exposure of the sample. As soon as the measurement with the first excitation wavelength is finished, the system moves the sample by around 10 µm to a pristine spot, automatically changes the required long-pass filter, and acquires a spectrum with the next excitation source. The measurement process is configurable by custom-written Labview software.

Measurements of PPIX monolayer luminescence were initiated immediately after LB deposition to limit any external influences or degradation of the monolayer. After the LB deposition

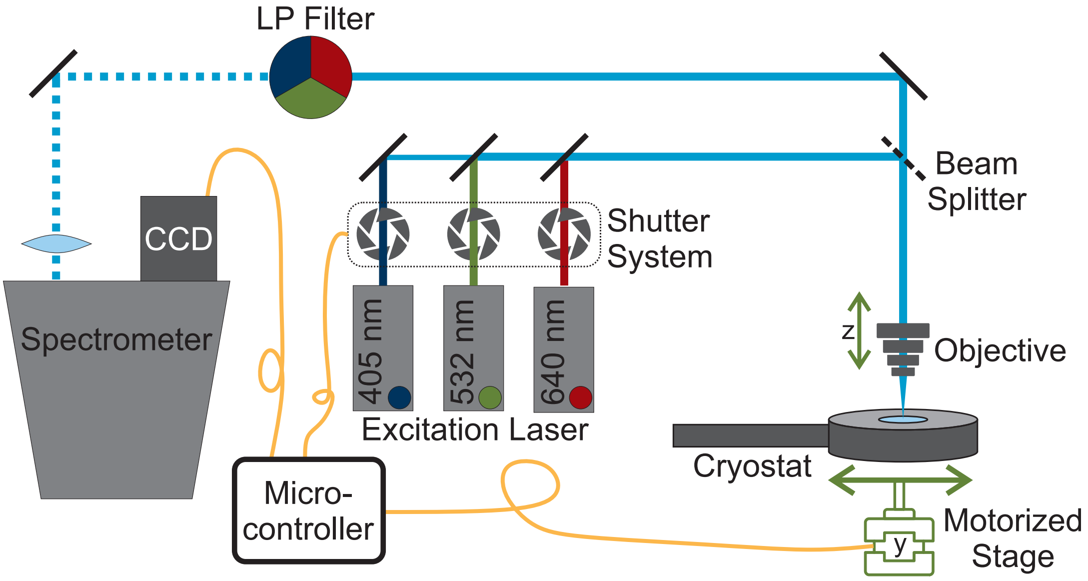

Figure A.4 Simplified schematic of the setup used to measure photoluminescence spectra and intensities with multiple excitation lasers. The excitation sources are combined using dichroic mirrors and can be individually accessed by opening or closing individually mounted shutters. The beams are routed through a microscope-style setup to access a sample mounted under vacuum conditions. A beam splitter routes the luminescence through an appropriate long-pass filter into a spectrometer for spectral analysis. A microcontroller automates sample acquisition by moving the cryostat to a pristine sample spot. It triggers a measurement by opening the laser shutter while simultaneously initiating a measurement with the CCD camera to minimize the influence of sample degradation.

process, the samples were quickly exposed to a flow of gaseous nitrogen to ensure they were completely dry, and they were transferred to the cryostat immediately afterward. The system was evacuated to below 5×10^{-6} mbar using a turbo pumping station for at least 1 h before the first measurements were initiated.

A.9. Electrical Characterization of Schottky Junctions with Protoporphyrin IX Monolayers

A.9.1. Ohmic Contact Formation

Electrical characterization of a metal–semiconductor junction is challenging because the second contact with the semiconductor, which is necessary to close the circuit and measure current, can have a significant impact on the measurement results. This can be prevented by ensuring that the contact exhibits ohmic behavior. In general, metal–semiconductor junctions are rectifying Schottky junctions, but ohmic behavior can be achieved depending on the engineering of the contact metals and the doping concentration in the vicinity of the junction [40].

The Schottky junctions investigated in this work are based on Si of various doping concentrations. Ohmic contacts were formed by locally increasing the doping concentration in the near-surface region of the material backside. A 50 nm thick layer of aluminum was deposited on the backside of the p-type Si samples by thermal evaporation. The samples were annealed at 550 °C for 5 min. This temperature approaches the eutectic temperature of 577 °C for Al–Si mixtures and, thus, leads to a diffusion of aluminum into the Si matrix. Al atoms act as p-type dopants in Si, which create a thin layer of highly doped p-type Si at the interface [319]–[321]. As described in Chapter 2, the depletion width of a Schottky junction is proportional to the inverse square root of the carrier concentration. Therefore, high doping concentrations yield a thin depletion layer, which can enable carrier tunneling through the junction. Such tunneling junctions exhibit ohmic properties. After annealing, another 50 nm of aluminum was deposited on top to establish a mechanically robust layer for contact formation.

Ohmic contacts to n-type Si were established based on the same principles, but the formation of the highly doped surface area is slightly more complex, as described in [321]–[323]. A 50 nm thick layer of 99 wt.% Au and 1 wt.% Sb was deposited by thermal evaporation on the backside of the samples and annealed at 500 °C for 5 min. This surpasses the eutectic temperature of 363 °C of Au and Si, leading to a eutectic formation at the interface. Upon cooldown, the Au is expelled from the Si as the system solidifies. Some antimony remains in the Si and acts as an n-type dopant, yielding the desired effect of surface doping. After annealing, 10 nm of Ti and 50 nm of Au were evaporated on the surface, serving as a contact layer.

A.9.2. Mercury Droplet Measurements

Electrical characterization of Schottky junctions upon the introduction of a PPIX monolayer between the semiconductor and the metal was performed on exemplary junctions of Hg and Si with various doping concentrations. A Hg droplet system, developed for controlled Hg growth experiments (EF-1400, BASi Research Products), was repurposed as a soft top contact for these experiments. The system comprises a Hg reservoir with a 150 µm capillary attached at the bottom. A plunger blocks the capillary to prevent unwanted draining of the reservoir. Droplets of reproducible size can be dispensed from the capillary by a timed lifting of this plunger, resulting in a Hg droplet hanging from the capillary.

A sample was mounted on an XYZ stage below the hanging Hg droplet to allow for accurate XY positioning and to bring the Hg droplet in contact with its surface with precision. A camera and backlight configuration enabled close monitoring of the approach process and was used to determine the contact area, assuming that a spherical contact with the diameter visible in this horizontal view was established. The capillary size served as a calibration reference. The Si samples were prepared with an ohmic contact (details given in the previous subsection) on their backside. They were mounted to a copper block on the XYZ stage using conductive double-sided copper tape. An SMU (2450, Keithley) applied a voltage and measured the current response of the junction through this backside contact and a contact wire in the Hg reservoir. The whole setup was contained in a nitrogen glove box to protect the operator from the toxic Hg and to ensure clean surfaces during measurement. A schematic view of the measurement setup and an image from the camera with a Hg droplet in contact with a sample is depicted in Fig. A.5.

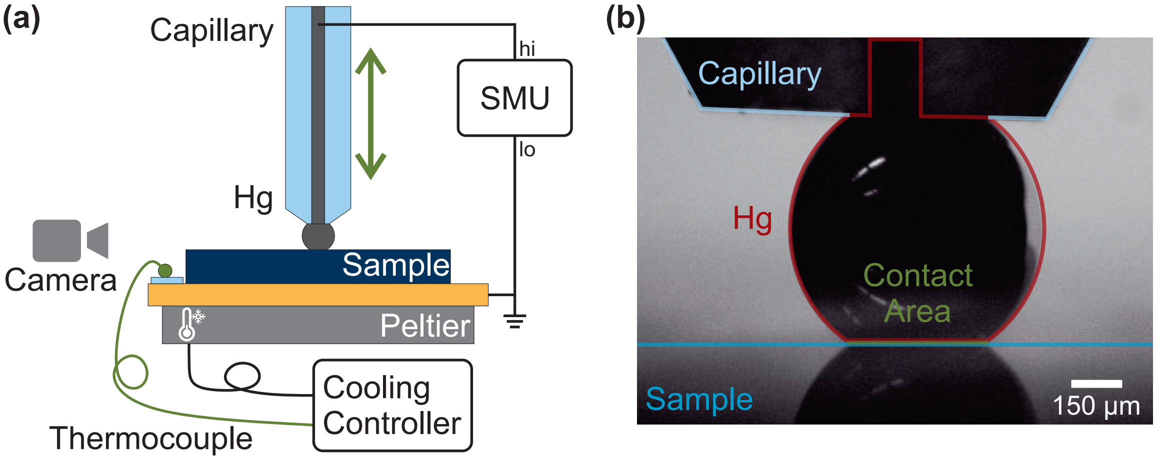

Figure A.5 (a) Schematic view of the Hg droplet setup used to analyze Hg–Si Schottky contacts. A small droplet of Hg is dispensed from a capillary, and the hanging droplet is subsequently brought into contact with the sample surface. The sample is mounted on a Peltier element which allows for temperature control. Contact with the sample is via the back surface through a thin copper sheet. (b) Camera image of a Hg droplet connecting the capillary and the sample surface. The contact area is determined by calibrating the image dimensions based on the known inner diameter of the capillary.

UI curves were acquired by scanning the voltage in 0.05 V increments, starting from the reverse bias direction from −1.5 V up to 1.5 V. This scan was repeated at least 3 times in both directions. The initial measurement at the maximum reverse bias was delayed by 10 s to exclude any capacitive charging effects.

Temperature-dependent UI curves were measured using a Peltier element to cool the samples. A current-controlled DC power supply powered the Peltier element. Its hot side was cooled using a system intended for cooling processing units in computer systems (Coreliquid P240, MSI). This comprised a radiator–pump combination filled with DI water. The original cooling unit was swapped for a slimmer aftermarket version to fit under the capillary, and the fans mounted to the radiator were removed to reduce the gas currents in the glove box. The high surface area of the radiator, in conjunction with the large thermal mass of the cooling water, enabled effective cooling for multiple hours. The current control and a thermocouple mounted to the cold side of the Peltier allowed for temperature control and accurate temperature measurements. Temperature-dependent measurements were recorded starting from room temperature and progressing to lower temperatures. While the Peltier element could also be used for sample heating, the Hg fumes released at elevated temperatures could present a health risk. They would have required more elaborate filtering of the exhaust air and Hg monitoring in the lab environment. Therefore, the temperatures were always kept at room temperature or below.

A.10. Static Water Contact Angle

SCA measurements were performed using a commercial system (OCA 15 Pro, DataPhysics Instruments) under ambient conditions. DI water droplets with a volume of 1 µL were dispensed from a high-precision syringe equipped with a blunt cannula and were manually placed on the sample surface while keeping the distance between cannula and sample as large as possible, minimizing the influence of the movement on the drop formation. Upon a short equilibration time of 5 s, a backlit image of the droplet side profile was taken and the SCA was determined by the SCA 20 (DataPhysics Instruments) control software. SCAs were averaged over at least 3 mutually non-overlapping spots on the sample surface.

A.11. *In Situ* Surface-Enhanced Attenuated Total Reflection Fourier Transform Infrared Spectroscopy

A.11.1. Sample Preparation

The *in situ* techniques used in this work are based on electrochemical measurements of samples specifically synthesized to generate surface enhancement through surface plasmon interaction and local field enhancement (the lightning rod effect). This was achieved through various approaches of depositing Au nanostructures on the IRE surface. Backside modified Si wafers (Irubis) were chosen as IREs due to their high IR transmissivity and their compatibility with standard semiconductor processes. A micromachined lamella structure on the backside of the wafers ensured normal incidence of the IR light to minimize reflective losses.

The samples were cleaned by ultrasonication in acetone (ULSI Grade, Microchemicals) and isopropanol (ULSI Grade, Microchemicals) at 400 W for 10 min each. After sonication, the samples were rinsed with isopropanol and dried under a stream of nitrogen. Oxygen plasma cleaning at 200 W for 10 min yielded surfaces free from organic contaminants. Cleaning was performed immediately before any further processing steps to minimize the readsorption of contaminants.

Black Silicon Etch

The surface structures developed over the course of this work required a roughening pretreatment, which was performed via a black Si etching process. A wet etching process was adapted from Branz *et al.* [35]. The native oxide covering the surface of the Si was removed by immersion in 5 % HF for at least 5 min, yielding a metastable H-termination on the surface [324]. The black Si etch was performed directly by placing a 100 µL droplet of 0.4 mM chloroauric acid ($HAuCl_4$, 49 % Au basis, Sigma-Aldrich) on the front of the wafer, followed by a 100 µL droplet of 1.7 % HF and 20 % hydrogen peroxide (H_2O_2, 31 %, BASF), for 5 min before rinsing in DI water. Afterwards, the backside was protected using a soft-baked photoresist (S1818, Microposit). The black Si etch resulted in high aspect ratio features on the surface, which were slightly modified by immersion in 0.4 % potassium hydroxide (KOH, 85 % KOH basis, Sigma-Aldrich) at a temperature of 30 °C for 10 s [325].

Gold Electroless Deposition

One method used to achieve metallization of the surface with Au nanostructures was electroless deposition, which was adapted from Miyake *et al.* [33]. The samples were initially treated in a 5 % HF bath for 2 min to remove the native oxide. Afterwards, electroless deposition was performed by immersion in a 50 °C warm 1:1:1 volumetric mixture of 2 % HF, 0.3 M sodium sulfite (Na_2SO_3, 97 %, Merck) with 0.1 M sodium thiosulfate ($Na_2S_2O_3$, 99.5 %, Sigma-Aldrich) and 0.1 M ammonium chloride (NH_4Cl, 99.5 %, Sigma-Aldrich), and 30 mM sodium tetrachloroaurate ($NaAuCl_4$, 99 %, Sigma-Aldrich), mixed in that order. The samples were immersed for 35 s to achieve good coverage, adhesion, and surface enhancement. They were immediately dried under a stream of nitrogen after removal from the solution, then rinsed with DI water and dried again. The photoresist protecting the back side of the sample was removed by immersion in acetone and isopropanol.

This Au deposition technique was carried out on three different sample types presented in this work. The FSG sample was synthesized analogously to prevalent literature samples, while the BSG and BSGE samples are adaptions using black Si etching as a pre-treatment for enhanced surface roughness. The BSG and BSGE samples differed by a 30 nm Au layer thermally evaporated onto the BSGE samples after electroless deposition. This layer was intended to enhance the surface conductivity of the samples to reduce the electrochemical time constants of the system and to protect any Si that was left exposed by the electroless deposition.

Gold Electrodeposition

An alternative method for depositing Au layers, developed by Andvaag *et al.* [34], was adapted for this work. Electrodeposition requires the surface to be electrically conductive, which is generally not the case for IRE samples. While the Si could be doped to achieve conductivity, the associated free carrier absorption would lead to a significant decrease in IR transmission. This issue was solved by introducing an ITO layer as an intermediate between the Si and the Au, which also serves as an adhesion promoter between the two materials. A 50 nm layer of ITO was sputtered onto the IRE samples, which were cleaned using the aforementioned procedure. The layer was annealed at 400 °C under ambient conditions for 1 h to improve its conductivity and transparency [301]. Annealed samples were mounted into the electrochemical cell used for *in situ* characterization, as described in more detail in Sec. A.11.3.

The electrolyte contained 0.1 M sodium fluoride (NaF, 99 %, Sigma-Aldrich), 250 µM $NaAuCl_4$, and 100 µM MOP (97 %, Sigma-Aldrich). Electrodeposition of Au was initiated by three CV scans from $-1\,V_{Ag/AgCl}$ to $1\,V_{Ag/AgCl}$ at a speed of $20\,mV\,s^{-1}$. Additional scans with a reduced potential window from $-1\,V_{Ag/AgCl}$ to $0.05\,V_{Ag/AgCl}$ led to the growth of a Au layer. The amount of signal enhancement achieved by the deposited Au was monitored at intermediate steps, which was possible because the deposition setup allowed for *in situ* characterization. Steady-state FTIR measurements comparing the spectrum at a potential of $0.3\,V_{Ag/AgCl}$ to the spectrum at $-0.9\,V_{Ag/AgCl}$ showed the intensities of the MOP peaks, which indicated the progress of the deposition. The enhancement reached a maximum before the signal decreased as more and more Au was deposited. Therefore, the deposition process was stopped after 40 CV cycles.

A.11.2. Scanning Electron Microscopy

SEM images were recorded on an NVision 40 microscope (Zeiss) at varying magnifications, detecting secondary electrons with an in-lens detector.

A.11.3. Electrochemical Characterization

In situ studies were performed using an in-house-built electrochemical cell, which contained mirror optics and allowed access to the backside of the sample for ATR-FTIR measurements as schematically depicted in Fig. 8.2(a). While structural components were 3D printed, all other plastic components in contact with the electrolyte were CNC-milled polyether ether ketone (PEEK), a chemically resistant material commonly used in electrochemistry applications. The cell volume was kept as small as possible and was around 3.5 mL in total. Multiple access ports allowed the addition of gas lines and electrodes, which could be connected with a ferrule and fitting system designed for chromatography applications, which mainly use inert plastic components made from PEEK or fluoropolymers (Super Flangeless, IDEX). A sapphire window at the top of the cell was used for visual control of the electrolyte level and sample condition. This window could also be used for optical excitation in future experiments. The sample and window ports were sealed using ethylene propylene diene monomer rubber (EPDM) seals. The cell was mounted on a spring-loaded system for accurate alignment with the IR beam. All experiments were performed with the electrochemical cell mounted inside the FTIR system under vacuum conditions; it was important to ensure that all ports were sealed adequately.

The cell was set up in a three-electrode configuration, with the sample IRE used as the WE. A Au wire was coiled and added toward the top of the cell to serve as the CE and a low-leakage Ag/AgCl (Driref-2SH, World Precision Instruments) electrode was used as a RE. The setup of the measurement electronics depended on the type of experiment to be performed. A digital potentiostat (Reference 1010E, Gamry) was used for steady-state experiments, electrochemical impedance spectroscopy, CV, chronoamperometry, and electrodeposition. The lack of an external hardware trigger necessitated using an analog potentiostat for step scan experiments (POS2, Bank Electronic), in combination with an arbitrary waveform generator (33250A, Agilent) controlling the timing and communication.

A.11.4. IR Measurements

FTIR measurements were performed on a Vertex 70V system (Bruker). A photovoltaic liquid nitrogen-cooled mercury cadmium telluride detector was used due to its superior response time. The external angle of incidence of the IR measurement geometry was set to 55°, following prior investigations by Morhart *et al.* on the signal intensity for such an IRE design [326].

Steady-state measurements of the IRE were performed, comparing the adsorbed and desorbed state of MOP to determine the sensitivity of the nanostructured Au films. These experiments were carried out in an aqueous electrolyte containing 100 mM $LiClO_4$ (98 %, Sigma-Aldrich) and 100 mM MOP. The liquid was bubbled with N_2 before the measurement to displace any dissolved CO_2. After the liquid was transferred to the electrochemical cell, 10 CV scans in the range of $-1.1\,V_{Ag/AgCl}$ to $0.5\,V_{Ag/AgCl}$ were run to clean and condition the sample. Afterwards, steady-state spectra were recorded by averaging over 128 scans with a spectral resolution of $4\,cm^{-1}$ at $-0.9\,V_{Ag/AgCl}$ (reference measurement) and subsequently at $0.3\,V_{Ag/AgCl}$ (sample measurement). All spectra reported in this work were produced assuming the desorbed state as the reference and the adsorbed state as the sample spectrum.

Time-dependent *in situ* FTIR analysis was carried out using either step scanning or rapid scanning, depending on the timescale of interest. As described in previous sections, the data acquisition was distributed over multiple repetitions of an identical experiment in the case of step scanning. Measurements were performed by repeatedly switching the applied voltage from $-0.9\,V_{Ag/AgCl}$ to $0.3\,V_{Ag/AgCl}$ and back. The positive potential was held for 164 ms and the negative potential for 41 ms. Data were recorded in 50 µs intervals and averaged over

5 repetitions. The initial 10 spectra before the switch to positive potentials were averaged and used as the reference spectrum. Experiments on longer time scales were performed by utilizing rapid scan during electrochemical chronoamperometry measurements. Here, spectra were acquired every 60 ms.

The resulting three-dimensional data were analyzed using the OPUS software (Bruker). Peak intensities were extracted by integrating over the peak area of every spectrum in the wavenumber range of interest. The background was excluded through a linear fit to acquire the baseline. Peak positions were determined by fitting a Gaussian profile to each spectrum in the region of interest and determining the center of the distribution.

A.12. X-Ray Diffraction

Diffraction experiments were conducted on in-house-grown $\mathrm{Al}_x\mathrm{Ga}_{1-x}\mathrm{N}$ samples to determine the Al to Ga ratios. Experiments were conducted with a Smartlab diffractometer (Rigaku) equipped with a copper Kα source and a HyPix-3000 detector (Rigaku). A germanium monochromator allowed for the acquisition of high-resolution diffraction patterns. Sample alignment progressed through an automated alignment procedure controlled by the Smartlab Studio software (Rigaku), aligning the sample surface parallel to the beam in the x and y directions. A second alignment step was corrected for off-cut surfaces by aligning the sapphire (0001) substrate peak to 41.7°. Finally, 2θ-ω scans of the (0002) diffraction peak from the AlGaN samples and the sapphire (0001) diffraction peak were performed to accurately determine the lattice constant c of the AlGaN samples.

B. Supplementary Data

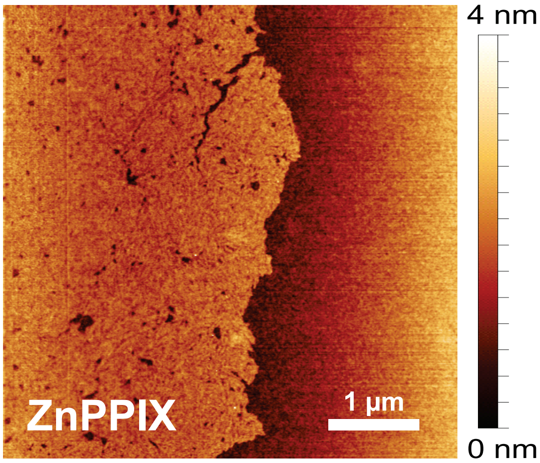

Figure B.1 Wide scan range AFM micrograph of a ZnPPIX LB layer deposited at a pressure of 2.5 mN m^{-1}, highlighting the inhomogeneity at larger scales that makes it challenging to accurately determine the relative coverage using high-magnification techniques such as AFM.

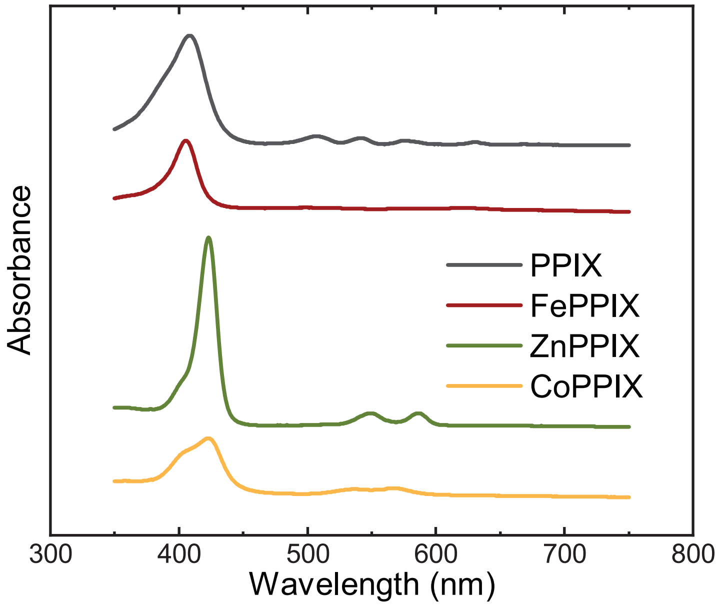

Figure B.2 Comparison of the UV–Vis absorbance spectra of all PPIX variants analyzed in this work. All spectra were recorded using a 5 µM concentration of the respective molecule dissolved in DMSO. The optical path length of 10 mm was identical for all measurements. All spectra exhibit a predominant peak located around 400 to 450 nm (Soret band) accompanied by smaller transitions at longer wavelengths (Q bands). The number of Q bands and the relative intensity vary between the different molecules. In addition, the molar extinction coefficient of the Soret band of ZnPPIX appears to be significantly higher than those of all other protoporphyrins.

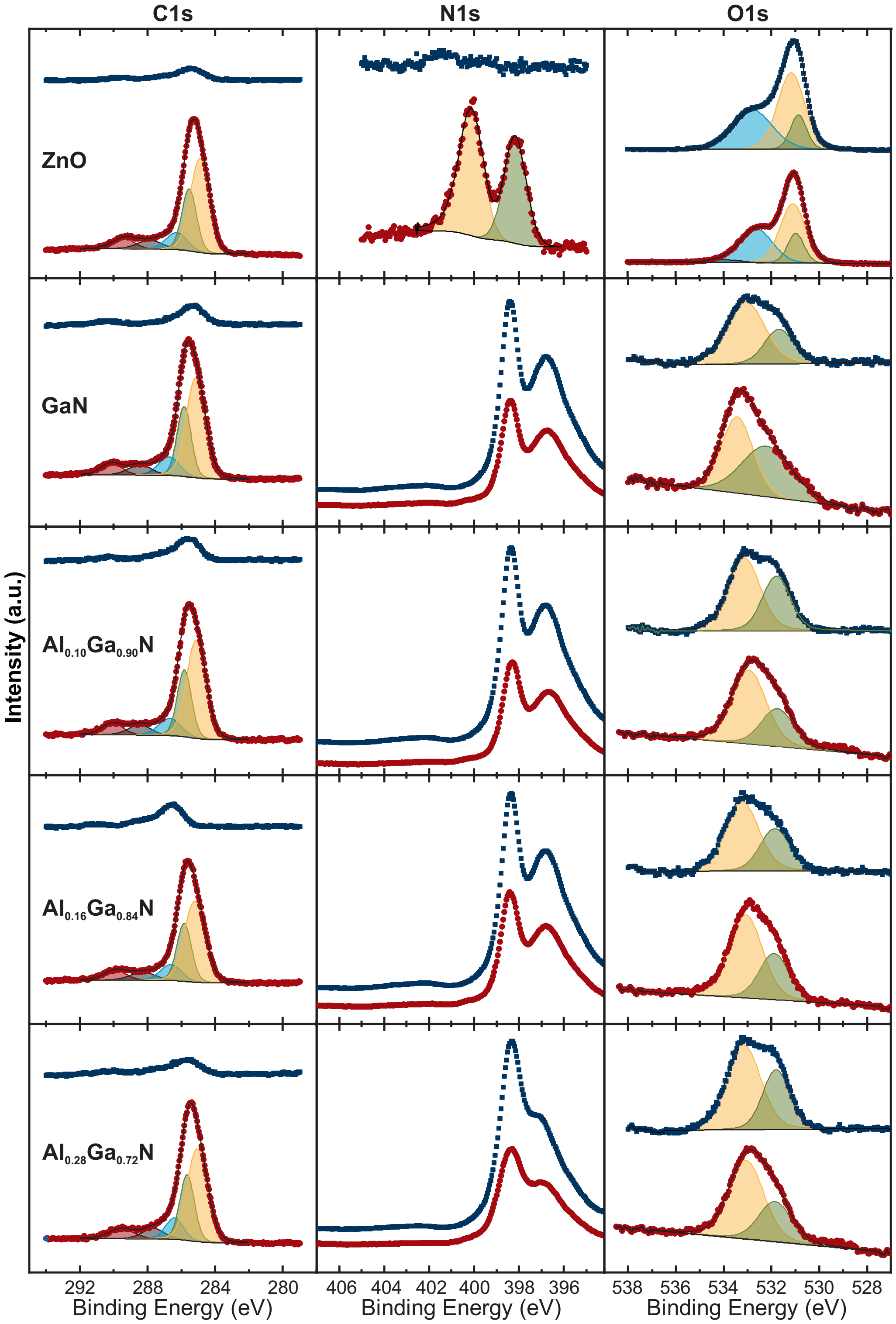

Figure B.3 XPS spectra of the reference and PPIX monolayer samples of all investigated substrates not shown in the main text.

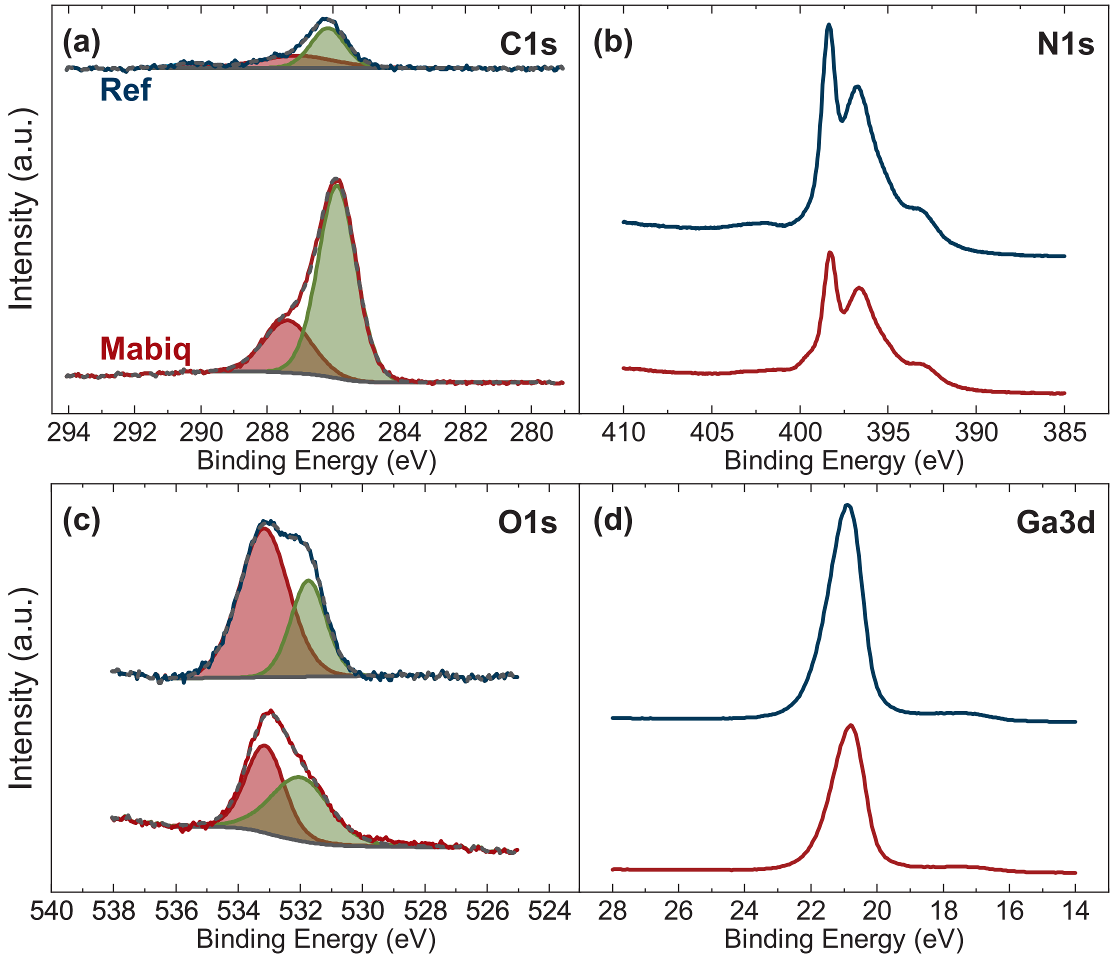

Figure B.4 XPS spectra of the reference and Mabiq monolayer samples of GaN.

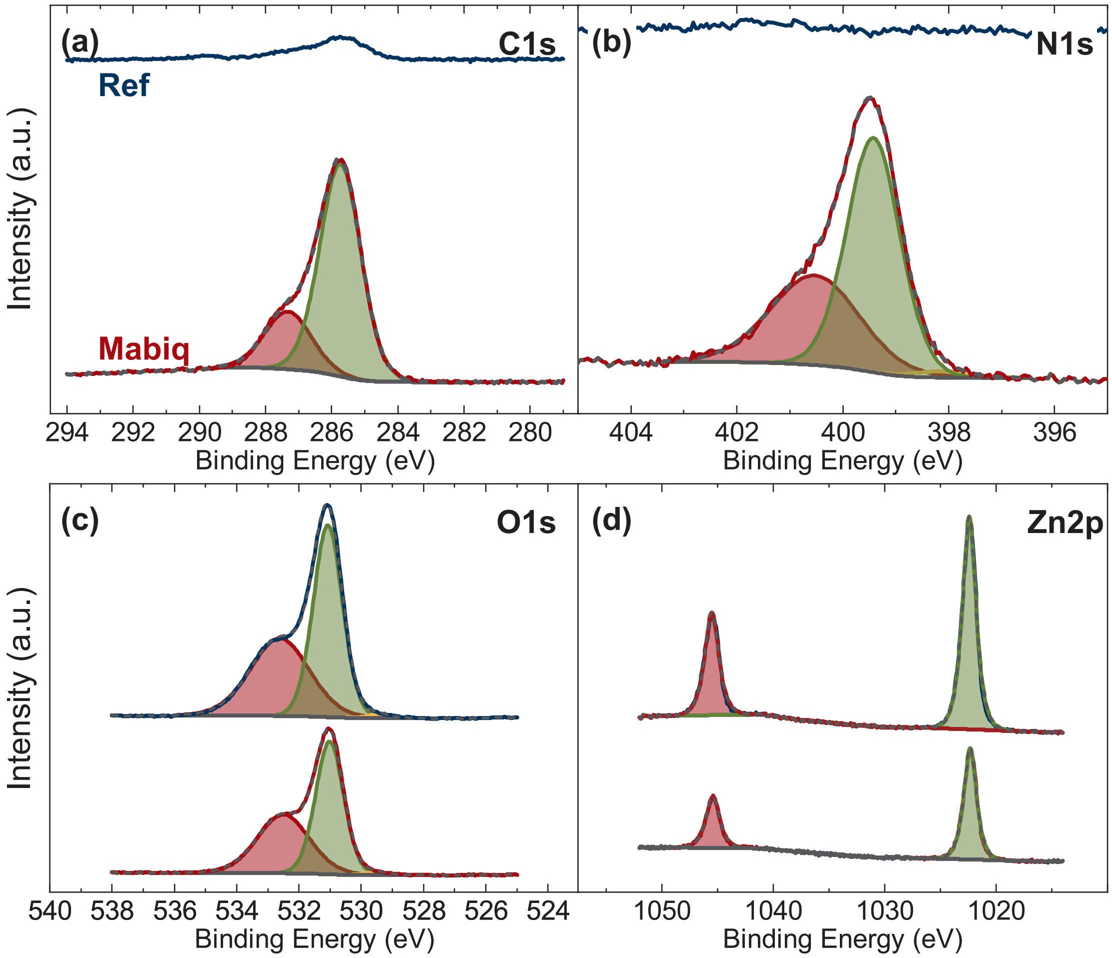

Figure B.5 XPS spectra of the reference and Mabiq monolayer samples of ZnO.

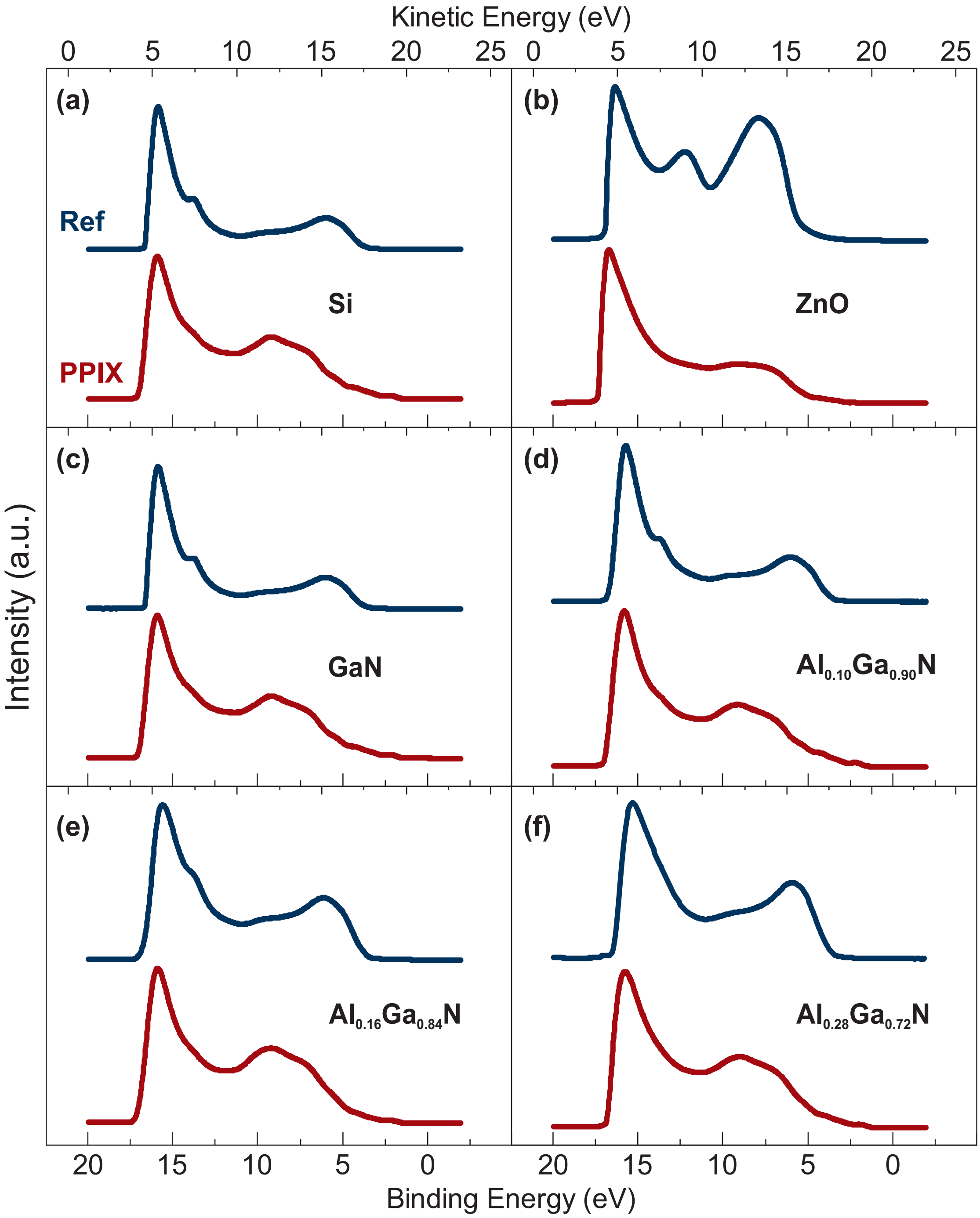

Figure B.6 UPS spectra of the reference and PPIX monolayer samples of all investigated substrates except Au.

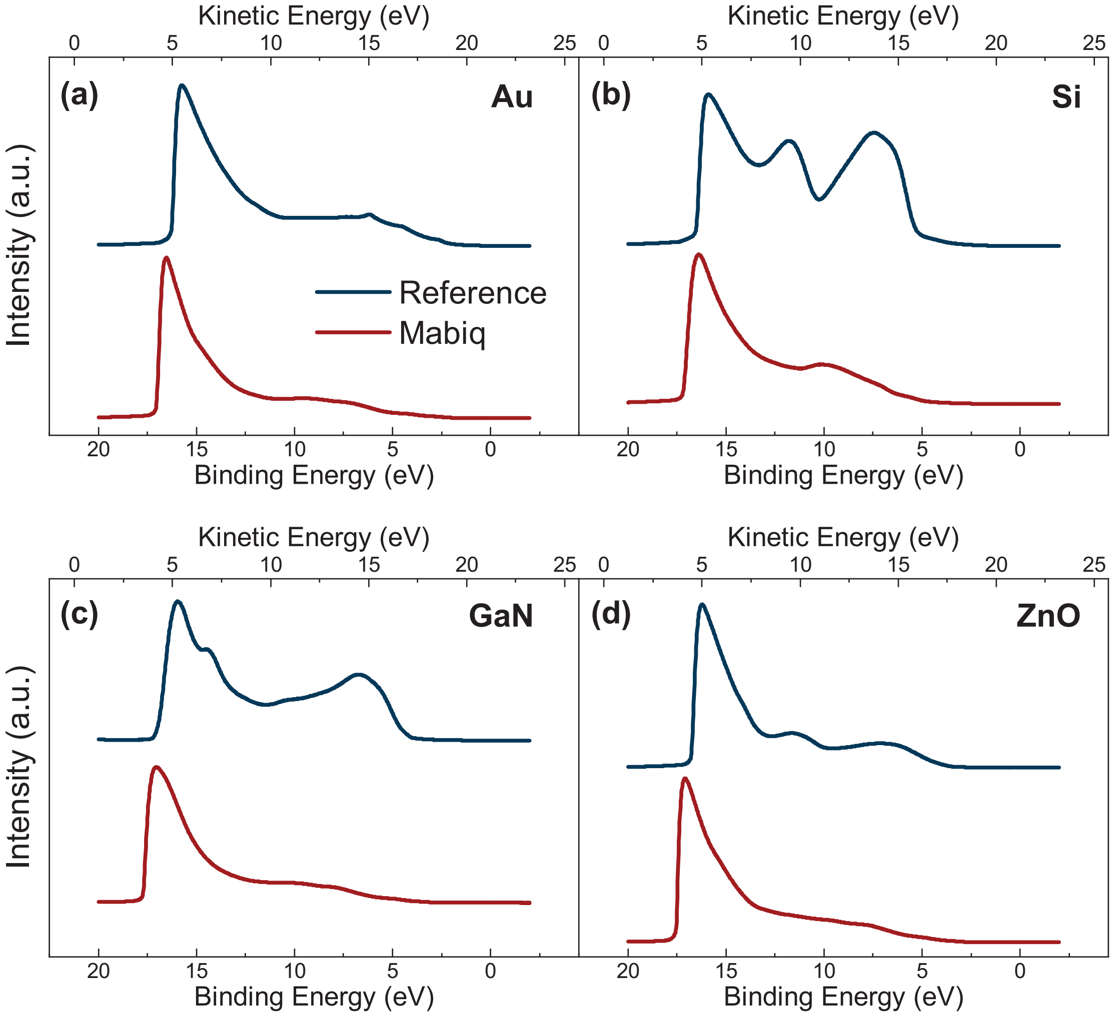

Figure B.7 UPS spectra of (a) Au, (b) Si, (c) GaN, and (d) ZnO reference substrates and Mabiq LB layer samples, showing a significant attenuation of the substrate-specific features for the LB layer samples.

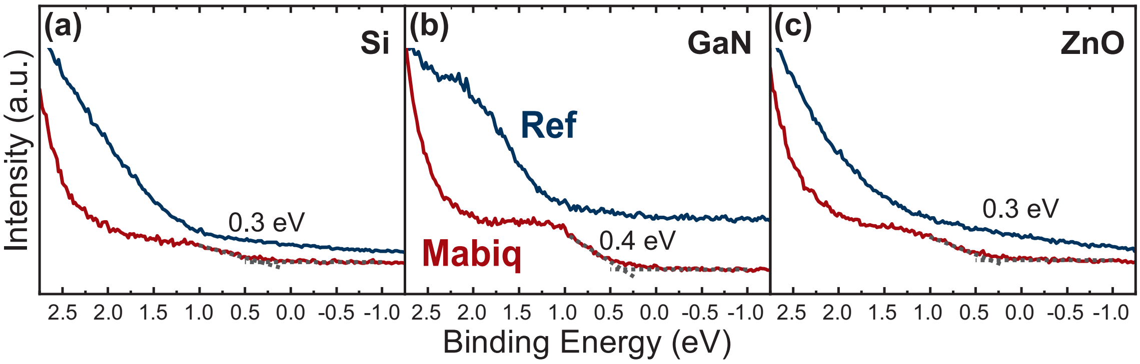

Figure B.8 Low binding energy regions of (a) Si, (b) GaN, and (c) ZnO reference substrates and samples covered with a Mabiq LB layer. Low-intensity peaks for the LB layer samples could point at partially occupied LUMO orbitals of the Mabiq. While the onset of the peak is at the expected position for GaN and ZnO, it is slightly higher than expected for the Si sample.

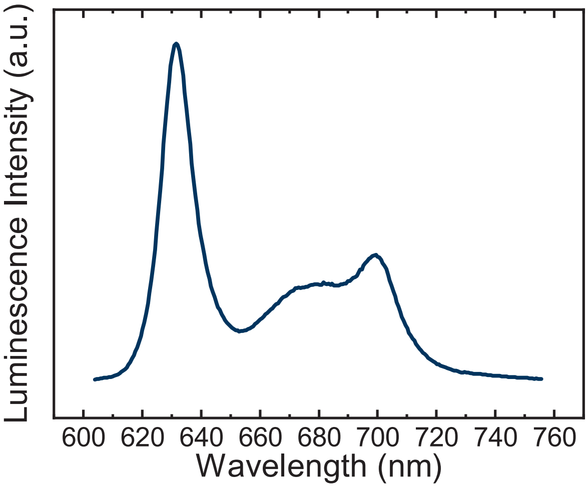

Figure B.9 Photoluminescence spectrum of PPIX dissolved in DMSO at a concentration of 50 µM for illumination at 532 nm. The spectrum was obtained with the same setup used for the solid-state samples but using an alternative detection path excluding the cryostat. While overall similar in shape to the LB layer samples, the peak ratios, width, and position are slightly shifted.

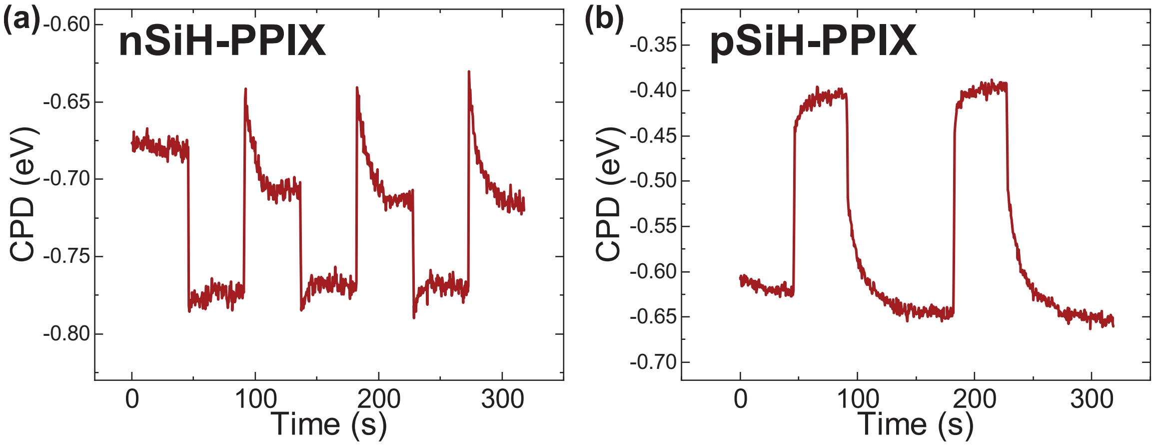

Figure B.10 SPV measurements of (a) n-type and (b) p-type Si after H-termination and covered with a PPIX LB layer in the opposite orientation to most of the LB layers investigated in this work, using the same 880 nm illumination source as shown in Fig. 6.1.

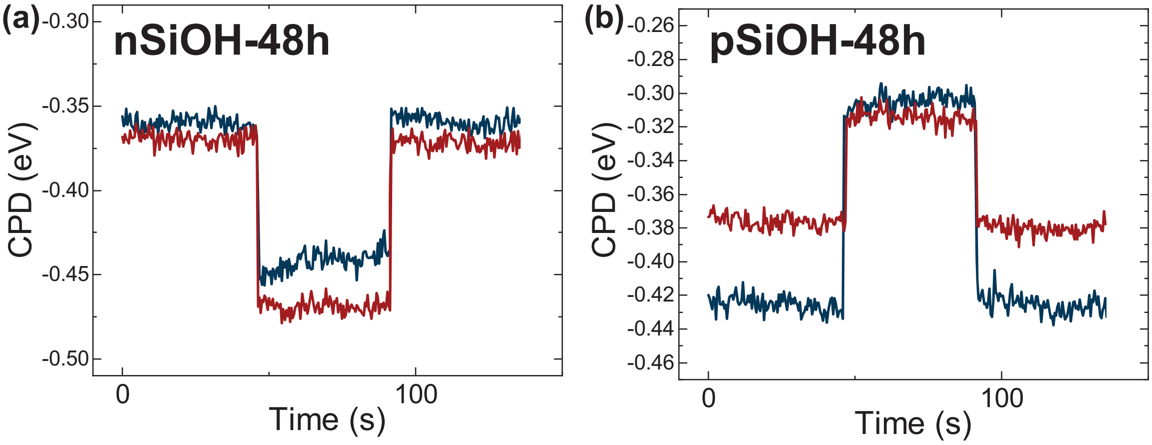

Figure B.11 SPV measurements of (a) n-type and (b) p-type Si with oxygen plasma treatment after aging for roughly 48 h in a vacuum desiccator using the same 405 nm and 880 nm illumination sources as shown in Fig. 6.1.

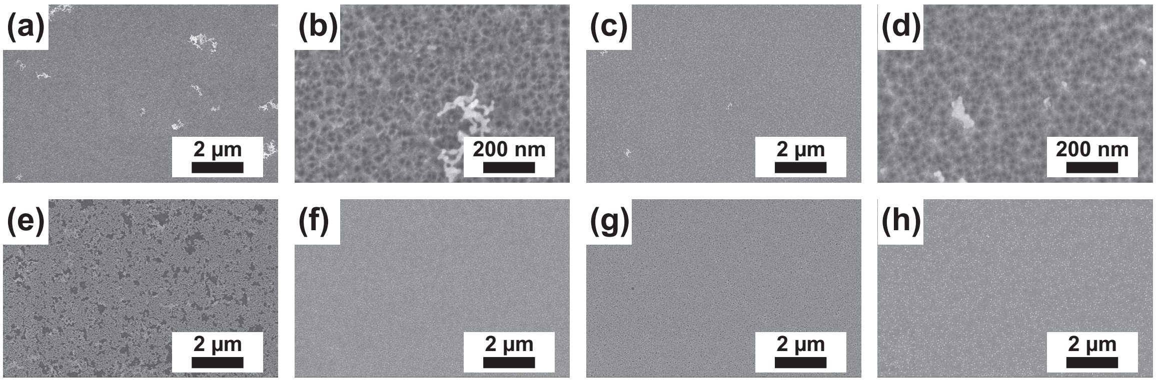

Figure B.12 Comparison of the morphologies of all investigated surfaces by SEM. (a)–(b) Black Si-treated Si surface. (c)–(d) Black Si-treated Si surface after KOH etching. (e) Black Si-treated Si surface after KOH etching and electroless deposition. (f) Black Si-treated Si surface after KOH etching, electroless deposition, and evaporation. (g) Electroless-deposited Au on polished Si. (h) Electrodeposited Au on ITO.

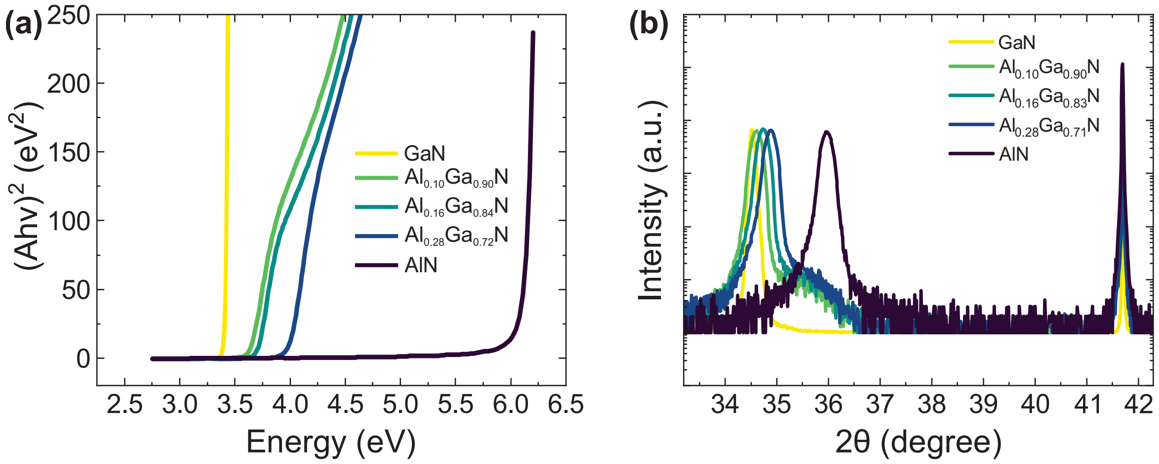

Figure B.13 (a) Tauc plot of the UV–Vis transmission data for the $Al_xGa_{x-1}N$ samples used in the analysis of charge transport between PPIX and semiconductors, showing increasing band gap with increasing Al content. (b) High-resolution 2θ-ω scans of the (0002) diffraction peak of the same AlGaN samples and the sapphire (0001) diffraction peak. All samples were aligned to the known position of the sapphire (0001) peak at 41.7° to exclude any errors from off-cut surfaces.

Table 2 Overview of the material parameters and derived Al content extracted from XRD and UV–Vis measurements. Comparison of the band gap (UV–Vis) or lattice constant (XRD) with literature values yields the relative Al content in the substrates. The average of both results was used in this work [327].

	(0002) Diffraction (2θ, degrees)	Lattice Constant c (Å)	Al Content (XRD, %)	Band Gap (eV)	Al Content (UV–Vis, %)
GaN	34.50 ± 0.01	5.199 ± 0.001	0	3.42 ± 0.03	0
$Al_{0.10}Ga_{0.90}N$	34.63 ± 0.01	5.180 ± 0.001	9 ± 1	3.63 ± 0.03	11 ± 2
$Al_{0.16}Ga_{0.84}N$	34.74 ± 0.01	5.164 ± 0.001	17 ± 1	3.71 ± 0.03	15 ± 2
$Al_{0.28}Ga_{0.72}N$	34.88 ± 0.01	5.144 ± 0.001	27 ± 1	4.00 ± 0.03	29 ± 2
AlN	35.97 ± 0.01	4.993 ± 0.001	100	6.15 ± 0.03	100

Bibliography

[1] S. Teske, Ed., *Achieving the Paris Climate Agreement Goals*. Cham, Switzerland: Springer-Verlag, 2019, pp. 1–491.

[2] P. Friedlingstein, “A steep road to climate stabilization,” *Nature*, vol. 451, no. 7176, pp. 297–298, 2008.

[3] A. A. Kebede, T. Kalogiannis, J. Van Mierlo, and M. Berecibar, “A comprehensive review of stationary energy storage devices for large scale renewable energy sources grid integration,” *Renew. Sustain. Energy Rev.*, vol. 159, 2022, Art. no. 112213.

[4] A. Evans, V. Strezov, and T. J. Evans, “Assessment of utility energy storage options for increased renewable energy penetration,” *Renew. Sustain. Energy Rev.*, vol. 16, no. 6, pp. 4141–4147, 2012.

[5] M. Beaudin, H. Zareipour, A. Schellenberglabe, and W. Rosehart, “Energy storage for mitigating the variability of renewable electricity sources: An updated review,” *Energy Sustain. Dev.*, vol. 14, no. 4, pp. 302–314, 2010.

[6] E. Rivard, M. Trudeau, and K. Zaghib, “Hydrogen storage for mobility: A review,” *Materials*, vol. 12, no. 12, 2019, Art. no. 1973.

[7] F. A. Rahman *et al.*, “Pollution to solution: Capture and sequestration of carbon dioxide (CO_2) and its utilization as a renewable energy source for a sustainable future,” *Renew. Sustain. Energy Rev.*, vol. 71, pp. 112–126, 2017.

[8] G. A. Olah, G. K. Prakash, and A. Goeppert, “Anthropogenic chemical carbon cycle for a sustainable future,” *J. Am. Chem. Soc.*, vol. 133, no. 33, pp. 12 881–12 898, 2011.

[9] X. Zhang, G. Zhang, C. Song, and X. Guo, “Catalytic conversion of carbon dioxide to methanol: Current status and future perspective,” *Front. Energy Res.*, vol. 8, Art. no. 621119, 2021.

[10] Z. Yan, J. L. Hitt, J. A. Turner, and T. E. Mallouk, “Renewable electricity storage using electrolysis,” *Proc. Natl. Acad. Sci. USA*, vol. 117, no. 23, pp. 12 558–12 563, 2020.

[11] B. Kumar, M. Llorente, J. Froehlich, T. Dang, A. Sathrum, and C. P. Kubiak, “Photochemical and photoelectrochemical reduction of CO_2,” *Annu. Rev. Phys. Chem.*, vol. 63, no. 1, pp. 541–569, 2012.

[12] X. Tao, Y. Zhao, S. Wang, C. Li, and R. Li, “Recent advances and perspectives for solar-driven water splitting using particulate photocatalysts,” *Chem. Soc. Rev.*, vol. 51, no. 9, pp. 3561–3608, 2022.

[13] M. D. Burkart, N. Hazari, C. L. Tway, and E. L. Zeitler, “Opportunities and challenges for catalysis in carbon dioxide utilization,” *ACS Catal.*, vol. 9, no. 9, pp. 7937–7956, 2019.

[14] L. K. Putri, B.-J. Ng, W.-J. Ong, S.-P. Chai, and A. R. Mohamed, “Toward excellence in photocathode engineering for photoelectrochemical CO_2 reduction: Design rationales and current progress,” *Adv. Energy Mater.*, vol. 12, no. 41, 2022, Art. no. 2201093.

[15] K. Maeda, “Metal-complex/semiconductor hybrid photocatalysts and photoelectrodes for CO_2 reduction driven by visible light,” *Adv. Mater.*, vol. 31, no. 25, 2019, Art. no. 1808205.

[16] L. M. Kustov, “Catalysis by hybrid nanomaterials,” *Molecules*, vol. 26, no. 2, 2021, Art. no. 352.

[17] S. Sato *et al.*, “Electrical matching at metal/molecule contacts for efficient heterogeneous charge transfer,” *ACS Nano*, vol. 12, no. 2, pp. 1228–1235, 2018.

[18] E. A. Reyes Cruz *et al.*, “Molecular-modified photocathodes for applications in artificial photosynthesis and solar-to-fuel technologies,” *Chem. Rev.*, vol. 122, no. 21, pp. 16 051–16 109, 2022.

[19] D. A. Garcia Osorio, G. Neri, and A. J. Cowan, “Hybrid photocathodes for carbon dioxide reduction: Interfaces for charge separation and selective catalysis,” *ChemPhotoChem*, vol. 5, no. 7, pp. 595–610, 2021.

[20] H. Tian, “Molecular catalyst immobilized photocathodes for water/proton and carbon dioxide reduction,” *ChemSusChem*, vol. 8, no. 22, pp. 3746–3759, 2015.

[21] J. Shen *et al.*, “Electrocatalytic reduction of carbon dioxide to carbon monoxide and methane at an immobilized cobalt protoporphyrin,” *Nat. Commun.*, vol. 6, no. 1, 2015, Art. no. 8177.

[22] J. Shen, Y. Y. Birdja, and M. T. M. Koper, “Electrocatalytic nitrate reduction by a cobalt protoporphyrin immobilized on a pyrolytic graphite electrode,” *Langmuir*, vol. 31, no. 30, pp. 8495–8501, 2015.

[23] J. A. Mennel, H. Pan, S. W. Palladino, and C. J. Barile, “Electrocatalytic CO_2 reduction by self-assembled monolayers of metal porphyrins,” *J. Phys. Chem. C*, vol. 124, no. 36, pp. 19 716–19 724, 2020.

[24] X. Zhang *et al.*, “Highly selective and active CO_2 reduction electrocatalysts based on cobalt phthalocyanine/carbon nanotube hybrid structures,” *Nat. Commun.*, vol. 8, no. 1, 2017, Art. no. 14675.

[25] S. A. J. Boyce, J. Moutet, L. Niederegger, T. Simler, G. Nocton, and C. R. Hess, “Influence of a lanthanide ion on the Ni site of a heterobimetallic 3d–4f Mabiq complex,” *Inorg. Chem.*, vol. 60, no. 1, pp. 403–411, 2021.

[26] K. Rickmeyer, L. Niederegger, M. Keilwerth, and C. R. Hess, “Multifaceted role of the noninnocent Mabiq ligand in promoting selective reduction of CO_2 to CO,” *ACS Catal.*, vol. 12, no. 5, pp. 3046–3057, 2022.

[27] R. Lauenstein *et al.*, “The central role of the metal ion for photoactivity: Zn– *vs.* Ni–Mabiq,” *Chem. Sci.*, vol. 12, no. 21, pp. 7521–7532, 2021.

[28] A. Listorti, B. O’Regan, and J. R. Durrant, “Electron transfer dynamics in dye-sensitized solar cells,” *Chem. Mater.*, vol. 23, no. 15, pp. 3381–3399, 2011.

[29] R. L. Milot, G. F. Moore, R. H. Crabtree, G. W. Brudvig, and C. A. Schmuttenmaer, “Electron injection dynamics from photoexcited porphyrin dyes into SnO_2 and TiO_2 nanoparticles,” *J. Phys. Chem. C*, vol. 117, no. 42, pp. 21 662–21 670, 2013.

[30] J. B. Asbury, E. Hao, Y. Wang, H. N. Ghosh, and T. Lian, “Ultrafast electron transfer dynamics from molecular adsorbates to semiconductor nanocrystalline thin films,” *J. Phys. Chem. B*, vol. 105, no. 20, pp. 4545–4557, 2001.

[31] D. F. Zigler *et al.*, “Disentangling the physical processes responsible for the kinetic complexity in interfacial electron transfer of excited Ru(II) polypyridyl dyes on TiO_2,” *J. Am. Chem. Soc.*, vol. 138, no. 13, pp. 4426–4438, 2016.

[32] M. Jurow, A. E. Schuckman, J. D. Batteas, and C. M. Drain, “Porphyrins as molecular electronic components of functional devices,” *Coord. Chem. Rev.*, vol. 254, no. 19–20, pp. 2297–2310, 2010.

[33] H. Miyake, S. Ye, and M. Osawa, “Electroless deposition of gold thin films on silicon for surface-enhanced infrared spectroelectrochemistry,” *Electrochem. Commun.*, vol. 4, no. 12, pp. 973–977, 2002.

[34] I. R. Andvaag, T. A. Morhart, O. J. Clarke, and I. J. Burgess, “Hybrid gold-conductive metal oxide films for attenuated total reflectance surface enhanced infrared absorption spectroscopy,” *ACS Appl. Nano Mater.*, vol. 2, no. 3, pp. 1274–1284, 2019.

[35] H. M. Branz, V. E. Yost, S. Ward, K. M. Jones, B. To, and P. Stradins, “Nanostructured black silicon and the optical reflectance of graded-density surfaces,” *Appl. Phys. Lett.*, vol. 94, no. 23, 2009, Art. no. 231121.

[36] A. Quirk, B. Unni, and I. J. Burgess, “Surface enhanced infrared studies of 4-methoxypyridine adsorption on gold film electrodes,” *Langmuir*, vol. 32, no. 9, pp. 2184–2191, 2016.

[37] A. Polman, M. Knight, E. C. Garnett, B. Ehrler, and W. C. Sinke, “Photovoltaic materials: Present efficiencies and future challenges,” *Science*, vol. 352, no. 6283, 2016.

[38] J. Liu, Y. Yao, S. Xiao, and X. Gu, “Review of status developments of high-efficiency crystalline silicon solar cells,” *J. Phys. D: Appl. Phys.*, vol. 51, no. 12, 2018, Art. no. 123001.

[39] M. Levinshtein, S. Rumyantsev, and M. Shur, Eds., *Handbook Series on Semiconductor Parameters*. Singapore, Singapore: World Scientific, 1996.

[40] S. M. Sze, Y. Li, and K. K. Ng, *Physics of Semiconductor Devices*, 4th ed. New York, NY, USA: Wiley-Interscience, 2021.

[41] G. W. Trucks, K. Raghavachari, G. S. Higashi, and Y. J. Chabal, “Mechanism of HF etching of silicon surfaces: A theoretical understanding of hydrogen passivation,” *Phys. Rev. Lett.*, vol. 65, no. 4, pp. 504–507, 1990.

[42] J. Dabrowski and H.-J. Müssig, *Silicon Surfaces and Formation of Interfaces*. Singapore, Singapore: World Scientific, 2000.

[43] N. Kaminski and O. Hilt, “SiC and GaN devices – wide bandgap is not all the same,” *IET Circuits Devices Syst.*, vol. 8, no. 3, pp. 227–236, 2014.

[44] T. Narita *et al.*, “Progress on and challenges of p-type formation for GaN power devices,” *J. Appl. Phys.*, vol. 128, no. 9, 2020, Art. no. 090901.

[45] I. Akasaki and H. Amano, “Breakthroughs in improving crystal quality of GaN and invention of the p-n junction blue-light-emitting diode,” *Jpn. J. Appl. Phys.*, vol. 45, no. 12, pp. 9001–9010, 2006.

[46] S. Nakamura, T. Mukai, and M. Senoh, “High-power GaN p-n junction blue-light-emitting diodes,” *Jpn. J. Appl. Phys.*, vol. 30, no. 12A, pp. L1998–L2001, 1991.

[47] T. Mattila and A. Zunger, “Predicted bond length variation in wurtzite and zinc-blende InGaN and AlGaN alloys,” *J. Appl. Phys.*, vol. 85, no. 1, pp. 160–167, 1998.

[48] N. Susilo *et al.*, “Precise determination of polarization fields in c-plane GaN/$Al_xGa_{1-x}N$/GaN heterostructures with capacitance–voltage-measurements,” *Jpn. J. Appl. Phys.*, vol. 58, no. SC, 2019, Art. no. SCCB08.

[49] S.-C. Lin *et al.*, “Experimental determination of electron affinities for InN and GaN polar surfaces,” *Appl. Phys. Express*, vol. 5, no. 3, 2012, Art. no. 031003.

[50] Y.-C. Tsai and C. Bayram, “Band alignments of ternary wurtzite and zincblende III-nitrides investigated by hybrid density functional theory,” *ACS Omega*, vol. 5, no. 8, pp. 3917–3923, 2020.

[51] C. I. Wu, A. Kahn, E. S. Hellman, and D. N. E. Buchanan, “Electron affinity at aluminum nitride surfaces,” *Appl. Phys. Lett.*, vol. 73, no. 10, pp. 1346–1348, 1998.

[52] P. G. Moses, M. Miao, Q. Yan, and C. G. Van de Walle, “Hybrid functional investigations of band gaps and band alignments for AlN, GaN, InN, and InGaN,” *J. Chem. Phys.*, vol. 134, no. 8, 2011, Art. no. 084703.

[53] H. Yamashita, K. Fukui, S. Misawa, and S. Yoshida, “Optical properties of AlN epitaxial thin films in the vacuum ultraviolet region,” *J. Appl. Phys.*, vol. 50, no. 2, pp. 896–898, 1979.

[54] S. P. Grabowski *et al.*, “Electron affinity of $\mathrm{Al}_x\mathrm{Ga}_{1-x}\mathrm{N}$(0001) surfaces,” *Appl. Phys. Lett.*, vol. 78, no. 17, pp. 2503–2505, 2001.

[55] I. Shalish, Y. Shapira, L. Burstein, and J. Salzman, “Surface states and surface oxide in GaN layers,” *J. Appl. Phys.*, vol. 89, no. 1, pp. 390–395, 2000.

[56] S. W. King *et al.*, “Cleaning of AlN and GaN surfaces,” *J. Appl. Phys.*, vol. 84, no. 9, pp. 5248–5260, 1998.

[57] L. L. Smith, S. W. King, R. J. Nemanich, and R. F. Davis, “Cleaning of GaN surfaces,” *J. Electron. Mater.*, vol. 25, no. 5, pp. 805–810, 1996.

[58] B. Sarkar *et al.*, “N- and p- type doping in Al-rich AlGaN and AlN,” *ECS Meet. Abstr.*, vol. MA2018-02, no. 38, 2018, Art. no. 1283.

[59] H. Amano, M. Kito, K. Hiramatsu, and I. Akasaki, “P-type conduction in Mg-doped GaN treated with low-energy electron beam irradiation (LEEBI),” *Jpn. J. Appl. Phys.*, vol. 28, no. 12 A, pp. L2112–L2114, 1989.

[60] C. Jagadish and S. Pearton, Eds., *Zinc Oxide Bulk, Thin Films and Nanostructures*. Oxford, UK: Elsevier, 2006.

[61] Ü. Özgür *et al.*, “A comprehensive review of ZnO materials and devices,” *J. Appl. Phys.*, vol. 98, no. 4, 2005, Art. no. 041301.

[62] V. Srikant and D. R. Clarke, “On the optical band gap of zinc oxide,” *J. Appl. Phys.*, vol. 83, no. 10, pp. 5447–5451, 1998.

[63] K. Jacobi, G. Zwicker, and A. Gutmann, “Work function, electron affinity and band bending of zinc oxide surfaces,” *Surf. Sci.*, vol. 141, no. 1, pp. 109–125, 1984.

[64] Z. Zhang and J. T. Yates, “Band bending in semiconductors: Chemical and physical consequences at surfaces and interfaces,” *Chem. Rev.*, vol. 112, no. 10, pp. 5520–5551, 2012.

[65] A. Zangwill, *Physics at Surfaces*. Cambridge, UK: Cambridge Univ. Press, 1988.

[66] K. Sell, I. Barke, S. Polei, C. Schumann, V. von Oeynhausen, and K.-H. Meiwes-Broer, “Surface photovoltage of Ag nanoparticles and Au chains on Si(111),” *Phys. Status Solidi B*, vol. 247, no. 5, pp. 1087–1094, 2010.

[67] W. H. Brattain, “Evidence for surface states on semiconductors from change in contact potential on illumination,” *Phys. Rev.*, vol. 72, no. 4, p. 345, 1947.

[68] W. H. Brattain and J. Bardeen, “Surface properties of germanium,” *Bell Syst. Tech. J.*, vol. 32, no. 1, pp. 1–41, 1953.

[69] L. Kronik, “Surface photovoltage phenomena: Theory, experiment, and applications,” *Surf. Sci. Rep.*, vol. 37, no. 1–5, pp. 1–206, 1999.

[70] W. Mönch, “Role of virtual gap states and defects in metal-semiconductor contacts,” *Phys. Rev. Lett.*, vol. 58, no. 12, pp. 1260–1263, 1987.

[71] R. T. Tung, “The physics and chemistry of the Schottky barrier height,” *Appl. Phys. Rev.*, vol. 1, no. 1, 2014, Art. no. 011304.

[72] K. B. Blodgett, “Monomolecular films of fatty acids on glass,” *J. Am. Chem. Soc.*, vol. 56, no. 2, p. 495, 1934.

[73] K. B. Blodgett, “Films built by depositing successive monomolecular layers on a solid surface,” *J. Am. Chem. Soc.*, vol. 57, no. 6, pp. 1007–1022, 1935.

[74] O. N. Oliveira, L. Caseli, and K. Ariga, “The past and the future of Langmuir and Langmuir–Blodgett films,” *Chem. Rev.*, vol. 122, no. 6, pp. 6459–6513, 2022.

[75] L. Xu, A. R. Tetreault, H. H. Khaligh, I. A. Goldthorpe, S. D. Wettig, and M. A. Pope, “Continuous Langmuir–Blodgett deposition and transfer by controlled edge-to-edge assembly of floating 2D materials,” *Langmuir*, vol. 35, no. 1, pp. 51–59, 2019.

[76] D. R. Talham, T. Yamamoto, and M. W. Meisel, “Langmuir–Blodgett films of molecular organic materials,” *J. Phys. Condens. Matter*, vol. 20, no. 18, 2008, Art. no. 184006.

[77] S. Paul *et al.*, “Langmuir-Blodgett film deposition of metallic nanoparticles and their application to electronic memory structures,” *Nano Lett.*, vol. 3, no. 4, pp. 533–536, 2003.

[78] M. C. Petty, *Langmuir-Blodgett Films: An Introduction*. Cambridge, UK: Cambridge Univ. Press, 1996.

[79] L. Wilhelmy, “Ueber die Abhängigkeit der Capillaritäts-Constanten des Alkohols von Substanz und Gestalt des benetzten festen Körpers,” *Ann. Phys.*, vol. 195, no. 6, pp. 177–217, 1863.

[80] H. Motschmann and H. Möhwald, *Handbook of Applied Surface and Colloid Chemistry*, K. Holmberg, Ed. Weinheim, Germany: Wiley, 2001.

[81] V. M. Kaganer, H. Möhwald, and P. Dutta, “Structure and phase transitions in Langmuir monolayers,” *Rev. Mod. Phys.*, vol. 71, no. 3, pp. 779–819, 1999.

[82] N. K. Adam, “The properties and molecular structure of thin films. Part II.—Condensed films,” *Proc. R. Soc. Lond.*, vol. 101, no. 712, pp. 452–472, 1922.

[83] X. Zhuang, D. Wilk, L. Marrucci, and Y. R. Shen, “Orientation of amphiphilic molecules on polar substrates,” *Phys. Rev. Lett.*, vol. 75, no. 11, pp. 2144–2147, 1995.

[84] K. Przykaza, K. Woźniak, M. Jurak, A. E. Wiącek, and R. Mroczka, “Properties of the Langmuir and Langmuir–Blodgett monolayers of cholesterol-cyclosporine A on water and polymer support,” *Adsorption*, vol. 25, no. 4, pp. 923–936, 2019.

[85] S. S. You *et al.*, “Comparison of the mechanical properties of self-assembled Langmuir monolayers of nanoparticles and phospholipids,” *Langmuir*, vol. 29, no. 37, pp. 11 751–11 757, 2013.

[86] A. Ulman, “Formation and structure of self-assembled monolayers,” *Chem. Rev.*, vol. 96, no. 4, pp. 1533–1554, 1996.

[87] D. K. Schwartz, “Mechanisms and kinetics of self-assembled monolayer formation,” *Annu. Rev. Phys. Chem.*, vol. 52, no. 1, pp. 107–137, 2001.

[88] S. P. Pujari, L. Scheres, A. T. Marcelis, and H. Zuilhof, “Covalent surface modification of oxide surfaces,” *Angew. Chem. Int. Ed.*, vol. 53, no. 25, pp. 6322–6356, 2014.

[89] E. L. Hanson, J. Schwartz, B. Nickel, N. Koch, and M. F. Danisman, “Bonding self-assembled, compact organophosphonate monolayers to the native oxide surface of silicon,” *J. Am. Chem. Soc.*, vol. 125, no. 51, pp. 16 074–16 080, 2003.

[90] A. Vega, P. Thissen, and Y. J. Chabal, “Environment-controlled tethering by aggregation and growth of phosphonic acid monolayers on silicon oxide,” *Langmuir*, vol. 28, no. 21, pp. 8046–8051, 2012.

[91] C. D. Bain, E. B. Troughton, Y. T. Tao, J. Evall, G. M. Whitesides, and R. G. Nuzzo, “Formation of monolayer films by the spontaneous assembly of organic thiols from solution onto gold,” *J. Am. Chem. Soc.*, vol. 111, no. 1, pp. 321–335, 1989.

[92] L. Wang, U. S. Schubert, and S. Hoeppener, “Surface chemical reactions on self-assembled silane based monolayers,” *Chem. Soc. Rev.*, vol. 50, no. 11, pp. 6507–6540, 2021.

[93] A. Henning *et al.*, “Aluminum oxide at the monolayer limit via oxidant-free plasma-assisted atomic layer deposition on GaN,” *Adv. Funct. Mater.*, vol. 31, no. 33, 2021, Art. no. 2101441.

[94] S. H. Gyepi-Garbrah and R. Šilerová, “The first direct comparison of self-assembly and Langmuir–Blodgett deposition techniques: Two routes to highly organized monolayers,” *Phys. Chem. Chem. Phys.*, vol. 4, no. 14, pp. 3436–3442, 2002.

[95] M. Sypabekova, A. Hagemann, D. Rho, and S. Kim, “Review: 3-aminopropyltriethoxysilane (APTES) deposition methods on oxide surfaces in solution and vapor phases for biosensing applications,” *Biosensors*, vol. 13, no. 1, 2022, Art. no. 36.

[96] A. R. Yadav, R. Sriram, J. A. Carter, and B. L. Miller, “Comparative study of solution-phase and vapor-phase deposition of aminosilanes on silicon dioxide surfaces,” *Mater. Sci. Eng. C*, vol. 35, no. 1, pp. 283–290, 2014.

[97] N. Gartmann, C. Schütze, H. Ritter, and D. Brühwiler, “The effect of water on the functionalization of mesoporous silica with 3-aminopropyltriethoxysilane,” *J. Phys. Chem. Lett.*, vol. 1, no. 1, pp. 379–382, 2010.

[98] H. Ma, H.-L. Yip, F. Huang, and A. K.-Y. Jen, “Interface engineering for organic electronics,” *Adv. Funct. Mater.*, vol. 20, no. 9, pp. 1371–1388, 2010.

[99] N. Ueno, *Physics of Organic Semiconductors*, W. Brütting, Ed. Weinheim, Germany: Wiley-VCH, 2012, vol. 2, pp. 65–89.

[100] A. Köhler and H. Bässler, *Electronic Processes in Organic Semiconductors*. Weinheim, Germany: Wiley, 2015.

[101] J. L. Brédas, J. P. Calbert, D. A. da Silva Filho, and J. Cornil, “Organic semiconductors: A theoretical characterization of the basic parameters governing charge transport,” *Proc. Natl. Acad. Sci. USA*, vol. 99, no. 9, pp. 5804–5809, 2002.

[102] J. Liu, X. Yang, and L. Sun, “Axial anchoring designed silicon–porphyrin sensitizers for efficient dye-sensitized solar cells,” *Chem. Commun.*, vol. 49, no. 100, pp. 11 785–11 787, 2013.

[103] X. Lu and S. Devaramani, “Electrochemical investigation of porphyrin and its derivatives at various interfaces,” in *Phthalocyanines and Some Current Applications*, Y. Yilmaz, Ed., Rijeka, Croatia: InTech, 2017, ch. 3.

[104] S. Ebin, P. M. Abbey, B. Alfy, and H. Mahesh, “Null exciton splitting in chromophoric Greek cross (+) aggregate,” *Angew. Chem. Int. Ed.*, vol. 57, no. 48, pp. 15 696–15 701, 2018.

[105] N. J. Hestand and F. C. Spano, “Molecular aggregate photophysics beyond the Kasha model: Novel design principles for organic materials,” *Acc. Chem. Res.*, vol. 50, no. 2, pp. 341–350, 2017.

[106] S. Ma, S. Du, G. Pan, S. Dai, B. Xu, and W. Tian, “Organic molecular aggregates: From aggregation structure to emission property,” *Aggregate*, vol. 2, no. 4, Art. no. e96, 2021.

[107] M. Kasha, “Energy transfer mechanisms and the molecular exciton model for molecular aggregates,” *Radiat. Res.*, vol. 20, no. 1, pp. 55–71, 1963.

[108] M. Kasha, H. R. Rawls, and M. Ashraf El-Bayoumi, “The exciton model in molecular spectroscopy,” *Pure Appl. Chem.*, vol. 11, no. 3–4, pp. 371–392, 1965.

[109] S. Narioka *et al.*, “The electronic structure and energy level alignment of porphyrin/metal interfaces studied by ultraviolet photoelectron spectroscopy,” *Appl. Phys. Lett.*, vol. 67, no. 13, pp. 1899–1901, 1995.

[110] H. Ishii and K. Seki, “Energy level alignment at organic/metal interfaces studied by UV photoemission: Breakdown of traditional assumption of a common vacuum level at the interface,” *IEEE Trans. Electron Devices*, vol. 44, no. 8, pp. 1295–1301, 1997.

[111] X. Crispin *et al.*, “Characterization of the interface dipole at organic/ metal interfaces,” *J. Am. Chem. Soc.*, vol. 124, no. 27, pp. 8131–8141, 2002.

[112] M. Willenbockel *et al.*, “The interplay between interface structure, energy level alignment and chemical bonding strength at organic–metal interfaces,” *Phys. Chem. Chem. Phys.*, vol. 17, no. 3, pp. 1530–1548, 2015.

[113] P. Li and Z.-H. Lu, "Interface engineering in organic electronics: Energy-level alignment and charge transport," *Small Sci.*, vol. 1, no. 1, 2021, Art. no. 2000015.

[114] H. Vázquez, Y. J. Dappe, J. Ortega, and F. Flores, "Energy level alignment at metal/organic semiconductor interfaces: "Pillow" effect, induced density of interface states, and charge neutrality level," *J. Chem. Phys.*, vol. 126, no. 14, 2007, Art. no. 144703.

[115] I. G. Hill, A. Rajagopal, A. Kahn, and Y. Hu, "Molecular level alignment at organic semiconductor-metal interfaces," *Appl. Phys. Lett.*, vol. 73, no. 5, pp. 662–664, 1998.

[116] M. T. Greiner, M. G. Helander, W.-M. Tang, Z.-B. Wang, J. Qiu, and Z.-H. Lu, "Universal energy-level alignment of molecules on metal oxides," *Nat. Mater.*, vol. 11, no. 1, pp. 76–81, 2012.

[117] S. Braun, W. Osikowicz, Y. Wang, and W. R. Salaneck, "Energy level alignment regimes at hybrid organic–organic and inorganic–organic interfaces," *Org. Electron.*, vol. 8, no. 1, pp. 14–20, 2007.

[118] C. Tengstedt, W. Osikowicz, W. R. Salaneck, I. D. Parker, C.-H. Hsu, and M. Fahlman, "Fermi-level pinning at conjugated polymer interfaces," *Appl. Phys. Lett.*, vol. 88, no. 5, 2006, Art. no. 053502.

[119] B. O'Regan and M. Grätzel, "A low-cost, high-efficiency solar cell based on dye-sensitized colloidal TiO_2 films," *Nature*, vol. 353, no. 6346, pp. 737–740, 1991.

[120] R. A. Marcus, "Electrostatic free energy and other properties of states having nonequilibrium polarization. I," *J. Chem. Phys.*, vol. 24, no. 5, pp. 979–989, 1956.

[121] R. A. Marcus, "On the theory of oxidation-reduction reactions involving electron transfer. I," *J. Chem. Phys.*, vol. 24, no. 5, pp. 966–978, 1956.

[122] R. A. Marcus, "Electron transfer reactions in chemistry: Theory and experiment (Nobel Lecture)," *Angew. Chem. Int. Ed.*, vol. 32, no. 8, pp. 1111–1121, 1993.

[123] W. F. Libby, "Theory of electron exchange reactions in aqueous solution," *J. Phys. Chem.*, vol. 56, no. 7, pp. 863–868, 1952.

[124] R. Marcus and N. Sutin, "Electron transfers in chemistry and biology," *Biochim. Biophys. Acta Bioenerg.*, vol. 811, no. 3, pp. 265–322, 1985.

[125] M. D. Newton, "Quantum chemical probes of electron-transfer kinetics: The nature of donor-acceptor interactions," *Chem. Rev.*, vol. 91, no. 5, pp. 767–792, 1991.

[126] P. F. Barbara, T. J. Meyer, and M. A. Ratner, "Contemporary issues in electron transfer research," *J. Phys. Chem.*, vol. 100, no. 31, pp. 13 148–13 168, 1996.

[127] N. R. Kestner, J. Logan, and J. Jortner, "Thermal electron transfer reactions in polar solvents," *J. Phys. Chem.*, vol. 78, no. 21, pp. 2148–2166, 1974.

[128] T. Sakata, K. Hashimoto, and M. Hiramoto, “New aspects of electron transfer on semiconductor surface: Dye-sensitization system,” *J. Phys. Chem.*, vol. 94, no. 7, pp. 3040–3045, 1990.

[129] J. J. Hopfield, “Electron transfer between biological molecules by thermally activated tunneling,” *Proc. Natl. Acad. Sci. USA*, vol. 71, no. 9, pp. 3640–3644, 1974.

[130] Y. Q. Gao and R. A. Marcus, “On the theory of electron transfer reactions at semiconductor/liquid interfaces. II. A free electron model,” *J. Chem. Phys.*, vol. 113, no. 15, pp. 6351–6360, 2000.

[131] S. Gosavi and R. A. Marcus, “Nonadiabatic electron transfer at metal surfaces,” *J. Phys. Chem. B*, vol. 104, no. 9, pp. 2067–2072, 2000.

[132] P. Hofmann, *Solid State Physics*, 2nd ed. Weinheim, Germany: Wiley-VCH, 2008.

[133] T. Förster, “Experimentelle und theoretische Untersuchung des zwischenmolekularen Übergangs von Elektronenanregungsenergie,” *Z. Naturforsch. A*, vol. 4, no. 5, pp. 321–327, 1949.

[134] T. Förster, “Zwischenmolekulare Energiewanderung und Fluoreszenz,” *Ann. Phys.*, vol. 437, no. 1–2, pp. 55–75, 1948.

[135] B. Valeur and M. Berberan-Santos, *Molecular Fluorescence, Principles and Applications*, 2nd ed. Weinheim, Germany: Wiley-VCH, 2013.

[136] P. M. Whitmore, A. P. Alivisatos, and C. B. Harris, “Distance dependence of electronic energy transfer to semiconductor surfaces: $^3n\pi^*$ pyrazine/GaAs(110),” *Phys. Rev. Lett.*, vol. 50, no. 14, pp. 1092–1094, 1983.

[137] L. Danos, R. Greef, and T. Markvart, “Efficient fluorescence quenching near crystalline silicon from Langmuir–Blodgett dye films,” *Thin Solid Films*, vol. 516, no. 20, pp. 7251–7255, 2008.

[138] N. Alderman, L. Danos, L. Fang, M. C. Grossel, and T. Markvart, “Light harvesting in silicon(111) surfaces using covalently attached protoporphyrin IX dyes,” *Chem. Commun.*, vol. 53, no. 89, pp. 12 120–12 123, 2017.

[139] J. Niederhausen, K. A. Mazzio, and R. W. MacQueen, “Inorganic–organic interfaces in hybrid solar cells,” *Electron. Struct.*, vol. 3, no. 3, 2021, Art. no. 033002.

[140] F. Niu, D. Wang, F. Li, Y. Liu, S. Shen, and T. J. Meyer, “Hybrid photoelectrochemical water splitting systems: From interface design to system assembly,” *Adv. Energy Mater.*, vol. 10, no. 11, 2020, Art. no. 1900399.

[141] J. Winnerl, R. Hudeczek, and M. Stutzmann, “Optical design of GaN nanowire arrays for photocatalytic applications,” *J. Appl. Phys.*, vol. 123, no. 20, 2018, Art. no. 203104.

[142] K. Maeda, K. Sekizawa, and O. Ishitani, “A polymeric-semiconductor–metal-complex hybrid photocatalyst for visible-light CO_2 reduction,” *Chem. Commun.*, vol. 49, no. 86, pp. 10 127–10 129, 2013.

[143] R. Kuriki, K. Sekizawa, O. Ishitani, and K. Maeda, “Visible-light-driven CO_2 reduction with carbon nitride: Enhancing the activity of ruthenium catalysts,” *Angew. Chem. Int. Ed.*, vol. 54, no. 8, pp. 2406–2409, 2015.

[144] K. Maeda, R. Kuriki, and O. Ishitani, “Photocatalytic activity of carbon nitride modified with a ruthenium(II) complex having carboxylic- or phosphonic acid anchoring groups for visible-light CO_2 reduction,” *Chem. Lett.*, vol. 45, no. 2, pp. 182–184, 2016.

[145] K. Maeda *et al.*, “Visible-light CO_2 reduction over a ruthenium(II)-complex/C_3N_4 hybrid photocatalyst: The promotional effect of silver species,” *J. Mater. Chem. A*, vol. 6, no. 20, pp. 9708–9715, 2018.

[146] Y. Sasaki, H. Kato, and A. Kudo, “$[Co(bpy)_3]^{3+/2+}$ and $[Co(phen)_3]^{3+/2+}$ electron mediators for overall water splitting under sunlight irradiation using Z-scheme photocatalyst system,” *J. Am. Chem. Soc.*, vol. 135, no. 14, pp. 5441–5449, 2013.

[147] F. Yoshitomi, K. Sekizawa, K. Maeda, and O. Ishitani, “Selective formic acid production via CO_2 reduction with visible light using a hybrid of a perovskite tantalum oxynitride and a binuclear ruthenium(II) complex,” *ACS Appl. Mater. Interfaces*, vol. 7, no. 23, pp. 13 092–13 097, 2015.

[148] M. S. Choe *et al.*, “A hybrid Ru(II)/TiO_2 catalyst for steadfast photocatalytic CO_2 to CO/formate conversion following a molecular catalytic route,” *Inorg. Chem.*, vol. 60, no. 14, pp. 10 235–10 248, 2021.

[149] C. D. Windle *et al.*, “Improving the photocatalytic reduction of CO_2 to CO through immobilisation of a molecular Re catalyst on TiO_2,” *Chem. Eur. J.*, vol. 21, no. 9, pp. 3746–3754, 2015.

[150] L. A. Faustino *et al.*, “Photocatalytic CO_2 reduction by Re(I) polypyridyl complexes immobilized on niobates nanoscrolls,” *ACS Sustain. Chem. Eng.*, vol. 6, no. 5, pp. 6073–6083, 2018.

[151] G. Zhao *et al.*, “Co-porphyrin/carbon nitride hybrids for improved photocatalytic CO_2 reduction under visible light,” *Appl. Catal. B*, vol. 200, pp. 141–149, 2017.

[152] C. Cometto *et al.*, “A carbon nitride/Fe quaterpyridine catalytic system for photostimulated CO_2-to-CO conversion with visible light,” *J. Am. Chem. Soc.*, vol. 140, no. 24, pp. 7437–7440, 2018.

[153] L. Lin, C. Hou, X. Zhang, Y. Wang, Y. Chen, and T. He, “Highly efficient visible-light driven photocatalytic reduction of CO_2 over g-C_3N_4 nanosheets/tetra(4-carboxyphenyl)porphyrin iron(III) chloride heterogeneous catalysts,” *Appl. Catal. B*, vol. 221, pp. 312–319, 2018.

[154] K. Muraoka, T. Uchiyama, D. Lu, Y. Uchimoto, O. Ishitani, and K. Maeda, “A visible-light-driven Z-scheme CO_2 reduction system using Ta_3N_5 and a Ru(II) binuclear complex,” *Bull. Chem. Soc. Jpn.*, vol. 92, no. 1, pp. 124–126, 2019.

[155] A. Nakada, T. Nakashima, K. Sekizawa, K. Maeda, and O. Ishitani, “Visible-light-driven CO_2 reduction on a hybrid photocatalyst consisting of a Ru(II) binuclear complex and a Ag-loaded TaON in aqueous solutions,” *Chem. Sci.*, vol. 7, no. 7, pp. 4364–4371, 2016.

[156] A. Nakada, H. Kumagai, M. Robert, O. Ishitani, and K. Maeda, “Molecule/semiconductor hybrid materials for visible-light CO_2 reduction: Design principles and interfacial engineering,” *Acc. Mater. Res.*, vol. 2, no. 6, pp. 458–470, 2021.

[157] R. Kuriki *et al.*, “Nature-inspired, highly durable CO_2 reduction system consisting of a binuclear ruthenium(II) complex and an organic semiconductor using visible light,” *J. Am. Chem. Soc.*, vol. 138, no. 15, pp. 5159–5170, 2016.

[158] B. Kumar, J. M. Smieja, and C. P. Kubiak, “Photoreduction of CO_2 on p-type silicon using Re(bipy-Bu^t)$(CO)_3$Cl: Photovoltages exceeding 600 mV for the selective reduction of CO_2 to CO,” *J. Phys. Chem. C*, vol. 114, no. 33, pp. 14 220–14 223, 2010.

[159] E. Torralba-Peñalver, Y. Luo, J.-D. Compain, S. Chardon-Noblat, and B. Fabre, “Selective catalytic electroreduction of CO_2 at silicon nanowires (SiNWs) photocathodes using non-noble metal-based manganese carbonyl bipyridyl molecular catalysts in solution and grafted onto SiNWs,” *ACS Catal.*, vol. 5, no. 10, pp. 6138–6147, 2015.

[160] M. Schreier, J. Luo, P. Gao, T. Moehl, M. T. Mayer, and M. Grätzel, “Covalent immobilization of a molecular catalyst on Cu_2O photocathodes for CO_2 reduction,” *J. Am. Chem. Soc.*, vol. 138, no. 6, pp. 1938–1946, 2016.

[161] M. Schreier *et al.*, “Efficient and selective carbon dioxide reduction on low cost protected Cu_2O photocathodes using a molecular catalyst,” *Energy Environ. Sci.*, vol. 8, no. 3, pp. 855–861, 2015.

[162] H. Kumagai, G. Sahara, K. Maeda, M. Higashi, R. Abe, and O. Ishitani, “Hybrid photocathode consisting of a $CuGaO_2$ p-type semiconductor and a Ru(II)–Re(I) supramolecular photocatalyst: Non-biased visible-light-driven CO_2 reduction with water oxidation,” *Chem. Sci.*, vol. 8, no. 6, pp. 4242–4249, 2017.

[163] G. Sahara *et al.*, “Photoelectrochemical reduction of CO_2 coupled to water oxidation using a photocathode with a Ru(II)–Re(I) complex photocatalyst and a CoO_x/TaON photoanode,” *J. Am. Chem. Soc.*, vol. 138, no. 42, pp. 14 152–14 158, 2016.

[164] F. Rauh, F. Pantle, and M. Stutzmann, “Morphology, energy level alignment, and charge transfer at the protoporphyrin IX–semiconductor interface,” *Langmuir*, vol. 39, no. 14, pp. 5095–5106, 2023.

[165] J. E. Pander, A. Fogg, and A. B. Bocarsly, “Utilization of electropolymerized films of cobalt porphyrin for the reduction of carbon dioxide in aqueous media,” *ChemCatChem*, vol. 8, no. 22, pp. 3536–3545, 2016.

[166] D. Khusnutdinova, A. M. Beiler, B. L. Wadsworth, S. I. Jacob, and G. F. Moore, “Metalloporphyrin-modified semiconductors for solar fuel production,” *Chem. Sci.*, vol. 8, no. 1, pp. 253–259, 2017.

[167] M. Parchine, J. McGrath, M. Bardosova, and M. E. Pemble, “Large area 2D and 3D colloidal photonic crystals fabricated by a roll-to-roll Langmuir–Blodgett method,” *Langmuir*, vol. 32, no. 23, pp. 5862–5869, 2016.

[168] E. Piosik, M. Kotkowiak, I. Korbecka, Z. Galewski, and T. Martyński, “Photo-switching of a non-ionic azobenzene amphiphile in Langmuir and Langmuir–Blodgett films,” *Phys. Chem. Chem. Phys.*, vol. 19, no. 34, pp. 23 386–23 396, 2017.

[169] A. Ładniak, M. Jurak, and A. E. Wiącek, “Langmuir monolayer study of phospholipid DPPC on the titanium dioxide–chitosan–hyaluronic acid subphases,” *Adsorption*, vol. 25, no. 3, pp. 469–476, 2019.

[170] M. Jurak, K. Szafran, P. Cea, and S. Martín, “Analysis of molecular interactions between components in phospholipid-immunosuppressant-antioxidant mixed Langmuir films,” *Langmuir*, vol. 37, no. 18, pp. 5601–5616, 2021.

[171] C. Li and T. Imae, “Protoporphyrin IX zinc(II) organization at the air/water interface and its Langmuir-Blodgett films,” *Langmuir*, vol. 19, no. 3, pp. 779–784, 2003.

[172] Z. Wang, J. Chen, S. Oyola-Reynoso, and M. Thuo, “The Porter-Whitesides discrepancy: Revisiting odd-even effects in wetting properties of n-alkanethiolate SAMs,” *Coatings*, vol. 5, no. 4, pp. 1034–1055, 2015.

[173] E. Bulard *et al.*, “The effect of bacterial adhesion on grafted chains revealed by the non-invasive sum frequency generation spectroscopy,” *Spectrosc. Int. J.*, vol. 27, pp. 571–579, 2012.

[174] G. Beamson and D. Briggs, *High Resolution XPS of Organic Polymers: The Scienta ESCA300 Database*. Weinheim, Germany: Wiley, 1992, pp. 210–212.

[175] P. Louette, F. Bodino, and J.-J. Pireaux, “Poly(pyrrole) (PPY) XPS reference core level and energy loss spectra,” *Surf. Sci. Spectra*, vol. 12, no. 1, pp. 84–89, 2005.

[176] S. J. Hartmann, A. A. Iurchenkova, T. Kallio, and E. O. Fedorovskaya, “Electrochemical properties of nitrogen and oxygen doped reduced graphene oxide,” *Energies*, vol. 13, no. 2, 2020, Art. no. 312.

[177] D. Wechsler *et al.*, “Wet-chemically prepared porphyrin layers on rutile TiO_2(110),” *Molecules*, vol. 26, no. 10, 2021, Art. no. 2871.

[178] G. Lovat *et al.*, “Hydrogen capture by porphyrins at the TiO_2 (110) surface,” *Phys. Chem. Chem. Phys.*, vol. 17, no. 44, pp. 30 119–30 124, 2015.

[179] D. Wechsler, C. C. Fernández, H.-P. Steinrück, O. Lytken, and F. J. Williams, “Covalent anchoring and interfacial reactions of adsorbed porphyrins on rutile TiO_2 (110),” *J. Phys. Chem. C*, vol. 122, no. 8, pp. 4480–4487, 2018.

[180] J. Köbl *et al.*, “Hungry porphyrins: Protonation and self-metalation of tetraphenylporphyrin on TiO_2 (110) - 1×1,” *ChemistrySelect*, vol. 1, no. 19, pp. 6103–6105, 2016.

[181] H. Nagatani and H. Watarai, “Two-phase stopped-flow measurement of the protonation of tetraphenylporphyrin at the liquid-liquid interface,” *Anal. Chem.*, vol. 68, no. 7, pp. 1250–1253, 1996.

[182] C. Bohling and W. Sigmund, “Self-limitation of native oxides explained,” *Silicon*, vol. 8, no. 3, pp. 339–343, 2016.

[183] S. Yamamoto *et al.*, “*In situ* x-ray photoelectron spectroscopy studies of water on metals and oxides at ambient conditions,” *J. Phys. Condens. Matter*, vol. 20, no. 18, 2008, Art. no. 184025.

[184] A. Y. Klyushin, T. C. R. Rocha, M. Hävecker, A. Knop-Gericke, and R. Schlögl, “A near ambient pressure XPS study of Au oxidation,” *Phys. Chem. Chem. Phys.*, vol. 16, no. 17, pp. 7881–7886, 2014.

[185] X. Zhang and S. Ptasinska, “Dissociative adsorption of water on an H_2O/GaAs(100) interface: In situ near-ambient pressure XPS studies,” *J. Phys. Chem. C*, vol. 118, no. 8, pp. 4259–4266, 2014.

[186] M. Y. Bashouti, K. Sardashti, J. Ristein, and S. H. Christiansen, “Early stages of oxide growth in H-terminated silicon nanowires: Determination of kinetic behavior and activation energy,” *Phys. Chem. Chem. Phys.*, vol. 14, no. 34, pp. 11 877–11 881, 2012.

[187] G. N. Derry, M. E. Kern, and E. H. Worth, “Recommended values of clean metal surface work functions,” *J. Vac. Sci. Technol. A*, vol. 33, no. 6, 2015, Art. no. 060801.

[188] N. Turetta, F. Sedona, A. Liscio, M. Sambi, and P. Samorì, “Au(111) surface contamination in ambient conditions: Unravelling the dynamics of the work function in air,” *Adv. Mater. Interfaces*, vol. 8, no. 10, 2021, Art. no. 2100068.

[189] M. Garg, B. R. Tak, V. R. Rao, and R. Singh, “Giant UV photoresponse of GaN-based photodetectors by surface modification using phenol-functionalized porphyrin organic molecules,” *ACS Appl. Mater. Interfaces*, vol. 11, no. 12, pp. 12 017–12 026, 2019.

[190] S. Kaushik *et al.*, “Surface modification of AlN using organic molecular layer for improved deep UV photodetector performance,” *ACS Appl. Electron. Mater.*, vol. 2, no. 3, pp. 739–746, 2020.

[191] F. Gotardo *et al.*, “Investigating the intersystem crossing rate and triplet quantum yield of protoporphyrin IX by means of pulse train fluorescence technique,” *Chem. Phys. Lett.*, vol. 674, pp. 48–57, 2017.

[192] K. Tvrdy, P. A. Frantsuzov, and P. V. Kamat, “Photoinduced electron transfer from semiconductor quantum dots to metal oxide nanoparticles,” *Proc. Natl. Acad. Sci. USA*, vol. 108, no. 1, pp. 29–34, 2011.

[193] A. Marcelli, I. J. Badovinac, N. Orlic, P. R. Salvi, and C. Gellini, “Excited-state absorption and ultrafast relaxation dynamics of protoporphyrin IX and hemin,” *Photochem. Photobiol. Sci.*, vol. 12, no. 2, pp. 348–355, 2013.

[194] J. M. Empey, C. Grieco, N. W. Pettinger, and B. Kohler, “Ultrafast electron injection and recombination dynamics of coumarin 343-sensitized cerium oxide nanoparticles,” *J. Phys. Chem. C*, vol. 125, no. 27, pp. 14 827–14 835, 2021.

[195] O. V. Prezhdo, W. R. Duncan, and V. V. Prezhdo, “Dynamics of the photoexcited electron at the chromophore–semiconductor interface,” *Acc. Chem. Res.*, vol. 41, no. 2, pp. 339–348, 2008.

[196] H. Yan *et al.*, “Conformational and binding effects on interfacial electron transfer from dual-linker sensitizers,” *J. Phys. Chem. C*, vol. 125, no. 16, pp. 8667–8676, 2021.

[197] L. Danos and T. Markvart, “Excitation energy transfer rate from Langmuir Blodgett (LB) dye monolayers to silicon: Effect of aggregate formation,” *Chem. Phys. Lett.*, vol. 490, no. 4–6, pp. 194–199, 2010.

[198] H. Angermann, K. Kliefoth, and H. Flietner, “Preparation of H-terminated Si surfaces and their characterisation by measuring the surface state density,” *Appl. Surf. Sci.*, vol. 104–105, pp. 107–112, 1996.

[199] B. Mondal, P. Sen, A. Rana, D. Saha, P. Das, and A. Dey, “Reduction of CO_2 to CO by an iron porphyrin catalyst in the presence of oxygen,” *ACS Catal.*, vol. 9, no. 5, pp. 3895–3899, 2019.

[200] A. Lashgari, C. K. Williams, J. L. Glover, Y. Wu, J. Chai, and J. Jiang, “Enhanced electrocatalytic activity of a zinc porphyrin for CO_2 reduction: Cooperative effects of triazole units in the second coordination sphere,” *Chem. Eur. J.*, vol. 26, no. 70, pp. 16 774–16 781, 2020.

[201] Y. Wu *et al.*, “Electroreduction of CO_2 catalyzed by a heterogenized Zn–porphyrin complex with a redox-innocent metal center,” *ACS Cent. Sci.*, vol. 3, no. 8, pp. 847–852, 2017.

[202] M. Abdinejad, K. Tang, C. Dao, S. Saedy, and T. Burdyny, “Immobilization strategies for porphyrin-based molecular catalysts for the electroreduction of CO_2,” *J. Mater. Chem. A*, vol. 10, no. 14, pp. 7626–7636, 2022.

[203] A. Call, M. Cibian, K. Yamamoto, T. Nakazono, K. Yamauchi, and K. Sakai, “Highly efficient and selective photocatalytic CO_2 reduction to CO in water by a cobalt porphyrin molecular catalyst,” *ACS Catal.*, vol. 9, no. 6, pp. 4867–4874, 2019.

[204] A. N. Marianov, A. S. Kochubei, T. Roman, O. J. Conquest, C. Stampfl, and Y. Jiang, “Resolving deactivation pathways of Co porphyrin-based electrocatalysts for CO_2 reduction in aqueous medium,” *ACS Catal.*, vol. 11, no. 6, pp. 3715–3729, 2021.

[205] R. González-Moreno *et al.*, “Following the metalation process of protoporphyrin IX with metal substrate atoms at room temperature,” *J. Phys. Chem. C*, vol. 115, no. 14, pp. 6849–6854, 2011.

[206] A. C. Papageorgiou *et al.*, “In vacuo porphyrin metalation on Ag(111) via chemical vapor deposition of $Ru_3(CO)_{12}$: Mechanistic insights,” *J. Phys. Chem. C*, vol. 120, no. 16, pp. 8751–8758, 2016.

[207] L. Egger *et al.*, “Charge-promoted self-metalation of porphyrins on an oxide surface,” *Angew. Chem. Int. Ed.*, vol. 60, no. 10, pp. 5078–5082, 2021.

[208] A. Baklanov *et al.*, “On-surface synthesis of nonmetal porphyrins,” *J. Am. Chem. Soc.*, vol. 142, no. 4, pp. 1871–1881, 2020.

[209] F. Klappenberger, A. Weber-Bargioni, W. Auwärter, M. Marschall, A. Schiffrin, and J. V. Barth, “Temperature dependence of conformation, chemical state, and metal-directed assembly of tetrapyridyl-porphyrin on Cu(111),” *J. Chem. Phys.*, vol. 129, no. 21, 2008, Art. no. 214702.

[210] M. Garg, T. R. Naik, C. S. Pathak, S. Nagarajan, V. R. Rao, and R. Singh, “Significant improvement in the electrical characteristics of Schottky barrier diodes on molecularly modified gallium nitride surfaces,” *Appl. Phys. Lett.*, vol. 112, no. 16, 2018, Art. no. 163502.

[211] A. M. Beiler, D. Khusnutdinova, B. L. Wadsworth, and G. F. Moore, “Cobalt porphyrin–polypyridyl surface coatings for photoelectrosynthetic hydrogen production,” *Inorg. Chem.*, vol. 56, no. 20, pp. 12 178–12 185, 2017.

[212] J. Li *et al.*, “Ultrathin mesoporous Co_3O_4 nanosheet arrays for high-performance lithium-ion batteries,” *ACS Omega*, vol. 3, no. 2, pp. 1675–1683, 2018.

[213] C. Alex, S. C. Sarma, S. C. Peter, and N. S. John, “Competing effect of Co^{3+} reducibility and oxygen-deficient defects toward high oxygen evolution activity in Co_3O_4 systems in alkaline medium,” *ACS Appl. Energy Mater.*, vol. 3, no. 6, pp. 5439–5447, 2020.

[214] M. Zhu, J. Chen, L. Huang, R. Ye, J. Xu, and Y.-F. Han, “Covalently grafting cobalt porphyrin onto carbon nanotubes for efficient CO_2 electroreduction,” *Angew. Chem. Int. Ed.*, vol. 58, no. 20, pp. 6595–6599, 2019.

[215] R. Giovannetti, “The use of spectrophotometry UV-Vis for the study of porphyrins,” in *Macro to Nano Spectroscopy*, J. Uddin, Ed., Rijeka, Croatia: InTech, 2012.

[216] Y. Agam, R. Nandi, A. Kaushansky, U. Peskin, and N. Amdursky, “The porphyrin ring rather than the metal ion dictates long-range electron transport across proteins suggesting coherence-assisted mechanism,” *Proc. Natl. Acad. Sci. USA*, vol. 117, no. 51, pp. 32 260–32 266, 2020.

[217] X.-F. Wang and O. Kitao, “Natural chlorophyll-related porphyrins and chlorins for dye-sensitized solar cells,” *Molecules*, vol. 17, no. 4, pp. 4484–4497, 2012.

[218] H. S. Stark, P. J. Altmann, S. Sproules, and C. R. Hess, “Structural characterization and photochemical properties of mono- and bimetallic Cu-Mabiq complexes,” *Inorg. Chem.*, vol. 57, no. 11, pp. 6401–6409, 2018.

[219] A. Wang, X. Y. Liu, C.-Y. Mou, and T. Zhang, “Understanding the synergistic effects of gold bimetallic catalysts,” *J. Catal.*, vol. 308, pp. 258–271, 2013.

[220] Z. Bian, S. Das, M. H. Wai, P. Hongmanorom, and S. Kawi, “A review on bimetallic nickel-based catalysts for CO_2 reforming of methane,” *ChemPhysChem*, vol. 18, no. 22, pp. 3117–3134, 2017.

[221] Q. Guan *et al.*, “Bimetallic monolayer catalyst breaks the activity–selectivity trade-off on metal particle size for efficient chemoselective hydrogenations,” *Nature Catal.*, vol. 4, no. 10, pp. 840–849, 2021.

[222] L. Wan *et al.*, “Bimetallic Cu–Zn catalysts for electrochemical CO_2 reduction: Phase-separated versus core–shell distribution,” *ACS Catal.*, vol. 12, no. 5, pp. 2741–2748, 2022.

[223] B. Seemala, C. M. Cai, R. Kumar, C. E. Wyman, and P. Christopher, “Effects of Cu–Ni bimetallic catalyst composition and support on activity, selectivity, and stability for furfural conversion to 2-methyfuran,” *ACS Sustain. Chem. Eng.*, vol. 6, no. 2, pp. 2152–2161, 2018.

[224] G. C. Tok, A. T. S. Freiberg, H. A. Gasteiger, and C. R. Hess, “Electrocatalytic H_2 evolution by the Co-Mabiq complex requires tempering of the redox-active ligand,” *ChemCatChem*, vol. 11, no. 16, pp. 3973–3981, 2019.

[225] Y. Xin *et al.*, “High-entropy alloys as a platform for catalysis: Progress, challenges, and opportunities,” *ACS Catal.*, vol. 10, no. 19, pp. 11 280–11 306, 2020.

[226] Felix Haag, “Atomic level studies of the surface-directed synthesis of novel organometallic and metal-organic two-dimensional assemblies,” Ph.D. dissertation, Dept. Phys., Tech. Univ. Munich, Garching, Germany, 2022, pp. 110–120.

[227] F. Haag *et al.*, “The flexible on-surface self-assembly of a low-symmetry Mabiq ligand: An unconventional metal-assisted phase transformation on Ag(111),” *J. Phys. Chem. C*, vol. 125, no. 42, pp. 23 178–23 191, 2021.

[228] C. Rameshan, M. Ng, A. Shavorskiy, J. Newberg, and H. Bluhm, "Water adsorption on polycrystalline vanadium from ultra-high vacuum to ambient relative humidity," *Surf. Sci.*, vol. 641, pp. 141–147, 2015.

[229] J. M. Dlugosch *et al.*, "Metallic top contacts to self-assembled monolayers of aliphatic phosphonic acids on titanium nitride," in *20th IEEE Int. Conf. Nanotechnology*, 2020, pp. 29–34.

[230] L. Wen *et al.*, "Enhancing the photovoltaic performance of GaAs/graphene Schottky junction solar cells by interfacial modification with self assembled alkyl thiol monolayer," *J. Mater. Chem. A*, vol. 6, no. 36, pp. 17 361–17 370, 2018.

[231] T. Ano *et al.*, "Controlling the Schottky barrier at the Pt/TiO_2 interface by intercalation of a self-assembled monolayer with oriented dipole moments," *J. Phys. Chem. C*, vol. 125, no. 25, pp. 13 984–13 989, 2021.

[232] M. Kühnel, S. V. Petersen, R. Hviid, M. H. Overgaard, B. W. Laursen, and K. Nørgaard, "Monolayered graphene oxide as a low contact resistance protection layer in alkanethiol solid-state devices," *J. Phys. Chem. C*, vol. 122, no. 18, pp. 9731–9737, 2018.

[233] C. A. Nijhuis, W. F. Reus, and G. M. Whitesides, "Molecular rectification in metal-SAM-metal oxide-metal junctions," *J. Am. Chem. Soc.*, vol. 131, no. 49, pp. 17 814–17 827, 2009.

[234] J. M. Dlugosch *et al.*, "Conductance switching in liquid crystal-inspired self-assembled monolayer junctions," *ACS Appl. Mater. Interfaces*, vol. 14, no. 27, pp. 31 044–31 053, 2022.

[235] M. A. Rampi and G. M. Whitesides, "A versatile experimental approach for understanding electron transport through organic materials," *Chem. Phys.*, vol. 281, no. 2–3, pp. 373–391, 2002.

[236] R. C. Chiechi, E. A. Weiss, M. D. Dickey, and G. M. Whitesides, "Eutectic gallium–indium (EGaIn): A moldable liquid metal for electrical characterization of self-assembled monolayers," *Angew. Chem. Int. Ed.*, vol. 47, no. 1, pp. 142–144, 2008.

[237] K. Theis-Bröhl, A. Saini, M. Wolff, J. A. Dura, B. B. Maranville, and J. A. Borchers, "Self-assembly of magnetic nanoparticles in ferrofluids on different templates investigated by neutron reflectometry," *Nanomaterials*, vol. 10, no. 6, 2020, Art. no. 1231.

[238] B. J. Raos, C. S. Doyle, M. C. Simpson, E. S. Graham, and C. P. Unsworth, "Selective pegylation of parylene-C/SiO_2 substrates for improved astrocyte cell patterning," *Sci. Rep.*, vol. 8, no. 1, 2018, Art. no. 2754.

[239] J. Watté, W. Van Gompel, P. Lommens, K. De Buysser, and I. Van Driessche, "Titania nanocrystal surface functionalization through silane chemistry for low temperature deposition on polymers," *ACS Appl. Mater. Interfaces*, vol. 8, no. 43, pp. 29 759–29 769, 2016.

[240] S. Udomsom, U. Mankong, P. Paengnakorn, and N. Theera-Umpon, "Novel rapid protein coating technique for silicon photonic biosensor to improve surface morphology and increase bioreceptor density," *Coatings*, vol. 11, no. 5, 2021, Art. no. 595.

[241] J. L. Vivero-Escoto and D. L. Vega, "Stimuli-responsive protoporphyrin IX silica-based nanoparticles for photodynamic therapy in vitro," *RSC Adv.*, vol. 4, no. 28, pp. 14 400–14 407, 2014.

[242] A. Issa and A. Luyt, "Kinetics of alkoxysilanes and organoalkoxysilanes polymerization: A review," *Polymers*, vol. 11, no. 3, 2019, Art. no. 537.

[243] N. S. K. Gunda, M. Singh, L. Norman, K. Kaur, and S. K. Mitra, "Optimization and characterization of biomolecule immobilization on silicon substrates using (3-aminopropyl)triethoxysilane (APTES) and glutaraldehyde linker," *Appl. Surf. Sci.*, vol. 305, pp. 522–530, 2014.

[244] N. Aissaoui, L. Bergaoui, J. Landoulsi, J.-F. Lambert, and S. Boujday, "Silane layers on silicon surfaces: Mechanism of interaction, stability, and influence on protein adsorption," *Langmuir*, vol. 28, no. 1, pp. 656–665, 2012.

[245] F. Zhang *et al.*, "Chemical vapor deposition of three aminosilanes on silicon dioxide: Surface characterization, stability, effects of silane concentration, and cyanine dye adsorption," *Langmuir*, vol. 26, no. 18, pp. 14 648–14 654, 2010.

[246] J. A. Howarter and J. P. Youngblood, "Optimization of silica silanization by 3-aminopropyltriethoxysilane," *Langmuir*, vol. 22, no. 26, pp. 11 142–11 147, 2006.

[247] B. Baur *et al.*, "Chemical functionalization of GaN and AlN surfaces," *Appl. Phys. Lett.*, vol. 87, no. 26, 2005, Art. no. 263901.

[248] M. Zhu, M. Z. Lerum, and W. Chen, "How to prepare reproducible, homogeneous, and hydrolytically stable aminosilane-derived layers on silica," *Langmuir*, vol. 28, no. 1, pp. 416–423, 2012.

[249] R. G. Acres *et al.*, "Molecular structure of 3-aminopropyltriethoxysilane layers formed on silanol-terminated silicon surfaces," *J. Phys. Chem. C*, vol. 116, no. 10, pp. 6289–6297, 2012.

[250] J. Li, Y. Qiao, D. Li, S. Zhang, and P. Liu, "Improving interfacial and mechanical properties of glass fabric/polyphenylene sulfide composites *via* grafting multi-walled carbon nanotubes," *RSC Adv.*, vol. 9, no. 56, pp. 32 634–32 643, 2019.

[251] S. H. Kwak, S.-R. Kwon, S. Baek, S.-M. Lim, Y.-C. Joo, and T. D. Chung, “Densely charged polyelectrolyte-stuffed nanochannel arrays for power generation from salinity gradient,” *Sci. Rep.*, vol. 6, no. 1, 2016, Art. no. 26416.

[252] X. Rao, M. Tatoulian, C. Guyon, S. Ognier, C. Chu, and A. Abou Hassan, “A comparison study of functional groups (amine vs. thiol) for immobilizing AuNPs on zeolite surface,” *Nanomaterials*, vol. 9, no. 7, 2019, Art. no. 1034.

[253] H. Min, P.-L. Girard-Lauriault, T. Gross, A. Lippitz, P. Dietrich, and W. E. S. Unger, “Ambient-ageing processes in amine self-assembled monolayers on microarray slides as studied by ToF-SIMS with principal component analysis, XPS, and NEXAFS spectroscopy,” *Anal. Bioanal. Chem.*, vol. 403, no. 2, pp. 613–623, 2012.

[254] Z. Yang *et al.*, “Effective removal of Cr(VI) from aqueous solution based on APTES modified nanoporous silicon prepared from kerf loss silicon waste,” *Environ. Sci. Pollut. Res.*, vol. 27, no. 10, pp. 10 899–10 909, 2020.

[255] R. Zeng *et al.*, “Construction of class I aldolases-like carboxyl-controlled-graphene oxide supported 3-aminopropyl-triethoxysilane heterogeneous catalysts for aldol reaction,” *Catal. Lett.*, vol. 150, no. 5, pp. 1230–1237, 2020.

[256] K. Bierbaum *et al.*, “A near edge X-ray absorption fine structure spectroscopy and X-ray photoelectron spectroscopy study of the film properties of self-assembled monolayers of organosilanes on oxidized Si(100),” *Langmuir*, vol. 11, no. 2, pp. 512–518, 1995.

[257] R. C. Shallcross, S. Olthof, K. Meerholz, and N. R. Armstrong, “Understanding the role of titanium dioxide (TiO_2) surface chemistry on the nucleation and energetics of hybrid perovskite films,” in *Organic, Hybrid, and Perovskite Photovoltaics XVIII*, K. Lee, Z. H. Kafafi, and P. A. Lane, Eds., vol. 10363, 2017, p. 10363I.

[258] B. S. Jursic and Z. Zdravkovski, “A simple preparation of amides from acids and amines by heating of their mixture,” *Synth. Commun.*, vol. 23, no. 19, pp. 2761–2770, 1993.

[259] H. Charville, D. Jackson, G. Hodges, and A. Whiting, “The thermal and boron-catalysed direct amide formation reactions: Mechanistically understudied yet important processes,” *Chem. Commun.*, vol. 46, no. 11, pp. 1813–1823, 2010.

[260] P. M. Dietrich *et al.*, “Quantification of Silane Molecules on Oxidized Silicon: Are there Options for a Traceable and Absolute Determination?” *Anal. Chem.*, vol. 87, no. 19, pp. 10 117–10 124, 2015.

[261] D. Meroni *et al.*, “A Close Look at the Structure of the TiO_2-APTES Interface in Hybrid Nanomaterials and Its Degradation Pathway: An Experimental and Theoretical Study,” *J. Phys. Chem. C*, vol. 121, no. 1, pp. 430–440, 2017.

[262] F. Rauh, J. Dittloff, M. Thun, M. Stutzmann, and I. D. Sharp, “Nanostructured black silicon as a stable and surface-sensitive platform for time-resolved in situ electrochemical infrared absorption spectroscopy,” *ACS Appl. Mater. Interfaces*, vol. 16, no. 9, pp. 6653–6664, 2024.

[263] M. Abdellah, A. M. El-Zohry, L. J. Antila, C. D. Windle, E. Reisner, and L. Hammarström, “Time-resolved IR spectroscopy reveals a mechanism with TiO_2 as a reversible electron acceptor in a TiO_2–Re catalyst system for CO_2 photoreduction,” *J. Am. Chem. Soc.*, vol. 139, no. 3, pp. 1226–1232, 2017.

[264] J. Heyes, M. Dunwell, and B. Xu, “CO_2 reduction on Cu at low overpotentials with surface-enhanced in situ spectroscopy,” *J. Phys. Chem. C*, vol. 120, no. 31, pp. 17 334–17 341, 2016.

[265] A. Otto, “Excitation of nonradiative surface plasma waves in silver by the method of frustrated total reflection,” *Z. Phys. A*, vol. 216, no. 4, pp. 398–410, 1968.

[266] E. Kretschmann and H. Raether, “Radiative decay of non radiative surface plasmons excited by light,” *Z. Naturforsch. A*, vol. 23, no. 12, pp. 2135–2136, 1968.

[267] F. Le *et al.*, “Metallic nanoparticle arrays: A common substrate for both surface-enhanced Raman scattering and surface-enhanced infrared absorption,” *ACS Nano*, vol. 2, no. 4, pp. 707–718, 2008.

[268] S. G. Sun, W. B. Cai, L. J. Wan, and M. Osawa, “Infrared absorption enhancement for CO adsorbed on Au films in perchloric acid solutions and effects of surface structure studied by cyclic voltammetry, scanning tunneling microscopy, and surface-enhanced IR spectroscopy,” *J. Phys. Chem. B*, vol. 103, no. 13, pp. 2460–2466, 1999.

[269] J. M. Delgado, J. M. Orts, J. M. Pérez, and A. Rodes, “Sputtered thin-film gold electrodes for in situ ATR-SEIRAS and SERS studies,” *J. Electroanal. Chem.*, vol. 617, no. 2, pp. 130–140, 2008.

[270] S. M. Rosendahl, B. R. Danger, J. P. Vivek, and I. J. Burgess, “Surface enhanced infrared absorption spectroscopy studies of DMAP adsorption on gold surfaces,” *Langmuir*, vol. 25, no. 4, pp. 2241–2247, 2009.

[271] M. Dunwell *et al.*, “The central role of bicarbonate in the electrochemical reduction of carbon dioxide on gold,” *J. Am. Chem. Soc.*, vol. 139, no. 10, pp. 3774–3783, 2017.

[272] S. J. Huo *et al.*, “Tunable surface-enhanced infrared absorption on Au nanofilms on Si fabricated by self-assembly and growth of colloidal particles,” *J. Phys. Chem. B*, vol. 109, no. 33, pp. 15 985–15 991, 2005.

[273] M. Osawa, K. Ataka, K. Yoshii, and T. Yotsuyanagi, “Surface-enhanced infrared ATR spectroscopy for in situ studies of electrode/electrolyte interfaces,” *J. Electron Spectrosc. Relat. Phenom.*, vol. 64–65, no. C, pp. 371–379, 1993.

[274] M. Osawa, “Dynamic processes in electrochemical reactions studied by surface-enhanced infrared absorption spectroscopy (SEIRAS),” *Bull. Chem. Soc. Jpn.*, vol. 70, no. 12, pp. 2861–2880, 1997.

[275] N. Ohta, K. Nomura, and I. Yagi, “Electrochemical modification of surface morphology of Au/Ti bilayer films deposited on a Si prism for in situ surface-enhanced infrared absorption (SEIRA) spectroscopy,” *Langmuir*, vol. 26, no. 23, pp. 18 097–18 104, 2010.

[276] A. Miki, S. Ye, and M. Osawa, “Surface-enhanced IR absorption on platinum nanoparticles: An application to real-time monitoring of electrocatalytic reactions,” *Chem. Commun.*, vol. 2, no. 14, pp. 1500–1501, 2002.

[277] A. E. Bjerke, P. R. Griffiths, and W. Theiss, “Surface-enhanced infrared absorption of CO on platinized platinum,” *Anal. Chem.*, vol. 71, no. 10, pp. 1967–1974, 1999.

[278] J. M. Delgado, J. M. Orts, and A. Rodes, “A comparison between chemical and sputtering methods for preparing thin-film silver electrodes for in situ ATR-SEIRAS studies,” *Electrochim. Acta*, vol. 52, no. 14, pp. 4605–4613, 2007.

[279] H. F. Wang, Y. G. Yan, S. J. Huo, W. B. Cai, Q. J. Xu, and M. Osawa, “Seeded growth fabrication of Cu-on-Si electrodes for in situ ATR-SEIRAS applications,” *Electrochim. Acta*, vol. 52, no. 19, pp. 5950–5957, 2007.

[280] O. J. Clarke and I. J. Burgess, “Electrodeposited gold nanodaggers on conductive metal oxide films provide substrates for dual-modality surface sensitive vibrational spectroscopy,” *J. Phys. Chem. C*, vol. 124, no. 24, pp. 13 356–13 364, 2020.

[281] V. T. Thi Phan, I. R. Andvaag, N. D. Boyle, G. T. Flaman, B. Unni, and I. J. Burgess, “Surface sensitive infrared spectroelectrochemistry using palladium electrodeposited on ITO-modified internal reflection elements,” *Phys. Chem. Chem. Phys.*, vol. 24, no. 5, pp. 2925–2933, 2022.

[282] S. Geiger, O. Kasian, A. M. Mingers, K. J. Mayrhofer, and S. Cherevko, “Stability limits of tin-based electrocatalyst supports,” *Sci. Rep.*, vol. 7, no. 1, pp. 1–7, 2017.

[283] J. D. Benck, B. A. Pinaud, Y. Gorlin, and T. F. Jaramillo, “Substrate selection for fundamental studies of electrocatalysts and photoelectrodes: Inert potential windows in acidic, neutral, and basic electrolyte,” *PLOS ONE*, vol. 9, no. 10, 2014, Art. no. e107942.

[284] M. Ko, H. U. Kim, and N. Jeon, “Boosting electrochemical activity of porous transparent conductive oxides electrodes prepared by sequential infiltration synthesis,” *Small*, vol. 18, no. 12, 2022, Art. no. 2105898.

[285] S. Koynov, M. S. Brandt, and M. Stutzmann, “Black nonreflecting silicon surfaces for solar cells,” *Appl. Phys. Lett.*, vol. 88, no. 20, 2006, Art. no. 203107.

[286] H. C. Yuan, V. E. Yost, M. R. Page, P. Stradins, D. L. Meier, and H. M. Branz, “Efficient black silicon solar cell with a density-graded nanoporous surface: Optical properties, performance limitations, and design rules,” *Appl. Phys. Lett.*, vol. 95, no. 12, Art. no. 123501, 2009.

[287] B. C. Barlow and I. J. Burgess, “Electrochemical evaluation of 4-(dimethylamino)pyridine adsorption on polycrystalline gold,” *Langmuir*, vol. 23, no. 3, pp. 1555–1563, 2007.

[288] J. Shao *et al.*, “Modulated photoluminescence spectroscopy with a step-scan Fourier transform infrared spectrometer,” *Rev. Sci. Instrum.*, vol. 77, no. 6, 2006, Art. no. 063104.

[289] M. Lepère *et al.*, “A mid-infrared dual-comb spectrometer in step-sweep mode for high-resolution molecular spectroscopy,” *J. Quant. Spectrosc. Radiat. Transf.*, vol. 287, 2022, Art. no. 108239.

[290] M. Gianella *et al.*, “High-resolution and gapless dual comb spectroscopy with current-tuned quantum cascade lasers,” *Opt. Express*, vol. 28, no. 5, pp. 6197–6208, 2020.

[291] H. Noda, K. Ataka, L. J. Wan, and M. Osawa, “Time-resolved surface-enhanced infra-red study of molecular adsorption at the electrochemical interface,” *Surf. Sci.*, vol. 427–428, pp. 190–194, 1999.

[292] A. Berná, J. M. Delgado, J. M. Orts, A. Rodes, and J. M. Feliu, “Spectroelectrochemical study of the adsorption of acetate anions at gold single crystal and thin-film electrodes,” *Electrochim. Acta*, vol. 53, no. 5, pp. 2309–2321, 2008.

[293] A. Rodes, J. M. Orts, J. M. Pérez, J. M. Feliu, and A. Aldaz, “Sulphate adsorption at chemically deposited silver thin film electrodes: Time-dependent behaviour as studied by internal reflection step-scan infrared spectroscopy,” *Electrochem. Commun.*, vol. 5, no. 1, pp. 56–60, 2003.

[294] E. Lins, S. Read, B. Unni, S. M. Rosendahl, and I. J. Burgess, “Microsecond resolved infrared spectroelectrochemistry using dual frequency comb IR lasers,” *Anal. Chem.*, vol. 92, no. 9, pp. 6241–6244, 2020.

[295] T. A. Morhart *et al.*, “Surface enhanced infrared spectroelectrochemistry using a microband electrode,” *Can. J. Chem.*, vol. 100, no. 7, pp. 495–499, 2022.

[296] H. Lange *et al.*, “Adsorption behavior of 4-methoxypyridine on gold nanoparticles,” *Langmuir*, vol. 27, no. 11, pp. 7258–7264, 2011.

[297] A. Agrawal *et al.*, “Resonant coupling between molecular vibrations and localized surface plasmon resonance of faceted metal oxide nanocrystals,” *Nano Lett.*, vol. 17, no. 4, pp. 2611–2620, 2017.

[298] I. R. Andvaag, E. Lins, and I. J. Burgess, “An effective medium theory description of surface-enhanced infrared absorption from metal island layers grown on conductive metal oxide films,” *J. Phys. Chem. C*, vol. 125, no. 40, pp. 22 301–22 311, 2021.

[299] I. Langmuir and V. J. Schaefer, “The effect of dissolved salts on insoluble monolayers,” *J. Am. Chem. Soc.*, vol. 59, no. 11, pp. 2400–2414, 1937.

[300] J. Chen, “Simulating stochastic adsorption of diluted solute molecules at interfaces,” *AIP Adv.*, vol. 12, no. 1, 2022, Art. no. 015318.

[301] Y. Hu, X. Diao, C. Wang, W. Hao, and T. Wang, “Effects of heat treatment on properties of ITO films prepared by rf magnetron sputtering,” *Vacuum*, vol. 75, no. 2, pp. 183–188, 2004.

[302] J. Gwamuri *et al.*, “Limitations of ultra-thin transparent conducting oxides for integration into plasmonic-enhanced thin-film solar photovoltaic devices,” *Mater. Renew. Sustain. Energy*, vol. 4, no. 3, pp. 1–11, 2015.

[303] J. R. Rumble, Ed., *CRC Handbook of Chemistry and Physics*, 102nd ed. Boca Raton, FL, USA: CRC Press, 2021.

[304] K. N. Lee *et al.*, “Surface chemical treatment for the cleaning of AlN and GaN surfaces,” *J. Electrochem. Soc.*, vol. 147, no. 8, p. 3087, 2000.

[305] A. Sherman, “In situ removal of native oxide from silicon wafers,” *J. Vac. Sci. Technol. B*, vol. 8, no. 4, pp. 656–657, 1990.

[306] M. Böhmisch, F. Burmeister, A. Rettenberger, J. Zimmermann, J. Boneberg, and P. Leiderer, “Atomic force microscope based Kelvin probe measurements: Application to an electrochemical reaction,” *J. Phys. Chem. B*, vol. 101, no. 49, pp. 10 162–10 165, 1997.

[307] P. A. Fernández Garrillo, B. Grévin, N. Chevalier, and Ł. Borowik, “Calibrated work function mapping by Kelvin probe force microscopy,” *Rev. Sci. Instrum.*, vol. 89, no. 4, 2018, Art. no. 043702.

[308] W. N. Hansen and G. J. Hansen, “Standard reference surfaces for work function measurements in air,” *Surf. Sci.*, vol. 481, no. 1–3, pp. 172–184, 2001.

[309] A. Liscio, V. Palermo, K. Müllen, and P. Samorì, “Tip-sample interactions in Kelvin probe force microscopy: Quantitative measurement of the local surface potential,” *J. Phys. Chem. C*, vol. 112, no. 44, pp. 17 368–17 377, 2008.

[310] C. Sommerhalter, T. W. Matthes, T. Glatzel, A. Jäger-Waldau, and M. C. Lux-Steiner, “High-sensitivity quantitative Kelvin probe microscopy by noncontact ultra-high-vacuum atomic force microscopy,” *Appl. Phys. Lett.*, vol. 75, no. 2, pp. 286–288, 1999.

[311] T. Schultz, “A unified secondary electron cut-off presentation and common mistakes in photoelectron spectroscopy,” *Electron. Struct.*, vol. 4, no. 4, 2022, Art. no. 044002.

[312] P. E. Laibinis, C. D. Bain, and G. M. Whitesides, "Attenuation of photoelectrons in monolayers of n-alkanethiols adsorbed on copper, silver, and gold," *J. Phys. Chem.*, vol. 95, no. 18, pp. 7017–7021, 1991.

[313] A. Jablonski, "Evaluation of procedures for overlayer thickness determination from XPS intensities," *Surf. Sci.*, vol. 688, pp. 14–24, 2019.

[314] B. R. Strohmeier, "An ESCA method for determining the oxide thickness on aluminum alloys," *Surf. Interface Anal.*, vol. 15, no. 1, pp. 51–56, 1990.

[315] C. J. Powell and A. Jablonski, "NIST electron inelastic-mean-free-path database 71, version 1.01999." 1999. Distributed by the National Institute of Standards and Technology.

[316] S. Tanuma, C. J. Powell, and D. R. Penn, "Calculations of electorn inelastic mean free paths. II. Data for 27 elements over the 50–2000 eV range," *Surf. Interface Anal.*, vol. 17, no. 13, pp. 911–926, 1991.

[317] H. Shinotsuka, S. Tanuma, C. J. Powell, and D. R. Penn, "Calculations of electron inelastic mean free paths. XII. Data for 42 inorganic compounds over the 50 eV to 200 keV range with the full Penn algorithm," *Surf. Interface Anal.*, vol. 51, no. 4, pp. 427–457, 2019.

[318] R. E. Scholten, "Enhanced laser shutter using a hard disk drive rotary voice-coil actuator," *Rev. Sci. Instrum.*, vol. 78, no. 2, 2007, Art. no. 026101.

[319] H. Card, "Aluminum—silicon Schottky barriers and ohmic contacts in integrated circuits," *IEEE Trans. Electron Devices*, vol. 23, no. 6, pp. 538–544, 1976.

[320] T. Hara, N. Ohtsuka, S. Enomoto, T. Hirayama, K. Amemiya, and M. Furukawa, "Low resistance Al/Si ohmic contacts on boron implanted shallow p^+ Si layers formed by halogen lamp annealing," *Jpn. J. Appl. Phys.*, vol. 22, no. 11A, p. L683, 1983.

[321] R. Dietmüller, "Hybrid organic-inorganic heterojunctions for photovoltaic applications," Ph.D. dissertation, Walter Schottky Inst., Tech. Univ. Munich, Garching, Germany, 2012.

[322] J. H. Werner, U. Spadaccini, and F. Banhart, "Low-temperature ohmic Au/Sb contacts to *n*-type Si," *J. Appl. Phys.*, vol. 75, no. 2, pp. 994–997, 1994.

[323] J. Q. Liu, C. Wang, T. Zhu, W. J. Wu, J. Fan, and L. C. Tu, "Low temperature fabrication and doping concentration analysis of Au/Sb ohmic contacts to *n*-type Si," *AIP Adv.*, vol. 5, no. 11, 2015, Art. no. 117112.

[324] E. Yablonovitch, D. L. Allara, C. C. Chang, T. Gmitter, and T. B. Bright, "Unusually low surface-recombination velocity on silicon and germanium surfaces," *Phys. Rev. Lett.*, vol. 57, no. 2, pp. 249–252, 1986.

[325] A. A. Fashina *et al.*, "Surface texture and optical properties of crystalline silicon substrates," *J. Renew. Sustain. Energy*, vol. 7, no. 6, 2015, Art. no. 063119.

[326] T. A. Morhart, B. Unni, M. J. Lardner, and I. J. Burgess, “Electrochemical ATR-SEIRAS using low-cost, micromachined Si wafers,” *Anal. Chem.*, vol. 89, no. 21, pp. 11 818–11 824, 2017.

[327] Y.-C. Tsai and C. Bayram, “Structural and electronic properties of hexagonal and cubic phase AlGaInN alloys investigated using first principles calculations,” *Sci. Rep.*, vol. 9, no. 1, 2019, Art. no. 6583.

List of Publications

The following publications were published over the course of this work. Due to a change in surname, publications prior to 2023 were published under the name “Felix Eckmann”.

First Author:

- **F. Rauh**, J. Dittloff, M. Stutzmann, I. D. Sharp, *Nanostructured Black Silicon as a Stable and Surface-Sensitive Platform for Time-Resolved In Situ Electrochemical Infrared Absorption Spectroscopy*, ACS Applied Materials and Interfaces, **16.5**, 6653–6664 (2024)
- **F. Rauh**, F. Pantle, M. Stutzmann, *Morphology, Energy Level Alignment and Charge Transfer at the Protoporphyrin IX - Semiconductor Interface*, Langmuir, **39.14**, 5095–5106 (2023)
- **F. Rauh**, O. Bienek, I. D. Sharp, M. Stutzmann, *Conversion of a 3D printer for versatile automation of dip coating processes*, Review of Scientific Instruments, **94**, 083901 (2023)

Co-Author:

- M. Kraut, F. Pantle, J. Winnerl, M. Hetzl, **F. Eckmann**, I. D. Sharp, M. Stutzmann, *Photo-induced selective etching of GaN nanowires in water*, Nanoscale, **11.16**, 7967-7975 (2019)
- L. Hüttenhofer, **F. Eckmann**, A. Lauri, J. Cambiasso, E.a Pensa, Y. Li, E. Cortes, I. D. Sharp, S. A. Maier, *Anapole Excitations in Oxygen-Vacancy-Rich $TiO_{2\text{-}x}$ Nanoresonators: Tuning the Absorption for Photocatalysis in the Visible Spectrum*, ACS nano, **14.2**, 2456–2464 (2020)
- A. MP Botas, J. P. Leitao, B. P. Falcao, M. Wiesinger, **F. Eckmann**, J. P. Teixeira, H. Wiggers, M. Stutzmann, Rute AS Ferreira, Rui N Pereira, *Silicon Nanoparticle Films Infilled with Al2O3 Using Atomic Layer Deposition for Photosensor, Light Emission, and Photovoltaic Applications*, ACS Applied Nano Materials, **3.6**, 5033-5044 (2020)
- M. Kraut, F. Pantle, S. Wörle, E. Sirotti, A. Zeidler, **F. Eckmann**, M. Stutzmann, *Influence of environmental conditions and surface treatments on the photoluminescence properties of GaN nanowires and nanofins*, Nanotechnology, **32.49**, 495703 (2021)
- M. J. Kloberg, H. Yu, E. Groß, **F. Eckmann**, T. Restle, T. F. Fässler, J. GC Veinot, B. Rieger, *Surface-Anisotropic Janus Silicon Quantum Dots via Masking on 2D Silicon Nanosheets*, Advanced Materials, **33.38**, 2100288 (2021)

- X. Jiang, P. Chotard, K. Luo, **F. Eckmann**, S. Tu, M. A Reus, S. Yin, J. Reitenbach, C. L. Weindl, M. Schwartzkopf, S. V Roth, P. Müller-Buschbaum, *Revealing Donor–Acceptor Interaction on the Printed Active Layer Morphology and the Formation Kinetics for Non-fullerene Organic Solar Cells at Ambient Conditions*, Advanced Energy Materials, **12.14**, 2103977 (2022)
- A. Henning, J. D. Bartl, L. Wolz, M. Christis, **F. Rauh**, M. Bissolo, T. Grünleitner, J. Eichhorn, P. Zeller, M. Amati, L. Gregoratti, J. J. Finley, B. Rieger, M. Stutzmann, I. D. Sharp, *Spatially-Modulated Silicon Interface Energetics Via Hydrogen Plasma-Assisted Atomic Layer Deposition of Ultrathin Alumina*, Advanced Materials Interfaces, **10.6**, 2202166 (2023)
- A. Shcherbakov, K. Synnatschke, S. Bodnar, J. Zerhoch, L. Eyre, **F. Rauh**, M. W. Heindl, S.Liu, J. Konecny, I. D. Sharp, Z. Sofer, C. Backes, F. Deschler, *Solution-processed NiPS3 thin films from Liquid Exfoliated Inks with Long-Lived Spin-Entangled Excitons*, ACS Nano, **17.11**, 10423–10430 (2023)
- A. Stadlbauer, L. Eyre, A. Biewald, **F. Rauh**, M. W. Heindl, S. Liu, J. Zerhoch, S. Feldmann, A. Hartschuh, Felix Deschler, *Control of Photoluminescence in Mixed-Phase Ruddlesden-Popper Hybrid Organic-Inorganic Lead-Iodide Perovskites with Photoexcitation Energy*, Advanced Optical Materials, 2301331 (2023)

The following manuscript is in preparation and will be submitted for publication in a peer-reviewed journal:

- **F. Rauh**, K. Rickmeyer, Z. Wang, M. Stutzmann, C. Hess, *Morphology and Energy Level Alignment of Mabiq Langmuir–Blodgett Films on Semiconductors*

Acknowledgements

Finally, I want to thank everyone who supported me during my work on this thesis. In particular, I want to thank:

- My supervisor **Prof. Dr. Martin Stutzmann** for the opportunity to work on this project. Your support, scientific guidance, trust, but also the freedom to develop and pursue my ideas enabled me to grow as a scientist. I greatly appreciate your valuable advice based on years of experience, which nevertheless left room to pursue my own approaches and allowed me to learn from my mistakes. This led me to gain a lot more insight into the process of scientific discovery and the accompanying challenges, which I am very thankful for.
- **Prof. Dr. Ian D. Sharp** for your scientific advice, especially regarding the development of in-situ analysis techniques. The opportunity to collaborate on the development of in-situ FTIR and transient absorption methods starting from a clean slate – despite being borderline frustrating at times – was a lot of fun and a great learning experience. I am very thankful for the time you were able to free up for my questions and requests in spite of your full schedule as a newly established professor with a growing team.
- **Johannes Dittloff** for your relentless efforts in developing stable gold surfaces and the detective work to find noise sources on the TA setup. Together, we were able to take on the challenges of unreproducible experiments and sometimes over-optimistic literature reports. I hope that our first results will enable you to discover the next big thing in in-situ spectroscopy!
- **Ken Lim** for making your way over to Germany to join me in tackling a rebuilding of our PL setup. I greatly appreciate the work you put into ironing out my bad coding and hunting for the tiniest of PL signals from the monolayers in the dark lab.
- **Jennifer Padberg** for daring to join me in discovering the field of molecular monolayers at the very beginning of my research work. Together, we learned how to perform Langmuir-Blodgett deposition and laid the groundwork in the synthesis and analysis.
- **Dr. Johanna Eichhorn**, **Dr. Constantin Walenta**, **Dr. Chang-Ming Jiang** and **Dr. Alex Henning** for your expertise and help in the setup of experiments and sharing your insights from other labs and fields of research.
- **Johannes Bartl** for numerous fruitful discussions and the support in surface functionalization reactions.
- **Prof. Dr. Martin Brandt** for always having an open ear and door. Your ability to translate problems between first-floor offices and PhD students surely has – more often than once

– prevented small issues from evolving into large problems.

- **Kerstin Rickmeyer**, **Zhenzhen Wang**, and **Prof. Dr. Corinna Hess** for initiating the collaboration and providing material as well as insight on Mabiq complexes.
- All collaborators, especially those within **ATUMS**, for the fruitful scientific discussions and the joint lab work. The ability to collaborate with scientists from other countries and fields presented me with opportunities to gain insight into new viewpoints and approaches, which I greatly value and appreciate.
- **Joana Figueiredo** and **Daniela Huber** for the administrative work and for your effort in keeping everything running as smoothly as possible.
- All former and current technicians of the WSI, in particular, **Claudia Paulus**, **Sonja Matich**, **Michael Fischer** and **Nick Schröder**, for the efforts you put into maintaining and improving the labs. Your experience in the lab and workshop greatly helped to realize custom experimental setups and allowed to carry out reproducible experiments.
- The IT team, in particular, **Paul Schmiedeke** and **Patrick Simon**, for caring for our IT systems in addition to your scientific work.
- **Florian Pantle** for your hands-on attitude and the ability to put function over form, which helped me to keep focus and prioritize relevant tasks instead of overoptimizing.
- **Theresa Hoffmann** for sharing tips and tricks in navigating the forms and pitfalls of university bureaucracy, especially regarding deadlines that I am always prone to miss. I really enjoyed the joint research stay in Canada, exploring the mountains and labs together.
- **Elise Sirotti** for your inspiring joyful attitude and relentless endurance in the face of setbacks. I sincerely hope that this endurance pays off in amazing results!
- **Andreas Zeidler** for the hours we spent learning basic plumbing and reverse-engineering of the evaporator system. I am thankful for the many thought-provoking and entertaining discussions and for always keeping the team spirit up.
- **Oliver Bienek** for joining me in late evening sessions fixing broken devices or contemplating weird measurement data.
- **Hannah Schamoni** for letting me join the group as a Master's student and guiding me through my first experiments. Your efforts raised my interest in organic semiconductor materials, which in the end led me to this topic and work.
- My fellow PhD students at the WSI, in particular, **Philipp Moser, Tobias Schreitmüller, Tim Rieth, Matthias Kuhl, Viktoria Kunzelmann, Laura Wagner, David Vogl, Anna Stadlbauer, Lukas Wolz, William Rauhaus, Fabio Del Giudice** for creating a great at-

mosphere, joyful coffee breaks and fun parties.

- My family, especially **Gitti**, **Norbert**, **Uta** and **Gerhard** for your advice and for supporting me in my decisions.
- **Stephanie** for your empathy, love, and trust.